University of Nottingham
UK | CHINA | MALAYSIA

Synthesis of porous materials for the removal of organic dyes in wastewater treatment

Dawei Lan, BEng, MSc

Thesis Submitted to the University of Nottingham for the degree of Doctor of Philosophy

May 2024

Abstract

The work in this thesis focuses on the synthesis of porous materials for wastewater treatment. These novel porous materials have enhanced functional performances than the original ones. There are three projects in this thesis (in chapter 4-6), including Co-doped UiO-66 for enhanced adsorption of organic dyes. Porous g-C_3N_4 for improved photodegradation of RhB, and g-C_3N_4/UiO-66 nanocomposites for promoted photodecomposition of RhB.

Firstly, a novel CoUiO-66 adsorbent was successfully prepared by doping the Co element into the framework of UiO-66 with an in-situ oil bath synthesis. This modification ensures that the materials retain relatively good crystallinity. The Co-doping has a major impact on the particle size and morphology of the original MOFs. The CoUiO-66 exhibits larger surface area and pore size than pristine UiO-66. Accordingly, the maximum adsorption amount of malachite green (MG) on CoUiO-66 (628.93 mg/g) was significantly larger compared with UiO-66 (343.64 mg/g), which was due to more active adsorption sites. In addition, the CoUiO-66 also showed a superior adsorption capacity on rhodamine B (RhB) (1106.22 mg/g). The CoUiO-66 material could be a promising adsorbent for wastewater treatment.

In the second part, a novel mesoporous g-C_3N_4 was fabricated with a one-pot route successfully. A series of characterisations revealed that the mesoporous sample maintained the typical structures of g-C_3N_4. The findings displayed that this mesoporous material had enlarged porosity and optical properties. The mesoporous g-C_3N_4 (99.60%) exhibited 3.88 times better photocatalytic efficiency than bulk g-C_3N_4

(25.63%) and a 11.19 times faster reaction rate in the same period.

Thirdly, a new composite of Zr-MOFs (UiO-66) and porous g-C_3N_4 was prepared through an in-situ preparation route. The photocatalytic properties of these obtained samples were measured through photodegradation of rhodamine B using visible light illumination. The nanocomposites were analysed by a series of characterizations. The photodegradation tests demonstrated that the nanocomposites (CNU-0.5) could achieve almost 100% efficiency in degrading RhB (60 mg/L, 100 mL) in 70 min under visible light. CNU-0.5 showed much better photocatalytic removal efficiency of RhB, which was 6.46 and 10.56 times higher than UiO-66 and g-C_3N_4. The improved photocatalytic performances were due to large surface area, enhanced optical adsorption, and excellent heterojunction.

Lastly, some recommendations are proposed for future work, such as more experiments could be performed to assess the practical potential. Like the effect of ion strength, easy recovery, and the test in some real water environments. Moreover, more investigations to reveal the mechanism and product in each process could be further studied, which is also very essential for the understanding of the interface mechanism of these reactions and inspiring the direction and relationship for the future design and synthesis of related functional materials.

Acknowledgement

First of all, I wish to express my heartfelt gratitude to all my supervisors. I really appreciate my main supervisor Prof. Tao Wu for his valuable guidance and patient support. I would not be able to complete my PhD career without his supervision. Professor Wu has given me many useful advice on my experiments and paperwork, which is of great essence on improving my academic career.

I am also thankful to my co-supervisors Dr. Mengxia Xu, Dr. Xiang Luo and Prof. Chenggong Sun. Their suggestions are very meaningful on my research life. I am very appreciative of the great opportunity to work on this research program.

I would also like to thank all the colleagues in CBI. Thank my roommates Huiwen Zhu and Jianwen Zhang for their help in my daily life, it is a precious friendship and unforgettable journey. Thank all the group members, including but not limited to, Fan Wang, Chengrui Xie, Gang Yang, Zeyu Guo, Quhan Chen, Yueying Zheng. Thanks for their various suggestions on scientific research, which inspired me a lot. Thank Carey, William and other colleagues for their contributions to the management and support of the laboratory.

Most importantly, I would like to express my thanks to my parents and old friends. It is their love and unconditional supports and encouragements that strengthen me to face every difficulty in my life.

Lastly, Thanks to the following fundings for the financial support:

- Ningbo Municipal Engineering Research Centre for Solid Carbonaceous Wastes Processing and Utilization Technologies

- Ningbo Science and Technologies Innovation 2025 Major Special Project
- Zhejiang Provincial Department of Science and Technology
- Ningbo Bureau of Science and Technology
- Key Laboratory for Carbonaceous Wastes Processing and Process Intensification Research of Zhejiang Province for providing experimental instruments and facilities.
- University of Nottingham Ningbo China for offering the PhD scholarship

Achievements

Published papers

- **Lan DW**, Zhu HW, Zhang JW, Li S, Chen QH, Wang CX, Wu T, Xu MX. Adsorptive removal of organic dyes via porous materials for wastewater treatment in recent decades: A review on species, mechanisms and perspectives[J]. Chemosphere, 2022, 133464. (ESI Highly cited paper)
- **Lan DW**, Zhu HW, Xie CR, Zhang JW, Wang F, Zheng YY, Guo ZY, Wu T, Xu MX. A green one-pot synthesis of mesoporous g-C_3N_4 for promoted organic dyes photodegradation in wastewater treatment. Industrial & Engineering Chemistry Research[J]. 2024, 63, 8, 3491–3503.
- **Lan DW**, Zhu HW, Xie CR, Zhang JW, Wang F, Zheng YY, Guo ZY, Wu T, Xu MX. Heterojunction of UiO-66 and porous g-C_3N_4 for boosted photocatalytic removal of organic dye. Applied Surface Science[J] Volume 655, 15 May 2024, 159623.
- Wang F, Zheng YY, Wei XG, **Lan DW**, Zhu JT, Chen YJ, Wo ZQ, Wu T. Controlled synthesis of Fe_3O_4/MnO_2 (3 1 0)/ZIF-67 composite with enhanced synergetic effects for the highly selective and efficient adsorption of Cu (II) from simulated copperplating effluents[J]. Environmental Research, 2023, 116940.
- Fan Wang, Yueying Zheng, Quhan Chen, Zijun Yan, **Dawei Lan**, Edward Lester, Tao Wu, A critical review of facets and defects in different MnO_2 crystalline phases and controlled synthesis – Its properties and applications in the energy field[J], Coordination Chemistry Reviews, Volume 500, 1 February 2024, 215537.

- Jianwen Zhang, Chenxi Wang, **Dawei Lan**, etc, Rational design of structured Co_3O_4@silicalite-1/SiC foam catalyst for microwave-assisted highly efficient conversion of bio-isopropanol to green propylene[J], Journal of Cleaner Production, 2024, 141537.

Manuscripts in submission

- **Lan DW**, Zhu HW, Zhang JW, Wang F, Zheng YY, Guo ZY, Wu T, Xu MX. Development of a Co-doped UiO-66 adsorbent for significantly enhanced adsorption of organic dyes from wastewater (Under review).

Award

Chinese scholarship council (CSC) scholarship, 2021.

Content

List of Figures

List of Tables

List of Abbreviations

XRD	X-ray diffraction
XPS	X-ray Photoelectron Spectroscopy
SEM	Scanning Electron Microscopy
TEM	Transmission Electron Microscope
TGA	Thermal Gravimetric Analysis
FTIR	Fourier Transform Infrared Spectroscopy
EDX	Energy X-ray spectroscopy
BET	Brunauer–Emmett–Teller
PL	Photoluminescence
MOFs	Metal-organic frameworks
MG	Malachite green
RhB	Rhodamine B
EIS	Electrochemical Impedance Spectroscopy

Chapter 1 Introduction

This chapter mainly introduces the significance of this research topic on wastewater treatment, the aim and objectives of this work, and the structure of this thesis is listed as well.

1.1 Background

The rapid pace of industrialization has brought so many conveniences to our life, meanwhile, a lot of problems accompanied with the development should draw our attention [1]. Up to now, it was estimated that over 100,000 of different commercial dyes and piments are documented with a production of 7×10^5 tons annually worldwide [2]. Various industries, such as rubber, textiles, cosmetics leather, gasoline, pharmaceutical, and food, have used different classes of dyes in the production [3]. Consequently, a considerable amount of coloured effluent derived from those industries discharge into natural environment, it is reported that dyes discharged into wastewater streams is approximately 100 tons/year [4]. Their presence in the hydrosphere possesses a serious threaten to both human and aquatic life.

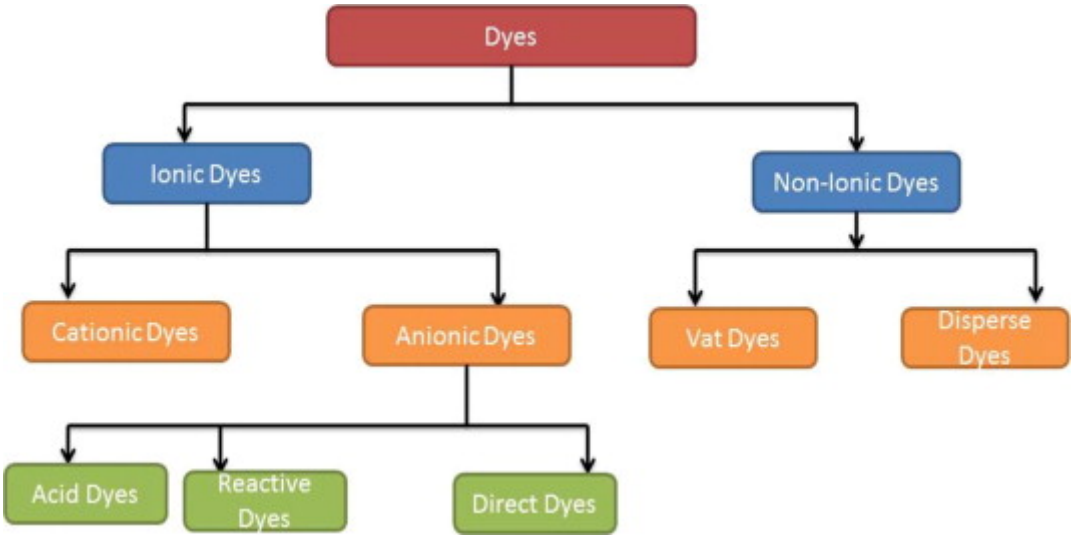

Figure 1.1 Categorization of dyes according to ionic charge [5].

Dyes can be used to modify the colour characteristics of different products from various industries. They are generally defined as ionizing and aromatic organic compounds which can connect themselves to surfaces to impart colour [6]. Dye molecules consist of chromophores and auxochromes, which are the two key components [7]. In addition, dyes can be classified in several ways, such as chemical structure, application to the fibre type and their solubility in aqueous solution. Also, dyes can be generally divided into anionic, cationic, and non-ionic dyes. The detailed categorization is illustrated in Figure 1.1. Anionic and cationic surfactants may have different efficiency on the dye adsorption on the basis of the dye type [8]. The presence of dyes in the hydrosphere possess serious pollution even at very low concentrations due to their strong visibility [9]. The oxygen transfer mechanism and the self-purification in water environment will be weakened when concentrated dye effluents with high pH are purged into water body [10]. The complex recalcitrant molecular structures of dyes make them inert and hard to biodegrade. It is already demonstrated that dyes are capable of reducing sunlight penetration and resisting photochemical, which has a negative impact on the photosynthesis of aquatic plants [11]. Furthermore, the degradation products of dyes are generally toxic or even mutagenic, carcinogenic, which has a potential risk to cause severe damage to human beings and aquatic life [12].

The discharge of dye effluent was not given much attention in the past. Only when health troubles related to the dye pollution started to arise in the past 30 years that this issue began to come into concern. Recently, a series of laws have been set on the

limitation of toxic coloured wastewater in hydrosphere by the environmental legislature [13]. Table 1.1 shows the international limitation standard of dye effluent pollutant. Levels of each index in dye effluent should reach the specification before discharging into natural environment. In that regard. It is of great essence to find effective technologies to decolourise the polluted water and attenuate the toxicity of dyes under the recommended water quality guidelines.

Table 1.1 International standard of dye effluent discharge into the environment [13]

Factor	Standard allowed
Biological oxygen demand	Below 30 mg/L
Chemical oxygen demand	Below 50 mg/L
Colour	Below 1 ppm
pH	Between 6–9
Suspended solids	Below 20 mg/L
Temperature	Below 42 °C
Toxic pollutants	Not allowed to be released

In recent decades, numerous methods have been developed for the removal of dyes from wastewater, such as coagulation, chemical oxidation [14], membrane separation, solvent extraction, photocatalytic degradation and adsorption, etc [15]. The existing methods are generally divided into physical, chemical, and biological methods [16].

Biological treatments, or called biodegradation, is the process of using metabolic potential of microorganisms to eliminate virous compounds [17]. This approach can transform pollutants into smaller molecules which are less deleterious to the

environment, which are common, simple and ecological. The method is generally operated via numerous microorganisms to decolorize dye molecules under aerobic or anaerobic environment [18]. Also, the biological process is feasible to lower concentration of contaminants, while physical or chemical methods do not have the capacity [19]. However, this approach is not sufficient enough to eliminate hazards from dye wastewater when it operates alone. It is indicated that bioremediation methods are insufficient in decolorization owing to the stable and complicated chemical structures and difficult biodegradation of dyestuff. Moreover, the main limitation of this process is that it requires a large amount of time consuming, land and less predictable [20].

Physical methods for dye removal are usually straightforward which are achieved by mass transfer mechanism [21]. Conventional physical processes include adsorption, coagulation, ion exchange, membrane separation, etc [22]. For their simplicity and efficiency, branches of physical processes are the most widely used methods for dye removal among the three classes. The physical way needs the least amount of chemicals [23]. Moreover, the physical methods are more predictable than others, for the reason that they do not require to deal with living organisms [24]. According to previous researches, adsorption has proven to be one of the most widely used wastewater treatment method, due to its efficiency and effectiveness in eliminating contaminants from wastewater [25]. Adsorption provides an alternative method for contaminated water treatment, especially when the adsorbents are cheap, easily accessible and require less pre-treatment processes [26].

Chemical methods are the routes which convert dyes into non-hazardous molecules via chemical reactions [27]. Conventional chemical methods include advanced oxidation, electrochemical process, ozonation, photochemical, ultraviolet irradiation, etc [28]. The efficiency of chemical processes is related to the interaction between contaminants and the nature of chemicals used in wastewater [29]. Most of these chemical techniques can decolorize wastewater and degrade toxic hazards efficiently. However, the production and deposition of sludge created by these methods will result in expensive cost [30]. Moreover, tremendous consumption of chemical reagents and electrical energy in the chemical techniques will give rise to some secondary pollution problems [31]. In addition, chemical methods usually require specific equipment and high electrical energy, which contributes the routes to be commercially unattractive [32]. To overcome these limitations, various advanced oxidation techniques has been proposed with simple, low- cost and environmental-friendly benefits. Photocatalysis is an example that shows great potential in wastewater treatment.

Although the development of wastewater treatment technology is rapidly advanced, it is still a challenging problem to find an economic and effective technology for the removal of dyes. Various techniques have their superiorities and restrictions for the eradication of contaminants. Among all these methods, adsorption and photocatalysis both show great potential in the field of dyes removal due to their cheapness, simplicity, and environmental friendliness [33].

1.2 Aim and objectives.

The aim of this work is to develop functional materials for the removal of organic dyes in wastewater treatment with excellent performance. In particular, this research will focus on the design and synthesis of porous materials for the adsorption and photocatalytic degradation of dyes, as both these routes are considered as promising methods in wastewater treatment. MOFs and g-C_3N_4 will be investigated as the potential candidates for the removal of organic dyes. In addition, the reaction mechanisms will be studied based on the characterization and experiments results. To achieve this aim, the specific objectives of this research can be divided into following parts:

1. To evaluate the effects of metal-dope modification method on the adsorption performance of MOFs materials, Zr-MOFs (UiO-66), as a typical MOFs material with excellent stability and good adsorption capacity, will be chose to be the candidate for proposed promoted adsorption performance on the removal of organic dyes.
2. To explore a feasible route to improve the photocatalytic property of bulk g-C_3N_4. By introducing mesoporous structures into the bulk g-C_3N_4, the effects of porosity on the photodecomposition performance of organic dyes will be investigated and confirmed.
3. To reveal the effects of heterojunction structure on the enhanced photocatalytic removal of dyes, UiO-66 and porous g-C_3N_4 will be chosen as the parent material to form heterojunction nanohybrids. A series of tests will be carried out to investigate the possibility of heterojunction method on promoting

photocatalytic degradation of organic dyes.

1.3 Structure of the thesis

The thesis can be mainly divided into seven chapters as follows:

Chapter one introduces the sever impacts of water pollution, particularly, the serious damage caused by dye pollution, and the significance for the removal of these contaminants.

A comprehensive review on recent literatures related to techniques and materials for the removal of organic dyes is the main content of chapter two. In particular, porous material, as a general category which has been used for diverse environmental applications such as adsorption and photocatalysis, is the focus in this study. The advancement of this kind of material in recent decades are mainly reviewed in this chapter.

In chapter three, it presents the basic experimental instruments for the functional tests of prepared materials, along with the primary characterisation analyses involved in this research.

An effective method to promote the adsorption performance of Zr-MOF material UiO-66 on organic dyes is presented in chapter four. Co-doping modification is employed as a feasible route for this improvement. A comparative study on the pristine and metal-doped sample is carried out to assess the impact of this modification method on adsorption performance.

Chapter five offers a novel approach to form porosity on bulk g-C_3N_4, which can enhance the photocatalytic activity significantly. Photodegradation experiments of RhB

and a number of characterisation tests are performed to reveal the possible mechanism and how the porosity structure can influence the photoactivity.

The formation of heterojunction structures derived from UiO-66 and g-C_3N_4, and how this heterojunction improves the photocatalytic degradation of organic dye is the topic of Chapter six. Measured by the degradation of RhB with visible light, a series of analysis results are performed to confirm the possibility of this method on the enhancement of photocatalytic performance.

Finally, conclusions of this research are made in Chapter seven, together with a few recommendations being made for prospective study.

Chapter 2 Literature review

In the last few decades, much more information on the environmental impacts of dyes usage has become gradually clear, and a number of techniques have been applied to control dyes pollution. Among all the removal techniques, adsorption and photocatalysis show promising potential to eliminate target pollutants. Therefore, we choose these two approaches as the platform to study the wastewater treatment. Moreover, it is widely regarded that the material used in the techniques is a key factor for the removal performance. To get a better understanding of the related research. We conduct a comprehensive review on the recent development of the common materials used for adsorption and photocatalysis.

2.1 Adsorption materials for the removal of organic dyes

Adsorption process is considered as one of the most effective techniques to eliminate dyes from wastewater. Apart from operating conditions, the properties of adsorbents also play a significant role in adsorption capacity [34]. An ideal adsorbent used for dye adsorption should have high surface area, excellent uptake capacity, easy accessibility, high selectivity, etc [35]. Furthermore, it has been validated that the surface properties of adsorbents have a vital effect on adsorption capacity [36]. Thus, it is of great importance to have a deep understanding of the interaction between the adsorbent properties and adsorption capacity. The choice of adsorbents is dependent on various aspects, so that diverse categories of adsorbents and numerous researches have been investigated to achieve the desired elimination of dyestuff from wastewater. Figure 2.1 illustrates some typical types of adsorbents which have showed excellent

potential in adsorption area.

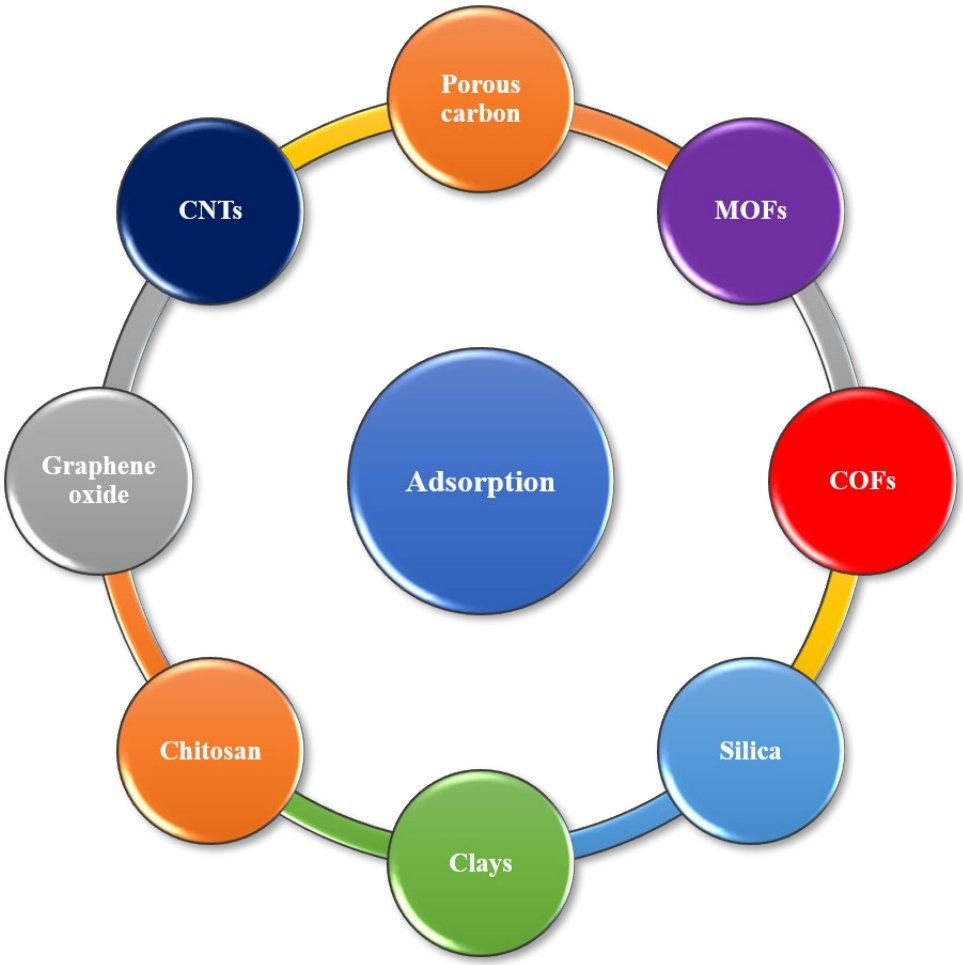

Figure 2.1 Porous materials for the adsorption of dyes

2.1.1 Porous carbon (PC)

Porous carbon (PC), known as the oldest adsorbent, has been widely used in wastewater treatment, owing to its excellent efficiency. PC is the term which defines the carbon-based materials containing abundant interior pore structure. Various properties, such as large surface area, sufficient porosity and numerous functional groups, make PC present versatile applications in environmental area, especially for adsorption process [37].

PC can be derived from a wide spectrum of carbonaceous rich materials, such as

coal, rice and agricultural waste [38]. The fabrication methods of PC can be divided into chemical and physical activation [39]. Physical activation involves two steps: the carbonization of precursor materials at relative low temperature (300-500 ℃), and then followed by activation in carbon dioxide or water vapor atmosphere in higher temperature (500-1000 ℃). Chemical activation is a well-known one step method which takes place in lower temperature and shorter time compared with physical approach [40]. The chemical activating agents play an important role in this activating way. Chemical agents, such as KOH, $ZnCl_2$, H_3PO_4, K_2CO_3, $EeCl_3$ have been proved to be effective activator in the preparation of PC[41]. In addition, precursors, activation time and temperature also have a great influence in this process [42].

Although PC exhibits outstanding adsorption capacity towards numerous pollutants, there are still several demerits that restrict its practical application, including expensive cost, regeneration problem, and poor selectivity [43]. On account of this circumstance, many researchers have focused on searching for economical route to fabricate PC [33]. Thus, biomass waste, as cost-effective, biodegradable and renewable source, has gradually gained researchers' attention [44]. The PC derived from these solid wastes are generally named as biochar. This approach can provide not only an economical way for PC preparation, but also an environmental-friendly solution for waste disposal. Since now, various precursors have been investigated for this approach [44].

Many researchers have utilized biochar for the adsorption of dyes. It was reported that biochar derived from Opuntia ficus-indica was examined to adsorb malachite green

with conventional activation. The findings indicated that this material exhibited efficient adsorption capacity. The surface area of the biochar was 33.62 m^2/g with a maximum uptake of 1341 mg/g [45]. In addition, some scholars used KOH modified biochar derived from lychee seed to investigate the adsorption of methylene blue (MB). This biochar presented a BET surface area of 153 m^2/g with a maximum adsorption capacity of 124.5 mg/g for MB. The results documented that this adsorption procedure was spontaneous and endothermic [46]. Moreover, it was reported that biochar derived from sludge-rice husk was examined to adsorb different dyestuffs. The material was pyrolyzed in 500 °C with a BET surface area of 29.18 m^2/g. Meanwhile, it showed effective adsorption towards Direct Red 4BS, Acid Orange II, React Blue 19, and Methylene Blue, and chemisorption have a main effect in this adsorption process [47].

2.1.2 Carbon nanotubes (CNTs)

Carbon nanotubes (CNTs) have gained enormous interests in various areas since the discovery in 1991 owing to their special properties [48]. CNTs are carbon nanomaterials which roll up graphitic carbon sheets into cylinders within nanometre scale [49]. In accordance with the different layers of graphene sheets, CNTs include two categories: single-walled (SWCNTs) and multi-walled carbon nanotubes (MWCBTs) [50]. The SWCNTs has one single graphene sheet, while MWCNTs are composed of more than one graphene sheets staking of concentric cylinders with an interspacing of 0.34 nm [51]. Figure 2.2 illustrates the typical structures of SWCNTs and MWCNTs. SWCNTs are generally well- defined with higher specific area and pore volume compared with MWCNTs. However, MWCNTs offer the benefits of easier

synthesis and lower cost of production compared to NNTMs [52]. The hollow and layered structures make CNTs present large specific area (150–1500 $m^{2/}g$) and excellent porosity. The length of CNTs ranges from nm to mm with 100 nm diameters. Moreover, the chemical bonds in CNTs are entirely sp^2 bonds, which offer CNTs outstanding mechanical strength [53]. All these unique properties of CNTs facilitate numerous applications in electronic, medical, space and military fields[54]. In addition, owing to the superior hydrophobicity and strong interaction with pollutants, CNTs have proved to be promising adsorbents towards various contaminants [55].

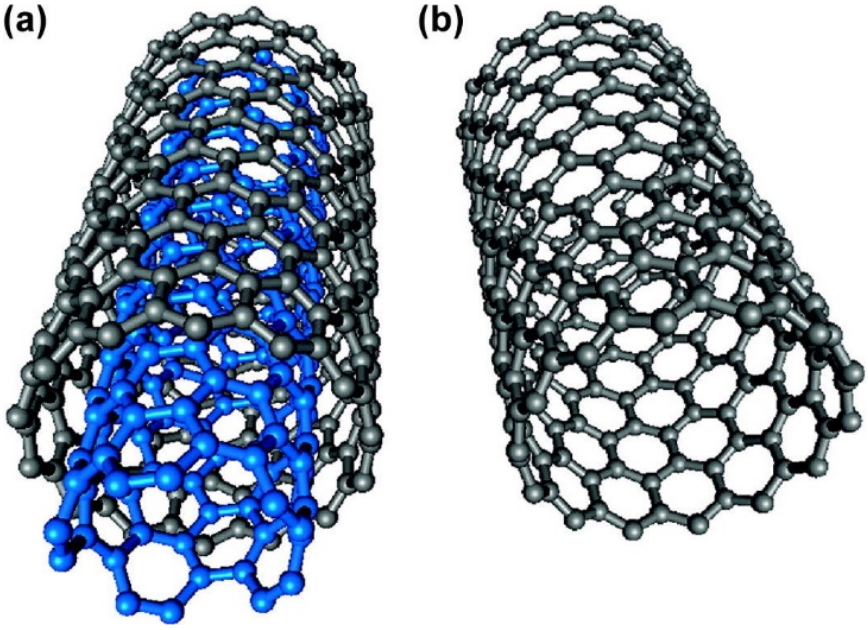

Figure 2.2 Typical structures of (a) MWCNTs and (b) SWCNTs [53]

To the best of our knowledge, the surface properties of adsorbents have a vital effect on the adsorption capacity. It was documented that adsorption capacity of MB showed a positive correlation with specific surface area and pore volume [56]. Another research compared the MB adsorption of AC and CNTs for, the findings indicated that the uptake capacity per unit mass of AC was higher than CNTs, and that of CNTs was higher than AC when surface area normalized [57]. Generally, CNTs are supposed to

possess four possible active site to adsorb foreign components, namely: (1) inner cavities, (2) interstitial channels, (3) external grooves, (4) external surface, as illustrated in Figure 2.3. Plenty of researches have been conducted to investigate the adsorption process via different sites. Findings revealed that most adsorption process occurs in the other three kinds of sites except the inner cavities [58]. Moreover, the nanoscale curvature and graphene layers chirality of CNTs are also postulated to play a vital role in the adsorption process. The different morphology may lead to different aggregation tendency for CNTs, which may further influence the adsorption capacity. When aggregation occurs within CNTs, new adsorption sites emerge while available outer surface declines [59]. Some researchers found that the surface area of CNTs play a more important role in adsorption process than pore volume [60]. Furthermore, it was reported that ultrasonication could promote the adsorption kinetics significantly, owing to the dispersion status of CNTs [61].

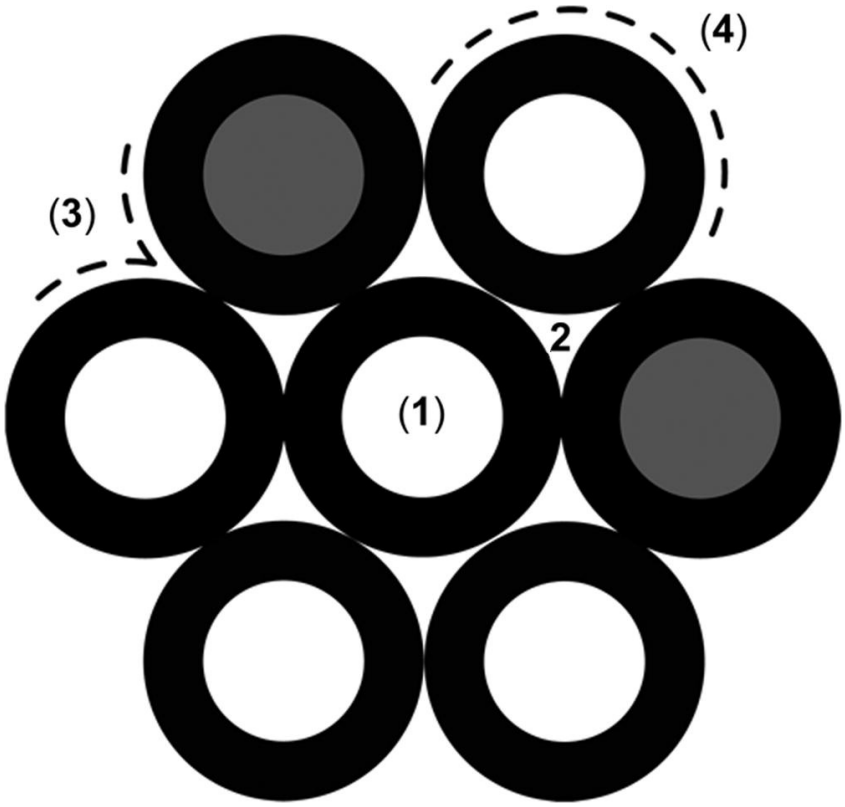

Figure 2.3 Possible adsorption sites in CNTs: (1) inner cavities, (2) interstitial channels, (3) external grooves, (4) external surface [62]

Surface modification, which can enhance dispersibility and reduce aggregation of CNTs in aqueous solutions, has proven to be an effective approach to increase the adsorption capacities towards organic dyes [63]. The active sites on CNTs provide their affinity to interact with other compounds, and functionalization is a key process to promote their efficiency. Acid treatment is a common approach for CNTs functionalized with various acids [64]. It was reported that CNTs modified with non-oxidizing acids possessed only a few of graphitic particles with oxygen functionalities, while CNTs oxidized with nitric acid under certain conditions contained an increasing number of defects. When the nanotubes are exposed to acid environment for enough time, functional groups and additional active sites can be induced into their structures. In

general, the surface on CNTs which exhibits abundant defects presents high surface reactivity for adsorption process [65]. Many researches have confirmed that modified CNTs exhibited a higher efficiency for dye adsorption than pristine CNTs [66, 67].

2.1.3 Graphene oxide and its derivatives

Graphene, as a 2D atomic crystal with the sheet composed of sp^2 bonded carbon atoms in a hexagonal lattice, has gained numerous attention since its discovery in 2004 [68]. Like other nanomaterials, Graphene also has its unique nano structure. Its thickness is just 0.334 nm, and the theoretical surface area can reach 2630 m^2/g, which is much higher than graphite and CNTs. Graphene presents several superior properties, such as high thermal conductivity, excellent electron mobility, exceptional flexibility and strong mechanical strength [69]. As shown in Figure 2.4, Graphene is the primary component for carbon allotropes in different dimensions., including 0D fullerene, 1D carbon nanotubes and 3D graphite [70]. Nevertheless, some limitations, such as easy agglomeration, limited adsorption ability, poor separation and regeneration, challenge the application of graphene. Based on the graphene theory, graphene oxide (GO), recognized as the oxidized form of graphene has been produced and applied to profuse environmental applications owing to its high surface area and plentiful functional groups [71]. The oxidation process can impact the physicochemical properties of GO significantly, the introduced oxygen-containing groups will restrain the electronic and mechanical properties, while enhance the hydrophilicity and colloidal suspension [72]. Consequently, as an important derivative of graphene family, GO has been investigated extensively for the adsorption of enormous contaminants [73]. The typical structures of

graphene and GO are illustrated in Figure 2.5.

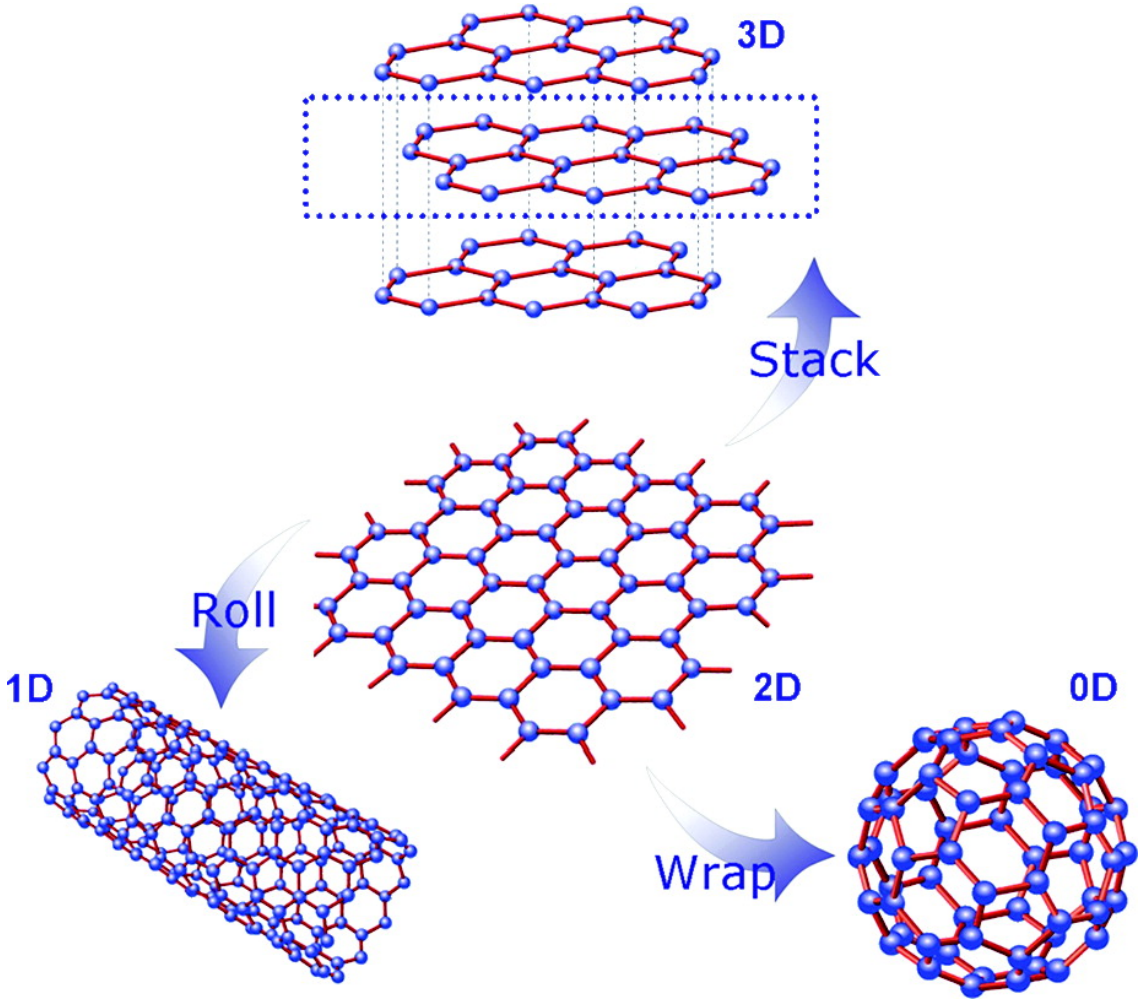

Figure 2.4 2D graphene and other carbon allotropes [70]

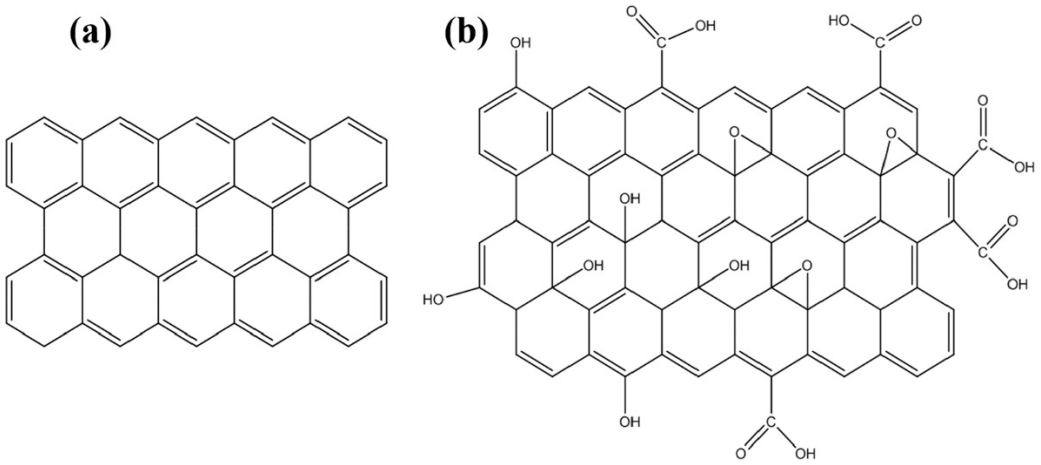

Figure 2.5 Structure of graphene(a) and graphene oxide(b) [74].

The common routes to fabricate GO include chemical oxidation and exfoliation, which can further prepare reduced graphene oxide (rGO), as shown in Figure 2.6. A

variety of synthesis approaches, such as Brodie, Staudenmaier and Hoffman method, have been studied since 1859. Brodie first used graphitizable carbons to produce graphite oxide (GrO) with oxidation process in 1859 [75]. Then forty years later, Staudenmaier added sulfuric acid to enhance the acidity of the mixture on the basis of Brodie method, it was reported that this method was more practical and pragmatical [76]. After that, Hummers documented a convenient method and produced GrO successfully with the mixture of graphite, sodium nitrate, sulfuric acid and potassium permanganate [77]. All these routes could oxidize graphite to diverse levels and increase the interlayer distance of GrO. This increasing interlayer distance weakened the interaction between graphitic layers [78]. Accordingly, GO could be produced from the exfoliation of GrO with ultrasonic or mechanical stirring method [79]. Furthermore, GO could convert into reduced graphene oxide (rGO) via chemical reduction. rGO is also of great significance for various applications, including graphene composites, coatings, paint, energy storage, etc [80].

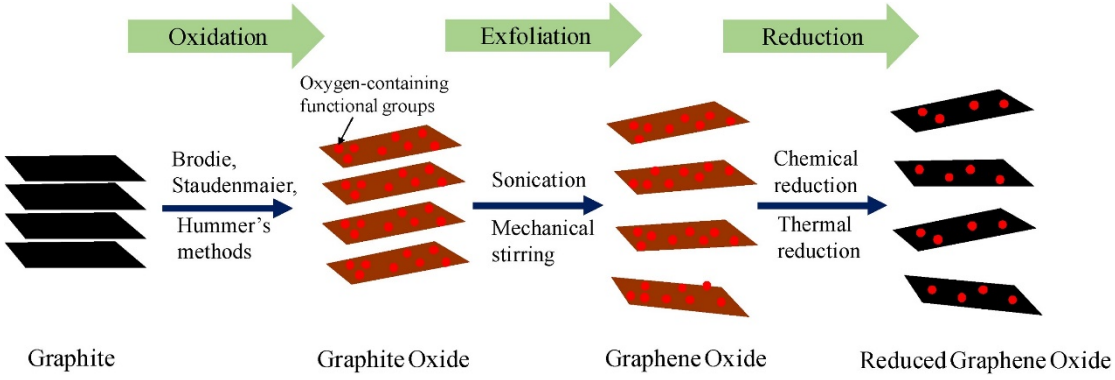

Figure 2.6 Typical routes to prepare GO and rGO from pristine graphite [73].

Many researches have been reported on the adsorption of dyes via Graphene and its derivatives. It was documented that GO was applied for the adsorption of methyl orange. The adsorption capacity was 16.83 mg/g, The findings also revealed that this

process was endothermic, and the oxidation degree of GO has a great effect on the adsorption process [81]. In addition, some scholars used GO for the adsorption of methyl green. The results indicated that maximum adsorption ability was 5.496 mmol/g predicted by Langmuir model, and the increasing temperature could promote the adsorption density of methyl green [82]. Furthermore, some researchers found that GO sponge presented an outstanding adsorption capacity for methylene blue, the removal efficiency could reach 99.1% in just 2 min. Its uptake capacity for methylene blue was 397 mg/g, and the findings implied that this process was endothermic chemical adsorption [83].

2.1.4 Metal-organic frameworks (MOFs)

Metal-organic frameworks (MOFs), an emerging crystalline category of porous materials, are constructed by metal-containing units and organic linkers with coordination networks, forming textured structures with permanent porosity [84]. Diverse categories of MOFs materials are presented in Figure 2.7. The metal secondary building units (SBUs) and organic linkers can be thousands of various compounds, this variety can lead to numerous kinds of MOFs with various topologies and pore structures. Solvothermal, microwave, sonochemistry, mechanochemical and electrochemical methods have been applied for preparing MOFs materials. Their exceptional characteristics, such as high crystallinity, porosity, thermal and mechanical stabilities, flexible frameworks and tailor ability, distinguish them from other porous materials. Moreover, the features of MOFs can be controlled precisely to achieve desired purposes or enhanced performances [85]. MOFs have received salient attention in past decades,

their merits enable MOFs with fantastic functionalities/properties for diverse applications, such as adsorption, catalysis, energy storage and drug delivery [86]. Among all these applications, MOFs have proven to possess exceptional potential for the adsorption of various pollutants in wastewater, especially for dyes adsorption [87].

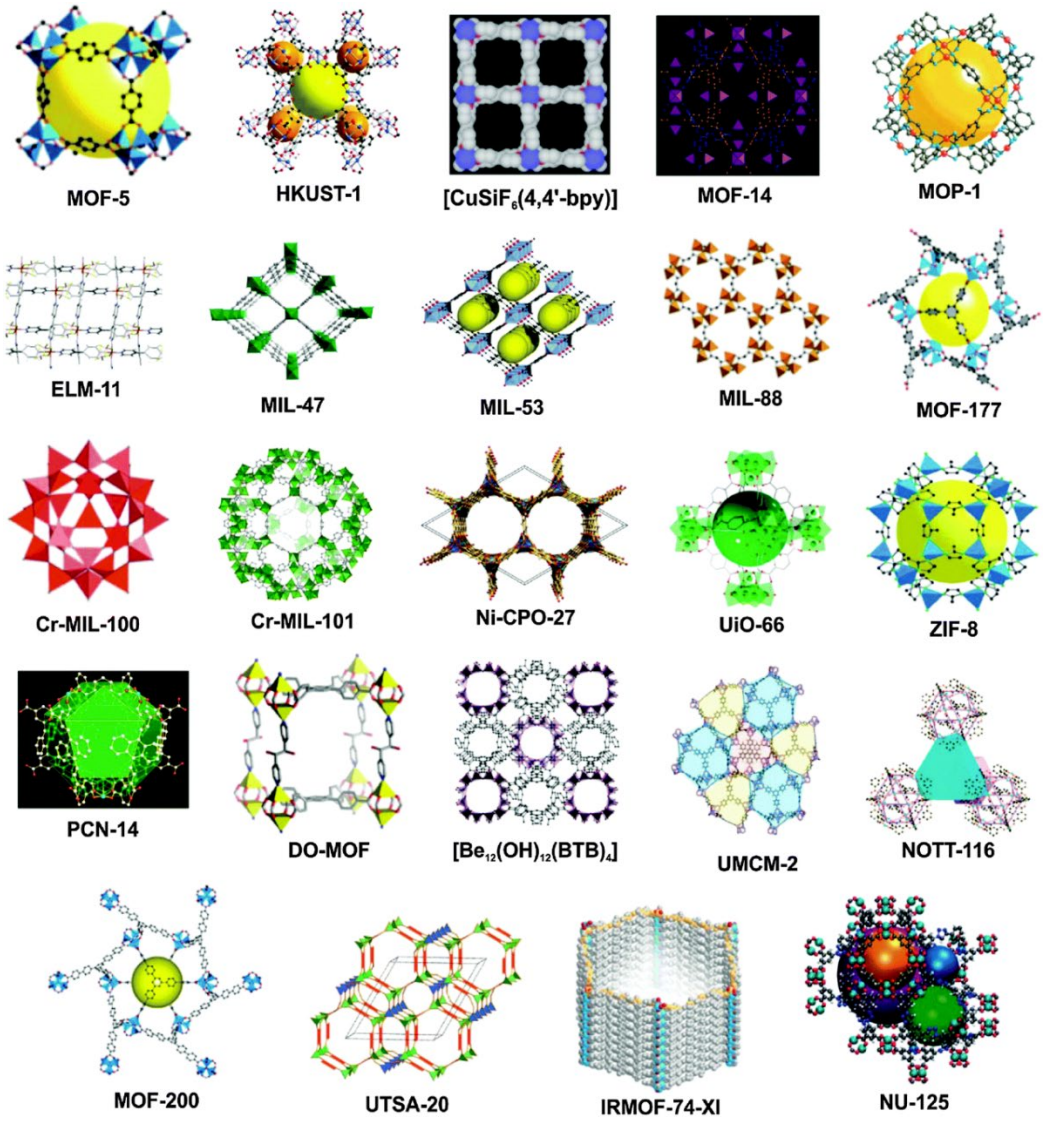

Figure 2.7 Typical structures of different porous MOFs [88]

The facile fabrication methods of MOFs facilitate their structure with complexity, uniformity and reproducibility. The uptake ability of MOFs can be rationally controlled by their structures, functionality and porosity [89]. Many efforts have been made to investigate the adsorption capacity of MOFs in recent decades. Some scholars used

MOF-235 to eliminate MO and MB. The adsorption abilities were 477 and 187 mg/g for MO and MB, respectively, which is much higher than activated carbon. The adsorption rate on MOF-235 was also found to be more efficient than that of activated carbon. The findings also revealed that this process was spontaneous and endothermic [90]. Similarly, it was reported that the open metal sites on MIL-100(Fe) were the effective active sites to absorb malachite green [91]. In addition, some MOFs with unique structures and dimensionalities exhibited superior adsorption performance towards organic pollutants. For example, 2D BUC-17 presented an effective adsorption performance towards CR, the adsorption capacity of CR was 4923.7 mg/g. It was estimated that the adsorption mechanisms could be ascribed to surface charge, π–π stacking interactions, ion-exchange, and H-bonding on the MOFs material [92]. Moreover, 3D pillared-layer MOFs are constructed with parallel pillar and 2D layers. A 3D stable Cu-based MOF was synthesized and used for RhB adsorption. This MOFs material also presented an excellent adsorption capacity [93].

The functionalization work generally includes metal node functionalization and linker functionalization [94]. The mixed-metal MOFs could be recognized as "molecular substitutional alloys", which exhibit modified properties compared with the single constituent. It was reported that HKUST-1 was selected as a precursor to produce Ni/Cu mixed porous material, Ni substituted partial Cu and promoted the adsorption performance for Congo red owing to the synergetic effect [95]. Similarly, it has been proved that Ce doped into UiO-66 can increase the adsorption sites and enhance π-π interactions [96]. Different from metal node functionalization, linker functionalization

is also an effective approach to turn the properties of MOFs. For example, amine group have already been introduced into diverse MOFs successfully. It was documented that MIL-125 and MIL-125-NH_2 were investigated for the adsorption of MB. The surface area of MIL-125-NH_2 was larger (1028 m^2/g) than that of MIL-125 (470 m^2/g), and the maximum adsorption capacity of MIL-125-NH_2 was also higher than that of MIL-125 consequently [97]. Moreover, it was reported that UiO-66-NH_2 which possessed more negative zeta potential exhibited larger adsorption ability towards cationic dyes [98]. In addition, other functional groups, such as $–SO_3H$ group, also proved that it can alter the surface charge of MOFs, which leaded to a different adsorption affinity to anionic and cationic dyes [99].

Defect engineering is another promising route to optimize the structure of MOFs. Acid modulators and post-synthetic treatment are the main approaches to produce defective MOFs [100]. As illustrated in Figure 2.8, defect engineering in MOFs can enhance various properties. For example, UiO-66 modulated by acetic acid exhibited a higher selective adsorption capacity, which was ascribed to higher BET surface area and larger positive Zeta potential [101]. In addition, some scholars fabricated defective UiO-66 with benzoic acid modulator. The results indicated that the defect engineering enlarged porosity and surface area of UiO-66, which contributed to promote the adsorption selectivity [102]. Particularly, it was reported that the defective strategy provided larger surface area and porosity without any cost of chemical stability [103].

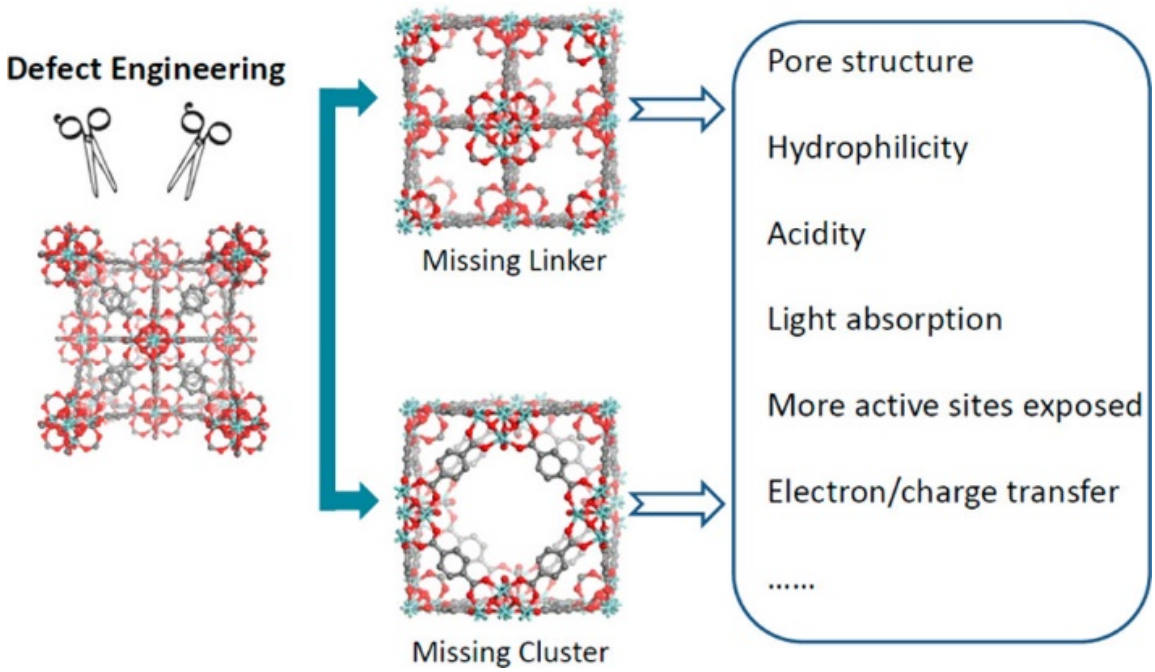

Figure 2.8 Crystallographic model of UiO-66 with defect engineering [104].

2.1.5 Covalent organic frameworks (COFs)

Covalent organic frameworks (COFs) are an emerging class of crystalline porous materials, which are constructed with various light elements via simultaneous polymerization and strong covalent bonds [105]. The building blocks of COFs present common characteristics of rigid structure and symmetric multi-connectivity. The structures and properties of COFs can be controlled precisely via choosing the building units and the synthesis conditions. Covalently crystalline structure provides COFs with exceptional attractive features, such as high surface area, small density, superior stability, tunable structure, facile functional design and permanent porosity [106]. The outstanding stability of COFs can be ascribed to the strong energy linkage and intermolecular force. Since its first discovery in 2005, numerous kinds of COFs have skyrocketed to a splendid level in the last few years. In virtue of the unique characteristics, COFs have attracted broad application researches, including adsorption,

separation, catalysis, sensors, optoelectronics, energy storage and drug delivery [107].

The COFs structures are generally predetermined by connecting the building blocks to construct polygonal skeletons. The COFs with different topology frameworks present various pore structures [108]. The porous materials can be divided into 2D and 3D COFs on the basis of the dimensions of building units. For 2D COFs, the frameworks are composed of 2D atomic layers with periodic organic blocks, which stack to form crystallize layered structures with aligned columns [109]. On the other hand, 3D COFs can be constructed by monomers with tetrahedral structure as building units. In particular, due to the existence of sp^3 carbon in the building blocks of 3D COFs, 3D COFs present larger surface area and pore volume, more open sites, and lower densities compared with 2D COFs [110]. The typical structures of 2D and 3D COFs are shown in Figure 2.9. The synthesis conditions play a vital role in the topologies and functionalities of COFs. Various synthetic routes have been documented, such as solvothermal, mechanochemical, microwave, Sono chemical, self-templated methods, etc. Crystallinity and porosity are the two dominant factors to evaluate the quality of COFs. Thus, the designed synthesis should meet both the requirements simultaneously, and the research concentrating on appropriate and facile synthesis methods is of valuable significance for the practical applications of COFs [111]. The multi-layered sheets in COFs provide numerous channels and active sites for trapping molecule onto COFs. Therefore, COFs have proven to be promising nanomaterials for environment remediation [112].

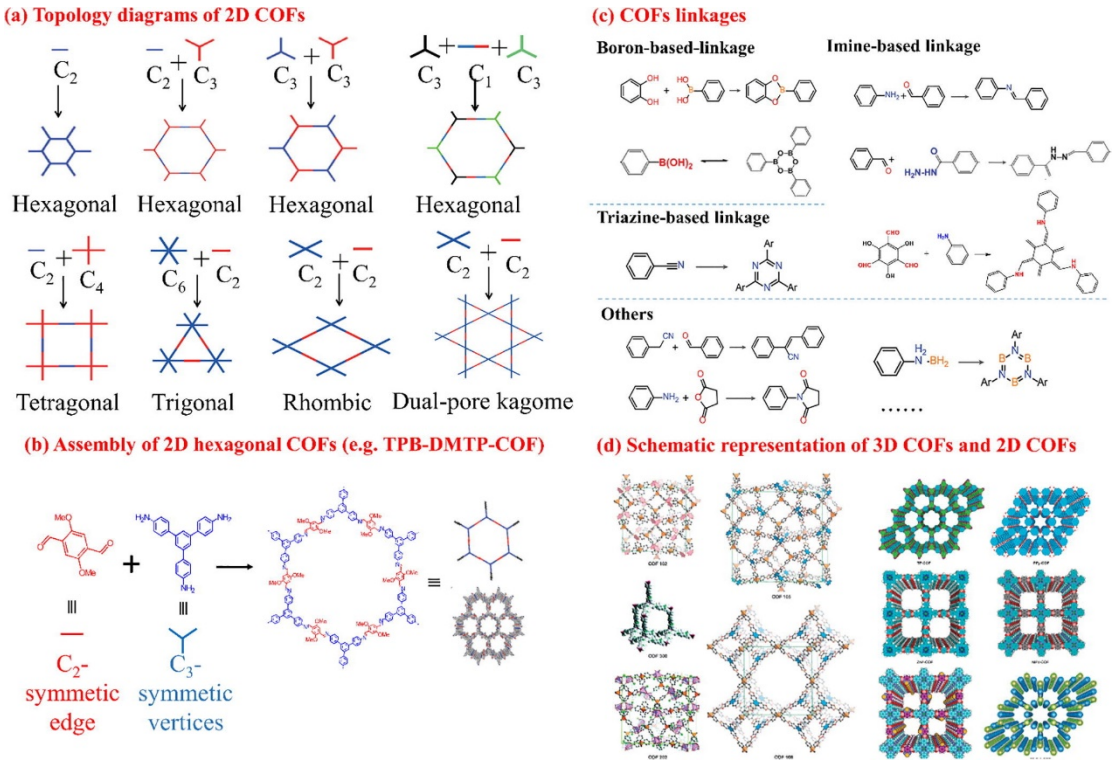

Figure 2.9. (a) Topology diagrams of 2D COFs; (b) assembly of 2D hexagonal COFs; (c) COFs' linkages; and (d) schematic representations of 3D COFs (left) and 2D COFs (right) [113].

Many researches have been reported for the synthesis of COFs and their adsorptive applications. Some scholars fabricated a new imine-linked COFs for dye removal, the produced COFs had a surface area of 328 m^2/g and an average pore diameter of 1.29 nm. The obtained materials showed a superior adsorption efficiency for direct fast scarlet 4BS, which was 8501 mg/g. It was suggested that this adsorption process was dominated by hydrogen and π-π interactions [114]. In addition, it was reported that two kinds of COFs were used for RhB adsorption. The maximum adsorption capacities were 725 mg/g and 970 mg/g for TPT-azine-COF and TPTTAPB-COF, respectively, which were highly in concert with the surface area values of each COFs. The outstanding adsorption efficiency and recyclability of these two COFs indicated that both the

materials could be promising candidates for RhB removal [115]. Moreover, various COFs have been applied for Congo Red removal till now. Novel COFs modified with metal ions were synthesized, namely COF-COOCa and COF-COONi. The abundant H-bonding sites and π-conjugated structures of the COFs could enhance the uptake efficiency of Congo Red. The results documented that the adsorption capacities were 704.2 mg/g and 781.3 mg/g for COF-COOCa and COF-COONi respectively, which were probably ascribed to the improved electrostatic interaction [116].

2.1.6 Chitosan

Chitosan is one of the most abundant and economical biopolymers which possesses great potential as a superior adsorbent towards various contaminants in wastewater, owing to its hydrophilicity, biodegradability and non-toxicity [117]. Chitosan was first produced from the alkaline de-acetylation of chitin in 1859. In this procedure, the acetyl groups on chitin are converted into free amine groups, which has an important impact on adsorption capacity [118]. Chitin, the precursor of chitosan, is also a well-known naturally abundant biopolymer, existing in various crustacean shells [119]. The utilization of crustaceans produces solid waste 1.2 million tons every year. In this concern, the extraction of chitin from crustaceans provides a promising approach to solve the problems of waste management and environmental pollution, and offers a new view to prepare high-value polymeric matrices with economical and sustainable precursors [120].

Due to its H-bonds, Chitosan is not soluble in water, organic and alkaline solutions. While it is soluble in acidic solvents owing to the protonation of amine groups on its

surface. Chemical properties of Chitosan are mainly related to its functional groups. The acetylated part associates by H-bonds and involves in hydrophobic relationship that enhance the stability of molecules in chitosan consequently, which affects its rigidity and strengthen the structural features conversely [121]. Particularly, the existences of free $–NH_2$ and $−OH$ active groups on the surface provide a range of potential chemical interactions with pollutants. Many researches have been studied on the adsorption capacity of chitosan in different forms [122]. It was reported that chitosan powder derived from shrimp wastes was examined for the adsorption of acid blue 9 and food yellow 3. The results demonstrated that the maximum adsorption abilities for acid blue 9 and food yellow 3 were 210 mg/g and 295 mg/g respectively [123]. In addition, some scholars investigated adsorption performance of chitosan flake towards some anionic dyes. The findings showed that the maximum uptake capacities of this chitosan for Direct Red 23 and Acid Green 25 were 155 mg/g and178 mg/g respectively [124].

Nevertheless, there are several demerits, such as solubility in acid, weak mechanical strength, gelation in water and low surface area restricting the practical application of this material. Thus, the research on chitosan modification is of great necessity to eliminate its drawbacks [125]. The modification of chitosan can be carried out by chemical and physical method. Physical process involves blending and conversion of chitosan. It was reported that converting chitosan flakes into beads was an effective approach to promote the adsorption ability via increasing the porosity and surface area [126]. The physical route generally expands the polymer chains and

reduces the crystalline state of chitosan, so as to enhance the access to internal adsorption sites and promote the diffusion process [127]. Moreover, chemical modification is another practical method to achieve the desired properties of chitosan. Different from physical way, the chemical method does not damage the chitosan structure, and introduces new derivatives with promotion capacities in diverse areas [128]. Such route can promote the adsorption abilities, mechanical strength, and chemical stability of chitosan especially in acidic solutions. Cross-linking, impregnation, and grafting are common approaches applied for chemical modification [129]. Cross-linking agents can associate chitosan chains with covalent bonds, which promote the mechanical strength and chemical stability of chitosan. In general, cross-linking can boost the uptake ability via reactive functional groups on cross-linking agents. Thus, it can improve adsorption capacity by enlarging the density of functional groups [130].

2.1.7 Clays

Clays can be defined as hydrous aluminosilicates possessing colloid fraction (<2μm) composed of soils, sediments, rocks and water with a layered structure. This category has similar compositions and common crystal structures such as quartz, carbonate and metal oxides [131]. Clay can be further classified according to its different layered structures. The clays possess undersized particles and sufficient porosity with large specific surface area, which provides clays strong interactions with various pollutants. Moreover, numerous exchangeable ions, such as Ca^{2+}, Mg^{2+}, K^{+} and SO_4^{2-}, Cl^{-}, NO_3^{-}, have been found on the surface of clays, these ions can also enhance

the adsorption process in some circumstances [132]. Based on low cost and superior adsorption capacity, clays have proven to be promising adsorbents for practical application in wastewater treatment. Many kinds of clays have already been applied in the adsorption of dyes, including smectites, serpentine, sepiolite, etc [133].

Although clays have shown excellent potential in dye adsorption. There are also some limitations that restrict the practical applications of clays, such as easy-aggregation and hydrophilicity. Thus, the modification of clays has become an increasing concern to enhance the adsorption capacity. Clay modification can be defined as introducing alien material to clay matrices which will promote the adsorption capacity for some specific pollutants [134]. Several methods, such as thermal treatment, acid activation, cationic surfactants and ion exchange have proven to be effective in boosting adsorption ability [135]. In general, clays exhibit no affinity towards anionic dyes due to negatively charge on their surface. Some scholars compared the adsorption capacity of bentonite with modified bentonite. The findings implied that CTAB-modified bentonite showed an obvious promotion in uptake ability for anionic dyes. The maximum adsorption capacity of Congo red was 210.10 mg/g for CTABMBn, which was much higher than 37.10 mg/g for raw bentonite [136]. In addition, thermal activation is another common route to improve adsorption performance, which involves the dehydration and dihydroxylation of clays. Some researchers used this method to modify palygorskite for the adsorption of MB. The results documented that the structure of palygorskite demolished gradually with the increase of activation temperature, and the adsorption capacity of modified-palygorskite could be enhanced in an appropriate

temperature range [137].

2.1.8 Mesoporous silica (MS)

Silica is one of the most abundant families of materials which exists as a component of natural minerals or synthetic product. Mesoporous silica (MS) is an important class of porous materials which is composed of sufficient inorganic–organic hybrid arrays with long-range order [138]. The MS has gained an increasing attention in water treatment owing to its exceptional properties, such as highly tunable textural, large surface area (up to 2370 m^2/g), big pore size (up to 50 nm), excellent thermal stability and low production cost [139]. As a promising adsorbent, MS has been synthesized and applied for adsorption of various pollutants in aqueous solution successfully. The high surface area allows MS materials numerous functionalization possibilities on their surface. Since now, the research on MS synthesis has afforded superb control on the morphology and chemistry of these nanoparticles. Consequently, MS materials can be tailored to suit for specific applications. In addition, the open pore structure on MS materials can enhance the access and transfer of pollutant molecules which will also improve the adsorption efficiency [140].

MS was first synthesized in 1990 with uniform pore size distribution which was known as FSM-16. After that, some more MS materials, such as MCM-41, MCM-48 and SBA-15, were developed by scholars in the intervening years [141]. These ordered materials exhibit hexagonal structures with broad walls and tunable pore structures. The morphologies of some MS materials are presented in Figure 2.11. The fabrication of MS nanoparticles can be achieved by plenty of similar routes under various pH and

temperature conditions [142]. The morphology and structure of MS can be controlled precisely via changing the synthesis condition. For example, micro emulsion templating is a typical method proposed by Schmidt-Winkel. The discovery of template-assisted method provides MS with large porosity and diverse kinds of functionalization, which is very useful to improve the removal efficiency towards pollutants [143]. Some scholars used SBA-15 for the adsorption of cationic dyes, the results demonstrated that electrostatic attraction was the key force for the interaction between MS nanoparticles and cationic dyes. The SBA-15 exhibited great affinity towards cationic dyes over anionic and neutral dyes, and the maximum adsorption capacity was 49.3 mg/g (methylene blue) and 66.4 mg/g (Janus Green B) [144]. Moreover, it was reported that controlling the shape of MS nanoparticles was a modified approach to improve the adsorption performance. The spherical particles had the maximum adsorption capacity among all the reported shapes, which was 234.6 mg/g for rhodamine B [145]. It was found that using natural products as templates for the fabrication of MS nanoparticles can reduce the production costs effectively. Recently, some researchers successfully synthesized 2D biomorphic MS nanoparticles with renewable petal cells. The 2D nanoparticles exhibited a higher adsorption capacity for MB than nonporous SiO_2 and traditional SBA-15 [146].

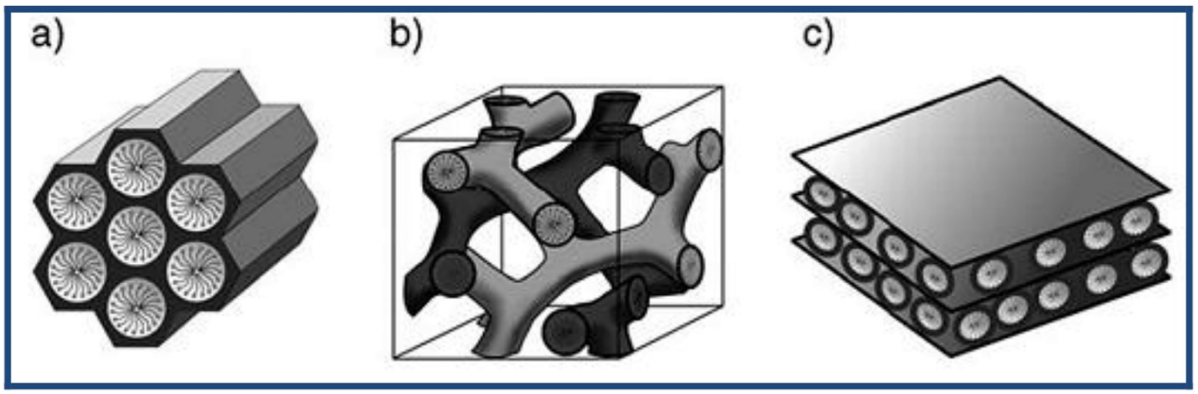

Figure 2.10 Structure of some typical mesoporous silica (a. MCM-41, b. MCM-48, c. MCM-50) [147]

However, bare MS nanoparticles generally exhibit some limitations on adsorption capacity, which may be ascribed to large surface energy, low colloidal stability and fast aggregation of MS nanoparticles. Thus, the modification of MS materials is very essential which can improve the adsorption performance practically [148]. Surface functionalization or grafting are common routes for MS modification. The functionalization on MS materials has proven to improve adsorption capacity of the nanoparticles effectively [149]. The grafting of functional groups on MS nanoparticles can enhance the colloidal stability and improve the dye molecule-MS nanoparticle surface interactions, such reversible interactions is very necessary which can promote the reusability of adsorbents [150]. Some scholars investigated magnetic core-shell silicates for the adsorption of Congo red. It was reported that this adsorption process was mainly dominated by electrostatic interaction, the adsorption capacity for Congo red was 54.6 mg/g [151].

2.2 Photocatalytic materials for the removal of organic dyes

Different from other conventional treatment techniques, photocatalysis, as an

emerging route of advanced oxidation processes (AOPs), exhibits to be a promising technique in pollutants degradation with its simple, green and sustainable features. Since its first discovery in 1972, photocatalysis has progressed significantly in many areas like H_2 evolution, CO_2 reduction and wastewater treatment. In general, it is widely recognised that semiconductor based photocatalysis can harvest solar light and degrade organic contaminants into CO_2 and H_2O with the aid of this abundant renewable energy, which make this process be an appealing option in wastewater treatment. To date, various materials have been studied as photocatalysts for the photocatalytic degradation of organic dyes, such as TiO_2, ZnO, Fe_2O_3, ZnS, WO_3, g-C_3N_4, etc.

2.2.1 TiO_2

TiO_2 is a typical material which has been investigated for many years since its first research as photocatalyst in 1972. Owing to its excellent reactivity, high stability, non-toxicity and low-cost, TiO_2 has been considered as promising candidate for various applications such as hydrogen generation, photovoltaic cells, sensing and environmental remediation [152]. As a common semiconductor, TiO_2 has a wide band gap energy of 3.0-3.2 eV generally that requires the excitation wavelength in the range of 315 to 400 nm, which indicates that it is response to UV light and can generate electrons and holes under UV irradiation [153]. When it is irradiated by the light with this wavelength, the electrons are excited and transfer from the valence band to conduction band of TiO_2. the photoinduced electrons/holes can react with H_2O molecules and molecular oxygen on the TiO_2 surface to form different radicals [154]. So that the efficiency of interfacial charge transfer is directly related to the photoactivity

of TiO_2. In wastewater treatment particularly, these generated radicals can take part in the decomposition of pollutants in wastewater. A general pathway of the pollutant degradation on TiO_2 surface is illustrated in Figure 2.12.

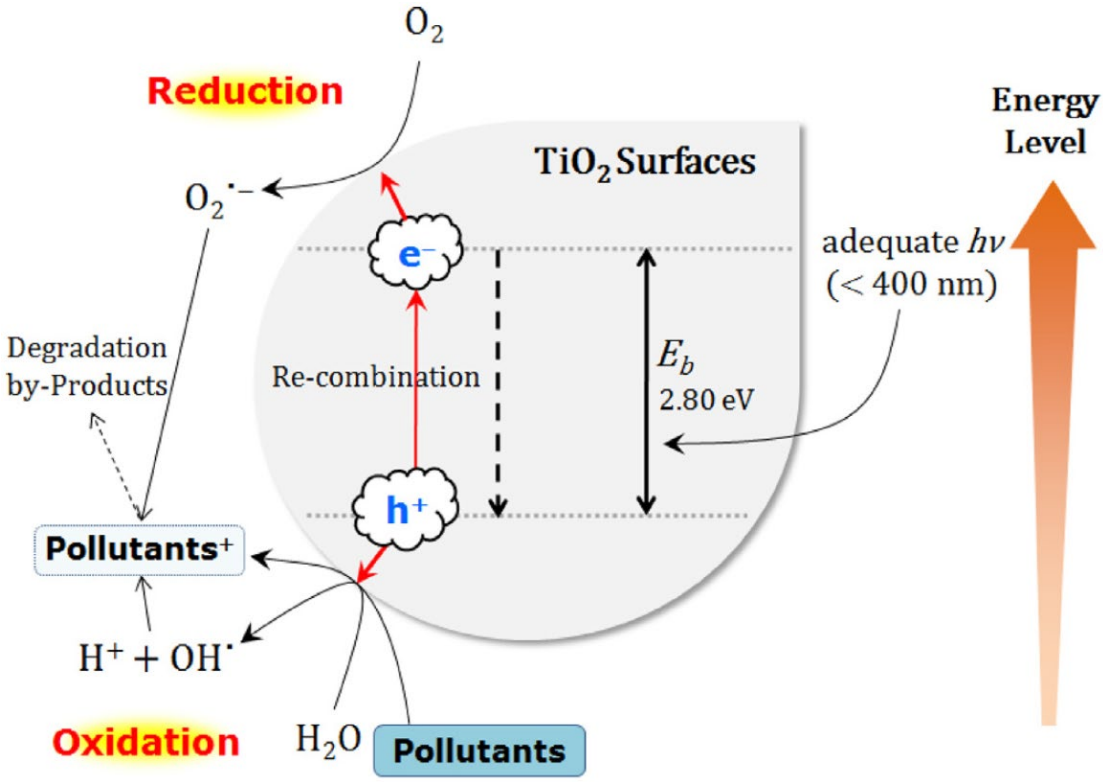

Figure 2.11 Mechanism of the photodegradation of pollutants on TiO_2 surface [155].

TiO_2 has been used to the removal of dyes for decades. It was reported that MB could be degraded completely by TiO_2 nanoparticles within 300 min. The findings indicated that the particle size had a great impact on photocatalytic performance [156]. It is recognized that various factors can affect the photoactivity of materials, such as particle size, surface area, crystalline phase, etc. As the photoactivity of TiO_2 is far from good enough, which could be attributed to fast recombination of electrons and holes, many efforts have been made to improve the photocatalytic performance of TiO_2. Elemental-doping modification is the most common method used to promote the photoactivity. It was reported that Au nanoparticle was coupled to TiO_2 nanofibers. The

results showed that the Au-doped TiO_2 had an obviously higher photocatalytic performance on the degradation of MB than the original TiO_2 [157]. Some scholars loaded carbon nanoparticle on TiO_2. It was reported that the synthesized material CNP-TiO_2 was stable and exhibited improved photocatalytic activity on the removal of reactive 120 compare with original TiO_2 [158]. In addition, the morphology of TiO_2 is also regarded as a significant factor on photoactivity, many focuses have been paid to control the morphology, so as to enhance the photocatalytic performance of TiO_2. TiO_2 could be tailored into different structures. Some researchers investigated the morphological effect of TiO_2 on the photodecomposition of MB. Various structures of TiO_2, such as cuboid, flower and cauliflower, were synthesized to assess the photocatalytic performance. The results indicated that the flower-like TiO_2 displayed the highest photoactivity compared with other prepared samples [159].

2.2.2 ZnO

ZnO is also a commonly studied oxides owing to its unique physicochemical and optical properties. As a typical n-type semiconductor, it has a broad band gap, large excitation binding energy, high redox potential, low-cost and excellent electrochemical stability, resulting in its promising candidates in photocatalysis [160]. Similar to TiO_2, ZnO possesses great quantum efficiency and absorbs the UV light mainly. Meanwhile, it exhibits a better photocatalytic performance and lower cost compared to TiO_2. In addition, ZnO is also environmental-friendly, which makes it great potential in various practical applications without threatening human and aquatic life [161]. ZnO exhibits three different crystal structures including wurtzite, rocksalt and cubic type, the wurtzite

structure is the most stable and common type of ZnO [162]. It is well known that manipulating the crystalline and shape of ZnO nanoparticles can result in the control of surface energy and photocatalytic performance. Thus, optimizing synthesis parameters can influence the size and structure of ZnO, so as to control the photoactivity [163].

It was reported that ZnO nanorods were prepared in different conditions. By tunning the synthetic parameters, the shape and size of ZnO nanorods could be controlled. The results indicated that the particle size of obtained photocatalysts made a main contribution to the photocatalytic process [164]. Mesoporous ZnO was also prepared to investigate the photocatalytic activity. With the addition of ethylene glycol and Cd^{2+}, ZnO nanorods with improved pore structures were synthesized successfully. The results showed that the mesoporous ZnO exhibited an obviously better photoactivity and reaction rate than that of the bulk ZnO on the degradation of MB [165]. In addition, some researchers fabricated different ZnO nanorods by controlling the pyrolysis process. It was reported that the calcination parameters had a great influence on the physical, chemical and photocatalytic properties of prepared ZnO nanorods. The samples synthesized under 300 ℃ showed the highest photodegradation of MO, which was attributed to the enhanced oxygen species and decreased oxygen vacancies [166].

In addition, there are also many other methods to improve the photoactivity of ZnO. Doping modification is a general route for the promotion of photocatalytic efficiency. Some researchers reported that the C-doped ZnO exhibited an improved photocatalytic property on the degradation of MB, which may be assigned to the

enhanced adsorption capacity, better UV adsorption and improved oxygen vacancies [167].In addition, Fe-doped ZnO nanoparticles were prepared to study its photocatalytic performance on the removal of MB. The results indicated that the Fe-doped materials showed obviously better photocatalytic property than the pure ZnO. Meanwhile, the magnetic property of the prepared sample can facilitate the recovery of the photocatalyst [168]. Moreover, K-doped ZnO was synthesized successfully with microwave-assisted method. The K-doped material showed improved surface area, higher visible light adsorption, and narrower band gap compared to pure ZnO, and consequently exhibited a enhanced photocatalytic performance on the removal of RhB [169].

2.2.3 Fe_2O_3

Fe_2O_3 is a general oxide semiconductor, dislike other oxides that can only be response to UV region, it is favourable for photocatalysis under visible light. Fe_2O_3 has a low band gap (2.0-2.2 eV) and excellent unitisation of visible light. Meanwhile, the stability and low cost make it great potential in practical applications. In general, Fe_2O_3 can be divided into three types based on the kinds of crystal structures, including α-Fe_2O_3, β-Fe_2O_3, ε-Fe_2O_3, etc. Particularly, the hexagonal α-Fe_2O_3 is most stable in room temperature among all these phases.

The same as TiO_2 and ZnO, many efforts have been made on the manipulating the synthesis process of Fe_2O_3, so as to modify its photoactivity. It was reported that porous Fe_2O_3 nanorods were fabricated with a chemical solution route. Owing to the enhanced porosity, the porous Fe_2O_3 exhibited 86.4% removal efficiency on the degradation of

RhB, which was obviously higher than that of the commercial Fe_2O_3 [170]. In addition, some researchers synthesized Fe_2O_3 nanotubes successfully with phase junctions and pore structures. The findings indicated that the obtained sample demonstrated 20 times better on photoactivity than commercial α-Fe_2O_3, which was probably attributed to the phase composition and improved porous structures [171]. Although many achievements have been made on the study of Fe_2O_3, its photocatalytic performance is still far away from satisfied when it works alone as catalyst. Thus, it comes a challenge and trend to explore feasible modification approaches to promote photoactivity of Fe_2O_3.

2.2.4 WO_3

WO_3 is a n-type semiconductor with five crystal structures at different temperatures. The γ-WO_3 exhibits the most stability in ambient environment. and thus it is most studied among all the phases. WO_3 has a narrow band gap ranging from 2.4 to 2.8 eV and shows a preferable optical adsorption in visible light region. Many benefits make WO_3 a promising alternative as photocatalyst for the degradation of organic pollutants, such as strong oxidizing activity, good visible light harvest, high stability, low cost and non-toxicity. Generally, it is known that the morphology of WO_3 has a great effect on the photoactivity, which could be manipulated by controllable synthesis conditions.

Many works have been reported to prepare WO_3 with various structures. Some researchers conducted a comparable investigation between rod-like and nanoparticle WO_3. It was found that the WO_3 nanorods showed an promoted photocatalytic

performance on the removal of RhB with a decreased surface area, which may be assigned to the improved delocalized electrons in WO_3 nanorods [172]. In addition, some researchers synthesized WO_3 hollow shell with different structures. The results demonstrated that the morphologies affected the photocatalytic properties of WO_3 significantly. The sphere-like sample displayed the highest photodegradation performance on organic pollutants [173]. Moreover, diverse approaches have been explored to further boost the photocatalytic performance of WO_3. It was reported that Ir nanoparticles was doped onto WO_3. The prepared material exhibited an improved photodegradation of Methylene Blue and Crystal Violet, which may be attributed to the decreased recombination of electron-hole [174]. In addition, a carbon doped WO_3 was prepared as a photocatalyst. This doping modification changed the band structure, introduced defects, and hindered the recombination rate. Consequently, this carbon dopant showed a promoted photoactivity on the removal of RhB [175].

2.2.5 g-C_3N_4

g-C_3N_4 is a new type of metal-free semiconductor. It possesses unique optical property, high stability and abundant source of the precursor, which makes it a multifunctional platform for different applications. The moderate band gap of g-C_3N_4 (~2.7 eV) facilitates it a superior harvest of visible light, resulting in a good potential for photocatalysis. Many disadvantages of bulk g-C_3N_4 such as low surface area, fast recombination of charger carriers, and poor redox potential, restrain its practical application.

Since now, many efforts have been explored to promote the photocatalytic

performance of g-C_3N_4. Nanostructure construction is a feasible modification method to improve photoactivity. It was reported that a mesoporous g-C_3N_4 was fabricated with hard template method. Due to the larger surface area and introduced nitrogen defects, the prepared sample exhibited 11 times better than bulk g-C_3N_4 on the photodegradation efficiency of RhB [176]. Some researchers reported hexagonal-prism g-C_3N_4 by supramolecular assembly method. The acetic acid facilitates the formation of pore structure in prepared samples with a BET surface area of 67.7 m^2/g. The obtained porous g-C_3N_4 showed a 13 times promotion on the photodegradation of RhB compared with bulk g-C_3N_4, which demonstrated that this method could be a feasible route to improve the photoactivity of g-C_3N_4 [177]. In addition, doping method has also been reported for the modification. Zr-doped g-C_3N_4 was prepared with a facile thermal condensation. The Zr-doped sample had a hierarchical mesostructured with improved BET surface area. Owing to the smaller recombination of electron/holes and narrowed bandgap, the prepared photocatalyst showed an obviously enhanced photocatalytic removal of RhB than bulk g-C_3N_4 [178].

2.3 Summary

This chapter firstly introduces the significance and techniques for the removal of organic dyes in wastewater treatment. Adsorption and photocatalysis are chosen as the focus approaches of this research. Therefore, recent advancements on the materials for adsorption and photocatalysis are summarized.

Adsorption has proven to be a practical and effective method to remove organic pollutants in wastewater owing to its various benefits, such as low cost, easy operation

and not produce harmful products. The adsorbent is one of the key aspects for this technique. Various materials have been investigated in this process. Amony these adsorbents, MOFs has shown great potential in the adsorption of organic dyes. UiO-66 is a typical Zr-MOFs material with high stability and surface area, which is preferable for adsorption process. Many studies have been on the adsorptive removal of organic dyes based on UiO-66. However, the adsorption performance of pristine UiO-66 is still not so satisfactory. Thus, to explore modification method on the improvement of adsorption capacity of UiO-66 on organic dyes is still worth further investigation.

Photocatalysis could also be a promising technique for the removal of organic dyes due to its high efficiency and low cost. To explore high effectiveness, good stability and cheap material is the main concern for this area. g-C_3N_4 is an emerging semiconductor which is low-cost, nontoxic and great response to visible light. Nevertheless, the photoactivity of g-C_3N_4 is still not so satisfied due to its low surface area and fast recombination of electron/hole. Thus, it is of great significance to find feasible approaches to enhance the photocatalytic performance on the removal of organic dyes.

Chapter 3 Methodology

3.1 Introduction

In this chapter, the basic experimental instruments and a series of primary characterisation methods that employed to characterize the materials are described. These techniques are very imperative to demonstrate the physical, chemical, and optical properties of the as-obtained materials. In addition, it is essential route to understand the relationship between the structures of the prepared samples and the performance, and to reveal the mechanisms of the adsorption or photocatalysis process.

3.2 Instruments

3.2.1 Oil bath device

The Oil bath method was employed as the primary approach to fabricate materials, which can tailor the structures of prepared samples by changing the synthesis parameters. For a general synthetic process, precursors were added into a solvent to obtain a homogeneous solution, then the dispersion was transferred into the oil bath device. With a consecutive stir in certain temperature, the samples could be final synthesized. It was shown in Figure 3.1

Figure 3.1 Oil bath device

3.2.2 Adsorption test device

Adsorption experiment is the key point to evaluate the performance of synthesized adsorbents. Thermostatic oscillator is the device employed in this work to control the experimental temperature and oscillation rate, which can highly influence the adsorption process and ensure the experiments conduct in desired parameters. As shown in Figure 3.2.

Figure 3.2 Thermostatic oscillator device.

3.2.3 Photoactivity test device

Photoactivity test is the primary experiments in photocatalysis to assess the performance. In this work, a basic photocatalytic reactor was established for the experiments. As displayed in Figure 3.3, it mainly includes a Xe lamp, a magnetic stirrer and a dark metal cover. The Xe lamp was applied to simulate visible light with certain

filter. The magnetic stirrer was used to make the reaction conduct thoroughly. And the dark cover was used to protect the reactor from other natural light.

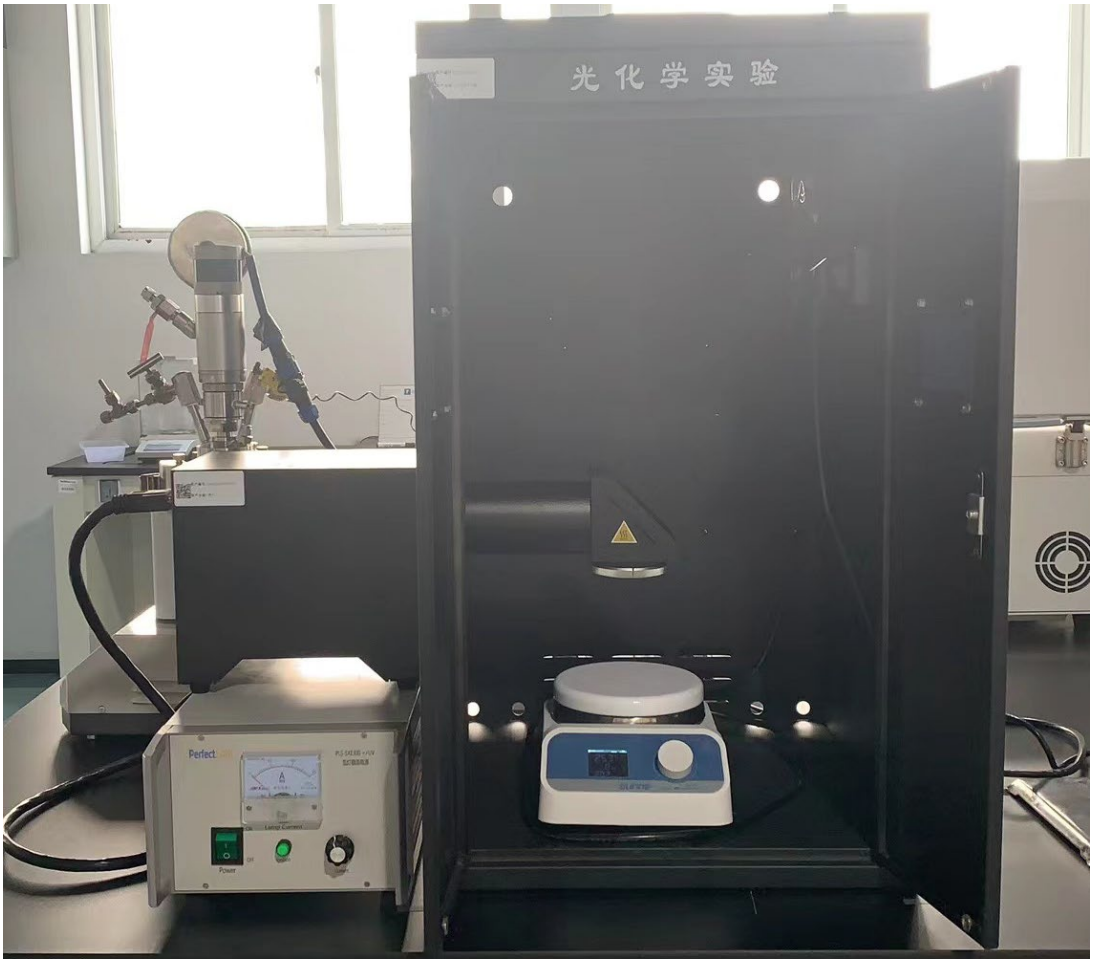

Figure 3.3 Photocatalytic reactor.

3.2.4 Concentration test device

The concentration of target pollutant in aqueous solution is a primary aspect in all the experiment to calculate the performance of as-obtained samples. UV-Vis spectrophotometer (PerkinElmer, LAMBDA 365) was employed to evaluate the concentration of dyes in certain conditions. With a standard curve of given organic dye, the concentration could be calculated based on the absorbance intensity.

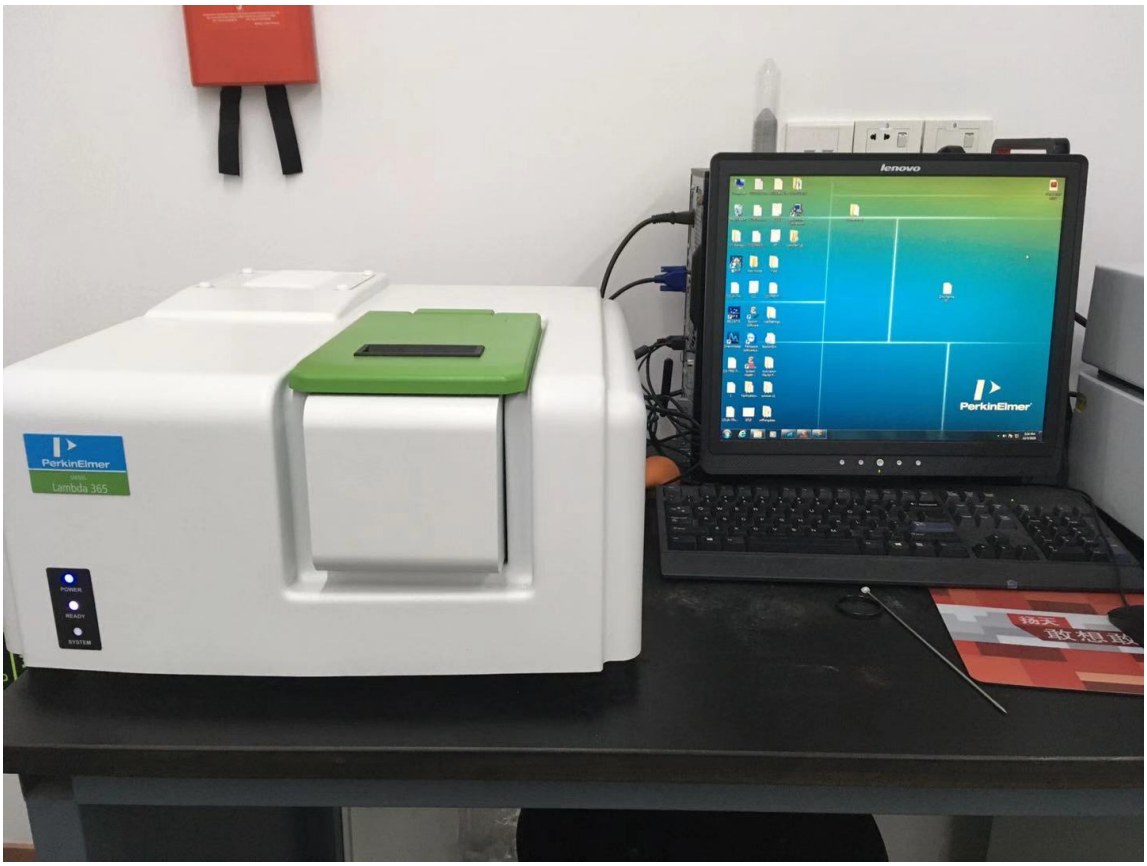

Figure 3.4 UV-Vis spectrophotometer

3.3 Method

Adsorption and photocatalytic test are mainly carried out to evaluate the functional performance of as-synthesized materials.

3.3.1 Adsorption test

Batch adsorption tests were performed to evaluate the adsorption performance of the obtained adsorbents. The dye solution with various concentration was obtained through dissolving different amounts of organic dyes into deionized water. Usually, 20 mg adsorbent was dispersed in 150 mL of MG or RhB solution, then the mixture was oscillated at 150 rpm and room temperature for a sufficient time. Then, the remaining

concentration of dyes was tested based on the maximum absorbance of UV-VIS spectrum (λ_{MG}=617 nm, λ_{RhB}=550 nm). The adsorption capacity was measured using the below equation.

$$Q_t = \frac{(C_0 - C_t)V}{m}$$

In which C_0 and C_t (mg/L) stands for initial the residual concentration in given time of organic, respectively. V (L) represents solution volume. m (g) symbolizes the mass of adsorbents. While Q_t represents the uptake capacity in a certain time.

3.3.2 Photocatalytic test

The photocatalytic properties of the samples were evaluated by the photodegradation of RhB in aqueous solution. For a typical photocatalytic experiment, 20 mg of the obtained photocatalyst was added into 100 mL of RhB solution (60 mg/L). The mixture was magnetically stirred in dark environment for 1 h to reach adsorption-desorption equilibrium. Afterwards, the suspension solution was irradiated by a 300W Xe lamp with a 400 nm cut-off filter as visible light source. Then 2 mL of the solution was taken out with regular intervals of 10 min and separated with centrifugation. The RhB concentration was measured using UV-Vis spectrophotometer with a maximum adsorption wavelength of 550 nm. To further study the mechanism of this photocatalytic process, the trapping experiments were carried out in the same conditions with the addition of three different scavengers, namely, isopropyl alcohol (IPA), benzoquinone (BQ) and EDTA-2Na. All the experiment results were conducted in triplicate and the average value was calculated for further study.

3.4 Characterizations

3.4.1 X-ray diffraction (XRD)

X-ray diffraction (XRD), a significant technique in the realm of structural analysis, holds immense importance within the domain of catalytic material research. This method serves as a characterization tool that elucidates crystal structures through the interaction between X-rays and crystals, thereby contributing significantly to our understanding of these materials' properties and behaviours. X-rays constitute a type of electromagnetic radiation characterized by a wavelength (λ) spanning from 0.2 to 10 nm. This wavelength range places X-rays at the atomic scale, considerably shorter than that of visible light. Consequently, X-rays exhibit elevated energy levels, enabling them to penetrate matter more profoundly. The X-ray scattering technique holds a notable advantage over alternative analytical methods due to its non-destructive nature.

XRD is a main technique used to evaluate the crystal structure of material, such as crystalline phases and the distance between lattice planes. Due to the fact that the distinctive diffraction peaks in the XRD spectra of individual samples correspond to their specific crystallographic planes, it becomes feasible to ascertain the composition of crystal phases and lattice parameters of the sample. This can be achieved by comparing the unique peaks obtained from the X-ray diffraction analysis of the test sample with those present in a standard reference card for pure substances.

Upon encountering matter, X-ray photons engage in various interactions, resulting in diverse absorption and scattering effects. A coherent scattering arises when photons interact with electrons situated around atomic nuclei. The energy of the scattered wave

remains the same, and its phase relationship with the incident wave is preserved. Consequently, the X-ray photons that strike all atoms within an irradiated volume disperse in multiple directions, giving rise to distinctive diffraction patterns. These patterns can be studied to explore and analyse the crystal structure of materials. The fundamental principle of these methods relies on the diffraction of X-rays by regularly spaced atomic planes, coupled with the measurement of the angle or energy distribution of the diffracted signal. The enhancement of scattered rays from a crystal plane occurs when the optical path difference aligns with an integral multiple of the wavelength. This phenomenon is described by the Bragg equation:

$$n\lambda = 2d\sin\theta$$

In which n represents the order of diffraction, λ is the incident wavelength, d is the lattice spacing and θ is the angle of the diffracted beam. In a particular crystalline, Interference enhancement and the formation of an XRD pattern are achievable only when the incident angle adheres to the Bragg equation.

Typically, diffraction data are depicted as an intensity distribution correlated with the 2θ angle. The information that can be extracted is illustrated in Figure 3.5.

1) By comparing the peaks obtained from the XRD instrument with standard card, it becomes possible to ascertain the composition of unknown materials.
2) For a mixture sample, the peaks observed in the XRD pattern are a cumulative result of the diffraction patterns originating from all constituent phases.

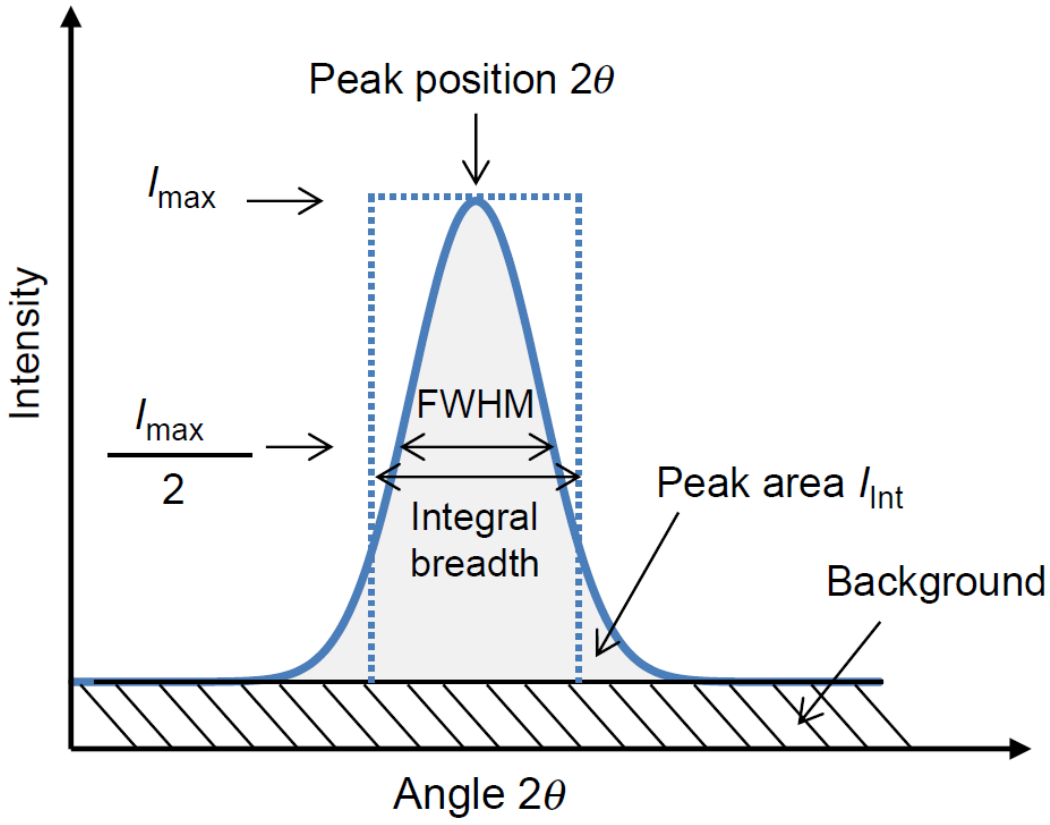

Figure 3.5 Typical XRD pattern of diffraction peak

XRD patterns were acquired by D8 Advance-Bruker using Cu-Ka radiation with 40 kV and 40 mA. The diffraction (2θ) was recorded in the range of 5-80° with a step size of 0.01° to ensure all the featured peaks could be included. For the preparation of XRD tests, the sample should be ground into a fine powder and evenly spread onto the sample holder to form a flat and tightly packed surface.

3.4.2 X-ray Photoelectron Spectroscopy (XPS)

X-ray Photoelectron Spectroscopy (XPS) has broad utility for the analysis of material surface characteristics. In general, details like the molecular structure, chemical state and elemental composition of the sample's surface could be verified from the shape and position of XPS peaks. In addition, the qualitative and quantitative information of elements can be obtained through the characteristic binding energies of

electrons. This is a relatively non-destructive and well-established method.

The fundamental principle underlying XPS qualitative analysis on elemental composition is photoionization: When the X-ray irradiates on the surface of the material, the inner atom or electrons will absorb the photons. Upon absorbing the photon, the electron obtains more energy, allowing it to overcome the attraction of the atomic nucleus and detach from its binding. Subsequently, it is emitted from the atom with a distinct kinetic energy, transitioning into an independent photoelectron. While the atoms that lose electrons in this process transform into excited-state ions. The Einstein formular of photoelectric emission is described as following:

$E_k=h\nu-EB$

In which Ek represents the kinetic energy of excited photoelectrons, hν stands for the energy of X-ray photons, and EB is the binding energy of atomic orbital. It is evident from the equation that the energy of the photoelectron is distinct for a particular monochromatic excitation source and a specific atomic orbit. With a constant excitation source energy, the energy of the photoelectron is solely determined by the element's identity and the specific atomic orbital that undergoes ionization. Hence, it becomes possible to conduct a qualitative analysis of substance elements by examining the binding energy of photoelectrons.

The fundamental principle of XPS for qualitative analysis lies in its ability to provide insights into the chemical states and molecular structures of elements. In XPS, a sample is bombarded with X-rays, causing inner-shell electrons to be ejected from the atoms. These emitted photoelectrons carry information about the binding energies of

the electrons, which are specific to the chemical environment of the atom. By measuring these binding energies, researchers can deduce the types of elements present and their chemical states within the sample. Additionally, the energy shifts and peak shapes in the XPS spectrum provide details about the electronic interactions, oxidation states, and molecular configurations of the elements. Comparing the obtained spectra with reference spectra or databases allows for the identification of chemical compounds and structural arrangements. In summary, XPS qualitative analysis leverages the distinct binding energies and spectroscopic signatures of emitted photoelectrons to unveil the chemical compositions and molecular arrangements of elements within a sample.

In this study, XPS was performed by ESCALAB250 Xi (Thermo Fisher Scientific, America) with monochromatized Al Ka (hm = 1486.6 eV) radiation source for excitation. The obtained data was calculated by the spectrum calibration of C 1s at 284.6 eV[179].

3.4.3 Fourier Transform Infrared Spectroscopy (FTIR)

FTIR, or Fourier Transform Infrared Spectroscopy, is a powerful analytical technique used to study the interactions between molecules and gain insights into the composition, structure, and bonding of materials. It is widely utilized in various fields such as chemistry, physics, materials science, biology, and more. The principle of FTIR is based on the interaction of infrared (IR) radiation with matter.

Infrared radiation lies in the electromagnetic spectrum between visible light and microwave radiation. Molecules can absorb specific frequencies of infrared radiation, which correspond to the vibrational modes of their chemical bonds. Molecules are not

static; the atoms within them are in constant motion. These motions include stretching and bending vibrations of chemical bonds. Each type of bond and molecular structure has characteristic vibrational frequencies associated with it. When infrared radiation is passed through a sample, certain frequencies are absorbed by the sample's molecules. This absorption causes the molecules to undergo vibrational transitions from one energy state to another. The energy absorbed corresponds to the energy difference between these vibrational states.

A FTIR spectrometer consists of a source that generates infrared radiation, a sample compartment, and a detector. The basic principle of FTIR involves comparing the infrared light that passes through the sample with a reference beam of the same light that hasn't interacted with the sample. In FTIR, a Michelson interferometer is used to split the infrared beam into two paths. One path goes directly to the sample, while the other is directed to a fixed mirror. The light beams are then recombined, and the resulting interference pattern (an interferogram) is measured. The interferogram contains information about the frequencies absorbed by the sample. A mathematical process called Fourier transformation is applied to the interferogram to convert it from the time domain into the frequency domain. This yields a spectrum that shows the intensity of absorbed infrared radiation as a function of frequency. The resulting spectrum is a plot of infrared absorption (or transmittance) on the y-axis against the frequency (or wavenumber) on the x-axis. Peaks and patterns in the spectrum correspond to different types of molecular vibrations. By comparing the sample's spectrum to reference spectra or databases, researchers can identify the functional

groups and compounds present in the sample. FTIR provides valuable information about molecular structure, including functional groups, chemical bonds, and the presence of impurities or contaminants. Quantitative analysis can also be performed to determine the concentration of specific components in a mixture.

In summary, FTIR exploits the interaction of infrared radiation with molecules to analyse their vibrational modes and provide insights into molecular composition and structure. The Fourier transform process enhances the accuracy and sensitivity of the measurement, making FTIR a versatile and widely used analytical technique.

In this work, FTIR spectroscopy was observed at ambient temperature. by Thermo ESCALAB 250XI using attenuated total reflectance (ATR) technique to identify the functional groups and bonding composition of as-prepared samples. The range of 500 to 4000 cm^{-1} was covered during the scanning of the spectrum, with a resolution of 4 cm^{-1}, using the KBr disk as the background.

3.4.4 Scanning Electron Microscopy (SEM)

Scanning Electron Microscopy (SEM) is a powerful imaging technique used to obtain high-resolution, three-dimensional images of the surface morphology of various types of samples. It works by using a focused beam of electrons to scan the sample's surface, and the interactions between the electrons and the sample provide information that is used to create detailed images.

SEM uses an electron gun to generate a beam of high-energy electrons. This electron beam is usually generated using a heated tungsten filament or a field emission source. The electron beam is then focused using a series of electromagnetic lenses,

much like in an optical microscope. These lenses help to concentrate and direct the electron beam onto a small spot on the sample's surface.

The sample to be imaged must be carefully prepared to ensure proper imaging. This often involves coating the sample with a thin layer of conductive material, such as gold or carbon, to prevent charging effects caused by the interaction of the electron beam with the sample. When the high-energy electrons from the beam hit the sample's surface, various interactions occur. These interactions include elastic scattering (where the electrons bounce off without losing energy) and inelastic scattering (where the electrons transfer some of their energy to the sample).

One of the primary interactions used in SEM is secondary electron emission. When the primary electrons hit the sample, they can knock loose secondary electrons from the sample's surface. These secondary electrons are then collected and used to create the image. Different types of detectors are used to collect the secondary electrons, backscattered electrons, and other signals generated during the interactions. These signals are then processed to create images that reflect the topography and composition of the sample's surface. The electron beam is scanned across the sample's surface in a systematic pattern. As the beam moves, it interacts with different areas of the sample, and the resulting signals are used to create a detailed image. The collected signals are used to generate images that provide information about the sample's surface topography, texture, and composition. The brightness and contrast of the image are manipulated to highlight different features of interest.

Overall, SEM is a versatile technique that allows scientists and researchers to

investigate the microscopic structure of a wide range of materials, including biological specimens, metals, ceramics, polymers, and more. It provides valuable insights into the surface morphology and composition of these materials at very high resolutions, making it an essential tool in various fields of science and industry.

The SEM utilized in this work was a ZEISS Sigma VP, functioning at either 15kV or 20kV voltage, and equipped with a gold coating mechanism provided by LEICA EM SCD 500.

3.4.5 Transmission Electron Microscope (TEM)

Transmission Electron Microscope (TEM) operates on the principle of using a beam of electrons instead of visible light to achieve extremely high-resolution imaging and detailed analysis of specimens. It is a powerful instrument used to study the internal structure of materials at a very high resolution.

Instead of using visible light, TEMs use a beam of electrons to illuminate the sample. Electrons are generated by a heated filament (thermionic emission) or through field emission, and they are accelerated to a high energy. Electromagnetic lenses are used to focus the electron beam. These lenses are similar in function to optical lenses used in light microscopes, but they manipulate electron trajectories instead of light rays.

Samples for TEM need to be extremely thin (typically less than 100 nanometres thick) because electrons can only penetrate a limited distance into the material. This requires specialized sample preparation techniques such as ultramicrotomy or ion milling. When the high-energy electron beam interacts with the sample, several interactions occur: Electrons can scatter elastically off the atomic nuclei, providing

information about the crystal structure. They can lose energy through inelastic scattering processes, giving rise to phenomena like electron energy-loss spectroscopy (EELS). In addition, they can undergo diffraction, producing a diffraction pattern that reveals the crystallographic information of the sample.

The transmitted electrons carry information about the sample's structure. After passing through the sample, the electrons are focused onto a fluorescent screen or a digital detector. The resulting image is called a transmission electron micrograph (TEM image). TEMs can achieve very high levels of magnification, often in the range of 50,000x to 1,000,000x or more, allowing researchers to study nanoscale features. TEMs have incredibly high resolution, typically down to sub-angstrom levels. This allows for the visualization of individual atoms within a crystal lattice. Different techniques can be used to enhance the contrast in TEM images, such as phase contrast and dark-field imaging. These methods help reveal details that might not be visible in a standard TEM image. TEMs can perform various spectroscopic techniques, such as EELS and energy-dispersive X-ray spectroscopy (EDS), to analyse the chemical composition and electronic properties of the sample.

In summary, the principles of a Transmission Electron Microscope involve the generation and manipulation of a focused electron beam, interaction of the beam with a thin sample, and the formation of high-resolution images and spectroscopic data, making it a powerful tool for nanoscale research and imaging.

3.4.6 Thermal Gravimetric Analysis (TGA)

Thermal Gravimetric Analysis (TGA) is an analytical instrument used to

determine the changes in the mass of a sample as a function of temperature and time. This technique has been widely applied in various fields, including materials science, chemistry, pharmaceuticals, and environmental science. It is employed to study properties such as thermal stability, decomposition temperatures, moisture content, and reaction kinetics for a wide range of materials and compounds. The principle behind TGA involves the measurement of weight loss (or gain) as the sample is subjected to controlled temperature and atmosphere conditions.

A small quantity of the sample (usually a few milligrams to several grams) is accurately weighed and placed in a sample holder or crucible. This sample is typically positioned on a balance or microbalance, which is a precise and sensitive weighing device capable of measuring small mass changes. The sample holder containing the sample is placed inside a furnace or heating chamber. The temperature is controlled and gradually increased at a specific rate, which can be programmed based on the experimental requirements. The rate of temperature increase is known as the heating rate. Throughout the heating process, the TGA continuously measures the mass of the sample. This measurement is highly sensitive and accurate, capable of detecting even minute mass changes. The balance records the sample's mass in real-time. TGA instruments allow for precise control of the surrounding atmosphere. The atmosphere can be inert (e.g., nitrogen or argon), oxidizing (e.g., air), reducing, or controlled gas mixtures, depending on the analysis needs. The choice of atmosphere is critical for understanding sample reactions.

As the temperature increases, various physical and chemical changes may occur

within the sample. These changes can result in weight loss or gain, which is recorded by the TGA. The resulting data is typically plotted as a thermogravimetric curve, where the y-axis represents mass change, and the x-axis represents temperature or time. The TGA data provides valuable information about the sample, including: a. Identification of temperature ranges where the sample decomposes, loses volatiles, or undergoes chemical reactions. b. Determination of the composition of the sample, including the presence of moisture, solvents, or other volatile components. c. Analysis of reaction rates and mechanisms, including determination of activation energy.

The principle of a Thermal Gravimetric Analyzer involves precisely weighing a sample, heating it at a controlled rate while measuring its mass continuously, and analysing the resulting data to gain insights into its thermal behaviour, composition, and reactivity under various atmospheric conditions. This technique is invaluable for characterizing a wide range of materials and understanding their thermal properties.

In this work, the thermal stability of prepared sample was observed by TG/DTA 6300 USA. The temperature was heated from room temperature to 800 ℃ with an increasing rate of 5 ℃ /min under N_2 environment.

3.4.7 Nitrogen adsorption isotherms

Nitrogen adsorption isotherms are widely used in materials science and surface characterization to study the adsorption of nitrogen gas onto solid surfaces, particularly for determining the porosity and surface area of materials. The principle behind nitrogen adsorption isotherms is based on the interaction between nitrogen gas molecules and the surface of the material under controlled conditions.

Nitrogen gas (N_2) is chosen as the adsorbate because it is chemically inert and readily available. The adsorption process involves exposing the sample material to a controlled flow of nitrogen gas at various pressures and temperatures. Like the BET theory, nitrogen adsorption isotherms often focus on the formation of monolayers of adsorbate molecules on the surface of the material. In the low-pressure range, the adsorption is primarily due to the formation of a monolayer. At higher gas pressures, nitrogen molecules can adsorb in multiple layers, forming multilayer adsorption. This occurs when the surface sites are saturated with a monolayer, and additional gas molecules adhere to the existing layer(s). Multilayer adsorption can provide information about the pore size distribution and the extent of surface coverage.

Nitrogen adsorption data is often analysed using the Langmuir adsorption isotherm, which describes the relationship between gas pressure and the amount of gas adsorbed on the surface. The Langmuir isotherm assumes that adsorption occurs as gas molecules collide with available surface sites and form a monolayer. The Langmuir equation is typically used to fit experimental data. The BET (Brunauer-Emmett-Teller) equation, based on the BET theory, is also commonly used to analyse nitrogen adsorption isotherms, especially when considering multilayer adsorption. The BET equation can provide information about specific surface area and the number of gas molecules in a monolayer.

The shape of the nitrogen adsorption isotherm curve is indicative of the material's porosity. Specific features, such as the steepness of the adsorption curve at low pressures (indicating microporosity) or the plateau in the multilayer adsorption region

(indicating mesoporosity), provide insights into the material's pore structure. By analysing the nitrogen adsorption data, researchers can also calculate the pore size distribution of the material, providing information about the distribution of pore sizes within the sample. The specific surface area of a material is determined from the amount of gas adsorbed in the monolayer, typically expressed in units of square meters per gram (m^2/g). This measurement is useful for characterizing materials such as catalysts, adsorbents, and porous solids.

Nitrogen adsorption isotherms are based on the principle of studying the interaction between nitrogen gas and the surface of a solid material at various pressures and temperatures. Analysing the resulting data allows researchers to determine properties such as surface area, porosity, and pore size distribution, making it a valuable tool for characterizing materials with porous structures.

In this research, Nitrogen adsorption/desorption isotherms were used to identify he porous structures of samples by Micromeritics ASAP2460 analyser at -196 °C. The weighed samples were first degassed at the Degassing station for 12 h at 200 °C.

3.4.8 UV-VIS DRS

UV-VIS DRS, which stands for Ultraviolet-Visible Diffuse Reflectance Spectroscopy, is a technique used to analyse the absorption of light by solid materials in the ultraviolet (UV) and visible (VIS) regions of the electromagnetic spectrum. The principle of UV-VIS DRS involves measuring the diffuse reflectance of a sample over a range of wavelengths.

When light of a certain wavelength strikes a material, it can be absorbed by the

material if the energy of the photons matches the energy differences between electronic energy levels in the material. This absorption of light is associated with the excitation of electrons from lower to higher energy levels. Instead of measuring the absorbance of a sample directly, UV-VIS DRS measures the diffuse reflectance of the sample. In this technique, a broad-spectrum light source emits light, which is directed onto the sample. The light that is not absorbed by the sample is scattered in all directions (diffuse reflectance), and some of it is collected by a detector.

Samples for UV-VIS DRS are typically powdered or in the form of finely ground solids. The sample is uniformly spread over a substrate with a known reflectance (often a white reference material) to ensure accurate measurements. UV-VIS DRS involves two measurements: one of the sample and one of a reference (often a blank or the substrate without the sample). The reference measurement accounts for the light source intensity and any losses due to scattering or absorption by the substrate. UV-VIS DRS covers a broad spectral range, typically from 190 nanometres (nm) in the UV region to 800 nm or more in the visible region. This range allows for the analysis of a wide variety of materials.

UV-VIS DRS provides information about the absorption bands, which can be correlated with the electronic transitions occurring in the sample. The position and intensity of absorption peaks can reveal details about the material's composition, structure, and electronic properties. The properties make it widely used in materials science, chemistry, and analytical chemistry to study the electronic structure of materials, identify chemical compounds, and determine the concentration of absorbing

species. It is especially useful for characterizing catalysts, pigments, dyes, semiconductors, and nanoparticles.

UV-VIS DRS involves measuring the diffuse reflectance of a sample over a range of wavelengths to determine its absorption characteristics. This technique provides valuable information about the electronic structure and composition of solid materials in the UV and visible regions of the electromagnetic spectrum.

In this study, The UV-4100 spectrometer was used to measure the UV-VIS DRS over a range of 200 to 800 nm, utilizing $BaSO_4$ as the standard material for reflectance.

3.4.9 Photoluminescence (PL)

Photoluminescence is a fundamental process used in various applications, including fluorescence microscopy, semiconductor device characterization, luminescent materials, and quantum dots. It plays a crucial role in understanding the electronic properties of materials and has significant importance in both scientific research and technological advancements. The principle of photoluminescence is based on the interaction of photons (light particles) with a material, which results in the emission of light by that material.

Photoluminescence begins with the absorption of photons by a material. These photons typically have higher energy than the material's ground state electrons can absorb. When a photon is absorbed, it elevates an electron from its ground state to a higher energy level, creating an excited state. The absorbed energy causes the electrons in the material to become excited and move to higher energy levels or even create electron-hole pairs in semiconductors. After reaching these excited states, the electrons

are in an unstable condition. They tend to return to their lower energy states to achieve a more stable configuration. This transition back to lower energy states is where photoluminescence occurs.

As the excited electrons transition back to their lower energy states, they release the excess energy in the form of photons. These emitted photons have energy levels corresponding to the energy difference between the excited state and the ground state. The emitted photons typically fall within the visible or ultraviolet range of the electromagnetic spectrum. The emitted light is what we observe as photoluminescence. This emitted light can have various properties, such as colour, intensity, and duration, depending on the material and its properties.

3.4.10 Zeta potential

Zeta potential is a measure of the electrostatic potential at the shear plane (the boundary between the liquid phase and the stationary layer of fluid molecules adjacent to a charged particle or surface) of a charged particle or colloidal particle in a dispersion. The principle of zeta potential is a key concept in the field of colloid and surface chemistry, particularly in understanding the stability and behaviour of colloidal suspensions.

In colloidal systems, particles or surfaces often acquire a charge due to the presence of ions, adsorbed molecules, or other factors. This charge can be positive or negative, depending on the nature of the particles and the surrounding medium. When a particle is suspended in a liquid medium, it interacts with the surrounding ions in the solution. This interaction results in the formation of an electric double layer (EDL)

around the particle. The EDL consists of two layers: the inner layer, which contains ions of opposite charge to the particle's surface charge, and the outer layer, which contains ions with the same charge as the particle. The zeta potential is measured at a specific distance from the particle or surface, known as the shear plane. This plane is considered the point where the electrostatic potential is significant and influences the movement and interactions of particles.

Zeta potential is determined by measuring the electrophoretic mobility of the charged particles or surfaces in an electric field. This mobility is related to the velocity of the particles as they move under the influence of the applied electric field. The zeta potential is then calculated using the Smoluchowski equation or other mathematical models. This technique is a crucial parameter for assessing the stability of colloidal suspensions. Particles with a high absolute zeta potential value (positive or negative) are more likely to repel each other electrostatically, leading to greater dispersion stability. Conversely, particles with low zeta potential values are more likely to aggregate or flocculate. Zeta potential measurements can be used to study the effects of surface modification or the addition of dispersants or surfactants on the colloidal stability of particles. Altering the zeta potential can be a strategy to control the stability and behaviour of colloidal systems.

In summary, the zeta potential measurement provides critical information about the electrostatic interactions between particles or surfaces in colloidal dispersions. Understanding the zeta potential is essential for controlling the stability and behaviour of colloidal systems in various industries.

Chapter 4 One step synthesis of a Co-doped UiO-66 adsorbent for the enhanced adsorption of organic dyes from wastewater.

In this chapter, a novel CoUiO-66 adsorbent was fabricated with an oil bath synthesis route. This Co-doping modification ensures that the materials retain relatively good crystallinity. The adsorption performance was measured by the adsorption experiments on malachite green (MG) and rhodamine B (RhB). In addition, comprehensive characterizations of the obtained materials were performed to reveal and compare the structure of the pristine MOFs and the Co-doped one. Moreover, adsorption kinetics and isotherms were employed to explain the mechanism in this adsorption process. the CoUiO-66 also showed a superior adsorption capacity on rhodamine B (RhB) (1106.22 mg/g). The adsorption process was well described by both the pseudo-second order and Langmuir models, indicating it was dominated by chemisorption and the adsorbent had a homogeneous surface area for adsorption. In addition, recyclability and stability of the prepared adsorbents were tested to evaluate the practical potential.

4.1 Introduction

The widespread use of organic dyes in various industries has led to the discharge of a significant amount of wastewater containing these dyes into the aquatic environment. Due to their low biodegradability, strong stability and high toxicity, these effluents pose an increasing threat to human and the environment. Therefore, it is of

great importance to remove these risky contaminants before releasing to the environment. In recent decades, various approaches have been applied for the elimination of pollutants from wastewater, like ion exchange, chemical oxidation, biodegradation, photocatalytic degradation, and adsorption [19]. Among the various approaches, adsorption has many advantages such as high efficiency, simple operation and low cost, which has been shown to be a promising method for wastewater treatment [180].

Metal-organic frameworks (MOFs), as a rising category of porous nanomaterials constructed from metal centres with organic ligands [181], exhibit a number of special properties such as high porosity unique chemical versatility, and tailored functionality [182], which make them promising candidates for various applications such as adsorption [183], membrane separation [184], catalysis [185], energy storage [186], drug delivery [187] and sensing [188].In recent decades. MOFs have attracted great interest in adsorption and separation for water treatment. However, despite their superiority, most MOFs exhibit weak stability in the water environment, which is still a problem that limits their application. Therefore, hydrolytic stability is an important consideration in the selection of potential materials for wastewater treatment [189]. Among the reported MOFs, zirconium-based MOFs (UiO-66 series) have gained emerging interests owing to their remarkable adsorption performance and exceptional water stability [104]. UiO-66 is a member of the UiO family with the composition of $Zr_6O_4(OH)_4(BDC)_6$ [190]. It exhibits superior surface area, ultra microporous structure, excellent water and thermal stability [191].

The removal of various pollutants by UiO-66 during wastewater treatment has been the subject of numerous studies. Some scientists conducted a comparative analysis on the performance of untreated and functionalized UiO-66 as adsorbents. The results showed that both the untreated and functionalized UiO-66s had higher adsorption performance compared to commercial AC [192]. Moreover, Numerous approaches have been employed to modulate the framework of UiO-66 to enhance its uptake performance. For example, HCl was used as a modulator to promote the uptake ability of methyl orange by UiO-66. The acid-promoted MOFs exhibited a significantly larger uptake amount of 84.8 mg/g compared with untreated MOFs. [193]. In addition, defects rationally introduced to UiO-66 showed an obvious improvement on adsorption performance towards RhB. Compared with the original UiO-66 (108.8 mg/g), The uptake performance of defective UiO-66 on RhB (383.6 mg/g) was significant better [194]. Metal doped modification has proven to be another effective method, The titanium doped hybrid UiO-66 exhibits significantly improved capture ability towards Conge red in comparison with original samples, Which was 979.0 mg/g over 283.0 mg/g [195]. In addition, the Mn-doped UiO-66 with cubic morphology also showed an increase in adsorption capacity compared with pure UiO-66. The adsorption amount of the metal-doped samples toward tetracycline (184.49 mg/g) and Cr (VI) (32.77 mg/g) was 4.9 and 3.1 times greater, respectively, than that of UiO-66 [196]. Furthermore, UiO-66 with Co-doping modification exhibited an increased tetracycline elimination performance including both adsorption with photocatalysis process simultaneously [197]. Obviously, the doping method is a promising approach to improve adsorption

performance owing to its modification on pore structure and surface functionality. Although various works have been done on this field, there is still a huge demand to explore materials with more excellent adsorption performance and practical potential. Therefore, this method was employed in this work as an effective route to design and prepare new MOFs-based adsorbents on the elimination of pollutants.

In this work a different synthetic route was applied to prepare Co-doped UiO-66 adsorbents for the removal of organic dyes. Malachite green (MG) and rhodamine B (RhB) were used as target pollutants to measure the performance of obtained CoUiO-66 adsorbent in wastewater treatment. FT-IR, SEM, TEM, XRD, BET, EDS, TGA, XPS were used to characterize the structure of the synthesized materials. Various experimental work was performed systematically to test the adsorption capacity of CoUiO-66, along with a proposed mechanism to explain the observed results. Moreover, the recyclability of obtained samples was investigated to assess the potential for practical application. This research provided a helpful insight into the synthesis of metal-doped MOFs materials with excellent adsorption performance.

4.2 Experimental

4.2.1 Synthesis of samples

The Co-doped UiO-66 material was synthesized by an oil bath method. Typically, $ZrCl_4$, $CoCl_2$-$6H_2O$, and H_2BDC were dispersed in 100 mL DMF with a molar ratio of 1:2:1. Then, the suspension was magnetically stirred for 1 hour to achieve a homogeneous solution at ambient temperature. Afterwards, the mixture was used in a

round-bottom oil bath reactor kept at 120 ℃. With 24 h heating, the obtained precipitate was centrifuged and washed thoroughly using DMF and ethanol several times. The final products were collected after drying in vacuum at 65 °C overnight. In addition, the original UiO-66 was prepared by the same route without addition of $CoCl_2$-$6H_2O$. The general route was shown in Figure 4.1.

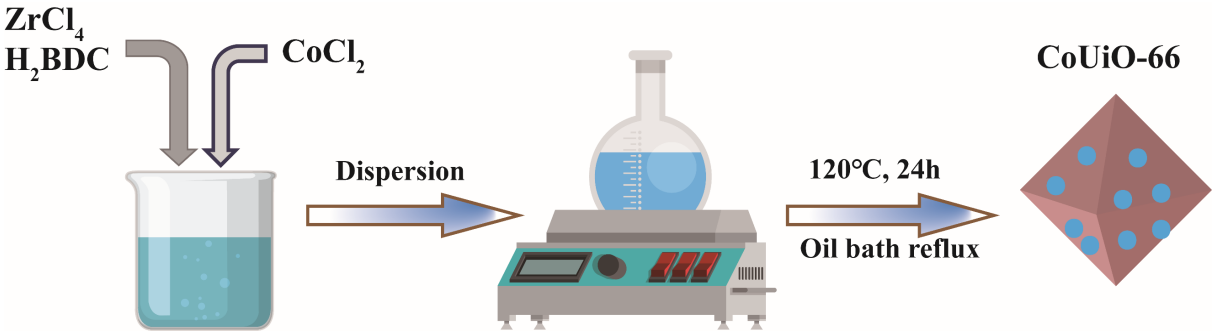

Figure 4.1 The synthesis route of Co-doped UiO-66

4.3 Results and Discussion

4.3.1 Phase and structure analyses

XRD tests were conducted to reveal the crystalline nature and composition of the synthesized samples. It was shown in Figure 4.2 that six characteristic peaks of all MOFs are found at 2θ=7.3°, 8.5°, 13.8°, 17.2°, 25.7°, 30.6°, which are associated with the UiO-66 crystal faces for (111), (200), (222), (400), (442) and (711), respectively [198]. The XRD patterns of the obtained materials were highly consistent with those of simulated UiO-66 and with those reported in the literature, confirming the successful preparation of UiO-66 and Co-doped MOFs [199, 200]. Moreover, the highly similar patterns indicated that the original crystalline structure of UiO-66 was not altered by this metal-doping modification process. Moreover, no diffraction peaks of Co species

were found in the patterns, indicating that the doped Co was probably highly dispersed and poorly loaded [201]. In addition, the intensity of the characteristic peaks of CoUiO-66 was slightly lower compared with the pristine UiO-66. It suggested that the bigger Zr atoms in the (Zr–O) clusters were partially replaced by smaller Co atoms, resulting in limited crystal growth and a shrunken crystal lattice in CoUiO-66 [195].

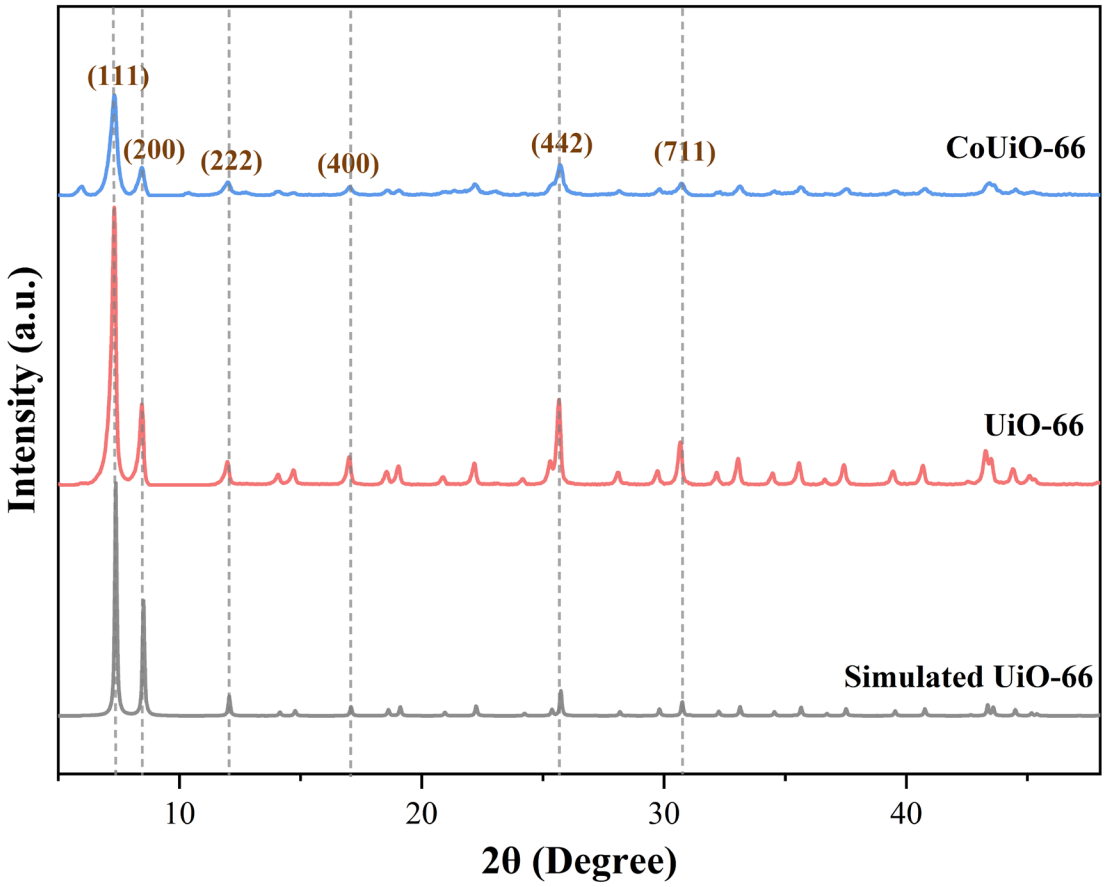

Figure 4.2 XRD (a) patterns of UiO-66 and CoUiO-66 samples.

Figure 4.3 showed the FTIR results of the samples. The image showed that the spectrum of UiO-66 and CoUiO-66 was almost identical, indicating that the functional groups of UiO-66 did not change during the modification process with the metal. First, a strong band around 3500 cm^{-1} was attributed to O-H groups, indicating that water molecules may be condensed in the frameworks [202]. A small peak was observed at

1650 cm^{-1} for pristine UiO-66, which was attributed to the C=O stretching vibration in the carboxylic acid derived from H_2BDC [203]. On the other hand, this similar peak could not be found in CoUiO-66, implying that the doping of Co ions may influence the formation of C=O bonds in UiO-66.The intense peaks between 1590 to 1400 cm^{-1} could be assigned to carboxyl groups in the H_2BDC with asymmetric and symmetrical vibrations [204]. Moreover, Moreover, the peaks situated at 770 and 650 cm^{-1} were associated with the vibrations of O-H and C-H bonds in the organic ligands. The peaks at 550 and 480 cm^{-1} could be assigned to Zr-O and Zr-O_2 stretching vibrations [205]. All the very similar bands between UiO-66 and CoUiO-66 convinced that no change of functional groups occurs during the Co-doped medication and the successful formation of UiO-66 based materials.

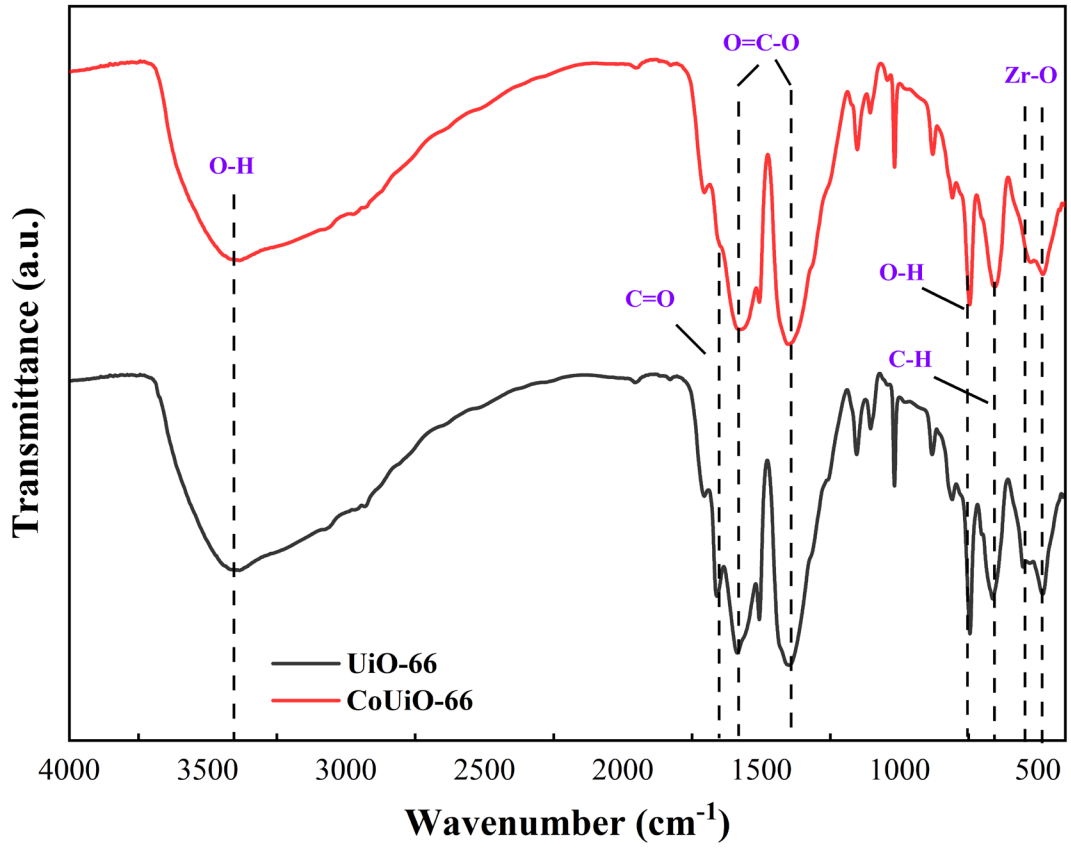

Figure 4.3. FTIR spectrum of UiO-66 and CoUiO-66 samples

XPS testes were applied for elucidating the surface composition and chemical state of prepared samples. As displayed in Figure 4.4, the survey spectrum in Fig. 6a showed obvious elemental peak of C, O and Zr, while the atomic ratio of Co was 0.54% which could be attributed to the inapparent peak of Co. Fig. 6e illustrated two peaks around 782.4 eV and 796.6 eV which stood for Co $2p_{3/2}$ and Co $2p_{1/2}$, suggesting that the doped Co formed Co-O bonds with O in CoUiO-66 [206]. In addition, according to the XRD analysis, there were no diffraction peaks associated with cobalt oxide species found in the XRD pattern, which demonstrated that the cobalt ion coordinated with oxygen atom successfully in the skeleton of pristine UiO-66. Furthermore, the Co 2p spectrum shown in Fig. 4e indicated that Co^{3+} was the dominate charge state in the materials [207]. The XPS results were also highly consistent with the previous findings that the Co element was doped in UiO-66 successfully.

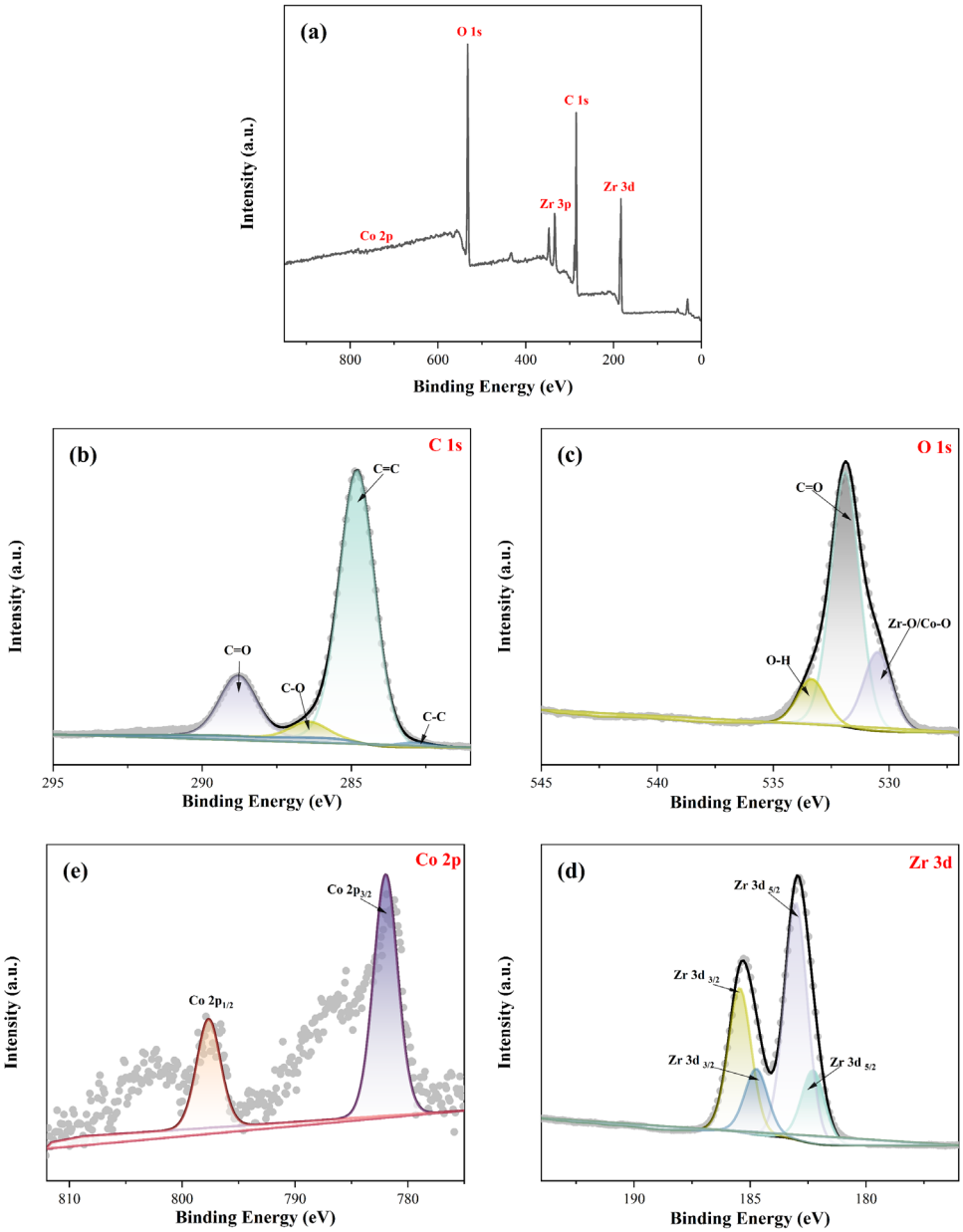

Figure 4.4 XPS results: survey (a), C 1s (b), O 1s (c), Zr 3d(d), Co 2p (d) of CoUiO-66.

4.3.2 Morphological analysis

As SEM images shown in Figure 4.5, the original UiO-66 has an agglomerated octahedral morphology with a uniform shape. On comparing with the parent UiO-66, the Co-doped modification method gives CoUiO-66 a well-defined and dispersive cubic morphology with a rougher surface. In addition, the average diameter of the

CoUiO-66 cubes was calculated to be 22.76 nm, which was significant smaller than that of original UiO-66 (85.36 nm), indicating that this metal-dope modification can cause an obviously smaller crystal size and higher dispersion. The remarkable difference in the particle size and morphology of parent UiO-66 and CoUiO-66 also suggested that the Co doping process had inhibited the growth of UiO-66 crystals.

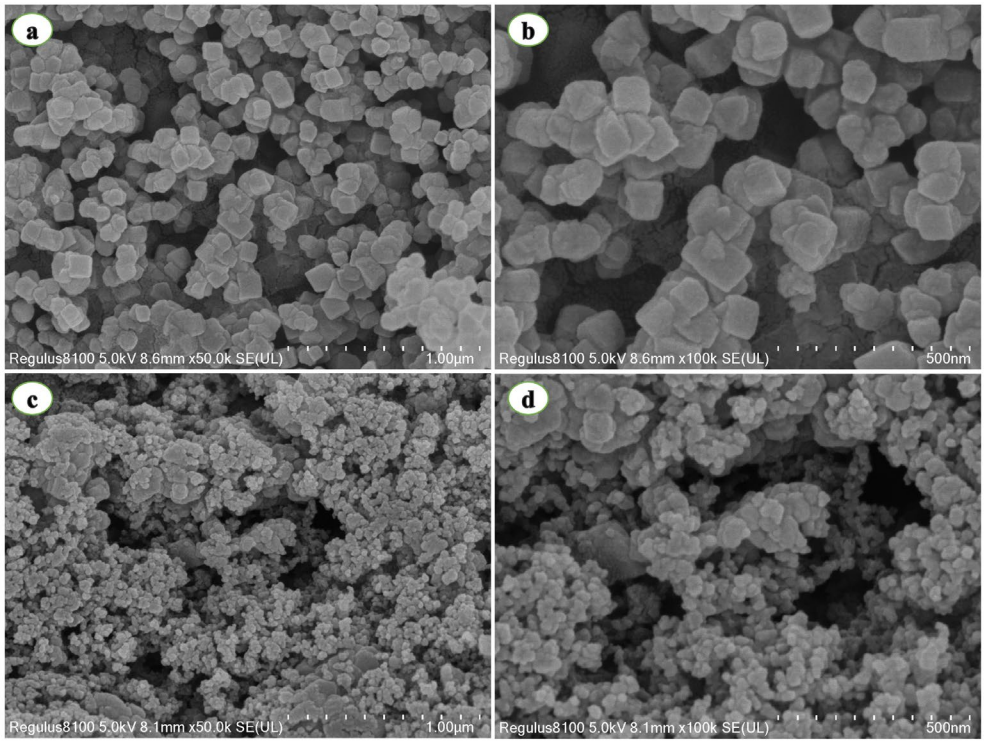

Figure 4.5. SEM images of UiO-66 (a-b) and CoUiO-66 (c-d).

Moreover, the TEM images in Figure 4.6 suggested that both the pristine UiO-66 and CoUiO-66 exhibited the homogeneous-phase crystal morphology, and no evident particle was observed on the surface of CoUiO-66, implying that no metal or metal oxide was attached on Co-doped UiO-66. Therefore, both the SEM and TEM results indicated that the Co-doped UiO-66 presented a homogeneous crystal morphology rather than a simple mixture of Co-related impurity with pure UiO-66, which further confirmed the previous analysis.

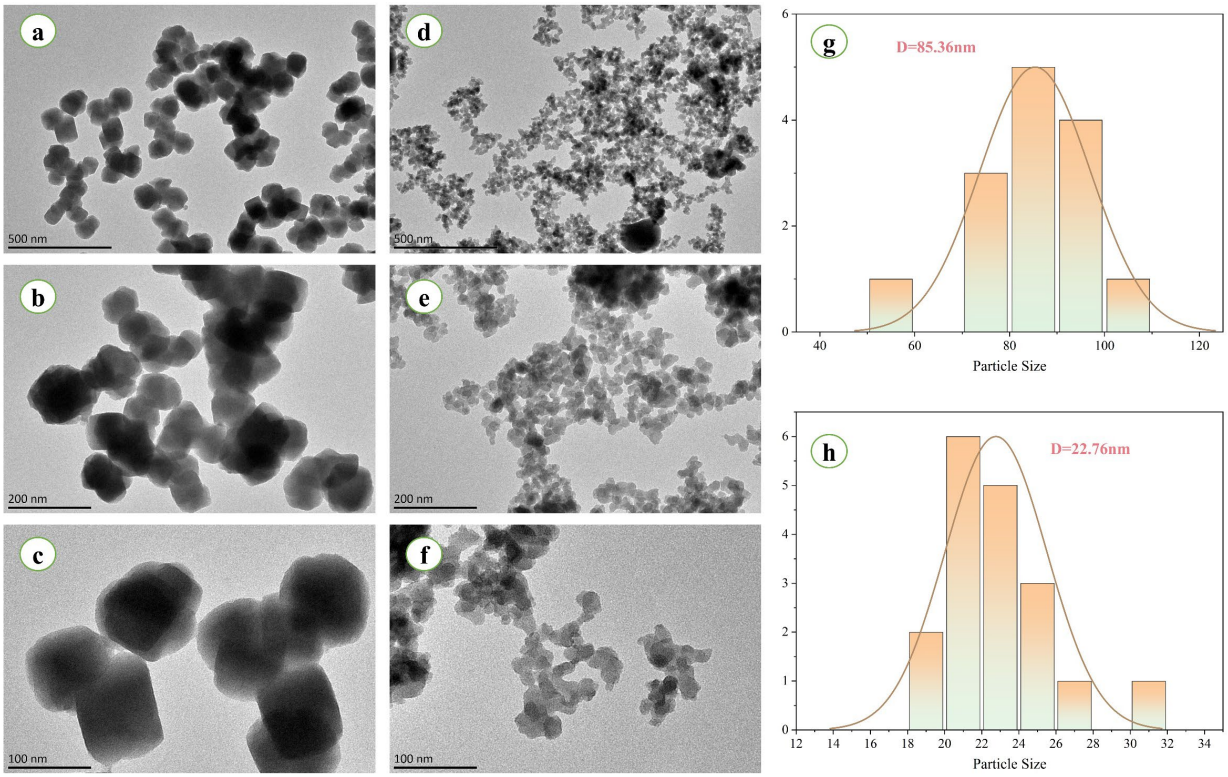

Figure 4.6 TEM images of UiO-66 (a, b, c) and CoUiO-66 (d, e, f) with different resolutions; Particle size distribution of UiO-66 (g) and CoUiO-66 (h).

In addition, the EDS elemental mappings of CoUiO-2 displayed in Fig. 4.7 demonstrated that the Co element was homogeneously dispersed in UiO-66, further confirming that the Co ion was successfully introduced into the framework of pristine UiO-66. Moreover, a pronounced Zr peak was observed in Fig. 4.7d, while the peak of Co was very weak, indicating that only a few of Co ion could be coordinated into the organic ligand and partially replaced the Zr atom, even though it had the same ratio compared with Zr ion during the synthesis process. Furthermore, ICP-MS test was carried out to evaluate the content of metal ratio. 50 mg of CoUiO-66 was dissolved in 100 mL of nitric acid. The results showed that the concentration of Zr and Co ion were 87.8 mg/L and 5.71 mg/L, respectively, which indicated that the content of Zr and Co

were 17.56% and 1.14%, the ratio of Zr/Co was 15.40. The ratio of Cobalt in CoUiO-66 further confirmed that only a small part of Co ion could be introduced into the structure of UiO-66.

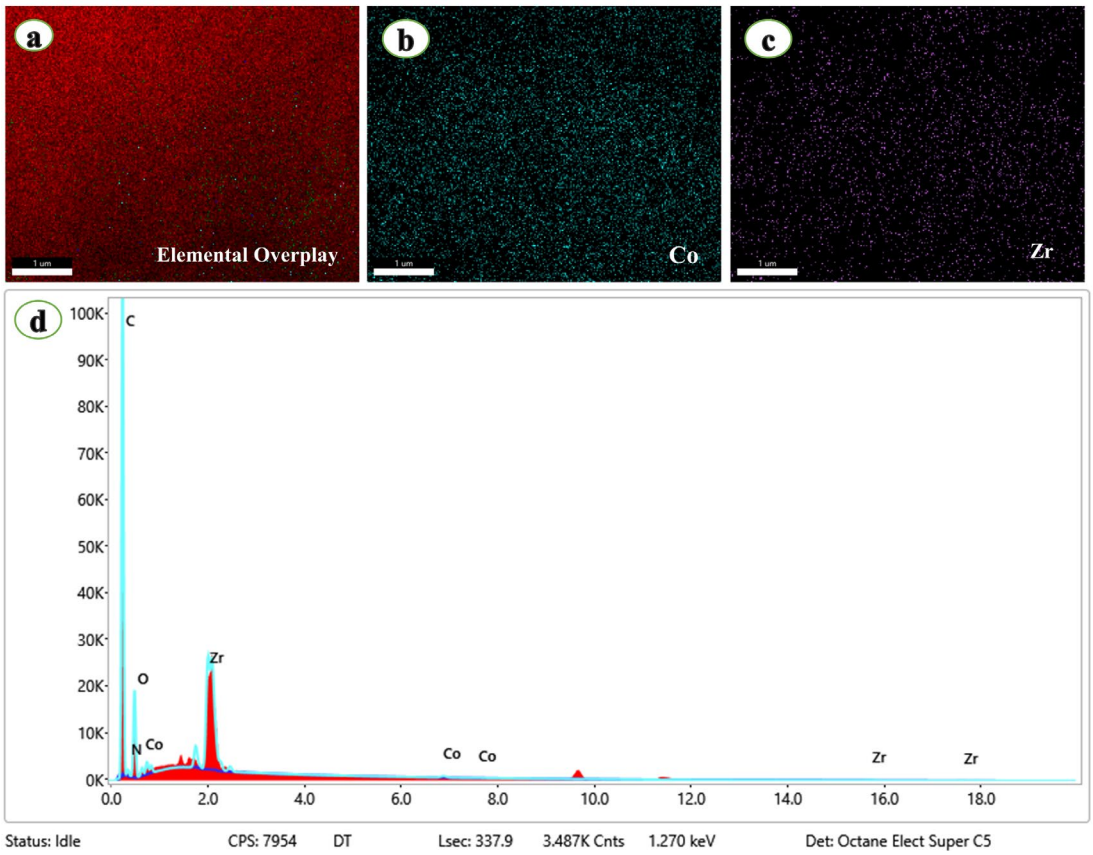

Figure 4.7 EDS elemental mappings of CoUiO-66: elemental overplay (a), Co (b), Zr (c), elemental peak (d).

4.3.3 Thermal stability analysis

The thermal stability of the MOF materials was measured by TGA tests with an increase to 800 ℃ under N_2 atmosphere. It was depicted in Figure 4.8 that the TG-DTG plot of the materials showed very similar trends with three weight loss stages ranging from 25 - 800 ℃. The first stage of mass loss observed around 100 ℃ could be assign with the desorption of H_2O molecule from the cavities of the nanoparticles [208]. The second stage between 200 - 500 ℃ could be the loss of DMF molecules and the

dihydroxylation process [209]. The third weight loss in the 500 - 600 ℃ could be attributed to the complete decomposition of the whole framework together with the formation of metal oxide. Therefore, the weight loss in this step could indicate the ratio of linkers in the framework structure [210]. Finally, the weight reduction was 57.48 and 62.61% for UiO-66 and metal-doped one at 800 ℃, respectively. The residual product of UiO-66 and CoUiO-66 was ZrO_2 and a mixture of ZrO_2 and Co_3O_4, respectively [211]. The Co-doped UiO-66 exhibited a similar curve and lower weight loss than pristine UiO-66, indicating that this doping of the Co element into the UiO-66 host was successful and more structural defects were introduced [212].

It is reported that "missing link Defect" can be generated in UiO-66. For the ideal structure of UiO-66, each Zr atom is coordinated to 12 organic links (BDC^{2-}). When metal salts were added into the synthetic process, the metal cation would compete with Zr^{2+} for organic ligands and change the coordination environment of the central ion and the organic ligand, resulting in the introduction of more defects. Based on all the analysis above, it was speculated that the Co doping modification caused the breakage of ZrO bond, introducing more defects, which could improve the surface area and pore size. These could be beneficial for the enhancement of adsorption performance.

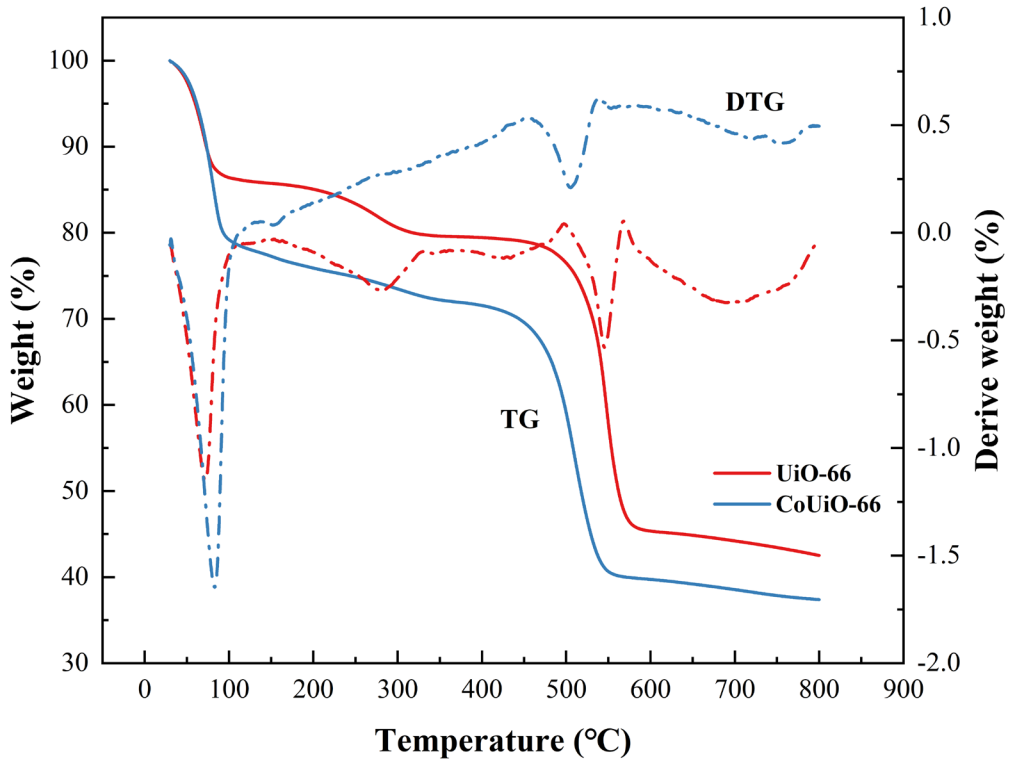

Figure 4.8 TGA-DTG curves of pristine UiO-66 and CoUiO-66.

4.3.4 Porosity analysis

The N_2 adsorption tests were used to further investigate the surface morphology and porosity of the obtained samples. As shown in Figure 4.9 and Table 4.1, all materials exhibited an obvious type I isotherm on the basis of IUPAC classification, suggesting that these materials were microporous structures [213]. Compared with original UiO-66, the Co-doped MOFs showed a evident promotion in surface area, pore volume and pore size. The S_{BET} improved from 855.73 to 966.46 m^2/g, and the other porosity parameters also showed a significant improvement, indicating that this modification Co successfully doped into the pore structure and had a great effect on the porosity of UiO-66. In general, larger S_{BET} and pore volume offers greater number of active sites, which is a positive factor to promote the uptake performance [214, 215].

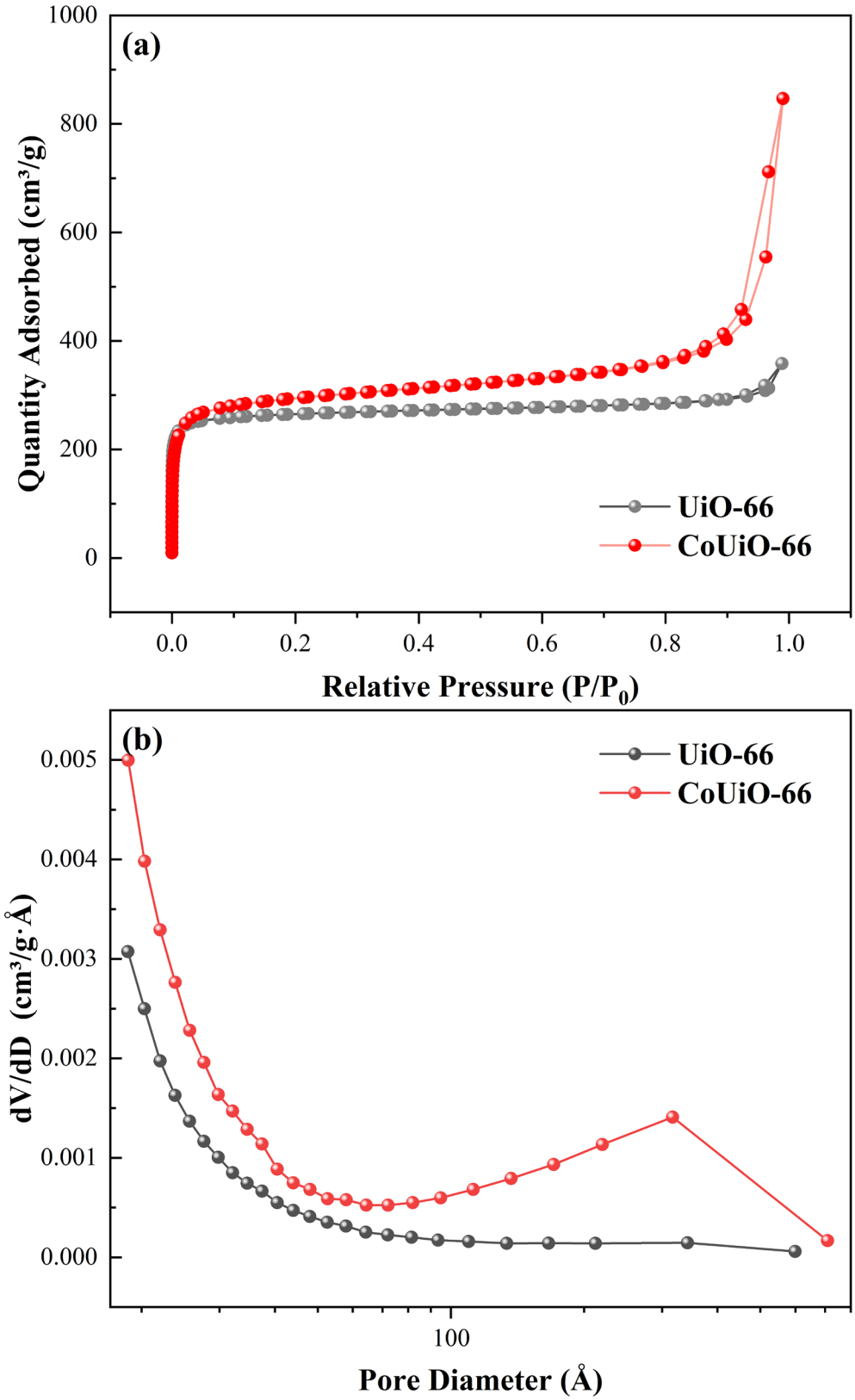

Figure 4.9 (a) N_2 adsorption-desorption isotherms and (b) pore size distribution of UiO-66 and CoUiO-66.

Table 4.1 Porosity parameters of UiO-66 and CoUiO-66

Samples	S_{BET} (m^2/g)	Pore volume (m^3/g)	Pore size (nm)
UiO-66	855.73	0.55	25.99
CoUiO-66	966.46	1.31	54.39

4.3.5 pH influence

pH was a main factor that can affect the structure of both adsorbents and dye molecules. Therefore, the adsorption capacities of UiO-66 and CoUiO-66 were investigated against MG in a range of pH (2-12). Fig. 10 shows that the maximum adsorption capacities are near pH=4. The adsorption capacities reached their minimum at pH 2, which was probably associated with the electrostatic repulsion between the positively charged UiO-66 series and MGH^+ that hinders the adsorption process [91]. After the adsorption capacities increased upward, they decreased from pH 4 to the end. It was reported that MG protonates in acidic solution, while it deprotonates at higher pH values [216]. As shown in Figure 4.10 and Figure 4.11, the isoelectric point of UiO-66 and CoUiO-66 were 9 and 8, respectively, indicating that all adsorbents ad dye molecules were positively charged at acidic pH condition. The maximum adsorption capacities at pH 4 suggests that electrostatic interaction is not the major force in this process. Moreover, it could speculate that other interactions such as π-π interactions, H-bonding, and physical adsorption could occur in this process [217].

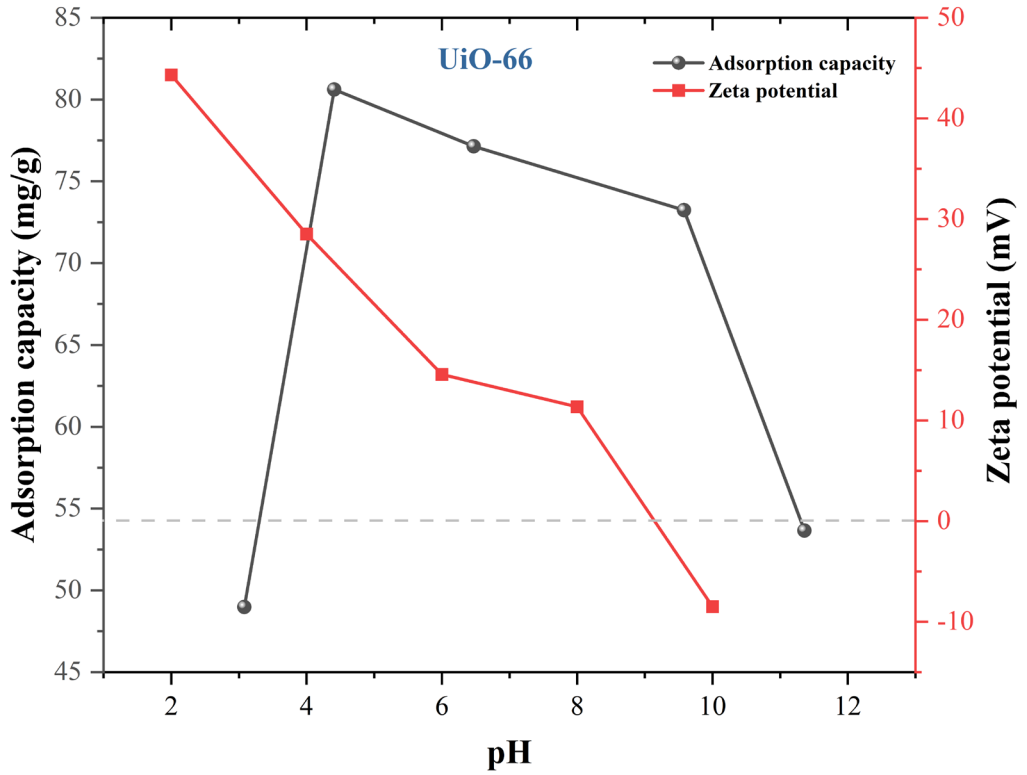

Figure 4.10 Adsorption capacities and Zeta potential of UiO-66

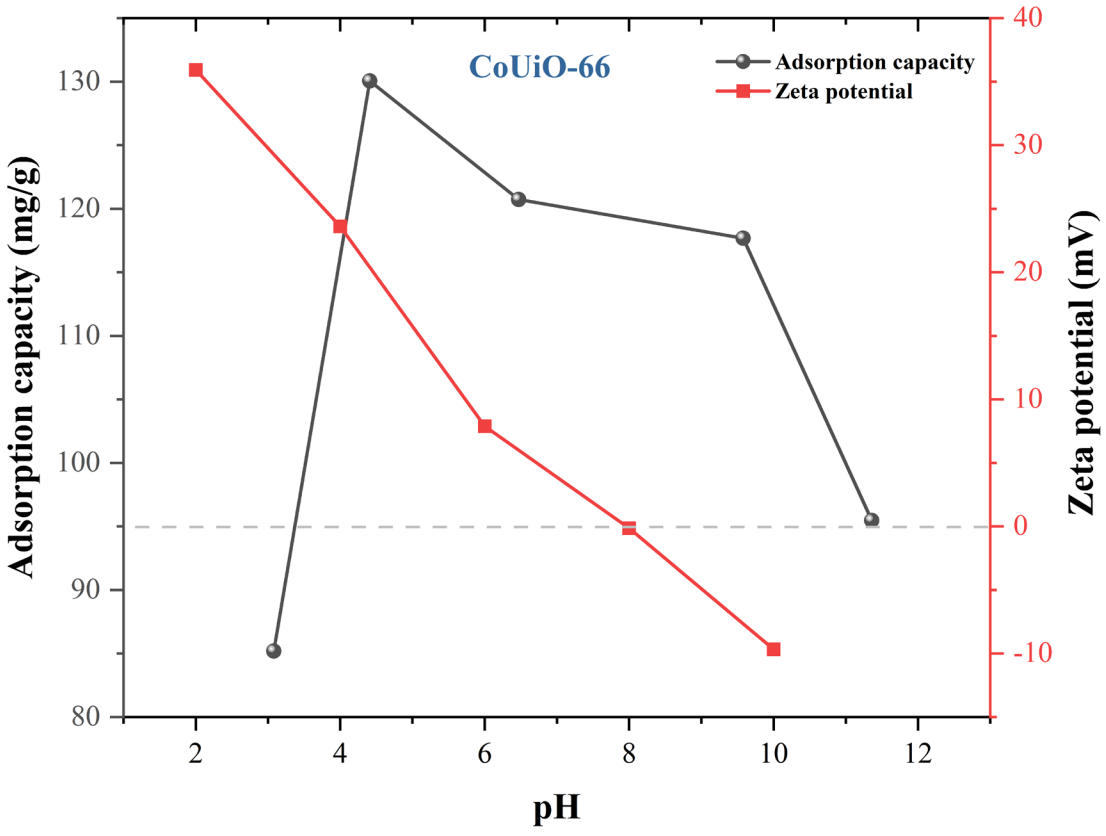

Figure 4.11 Adsorption capacities and Zeta potential of CoUiO-66

4.3.6 Adsorption kinetics

To get a better comprehension on the adsorption performance of the materials, the relation between reaction time with adsorption capacity was studied. The adsorption kinetic can evaluate the rate and mechanism of the adsorption process. In general, the first-order pseudo-model (Eq. 4.1) and the second-order pseudo-model (Eq. 4.2) were used to fit the experimental kinetic data.

$$q_t = q_e(1 - e^{-k_1 t}) \quad \text{4.1 [218]}$$

$$\frac{t}{q_t} = \frac{1}{k_2 q_e^2} + \frac{1}{q_e} t \quad \text{4.2 [218]}$$

$$q_t = k_p t^{0.5} + C \quad \text{4.3 [218]}$$

Figure 4.11 illustrated the adsorption kinetics of MG onto UiO-66 and Co-UiO-66, and the related results were computed and presented in Table 4.2. For MG adsorption, the batch experiments were typically performed for UiO-66 and CoUiO-66 under the conditions of 100 mg/L, 25 ℃, pH=4. As shown in Figure 4.11, the adsorption curve for the different samples showed a similar trend. The uptake rate increased rapidly in 60 minutes and then gradually reached equilibrium within 480 minutes. The rapid adsorption rate in the initial stage might be associated with the presence of abundant free active sites [219], and the adsorption sites gradually decreased with time and finally became saturated, leading to the equilibrium stage. It was reported that the pseudo-first order model was associated with physisorption and diffusion [220], while pseudo-second order was related to chemisorption process [221]. The fitting parameters were compiled in Table 3. It documented that the R^2 of the pseudo-second order model was notably higher compared with pseudo-first order model, implying that all adsorption

processes fitted the pseudo-second order model, which suggested that the processes were chemisorption [222]. In addition, Figure 4.12 showed that the Co-doped UiO-66 had a much higher adsorption rate and capacity, indicating that CoUiO-66 was a much better adsorbent than the original UiO-66. To evaluate the performance of CoUiO-66 as a potential adsorbent, further adsorption studies were performed on CoUiO-66 for another organic dye, RhB. As shown in Figure 4.13, CoUiO-66 exhibited superior adsorption performance for RhB, faster rate and higher uptake capacity than the adsorption of MG. In addition, the R^2 of the pseudo-second order model was obviously higher compared with pseudo-second order model, which was similar to the adsorption process of MG.

Table 4.2 Kinetic parameters for MG and RhB adsorption onto UiO-66 and CoUiO-66.

Samples	Pollutant	Pseudo-first order			Pseudo-second order		
		q_e (mg/g)	k_1 (min^{-1})	R^2	q_e (mg/g)	k_2	R^2
UiO-66	MG	74.329	0.021	0.989	79.744	4.4×10^{-4}	0.995
CoUiO-66	MG	126.346	0.023	0.989	138.125	2.6×10^{-4}	0.999
CoUiO-66	RhB	335.228	0.021	0.973	357.939	0.8×10^{-4}	0.998

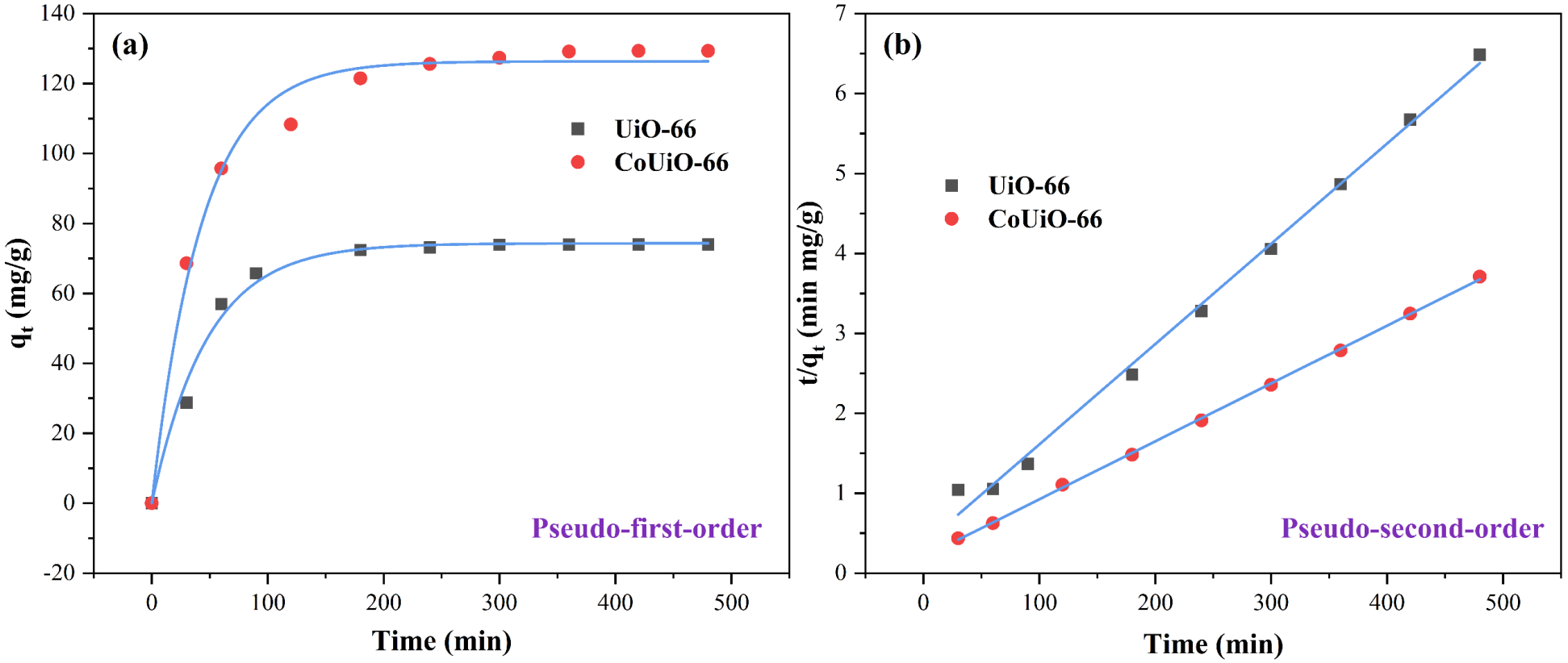

Figure 4.12 Adsorption kinetics on MG: (a) pseudo-first order; (b) pseudo-second order model of UiO-66 and CoUiO-66.

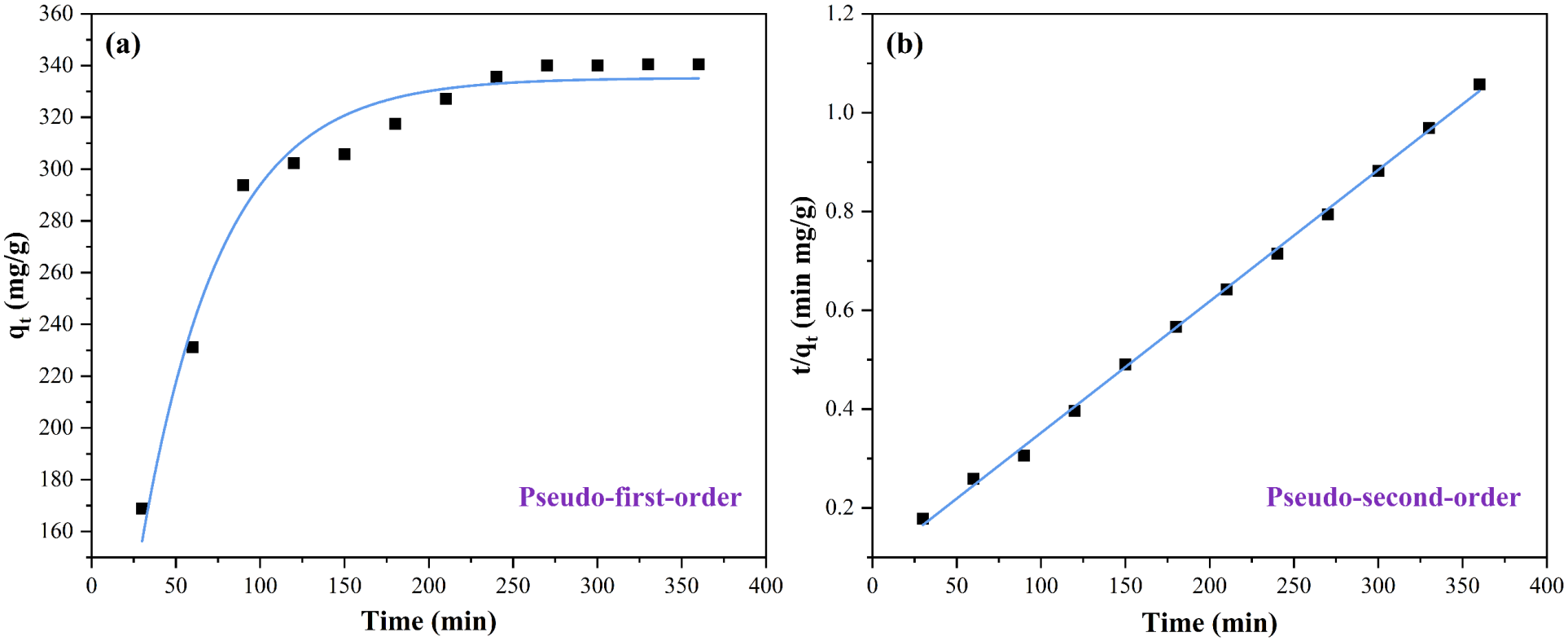

Figure 4.13 Adsorption kinetics of CoUiO-66 on RhB: (c) pseudo-first order; (d) pseudo-second order model

4.3.7 Adsorption isotherms

Adsorption isotherm could be employed to investigate the adsorption mechanism via assessing the equilibrium data at diverse initial dye concentrations. Langmuir and Freundlich isotherms are the most common used isotherm models. These can be expressed by Eq. 4.4 and Eq. 4.5 as follows:

Langmuir: $\frac{C_e}{q_e} = \frac{1}{q_m K_L} + \frac{C_e}{q_m}$ 4.4 [196]

Freundlich: $lnq_e = lnK_F + \frac{1}{n} lnC_e$ 4.5 [196]

The data of the batch experiments at different temperatures and the results of the adjustment were shown in Figure 4.14 and Table 4.3. It was depicted that the adsorption capacities promoted with rising temperature for both UiO-66 and CoUiO-66, indicating that the adsorption of MG was a spontaneous and endothermic process [209]. The maximum equilibrium adsorption capacities of CoUiO-66 on MG were 465.11, 578.03, and 629.93 mg/g at 15, 25, and 35 ℃. These results were significantly higher compared with pure UiO-66 and other materials reported in the literature. To further evaluate the adsorption performance of CoUiO-66, batch adsorption experiments with RhB were also performed, as shown in Figure 4.15. The maximum equilibrium adsorption capacities of RhB on CoUiO-66 were calculated to be 781.25, 925.92 and 1106.22 mg/g at 15, 25 and 35 ℃, respectively. The fitting results shown in Table 4.3 document that the Langmuir model was a higher fit compared with Freundlich model with better correlation coefficients. It was reported that the Langmuir isotherm was applied to explain the phenomenon of monolayer adsorption on a homogeneous surface and that the adsorption sites have identical affinity to the target molecules [223, 224]. On the basis of aforementioned analysis, the adsorption process of UiO-66 and Co-doped UiO-66 can be regarded as single-layer adsorption by chemisorption for both MG and RhB.

To evaluate the adsorption performance of MG and RhB by the prepared adsorbents, the results obtained in this work were compared with other similar literature reports (Table 4.4). It was displayed that the adsorption performance of this work is remarkably higher than that of most literature reports.

Table 4.3 Langmuir and Freundlich model parameters determined by curve fitting of UiO-66 and CoUiO-66.

Samples	Pollutants	Temperature (°C)	Langmuir isotherm			Freundlich isotherm		
			q_m (mg/g)	K_L (L/mg)	R^2	n	K_F	R^2
UiO-66	MG	15	161.031	0.016	0.998	2.304	6.494	0.876
		25	223.712	0.017	0.998	2.545	7.937	0.929
		35	343.644	0.021	0.994	2.521	9.3371	0.845
CoUiO-66	MG	15	465.116	0.008	0.995	1.643,	6.548	0.971
		25	578.031	0.007	0.995	1.507	6.583	0.981
		35	628.932	0.019	0.996	1.899	9.122	0.967
CoUiO-66	RhB	15	781.251	0.009	0.999	1.973	9.428	0.956
		25	925.925	0.017	0.997	2.276	11.414	0.953
		35	1106.219	0.079	0.998	4.165	15.366	0.855

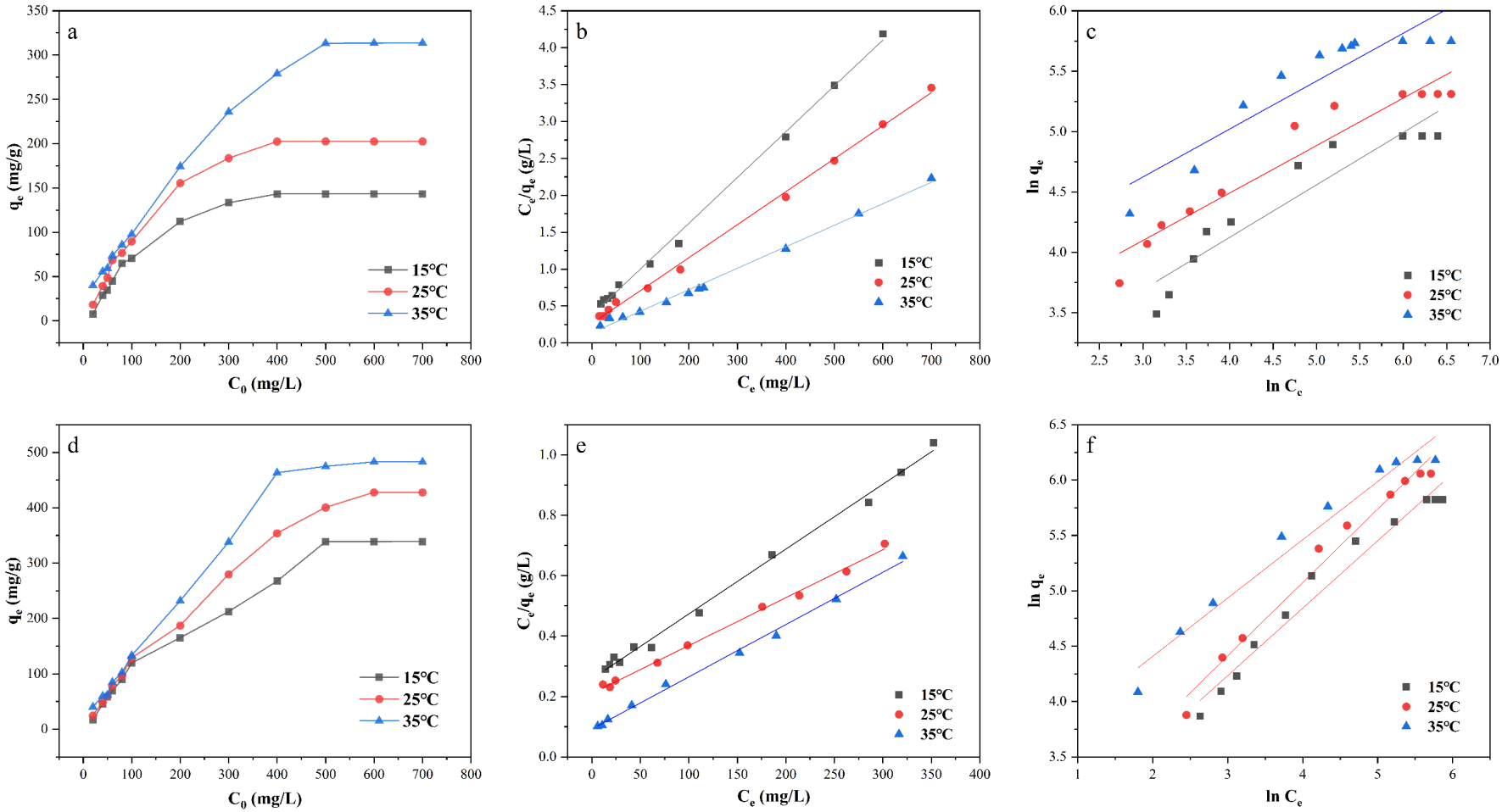

Figure 4.14 Adsorption isotherms of MG on UiO-66(a) and CoUiO-66 (d) at varied temperatures; Fitting the adsorption isotherm linear curves: (b) Langmuir model of UiO-66; (c) Freundlich model of UiO-66; (e) Langmuir model of CoUiO-66; (f) Freundlich model of CoUiO-66.

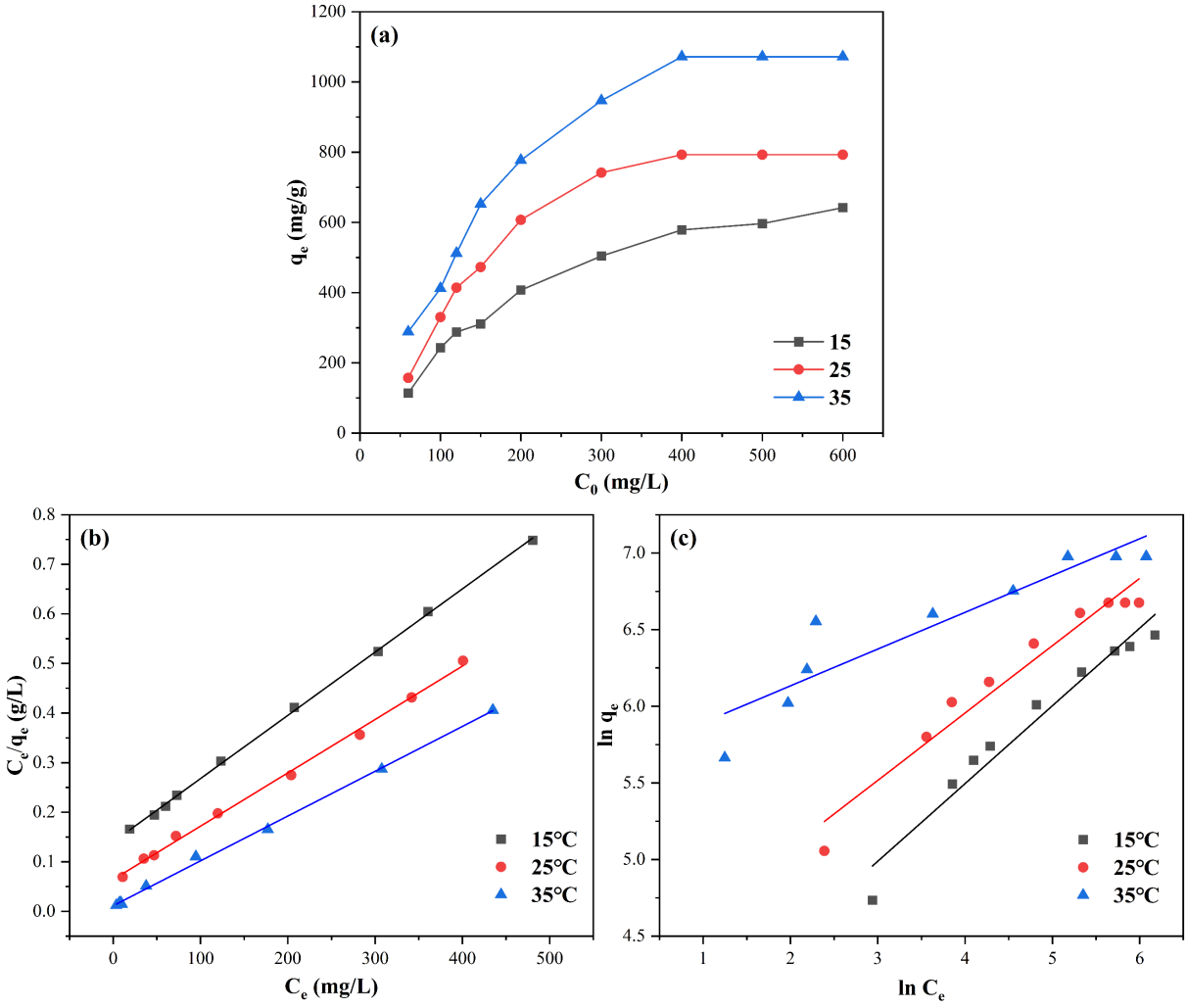

Figure 4.15 Adsorption isotherms of RhB on CoUiO-66 at varied temperature (a); Langmuir model (b); Freundlich model (c).

4.3.8 Reusability

Reusability is also one of the most important aspects for the practical and commercial application of adsorbents [225]. Therefore, the adsorption performance of the recycled adsorbents was tested after the adsorption reached equilibrium. The CoUiO-66 adsorbed with dye were obtained by centrifugation at 8000 rpm with10 min, then washed with diluted hydrochloric acid and water for three times and collected for reuse after drying at 100 ℃. The regenerated MOF samples were used for the adsorption experiments with successive 8 cycles. As shown in Figure 4.16, after ten regeneration cycles, it was found that the uptake amounts of MG and RhB on CoUiO-66 were 577.14 and 1029.16 mg/g in 35℃, retaining 91.76% and 93.93% of the adsorbed amount in the first time, respectively, indicating that this Co-doped MOFs had a great potential for the adsorption of organic pollutants in water purification.

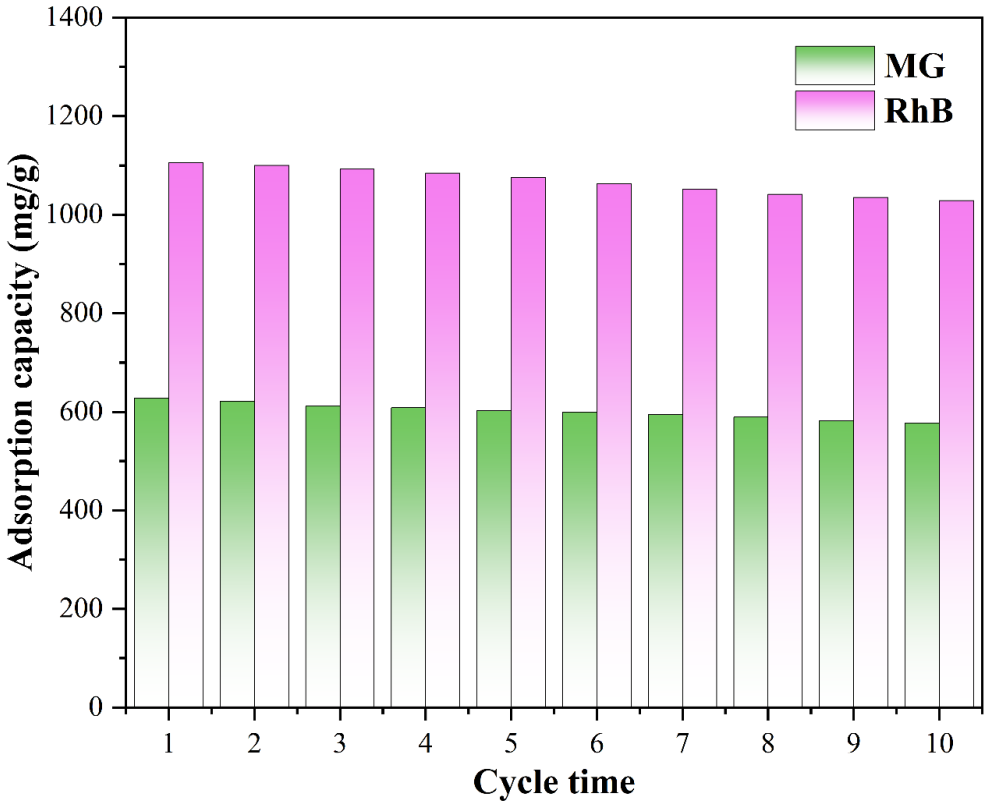

Figure 4.16 Regeneration of CoUiO-66 for adsorption performance of MG and RhB.

Table 4.4 Comparison of maximum adsorption capacities of MG and RhB

Samples	Pollutants	Adsorption capacities (mg/g)	Ref.
Biochar	MG	91.2	[226]
Biochar		67.6	[227]
MOF-2		185.4	[228]
Cellulose nanofibril		212.7	[229]
MCM-41/RH		285.0	[230]
Cu-MOFs/Fe_3O_4		113.7	[231]
MIL-53(Al)-NH_2		164.9	[232]
Fe_3O_4@SiO_2-NH_2		173.0	[233]
Fe_3O_4@AMCA-MIL53(Al)		329.6	[234]
CoUiO-66		628.9	This work
Biochar	RhB	123.5	[235]
Graphene oxide/Beta zeolite		64.5	[236]
A-rGO/Co_3O_4		102.9	[237]
SnS_2		200.0	[238]
Fe@ZIF-67		135.1	[239]
Fibrous $LaFeO_3$		182.6	[240]
MoS2/MIL-101		344.8	[241]
ZnO/Zr-MOF		918.9	[242]
RGO/REMO		243.4	[243]
CoUiO-66		1106.2	This work

4.4 Adsorption mechanism

To Further analyse the possible mechanism of the adsorption process, FTIR and XPS tests of the CoUiO-66 before and after adsorption were carried out. As shown in Figure 4.17, there were a few differences between pristine CoUiO-66 and absorbed sample. In general, the intensity of each diffraction peak was obviously decreased, suggesting the strong interaction between CoUiO-66 and dye molecules. The peaks of C=O stretching (1590 cm^{-1}) and O–H bending vibration (1400 cm^{-1}) diminished to a lower intensity, indicating the hydrogen bonding was formed by carboxyl and hydroxyl groups. The peak of C=C at 1509 cm^{-1} illustrated a decrease, which could be assigned to π-π stacking between the benzene ring of CoUiO-66 and dye molecules. Furthermore, there was also a decrease observed in the peak of Zr-O (480 cm^{-1}), implying that surface complexation over metal sites and dye molecules also had a great effect on the adsorption process. Thus, based on the previous analysis, the possible adsorption mechanism could be illustrated in Figure 4.18.

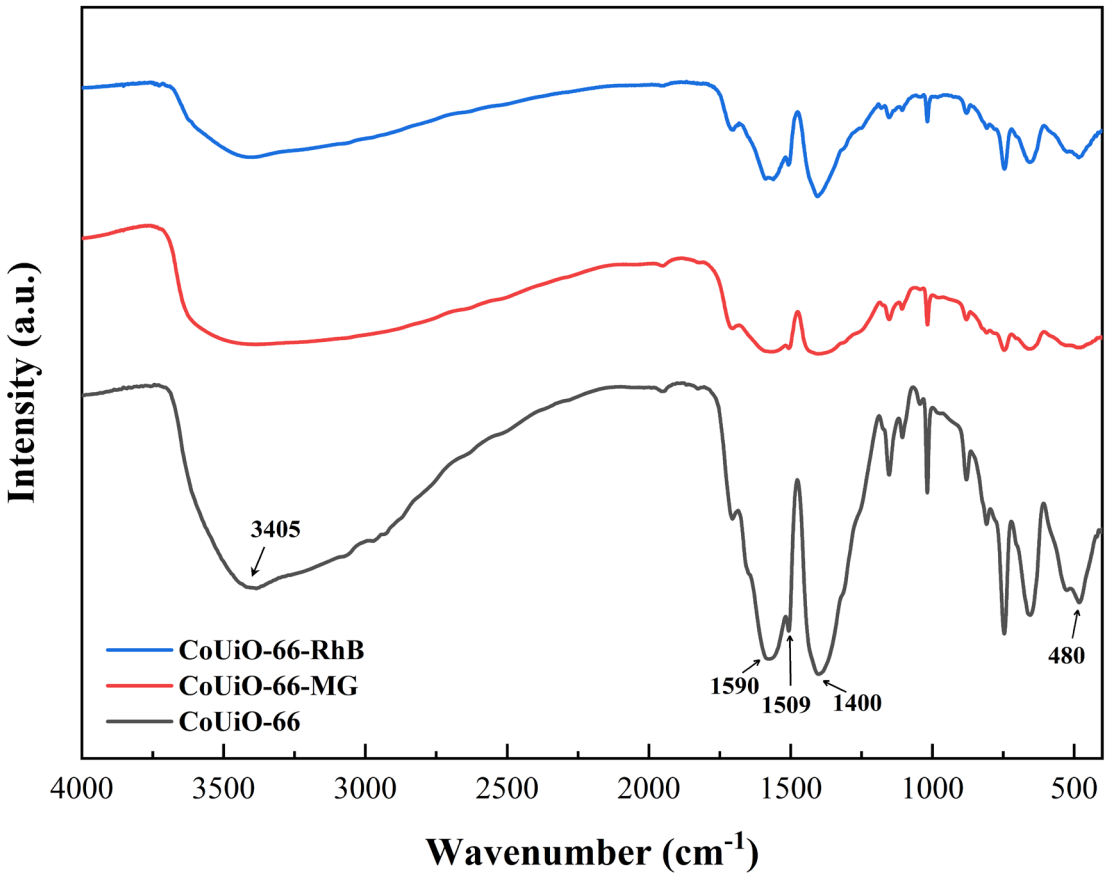

Figure 4.17 FTIR spectrum of CoUiO-66 before and after adsorption of MG and RhB

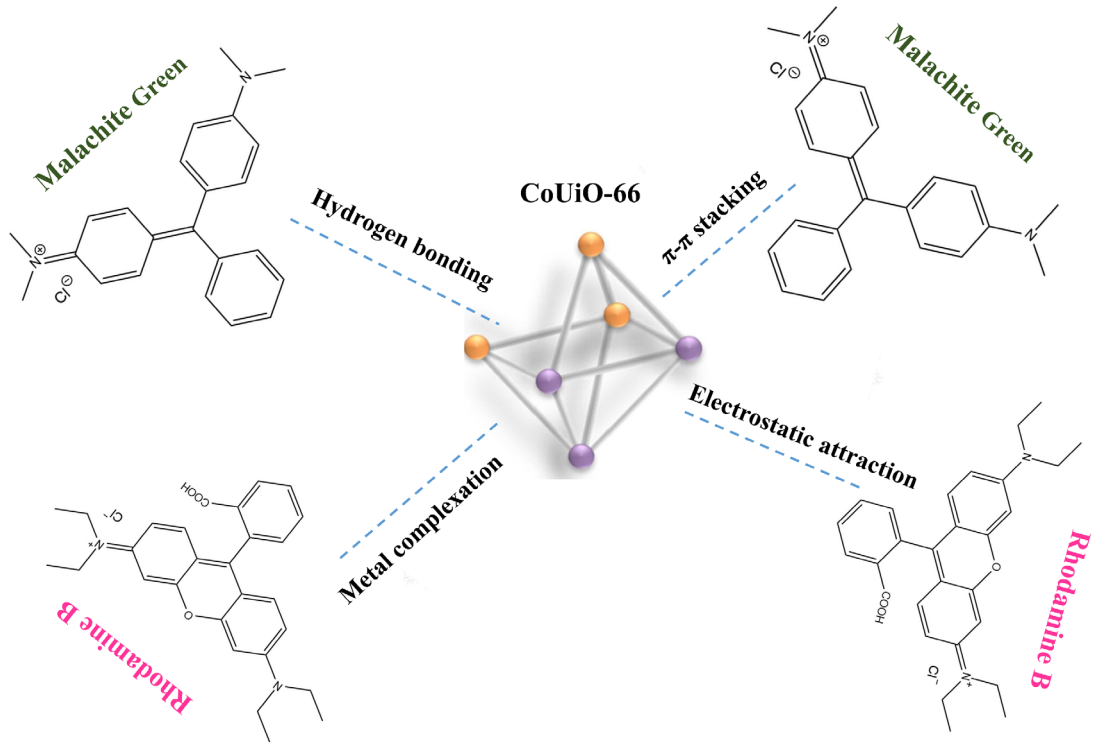

Figure 4.18 Schematic illustration of possible adsorption mechanism.

4.5 Summary

In summary, a new metal-doping modification UiO-66 adsorbent was successfully prepared with a simple in-situ growth. Both the UiO-66 and CoUiO-66 were analysed with a series of characterizations. Compared to the original MOFs, the metal-doped modification did not lead to a phase transition and increased porosity property of UiO-66. In addition, the Co-doping showed a significant effect on the crystal size. The average particle size of CoUiO-66 was 22.76 nm, which was much smaller than that of the parent MOFs. Meanwhile, the CoUiO-66 exhibited an improved BET surface area, which is a preferable factor for the adsorption process. The XRD, FTIR and XPS analysis suggested that there were no cobalt oxides and the derivates formed in the doping process, the Co ion was speculated to coordinated with oxygen atom successfully in the skeleton of pristine UiO-66. In addition, TGA results demonstrated that more defects were introduced into the framework of UiO-66 via the Co-doping modification. Based on the characterization results, the Co element could probably be introduced to the MOFs structure and donate the valence electrons, resulting in larger active sites for adsorption. Moreover, the batch adsorption experiments confirmed that the Co-doped process could significantly improve the adsorption performance. An excellent uptake capacity of MG (628.93 mg/g) on CoUiO-66 was observed, which was remarkably more excellent compared with UiO-66 (343.64 mg/g). Furthermore, the experimental results showed that CoUiO-66 also had superior adsorption capacity for RhB (1106.22 mg/g). We hope that this work will provide more insights into the in-situ synthesis of metal-doped MOFs and open a valuable pathway to MOFs-based adsorbents for the efficient removal of pollutants in environmental remediation.

Chapter 5 One-pot synthesis of mesoporous g-C_3N_4 for promoted photodegradation of organic dye.

In this chapter, a series of novel mesoporous g-C_3N_4 was prepared via a facile green approach. Comprehensive characterisation tests were carried out to reveal the structure of the obtained materials. The findings displayed that this mesoporous material had enlarged porosity and optical properties. The photocatalytic activity of the synthesized photocatalysts were evaluated by the photocatalytic degradation of RhB. In addition, the possible mechanism of this photodecomposition reaction was identified with ESR and trapping tests. Moreover, the stability of the prepared samples was assessed by a consecutive recycle test along with a XRD analysis, which could predict the practical application of the photocatalysts. This research offers a promising method for the synthesis of mesoporous g-C_3N_4 by an environmental-friendly and cost-effective route with remarkably high photoactivity.

5.1 Introduction

Photocatalysis is an appealing and green technique due to its direct utilisation of solar energy. Photocatalytic degradation is a new generation and green approach in water purification, which can convert toxic and non-biodegradable organic pollutants into H_2O, CO_2 and inorganic salts [244]. In the past few years, significant advancements have been achieved on the explore of excellent semiconductor photocatalysts for environmental remediation, such as TiO_2 [245], ZnO [246], CdS [247], $BiVO_4$ [248], WO_3 [172], MoS_2 [249], etc. Some researchers found that the Pd-doped TiO_2 showed a significant increment on the photodegradation of MO and MB. The maximum removal

Industrial & Engineering Chemistry Research [J]. 2024, 63, 8, 3491–3503.

efficiency could reach 92.6% and 99.4% for MO and MB under UV-light irradiation, respectively [250]. In addition, CdS was studied for the photodegradation of RhB, the findings indicated that the pure CdS had a photocatalytic degradation efficiency of 79.2% under visible light [251]. Moreover, some researchers investigated the photocatalytic activity of m-$BiVO_4$, the results showed that this photocatalyst had a removal efficiency of 64.8% on RhB within 210 min [252]. Although many works have been done on this area, many of the conventional photocatalysts could only be response to UV-light, but poor utilisation efficiency of visible light, which brings out a big limitation on practical applications, particularly on the utilisation of solar energy.

Among the numerous semiconductors investigated, graphitic carbon nitride (g-C_3N_4) has been an emerging star as photocatalyst owing to its low cost, good stability and nontoxicity [253]. g-C_3N_4 is tri-s-triazine polymer with layered structure which is most stable in all allotropes [254]. As a rising metal-free photocatalyst, this semiconductor has been investigated for the application of hydrogen evolution [255], CO_2 reduction [256] and pollutant degradation [257]. Compared with traditional photocatalysts, g-C_3N_4 has a more negative CB potential (-1.3 eV) and moderate energy gap (2.7 eV) [258]. Some researchers employed bulk g-C_3N_4 for RhB photocatalysis. The results revealed that the removal efficiency of this bulk sample was 68% under UV-light irradiation within 200 mins [259]. In addition, some researchers compared the photodegradation efficiency of nitrogen vacancy g-C_3N_4 with bulk sample. The findings indicated that the modified one (81%) had a higher removal efficiency compared with the bulk one (30%) [260]. Many progresses have been made in the research of g-C_3N_4 for photocatalysis. However, a series of limitations of this material still restricts its photocatalytic activity, such as low surface area, low-density active sites, poor visible light utilization and sluggish photogenerated carrier transfer [261].

Therefore, it is very imperative to find some new route to promote the photoactivity of g-C_3N_4.

A novel one-pot fabrication route of mesoporous g-C_3N_4 was employed in this study via calcining the mixture of melamine and ammonium sulphate, in which ammonium sulphate can affect the polycondensation process and promote the porosity of g-C_3N_4, thereby acting as a significant role in modifying the structures of g-C_3N_4. Different from other methods, the chemicals involved in this process is low-cost and nontoxic without using any corrosive acid or alkali, along with a simple operation procedure. Subsequently, a series of characterisations were carried out to study the structure of the obtained samples. Furthermore, photocatalytic experiments on RhB degradation with visible light illumination were also carried out for evaluating the photoactivities of the prepared photocatalysts. The results demonstrated that the mesoporous g-C_3N_4 had an obvious improvement on the photocatalytic performance than the bulk sample.

5.2 Experimental

5.2.1 Sample preparation

The mesoporous g-C_3N_4 was prepared using a simple thermal polymerisation method calcination method. In typical, 10 g melamine and a certain amount of $(NH_4)_2SO_4$ were mixed in 20 mL ethanol and stirred at room temperature for 1 h. After drying in an oven overnight, the mixture was placed into an alumina crucible and heated to 550 ℃ in a muffle at a rise rate of 5 ℃/min. Then the temperature was kept for 3 h. After cooling down to room temperature, the yellow samples were ground into powder and collected as g-C_3N_4. Based on the mass ratio of melamine and $(NH_4)_2SO_4$, the samples could be named as CN-X (X=0.5-2). The detailed route was illustrated in

Industrial & Engineering Chemistry Research [J]. 2024, 63, 8, 3491–3503.

Figure 5.1.

The bulk g-C_3N_4 was prepared by calcining melamine directly without any $(NH_4)_2SO_4$, which could be named as CN-0. The rest procedures were the same as mesoporous g-C_3N_4.

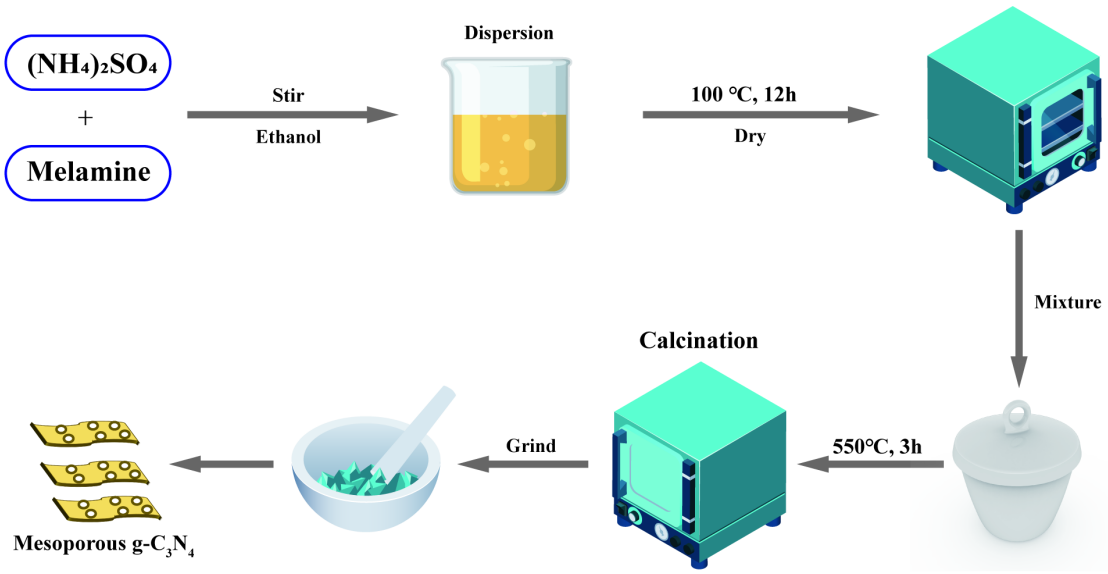

Figure 5.1 General synthetic route of mesoporous g-C_3N_4.

5.3 Results and Discussion

5.3.1 Phase structure analysis

XRD patterns were applied to measure the crystal structures of the samples. As displayed in Figure 5.2, the featured peak near 27.1° was ascribed to the graphite-like stacking of conjugated aromatic segments, indexing to (002) plane with an average interlayer distance of d = 0.326 nm [262]. The other featured peak situated near 13.1° could be indexed to (100) plane, corresponding to the in-plane structural packing motif of tri-s-triazine units [263]. It is documented that the van der Waals force exits between the layers of g-C_3N_4 [264]. Compared to CN-0, the peak intensity of CN-X was observed to decrease gradually with the increasing ratio of $(NH_4)_2SO_4$, indicating that

Industrial & Engineering Chemistry Research [J]. 2024, 63, 8, 3491–3503.

this compound had a significant impact on the exfoliation of bulk sample into nanosheets via overcoming the weak van der Waals force between the layers of g-C_3N_4 [265]. All the samples had similar diffraction peaks which were attributed to the characteristic peaks of g-C_3N_4 according to literatures, indicating that all the samples shared the same core crystal structures [266, 267]

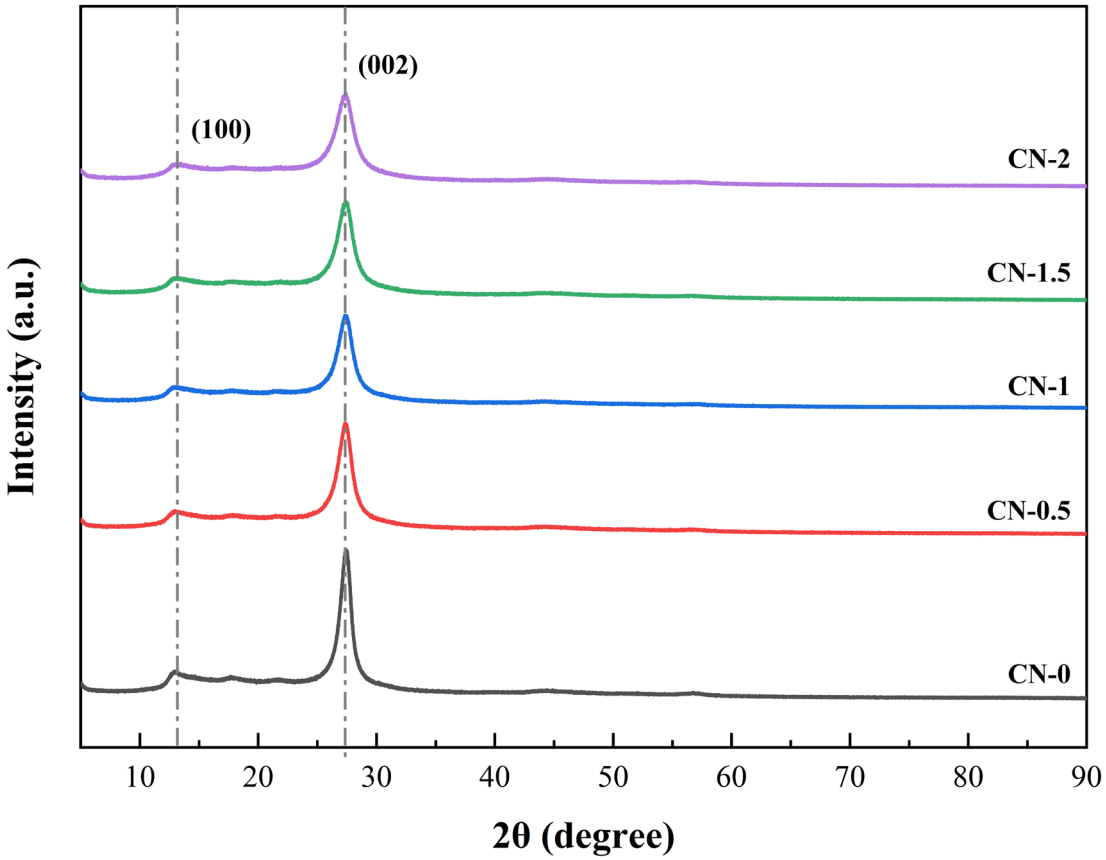

Figure 5.2 XRD patterns of the g-C_3N_4 series.

The interior molecular structures of the photocatalysts were further confirmed by FT-IR spectra. It was depicted in Figure 5.3 that the strong peak near 810 cm^{-1} could be ascribed to the vibration of triazine units [268]. The characteristic peaks located at 1100–1700 cm^{-1} were assigned to the typical stretching vibrations of aromatic C-N heterocycles [269]. Moreover, the peaks located between 2900-3500 cm^{-1} could be associated with the stretching vibration modes of uncondensed amine groups and H_2O molecules absorbed on the surface [270]. All these samples exhibited similar

Industrial & Engineering Chemistry Research [J]. 2024, 63, 8, 3491–3503.

pronounced adsorption peaks, and no obvious shift, confirming the formation of g-C_3N_4 typical structure.

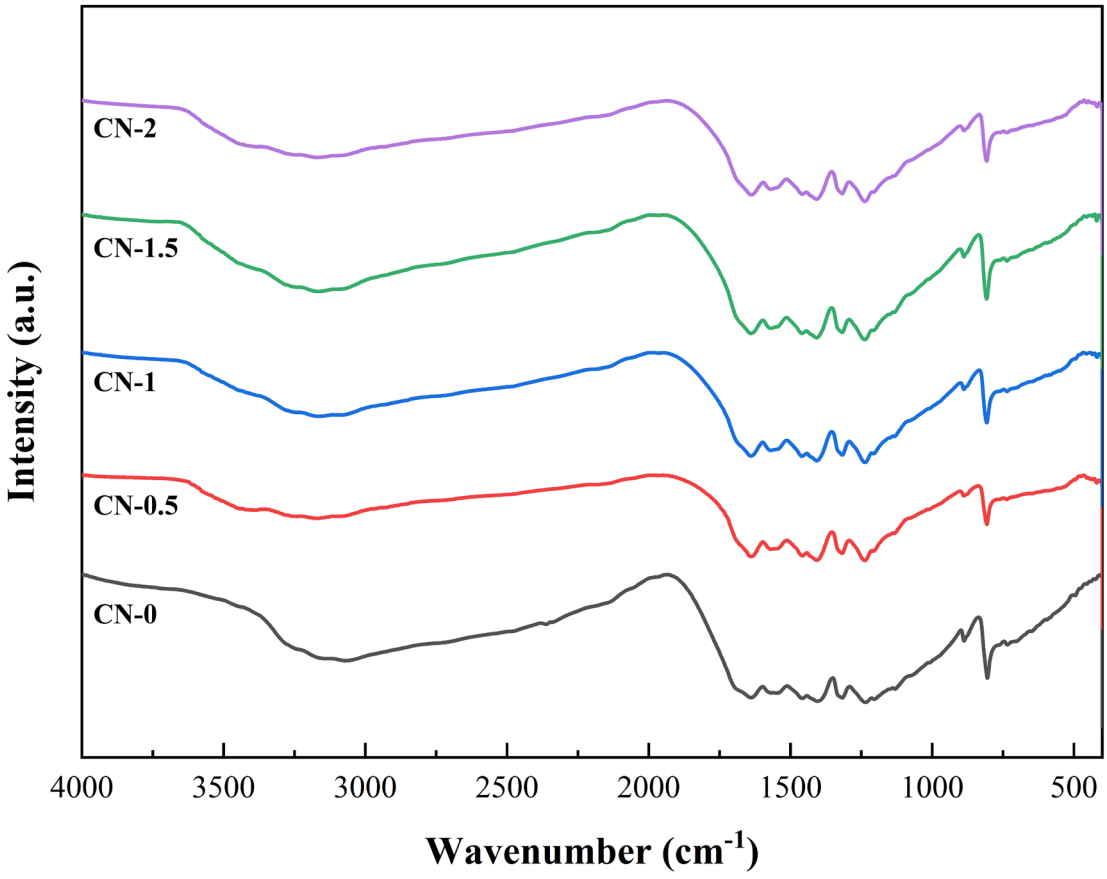

Figure 5.3 FT-IR spectrum of the obtained samples

Furthermore, XPS spectra were employed to identify the surface stoichiometry along with binding states of the samples in Figure 5.4. It was depicted from the XPS survey (Figure 5.4a) that both bulk and mesoporous g-C_3N_4 mainly consisted of carbon and nitrogen element, with a few amounts of oxygen. As displayed in Figure 5.4b, The C 1s of both samples were divided into three peaks with high similarity. For the bulk one, the peak around 284.80 eV was attributed to adventitious carbon as C-C bond. The C-N bond of heptazine units was identified with the peak near 286.46 eV, while the last peak situated around 288.17 eV could be associate with sp^2- carbon coordinated in triazine rings as N=C–N bond [271]. Moreover, N spectra of these materials were also very similar. In addition, the N 1s spectra illustrated in Figure 5.4c could be separated

Industrial & Engineering Chemistry Research [J]. 2024, 63, 8, 3491–3503.

into 4 components, The highest peak for bulk g-C_3N_4 situated at 398.70 eV was corresponding to sp^2-coordinated N as C-N=C bond. While the smaller peaks located around 401.28 and 400.17 eV were associated with amino groups (C-N-H) and bridging N atoms in C-N heterocycles as C_3-N bond. And the last peak located around 404.42 eV was associated with π-excitations [272]. The atomic ratio observed from XPS was displayed in Table.5.1. It was observed that the C:N ratio in these materials was highly close to the ideal value (0.75). Compared to the bulk one, CN-1.5 showed a little smaller C:N ratio along with an obviously larger O content, which suggested that the gasification of $(NH_4)_2SO_4$ during the thermal process brought in more oxygen to interact with the precursor. The oxygen molecules attacked the C-N heterocycles, leading to the substitution of some N with O atoms in the structure [273]. The XPS results and elemental composition of the materials are highly similar, proving the successfully preparation of g-C_3N_4 and not obvious change occurred in the structures.

Table 5.1 The surface atomic ratio of different elements in samples observed by XPS.

Sample	C (%)	N (%)	O (%)	C: N (%)
CN-0	42.50	51.61	5.81	82.35
CN-1.5	41.20	50.24	8.46	82.00

Industrial & Engineering Chemistry Research [J]. 2024, 63, 8, 3491–3503.

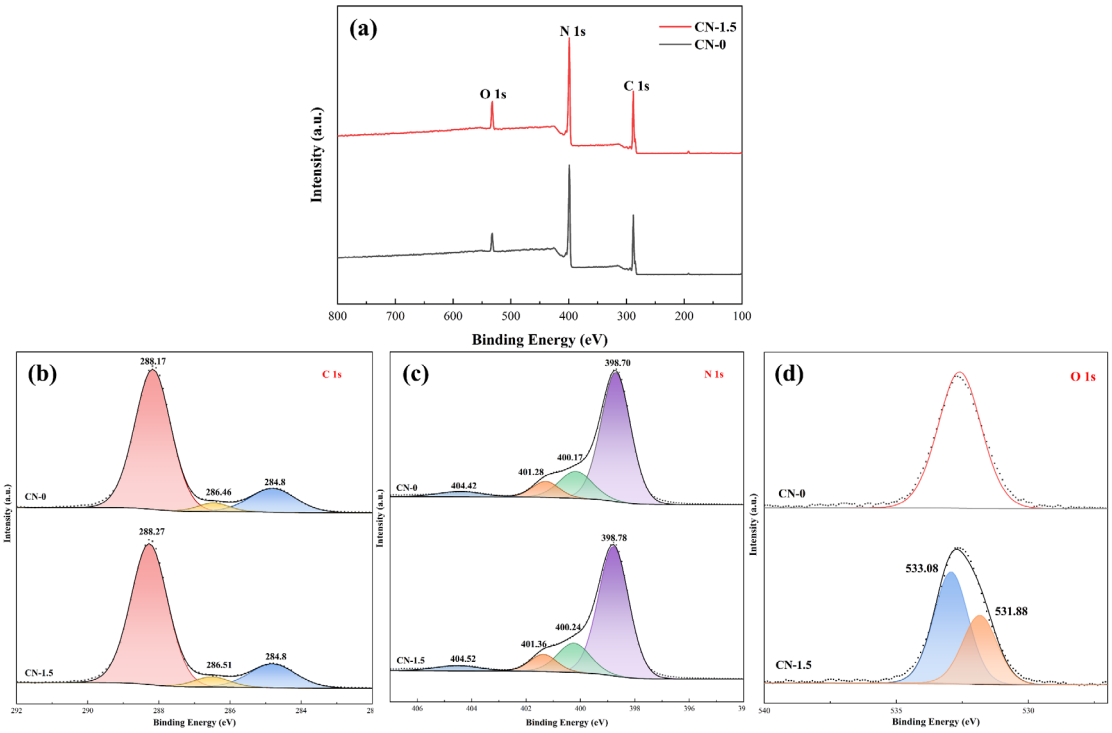

Figure 5.4 XPS spectrum of CN-0 and CN-1.5: survey (a), C 1s (b), N 1s (c), O 1s (d).

5.3.2 Morphology analysis

The morphology and microstructure of bulk g-C_3N_4 and mesoporous g-C_3N_4 were measured by SEM and TEM in Figure 5.5. As illustrated in Figure 5.5a, the bulk g-C_3N_4 exhibited solid agglomerates with several micrometres in size. While with the modification of $(NH_4)_2SO_4$, the mesoporous g-C_3N_4 displayed more rougher surface with many obvious irregular pores in SEM images (Figure 5.5b, 5.5c). In addition, the TEM results further confirmed the porosity of the modified g-C_3N_4. As shown in Figure 5.5e-f, the bulk g-C_3N_4 displayed a thick 2D sheet-like structure, while the mesoporous g-C_3N_4 had much smoother and thinner nanosheet structures with evident pores exists. All mesoporous samples exhibited a series number of in-plane mesoporous distributed in the entire layer structures [274]. The SEM and TEM findings demonstrated a significant difference between the morphology of CN-0 and CN-1.5.

Industrial & Engineering Chemistry Research [J]. 2024, 63, 8, 3491–3503.

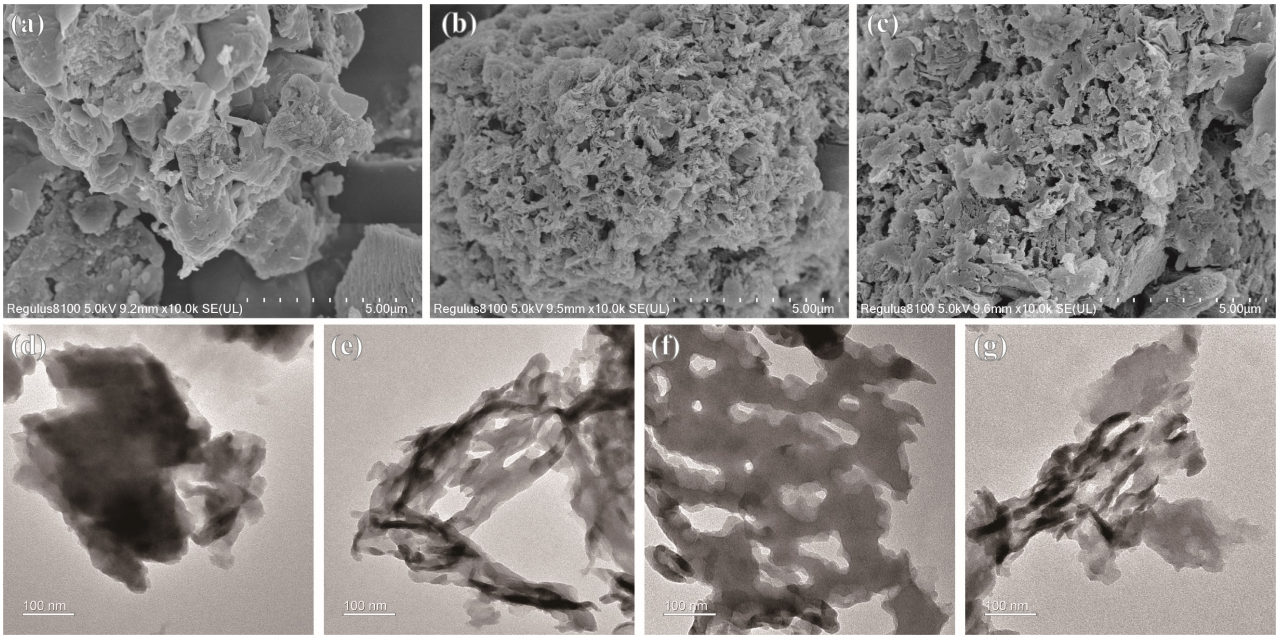

Figure 5.5 SEM results of CN-0 (a), CN-1 (b), CN-1.5 (c); TEM results of CN-0 (d), CN-1 (e), CN-1.5 (f), CN-2 (g).

N_2 sorption tests were carried out to further reveal the porosity of the samples. The isotherms of the samples displayed in Figure 5.6a implied that the bulk g-C_3N_4 (CN-0) and mesoporous one (CN-1.5) were type I and type IV based on the IUPAC classification, suggesting the typical mesoporous characteristics of CN-1.5 [275]. The pore size distribution illustrated in Figure 5.6(b-c) showed that the pore diameter of CN-1.5 was mainly in the region of 2-50 nm, while that of CN-0 was significantly larger. In addition, the porosity parameters of these samples were tabulated in Table 5.2. It was depicted that S_{BET} value of mesoporous sample (32.65 m^2/g) was 4.36 times larger compared with CN-0 (7.48 m^2/g). While the average pore size exhibited an obvious decrease in the mesoporous sample along with the increase in surface area. The value of 23.91 nm for average pore size also proved that it was a typical mesoporous material. In general, it is widely regarded that larger surface area means more active sites, which implies a promotion in photocatalytic performance. The N_2 sorption results confirmed the SEM-TEM analysis mentioned above and further proved the mesoporous structures

Industrial & Engineering Chemistry Research [J]. 2024, 63, 8, 3491–3503.

of CN-1.5.

Table 5.2 Textural parameters of CN-0 and CN-1.5

Sample	S_{BET} (m^2/g)	Pore size(nm)	Pore volume(cm^3/g)
CN-0	7.48	220.15	0.99
CN-1.5	32.65	23.91	0.19

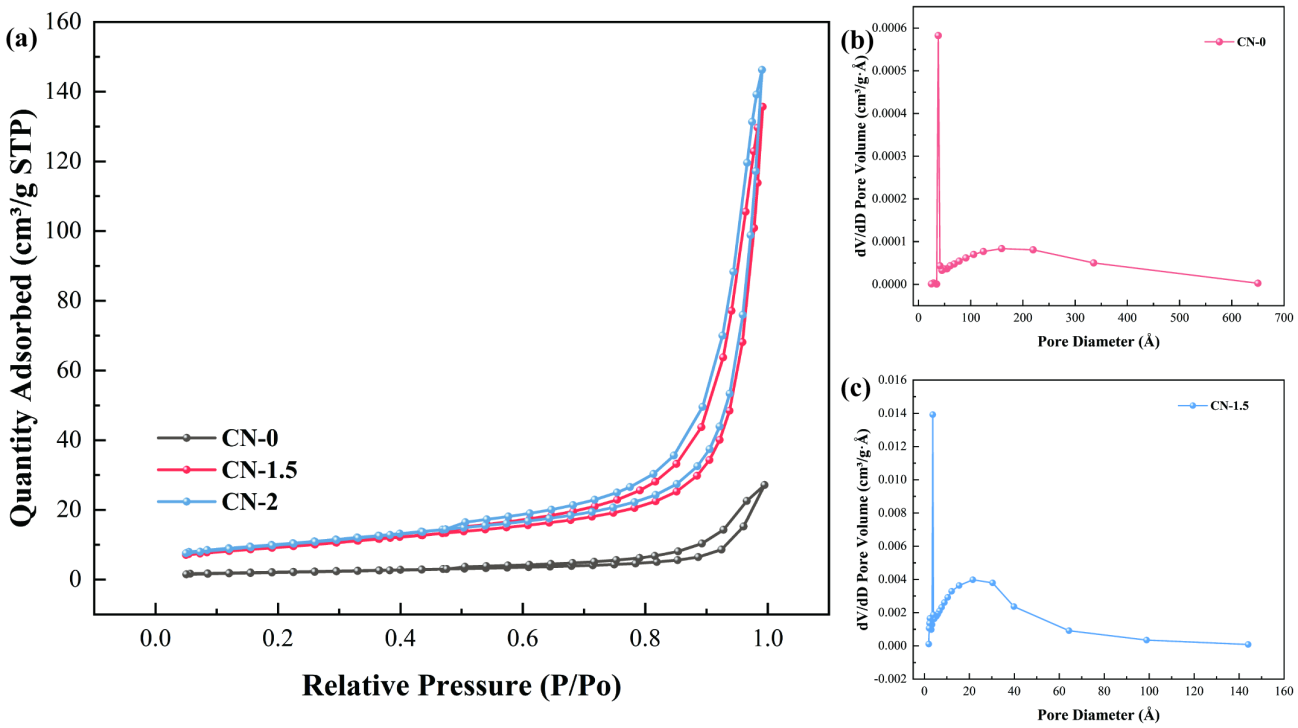

Figure 5.6 N_2 sorption isotherm (a); pore size distribution of CN-0 (b), and CN-1.5 (c).

5.3.3 Banding energy and optical structures

UV-VIS DRS was applied to probe the band structures of samples. It was observed in Figure 5.7 that a typical semiconductor spectrum with an adsorption edge of 400-450 nm was identified for both CN-0 and CN-1.5 The mesoporous sample had an obviously higher light absorbance with a small red shift compared with CN-0, which may be associated with multiple scattering effect by the porous property of CN-1.5, leading to the promoted ability to utilize visible light with enhanced photoactivity [276].

Industrial & Engineering Chemistry Research [J]. 2024, 63, 8, 3491–3503.

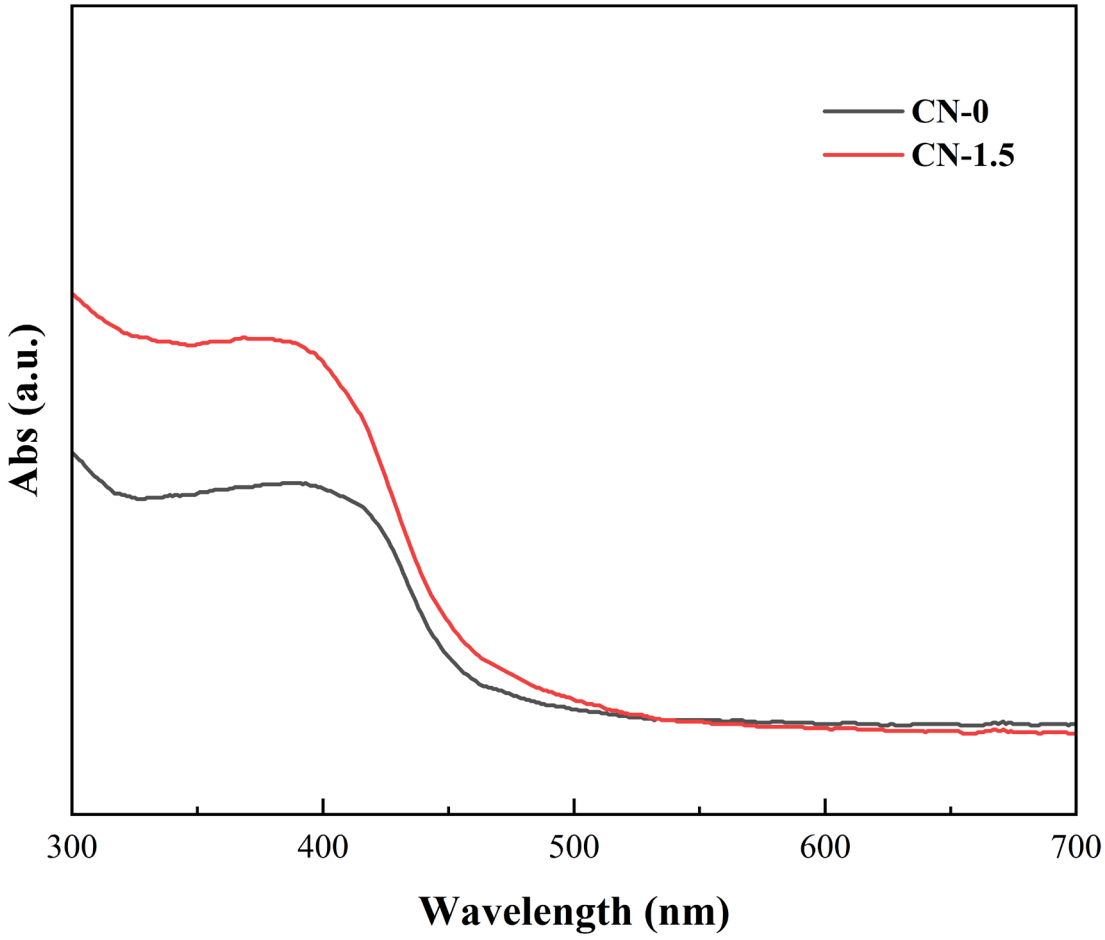

Figure 5.7 UV-VIS DRS spectrum of CN-0 and CN-1.5

In addition, the band gap (E_g) of photocatalysts could be computed according to the formula:

$$\alpha h\nu = A(h\nu - E_g)^{n/2} \quad 5.1$$

where a, h, v, Eg and A are the absorbance, Planck constant, optical frequency, bandgap energy and constant, respectively [277].

The band gap is determined by plotting the $(\alpha h\nu)^2$ versus hν which is known as the Tauc plot as shown in Figure 5.8. It was depicted that the band gap potential of CN-0 and CN-1.5 were 2.24 and 2.06 eV, respectively, this decrease was attributed to the improved O element doping that changed the properties [278]. In addition, the conduction band (CB) and valence band (VB) potential of g-C_3N_4 could be computed based on the following formula:

$E_{VB}=\chi-E^e+1/2E_g$ 5.2 [279]

$E_{CB}=E_{VB}-E_g$ 5.3 [279]

Based on reported literatures, the value of χ and E^e are 4.7 and 4.5 eV. Thus, the VB and CB potential of CN-0 were 1.32 and -0.92 eV, respectively. While those of CN-1.5 were 1.23 and -0.83 eV, respectively.

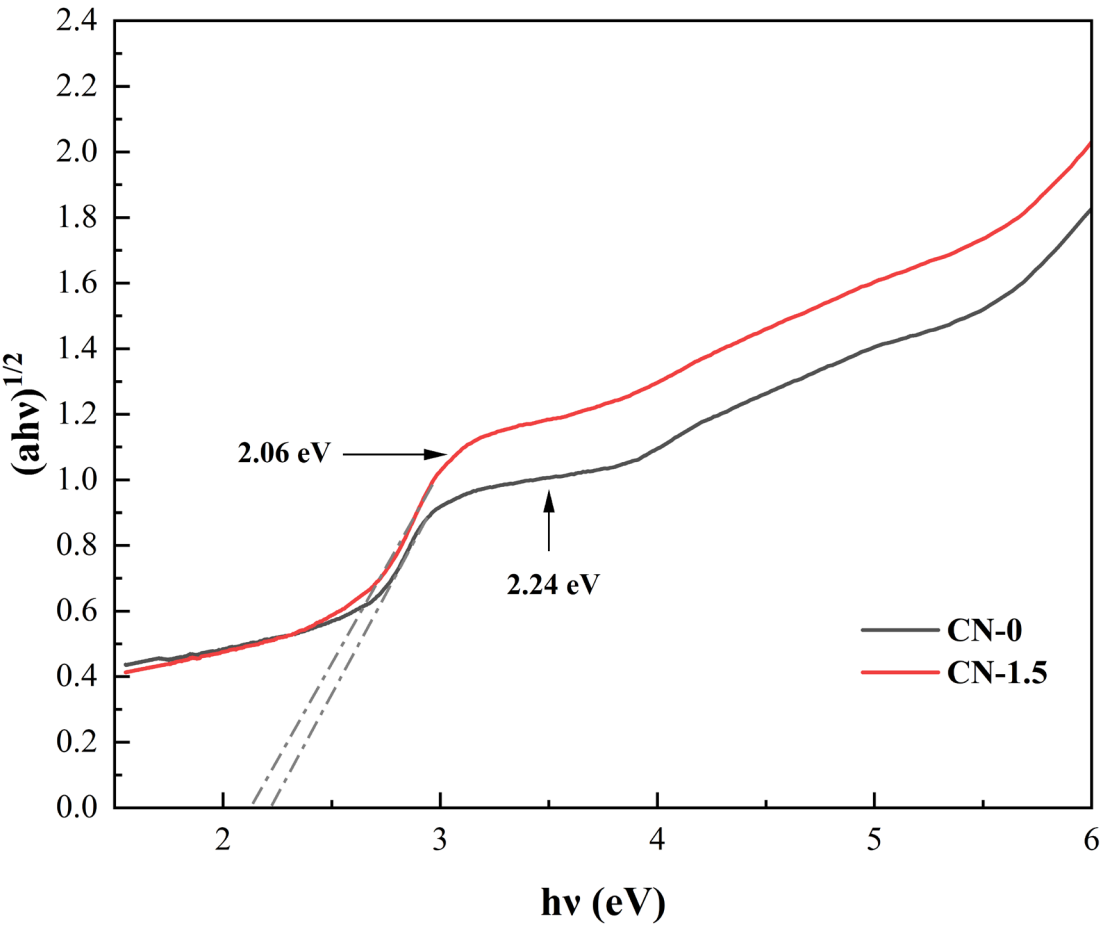

Figure 5.8 Tacu curve of CN-0 and CN-1.5.

Moreover, Photoluminescence (PL) tests were applied to further analyse the optical structures of CN-0 and CN-1.5 in Figure 5.9. The bulk sample CN-0 exhibited a pronounced emission peak around 450 nm, while the mesoporous one had a wide and much weaker peak situated around 460 nm with a small red shift compared with CN-0. The PL spectra were generated from the recombination of photo-induced charges [280]. Therefore, the smaller peak of CN-1.5 implied that this sample had much lower

Industrial & Engineering Chemistry Research [J]. 2024, 63, 8, 3491–3503.

efficiency on the electrons-hole recombination, and thus much more electrons/holes could be available during the photocatalytic reaction, so as to improve the photoactivity consequently [258].

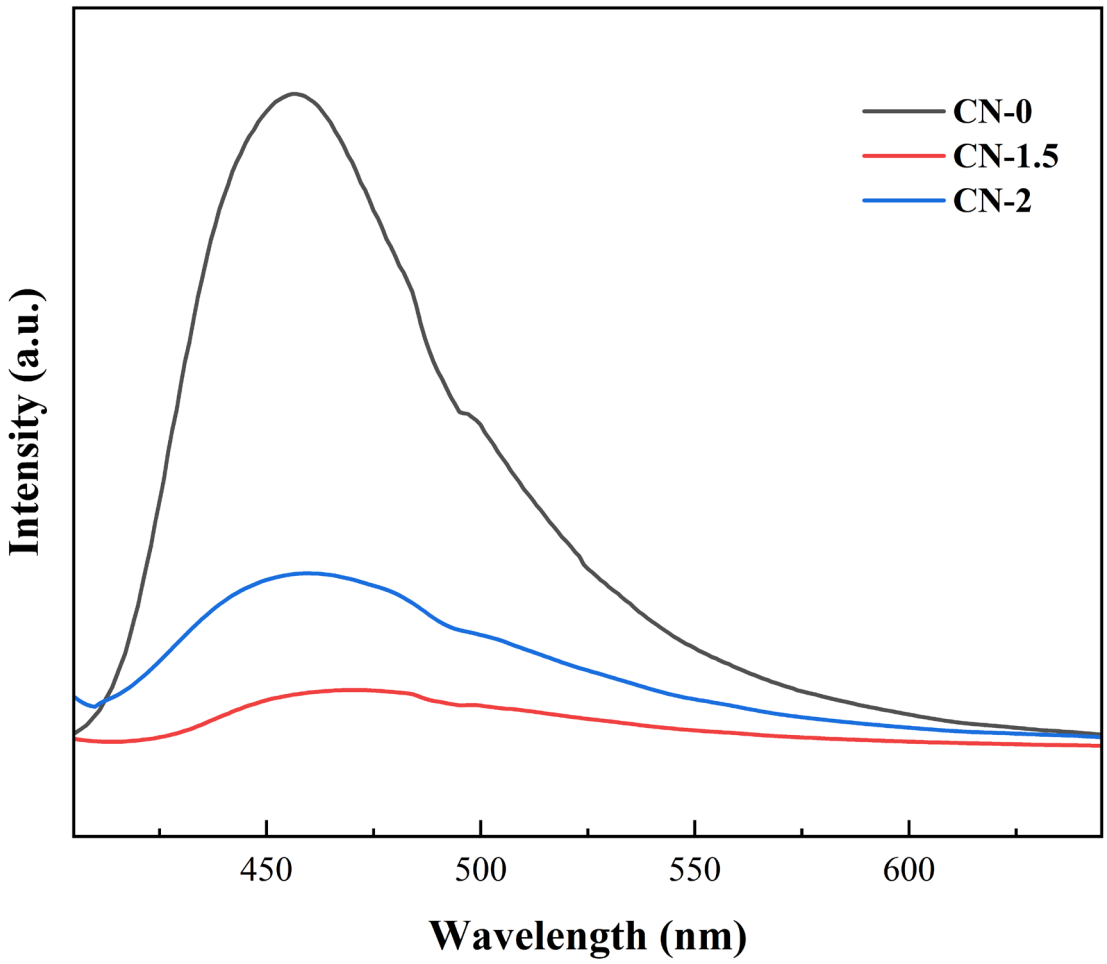

Figure 5.9 Photoluminescence spectra of the g-C_3N_4 series samples.

5.3.4 Photoelectrochemical analysis

Photoelectrochemical tests were also conducted to reveal the photoactivities of the materials, including photocurrent spectra and electrochemical impedance spectroscopy (EIS). In general, it is well known that the semicircle diameter in EIS can reflect the charge transfer resistance, a small semicircle diameter usually means a low charge transfer resistance. Meanwhile, A decrease in charge transfer resistance at the electrode-electrolyte interface leads to an increase in the rate of interfacial charge transport. It

Industrial & Engineering Chemistry Research [J]. 2024, 63, 8, 3491–3503.

was shown in Figure 5.10 that CN-1.5 had an obviously smaller arc radius, which suggested that the mesoporous sample owned a promoted separation and transfer effectiveness of photo-induced charger carriers [281]. Additionally, the photocurrent response results were displayed in Fig.5.11, it was illustrated that both the samples presented good stability with several photocurrent cycles. Moreover, CN-1.5 displayed an evident higher photocurrent intensity than the bulk one, indicating that it had a much better charge transfer and a lower recombination [282]. Both the findings implied that CN-1.5 should have a superior better photoactivity than the bulk samples, further confirming the analysis mentioned above.

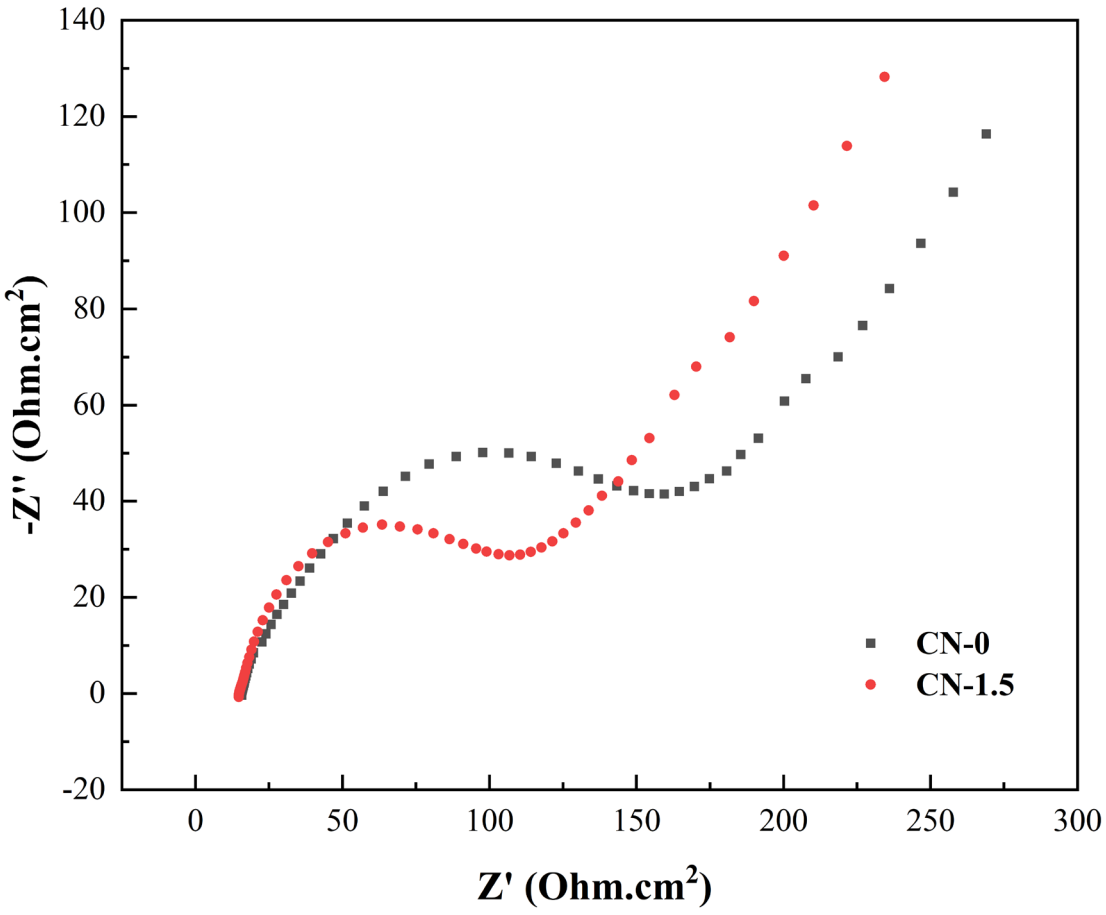

Figure 5.10 EIS plot of CN-0 and CN1.5

Industrial & Engineering Chemistry Research [J]. 2024, 63, 8, 3491–3503.

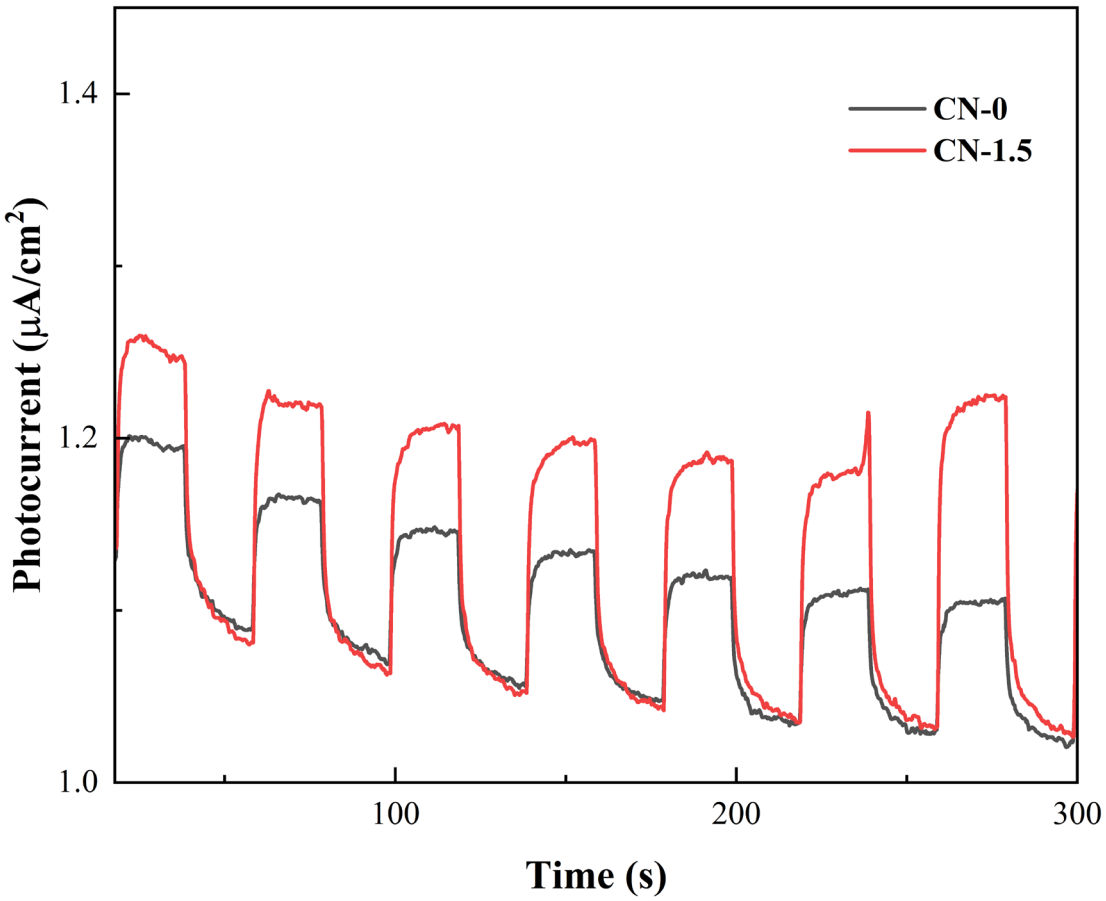

Figure 5.11 Photocurrent response of CN-0 and CN1.5

5.3.5 Photocatalytic tests

To identify the photoactivity of these photocatalysts, a series of photocatalytic experiments were performed via the photodecomposition of RhB with visible light. The removal efficiency was calculated via 1-C/C_0, where C_0 and C represent the concertation of RhB solution in initial time and given time. It was illustrated in Figure 5.12 that no evident decay was observed during the irradiation process in the blank group, which suggested that the RhB molecules were stable under visible light, so as that photocatalysts had a significant impact in this degradation process. For the dark stirring process, all the materials could achieve equilibrium in 60 min, while the mesoporous samples exhibited higher adsorption performance than the bulk one, which was attributed to the larger surface area to absorb RhB molecules. For the irradiation

Industrial & Engineering Chemistry Research [J]. 2024, 63, 8, 3491–3503.

process, all the mesoporous samples had obviously better removal efficiencies compared to CN-0 with the order of CN-1.5 > CN-1 > CN-0.5 > CN-2 > CN-0. The CN-1.5 showed the most excellent photocatalytic performance, it could achieve 99.41% removal efficiency in 100 min, which was 3.88 times better than that of CN-0 (25.63%) in the same period.

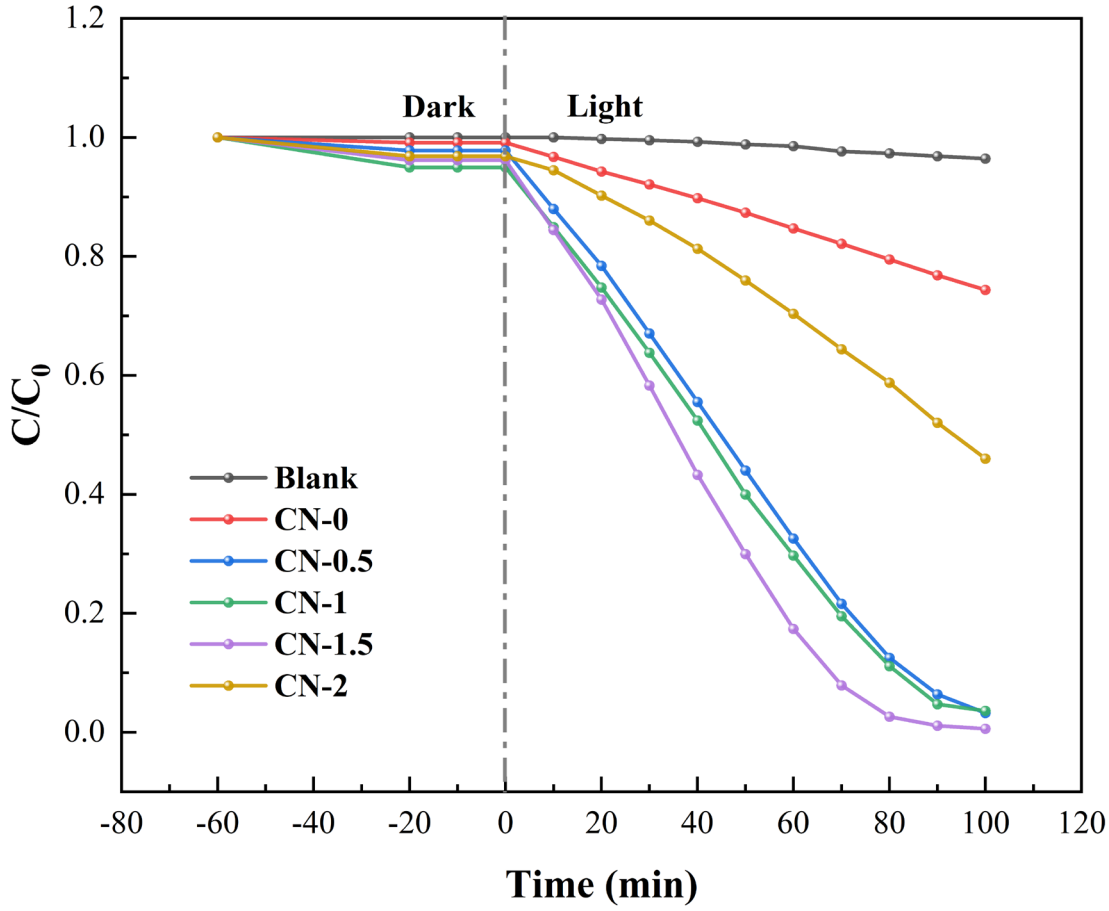

Figure 5.12 Photocatalytic removal test of RhB for blank group and CN-X samples.

In addition, kinetic model was used to further analyse the reaction rate of this photodegradation process according to the formula: $\ln (C_e/C_t) = kt$ [283]. Where C_e and C_t represent the RhB concentration at adsorption equilibrium and certain time t, k is the reaction rate. On the basis of the calculation results (Figure 5.13), CN-1.5 also showed the highest reaction efficiency of 0.02933 min^{-1}, while CN-0 was the lowest of 0.00262 min^{-1}. The reaction rate of CN-1.5 was 11.19 times faster compared with CN-0, which

Industrial & Engineering Chemistry Research [J]. 2024, 63, 8, 3491–3503.

further proved that the mesoporous g-C_3N_4 had significantly improved photoactivities than the bulk one, in corresponding with the above characterisation analysis results. Furthermore, the photoactivity of the prepared materials was compared with other literatures in Table 5.3 to further assess the photocatalytic performance of this work.

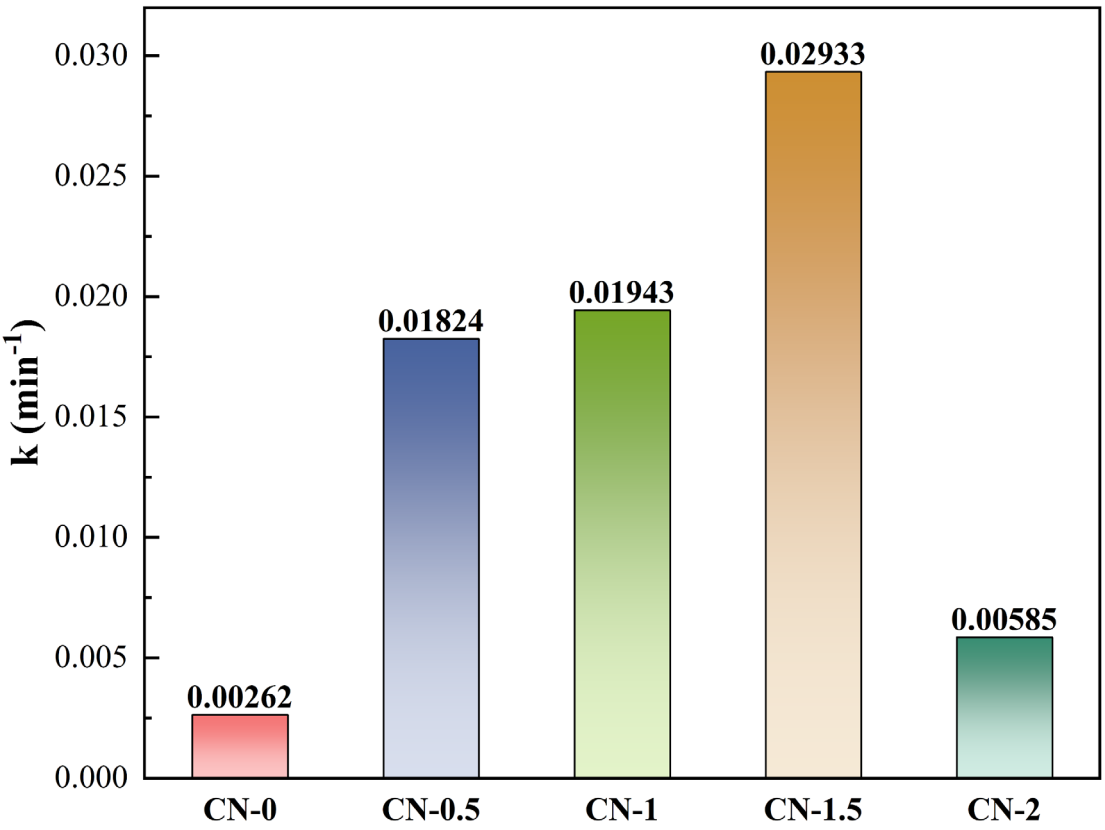

Figure 5.13 Photocatalytic rate of different porous CN-X samples.

Industrial & Engineering Chemistry Research [J]. 2024, 63, 8, 3491–3503.

Table 5.3 Photoactivity comparison of this work with reported literatures

Photocatalyst	RhB concentration	Amount (g/L)	Light source	Time (min)	Degradation (%)	Ref.
CQDs/Sb_2WO_6	10 mg/L	1	Visible light	120	83	[284]
MoS_2/NiFe LDH	20 mg/L	1	Visible light	120	90	[285]
ZnO-graphene-TiO_2	0.01 mM	1	Visible light	180	92	[286]
$AgIO_3/WO_3$	0.02	0.5	Visible light	140	100	[287]
TiO_2/ZrO_2	20 mg/L	0.8	Visible light	180	99	[288]
CdS /g-C3N_4	10 mg/L	1	Visible light	90	88	[289]
$NiFe_2O_4$/MIL-53(Fe)	0.03 mM	0.2	Visible light	180	95	[290]
CeO_2/BiOI	0.01 mM	0.5	Visible light	180	95	[291]
Bi_2MoO_6/UiO-66	10 mg/L	0.5	Visible light	120	96	[292]
CN-1.5	60 mg/L	0.2	Visible light	100	99	This work

The stability of prepared photocatalysts is another important factor to evaluate the practical potential for future application. The photocatalytic degradation experiments

Industrial & Engineering Chemistry Research [J]. 2024, 63, 8, 3491–3503.

were conducted for five consecutive cycles. As displayed in Figure 5.14a. the photocatalyst CN-1.5 demonstrated great stability and recyclability after five cycles. The removal efficiency remained to be 93.85%, which was a small decrease compared to the first cycle. In addition, the XRD results were collected for the pristine photocatalyst and the used one which has been recycled for five times. It was shown in Figure 5.14b that the XRD patterns were highly similar for the two samples, indicating that this photocatalyst maintained the same structure after the photocatalytic reaction and showed a great stability. The excellent recyclability and stability of the obtained mesoporous g-C_3N_4 implied that this material could a promising candidate for the practical application in the effective degradation of organic pollutants.

Industrial & Engineering Chemistry Research [J]. 2024, 63, 8, 3491–3503.

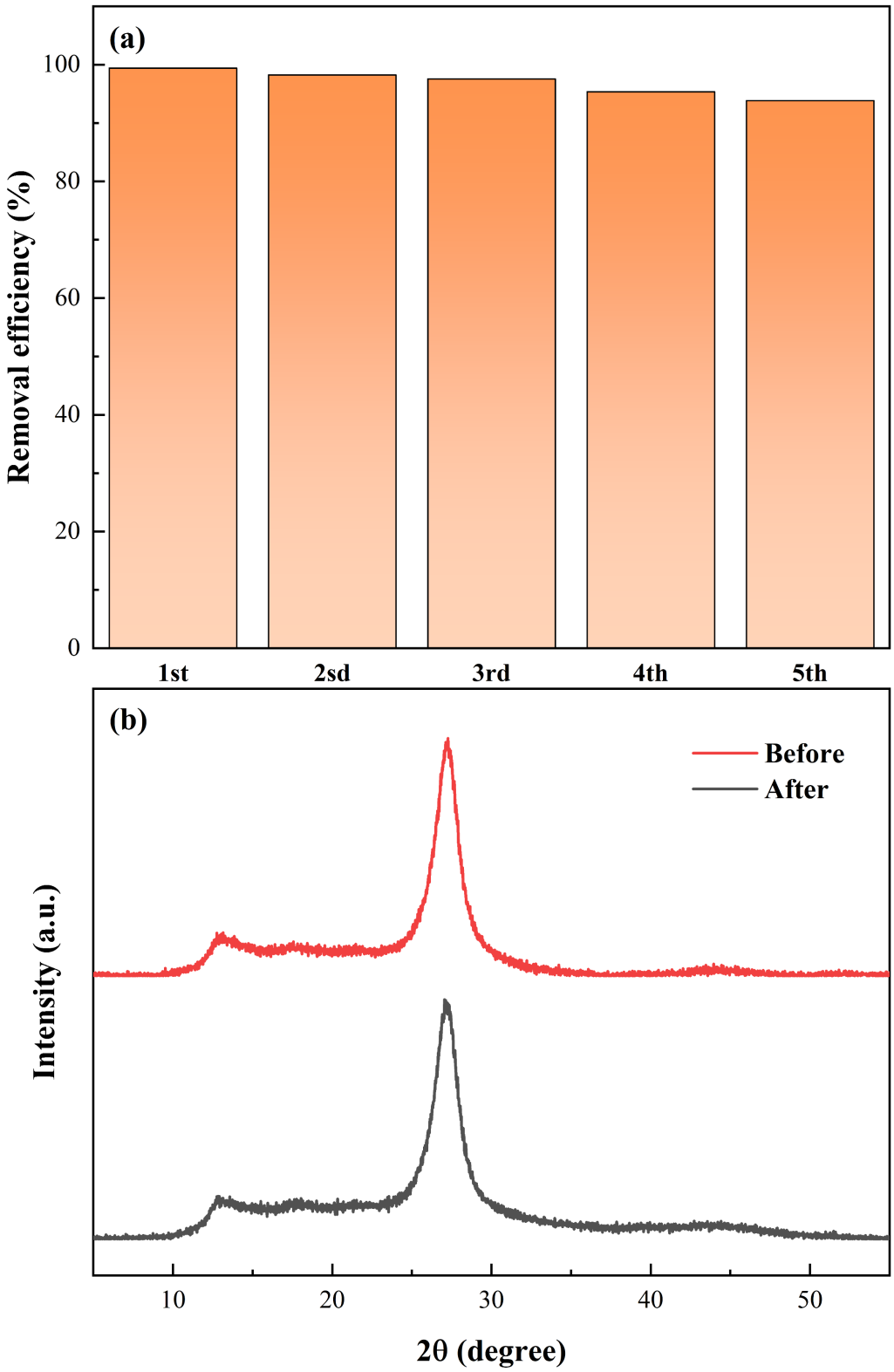

Figure 5.14 Removal efficiency of CN-1.5 on the degradation of RhB for five cycles (a); XRD patterns of CN-.15 before and after five cycles (b).

5.3.6 Proposed photocatalytic mechanisms

Industrial & Engineering Chemistry Research [J]. 2024, 63, 8, 3491–3503.

To further understand the mechanisms of the photocatalytic process, trapping experiments were conducted for verifying the radical species related to this photocatalytic process using BQ, EDTA-2Na and IPA as scavengers. As depicted in Figure 5.15, the reaction process was almost the same for the EDTA-2Na and blank group, while those of BQ and IPA group exhibited a significant decrease in the degradation process. The removal efficiencies of BQ and IPA group were 56.06% and 77.11%, respectively, much lower than original group (99.40%). In addition, the photocatalytic rate in Figure 5.16 also revealed that the reaction rate of BQ and IPA group was evidently supressed with the addition of the scavenger. The addition of BQ showed the lowest photocatalytic efficiency. The results above demonstrated that $\bullet O_2^-$ and •OH played significant roles during this reaction, and $\bullet O_2^-$ was the dominate factor in this photodecomposition of RhB. Meanwhile, there is no evidence that h^+ had an effect on the pathway of the reaction.

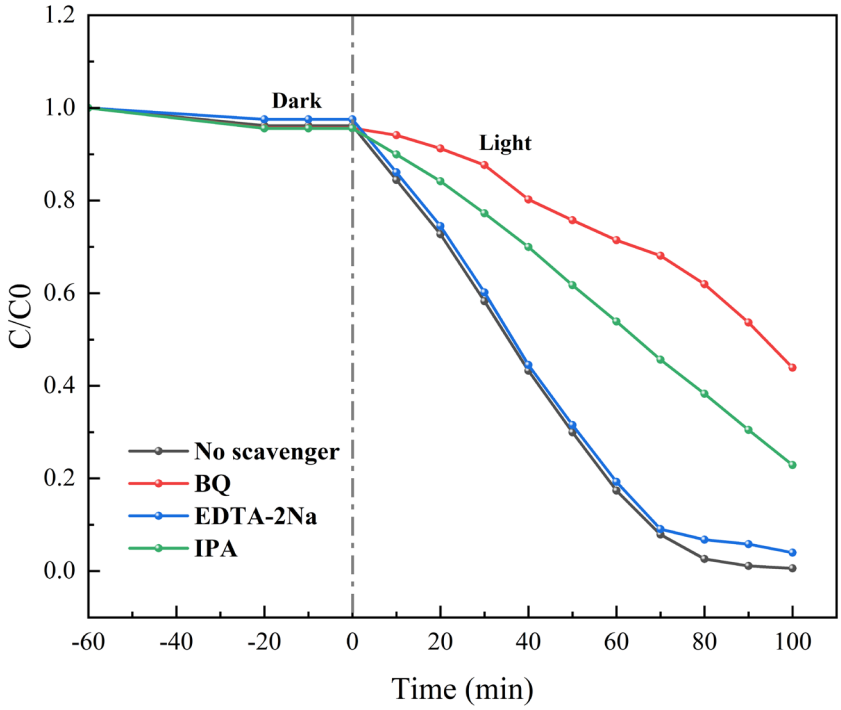

Figure 5.15 Photocatalytic removal of RhB with scavengers: No scavenger, BQ, EDTA-2Na, IPA groups.

Industrial & Engineering Chemistry Research [J]. 2024, 63, 8, 3491–3503.

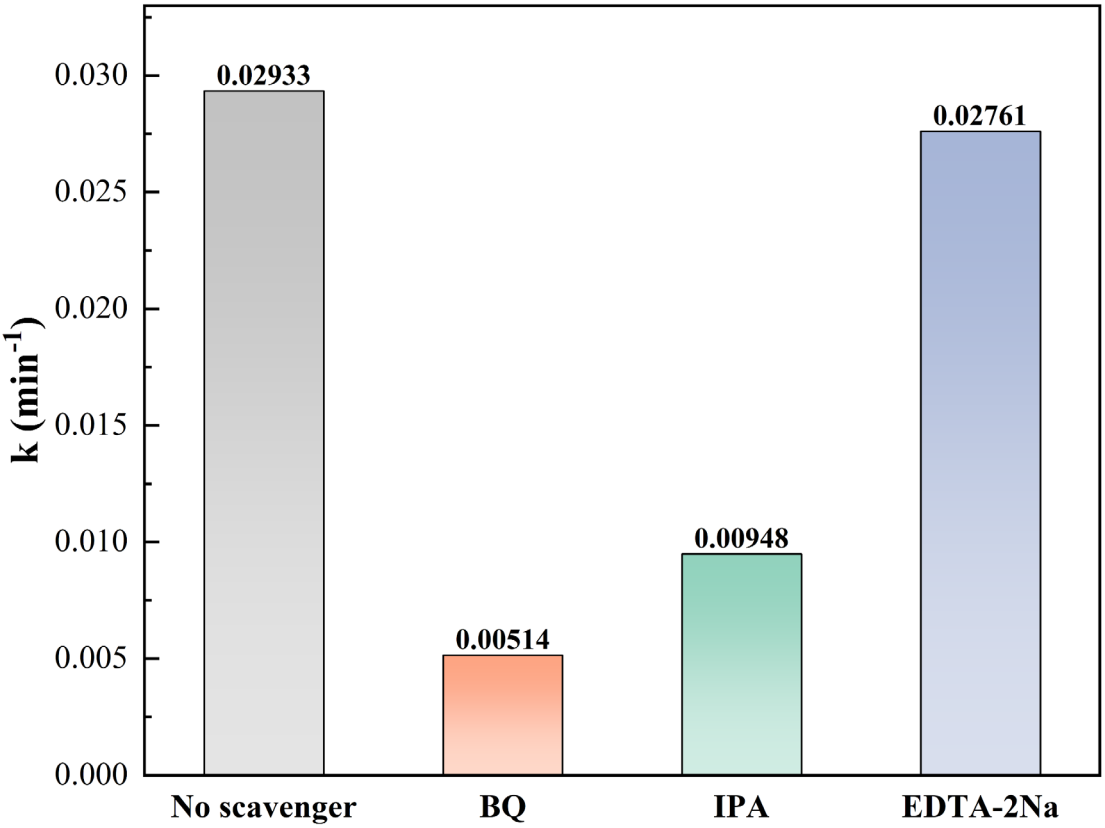

Figure 5.16 Photocatalytic rate with different scavengers: No scavenger, BQ, EDTA-2Na, IPA groups.

In addition, ESR tests were employed to further confirm the contributions of the active radicals in this reaction using DMPO as trapping chemical. The results were obtained in Figure 5.17, it was clearly shown that on evident signals were observed in dark environment. In contrast, with the visible light illumination, pronounced peaks were found for both DMPO/$\bullet O_2^-$ and DMPO/•OH, which also proved the existence of these two radicals in this photocatalytic reaction. Moreover, the signals of DMPO/$\bullet O_2^-$ were much clearer and stronger than that of DMPO/•OH, further documented that the $\bullet O_2^-$ was the dominated species in this reaction.

Industrial & Engineering Chemistry Research [J]. 2024, 63, 8, 3491–3503.

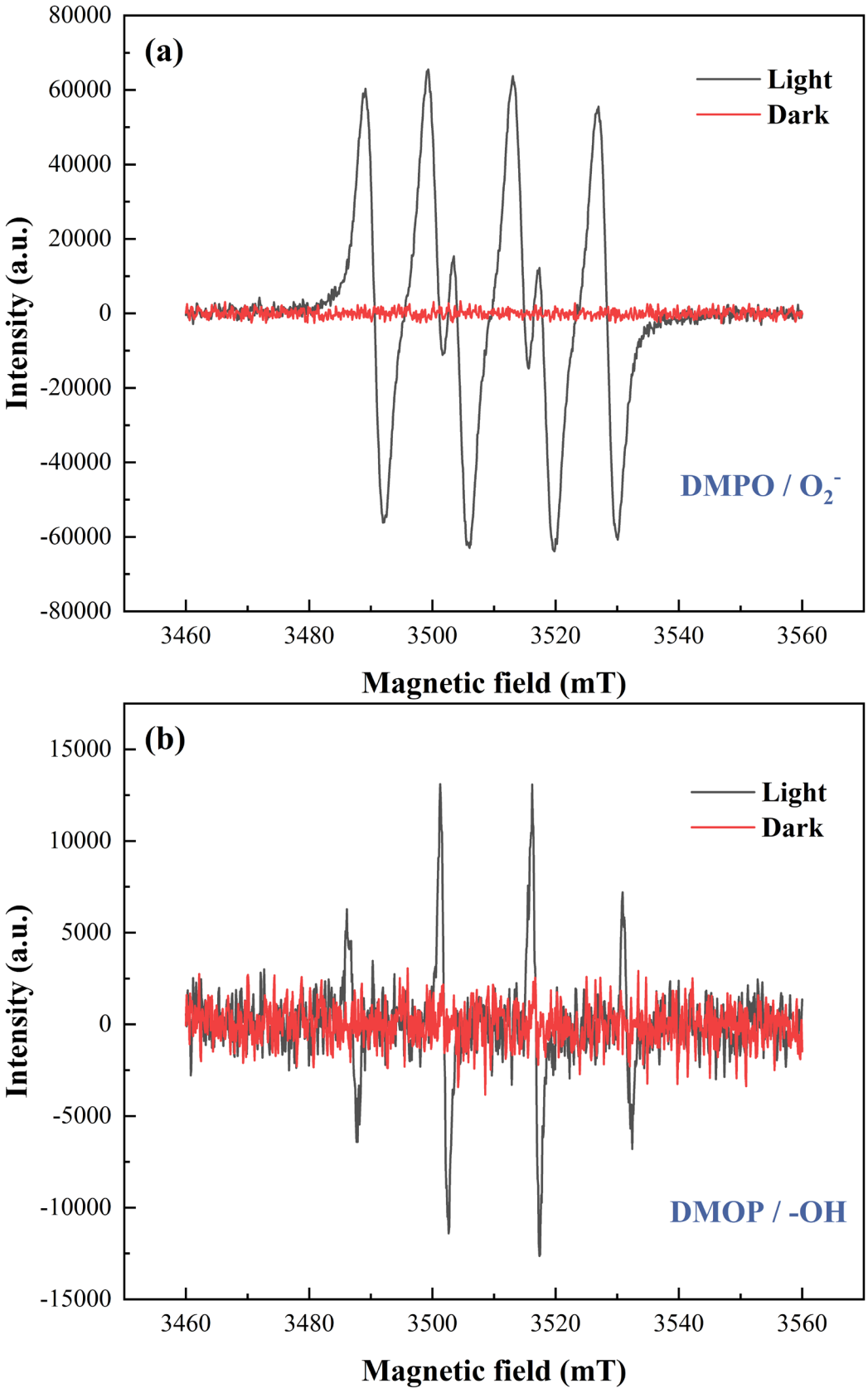

Figure 5.17 ESR signals of the (a) DMPO-•O_2^-; (b) DMPO-•OH^- with visible light irradiation for CN-1.5.

Industrial & Engineering Chemistry Research [J]. 2024, 63, 8, 3491–3503.

Furthermore, as CN-1.5 had a narrower band gap than CN-0, which mean that it can generate promoted electron and hole with the visible light irradiation, e^- induced in the VB of photocatalysts could transfer in their CB with h^+ left still. According to the band gag energy results above, the CB of CN-1.5 was negative than the $O_2/•O_2^-$ potential (-0.33 eV vs. NHE), implying that the induced electron can reduce the adsorbed O_2 molecules into $•O_2^-$. In contrast, the VB of CN-1.5 was 1.23 eV, which was too negative than the •OH/OH- potential (2.38 eV vs. NHE), indicating that the generated h^+ in CN-1.5 could not directly oxidize H_2O into •OH. As a result, the RhB molecules were absorbed onto the surface of CN-1.5 with improved BET surface area firstly. Then the target molecules could be excited into RhB* with light illumination, and then followed with an e^- transfer from RhB* to mesoporous g-C_3N_4. Lastly, the RhB^+ was degraded by $•O_2^-$ and• OH. The whole proposed reaction process could be summarized as follows equations and Figure 5.18:

$RhB + h\nu \rightarrow RhB^* \rightarrow RhB^{•+} + e^-$

$CN\text{-}1.5 + h\nu \rightarrow h^+ + e^-$

$O_2 + e^- \rightarrow •O_2^-$

$•O_2^- + 2H^+ + e^- \rightarrow H_2O_2$

$H_2O_2 + e^- \rightarrow •OH + OH^-$

$RhB^{•+} + •O_2^-/•OH \rightarrow$ Final products

Industrial & Engineering Chemistry Research [J]. 2024, 63, 8, 3491–3503.

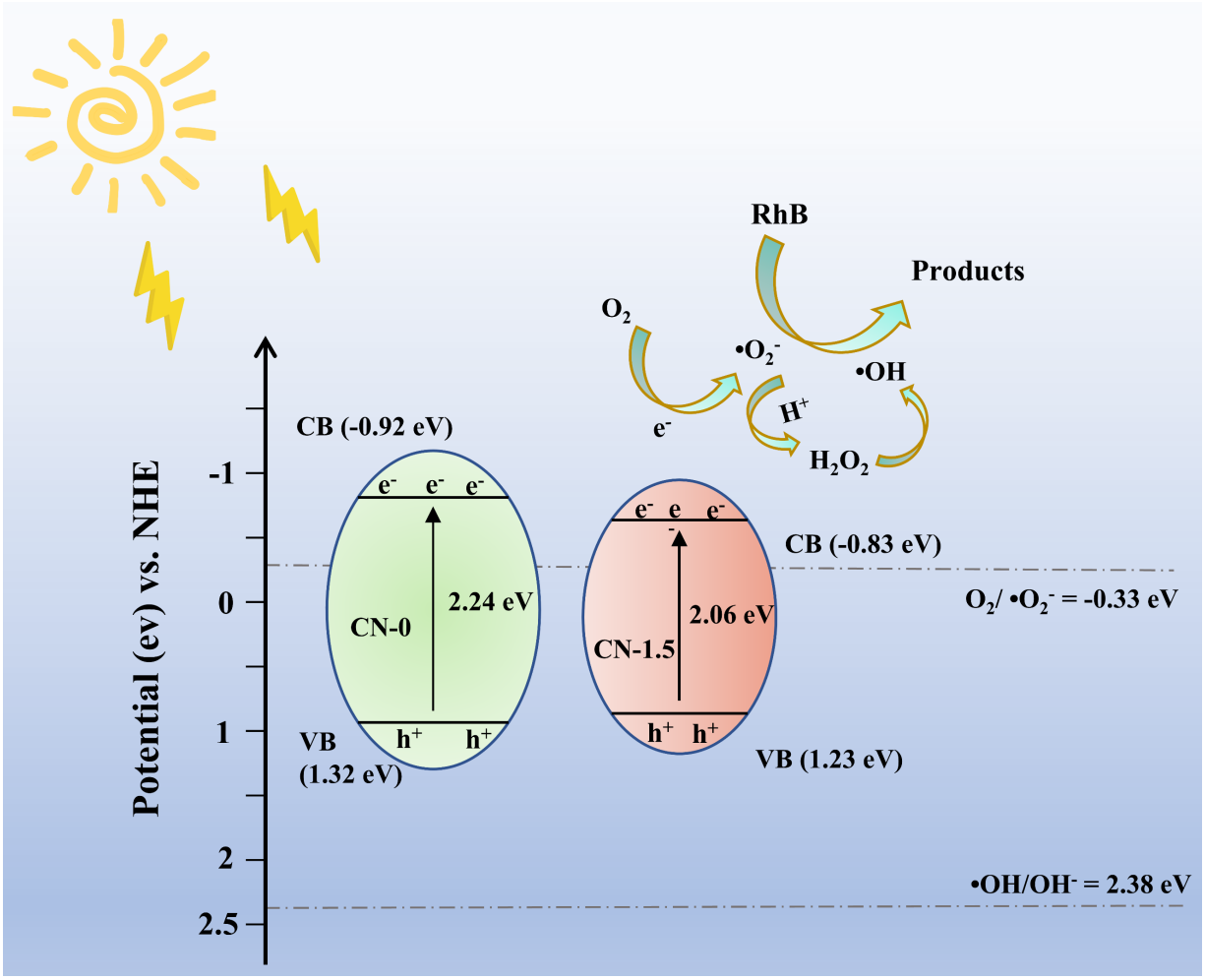

Figure 5.18 Proposed mechanism of this photodegradation reaction.

5.4 Summary

In summary, mesoporous g-C_3N_4 photocatalysts were prepared with a green and simple route. This mesoporous feature of the samples was verified by SEM, TEM and BET analysis. With an improved surface area and more O-doping ratio, the mesoporous sample exhibited promoted optical adsorption ability and preferable transfer efficiency of charge carriers. The highest photoactivity was obtained by CN-1.5. It could achieve 99.60% removal efficiency in 100 min under light irradiation, exhibiting 3.88 times better compared to CN-0 (25.63%) in the same period. Meanwhile, the photocatalytic rate of CN-1.5 (0.02933 min^{-1}) was also 11.19 times faster compared with CN-0 (0.00262 min^{-1}). Furthermore, the band energy and ESR analysis further revealed the

Industrial & Engineering Chemistry Research [J]. 2024, 63, 8, 3491–3503.

possible mechanism in this reaction. This study could offer a promins method for the preparation of low cost and green mesoporous g-C_3N_4 with effective photoactivity.

Industrial & Engineering Chemistry Research [J]. 2024, 63, 8, 3491–3503.

Chapter 6 Heterojunction of UiO-66 and porous g-C_3N_4 for boosted photocatalytic removal of organic dye.

In this chapter, a novel nanohybrid of Zr-MOFs (UiO-66) and porous g-C_3N_4 was prepared through an in-situ preparation route. The photocatalytic properties of these obtained samples were measured via the photodegradation of rhodamine B using visible light illumination. A series of characterization analysis were performed to demonstrate the structure of the heterojunctions and the possible reason for the enhancement on the photoactivity. In addition, the proposed mechanism of the photocatalytic removal process was identified with the analysis of ESR tests and trapping experiments. Moreover, the photoactivity tests in real water and stability tests along with XRD analysis were performed to evaluate the practical possibility of the photocatalysts. This study offers valuable insights into the preparation of MOF-based photocatalysts with exceptional effectiveness for the removal of contaminants in wastewater treatment.

6.1 Introduction

Stable photocatalysts with excellent photocatalytic performance are the key to the practical application of photocatalysis. Semiconductors are the most important materials used as photocatalysts. Various semiconductors have been used for photodegradation of organic pollutants, including TiO_2 [288], ZnO [293], g-C_3N_4 [283], CdS [294], $BiVO_4$ [295], Fe_2O_3 [296], MoS_2 [249], etc. However, photocatalysis with semiconductors are still far from practical applications due to many demerits, like fast recombination of photo-induced charges, low utilization of solar energy and limited surface active sites. Therefore, design new photocatalysts with tunable functionality and excellent efficiency is still of great significance and remains imperative challenges

Applied Surface Science [J] Volume 655, 15 May 2024, 159623.

in this filed.

Due to the exceptional porosity and controllable, tunable structural properties, metal-organic framework (MOF), composed of metal clusters and organic ligands, has garnered significant interest as a rising class of porous crystalline materials in recent years. [297]. Moreover, their distinct chemical versatility and tailored functionality make them promising candidates for various applications such as adsorption [193], sensing [188], membrane separation [298], drug delivery [187], energy storage [186] and photocatalysis [299]. In particular, the large surface area, tunable pore structure and semiconductor performance of some MOFs make them good candidates in photocatalytic degradation. Some researchers used ZIF-8 as photocatalysts for the removal of MB. The results demonstrated that the photodegradation could achieve 82.3% after 120 min under UV-light irradiation [300]. In addition, MIL-125 was synthesized by microwave method and applied for photocatalysis. This MOF had a photodegradation efficiency of 96.77% in 6h with light irradiation [301]. Moreover, some researchers investigated the photoactivity of MIL-539(Fe) on the degradation of organic dyes. The results displayed that this material had a degradation efficiency of 25% and 44%, on MG and RhB after 6 h visible light irradiation [302]. The photocatalytic activities of most pristine MOFs are not so satisfied. Accordingly, the bandgaps of most MOFs range from 1.0 to 5.5 eV. Most of the MOFs materials have a wide bad gap, resulting in the merely sensitive to UV-light rather than visible light, which limited their utilization of solar energy [303]. Hence, it is crucial to investigate viable approaches for enhancing the photocatalytic activities of MOFs materials.

Heterojunction is regarded as a feasible alternative to overcome the limitations of UiO-66 on photocatalysis. g-C_3N_4 was chosen as a potential counterpart to construct binary heterojunction. There have been several heterojunctions of UiO-66 and g-C_3N_4

reported for the improvement of photoactivity. Various approaches have been employed to prepare UiO-66/g-C_3N_4 heterojunctions. It was reported that this composite was prepared by annealing for the improved photoactivity on H_2 generation, the obtained UiO-66/g-C_3N_4 nanohybrid showed 17 times faster than that of pristine g-C_3N_4 on the H_2 production rate [304]. Some scholars synthesized UiO-66/g-C_3N_4 composites with electrostatic self-assembly route for promoted CO_2 reduction [305]. In addition, several works have been done on the removal of pollutants in wastewater treatment. It was reported that the UiO-66/g-C_3N_4 heterojunction was fabricated using ball-milling method for the photocatalytic reduction of Cr(VI) [306]. Some researchers prepared g-C_3N_4/UiO-66 nanohybrids with annealing method, which showed an improved photodegradation performance on the removal of methylene blue (MB) [307]. Some scholars prepared the same heterojunctions with solvothermal method for the photodecomposition of rhodamine B (RhB) [308]. Nevertheless, there are still much room for the improvements both on photoactivity and synthetic method of g-C_3N_4/UiO-66 heterojunction.

In this work, an in-situ growth method with oil bath was employed to synthesize UiO-66/g-C_3N_4 heterojunction photocatalysts. (Figure 6.1). It was widely regarded that various modification methods can improve the performance of g-C_3N_4. Inspired by reported literatures, porous g-C_3N_4 was prepared firstly to promote the photoactivity of bulk g-C_3N_4. Then the porous g-C_3N_4 powder was added into the homogeneous solution of UiO-66 precursor. Via a totally different fabrication method in oil bath, UiO-66/g-C_3N_4 nanohybrids were successfully prepared with remarkably enhanced photoactivity. Then, a series of characterisation tests were conducted to analyse the structure of the obtained materials. To evaluate the photocatalytic properties of the materials, photodecomposition tests of RhB using visible light illumination were also carried out.

Applied Surface Science [J] Volume 655, 15 May 2024, 159623.

The results showed that the new hybrids can utilize visible light and have excellent photocatalytic performance.

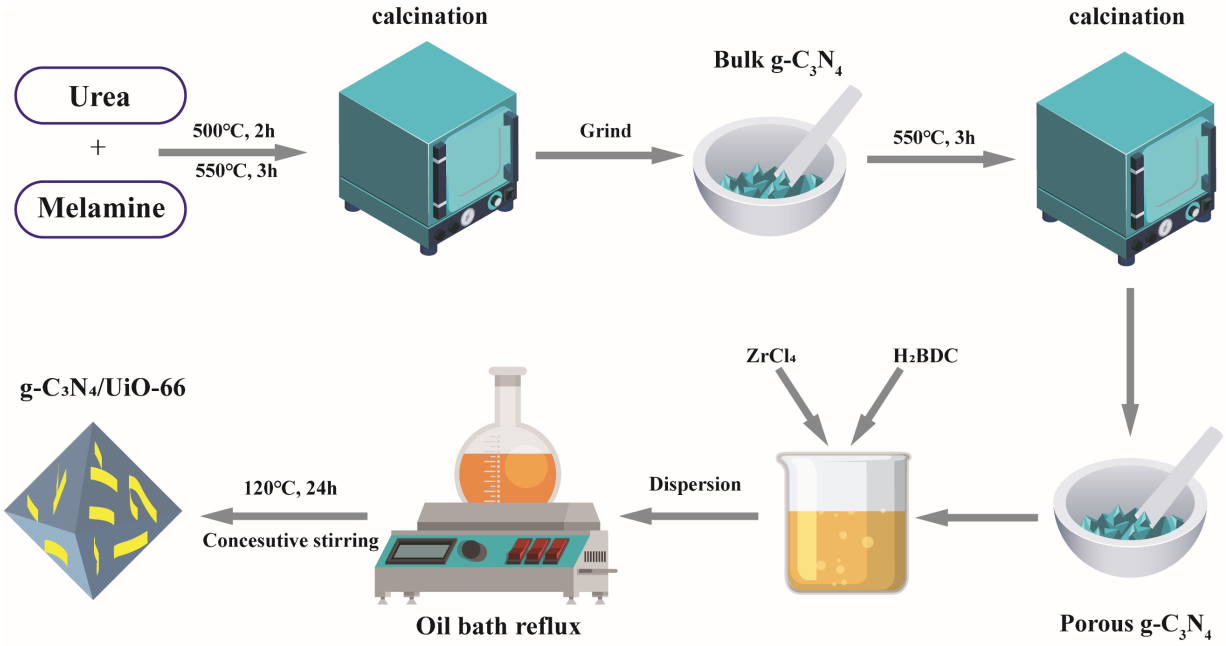

Figure 6.1 The preparation details of the g-C_3N_4/UiO-66 nanohybrids

6.2 Experimental

6.2.1 Porous g-C_3N_4 synthesis

Porous g-C_3N_4 was fabricated using the thermal polymerisation method following previous literature [1]. Typically, 5 g melamine and 10 g urea were dispersed in 50 mL of ethanol and subjected to magnetic stirring for 1 hour. Following an overnight drying period, the dried mixture was transferred to a crucible with cover and heated for 3 h at a rise rate of 5 ℃/min to 500 ℃ in furnace. The temperature was then raised to 550 ℃ for 3 hours at the same heating rate. When the temperature cooled down, the final product was ground into yellow powder and obtained as bulk g-C_3N_4.

Then the obtained yellow sample was dispersed uniformly without cover in an alumina crucible and then heated with a rise rate of 5 ℃/min to 550 ℃, and then kept for 3 hours. Upon reaching room temperature, the final material was ground into

Applied Surface Science [J] Volume 655, 15 May 2024, 159623.

powder and collected as porous g-C_3N_4.

6.2.2 UiO-66 synthesis

UiO-66 was synthesised by oil bath. For this purpose, 3 mmol $ZrCl_4$ and 3 mmol H_2BDC were mixed in 80 mL DMF. The mixture was stirred for 1 h to obtain a homogeneous solution. Afterwards the solution was put into a bottom flask where the reactor was transferred into an oil bath and kept at 120 ℃ for 24 h. Upon reaching ambient temperature, the obtained powder was rinsed with DMF and ethanol for three times. Lastly, the sample was collected after drying at 80 ℃ for enough time.

6.2.3 UiO-66/g-C_3N_4 nanohybrids synthesis

A series of heterojunction photocatalysts were prepared by a solvothermal method in an oil bath with various mass ratios of g-C_3N_4 to $ZrCl_4$. Porous g-C_3N_4 nanosheet was grown in-situ onto UiO-66. Generally, 4 mmol $ZrCl_4$ and 4 mmol H_2BDC were dissolved in 200 mL DMF. When the mixture was stirred for 30 min to get a homogeneous solution, a certain amount of porous g-C_3N_4 was mixed into the dispersion. The suspension was stirred for 1 h and then put into a bottom flask. After that, the flask was placed in oil bath at 120 ℃ for 24 h with continuously magnetic stirring. After natural cooling, the materials were washed with fresh DMF and ethanol for three times. Then final resultant solids were collected after drying and named as CNU-0.2, CNU-0.5, CNU-1 and CNU-2, according to different ratio of porous g-C_3N_4 to $ZrCl_4$.

6.3 Results and Discussion

6.3.1 Phase analysis

The XRD results of UiO-66, porous g-C_3N_4 and CN-X composites were recorded

in Figure 6.2. The findings indicated that the pattern of UiO-66 was coincident with the simulated pattern from literature, which means that the fabrication of this MOF material was successful [309]. The crystalline structure of the fabricated porous g-C_3N_4 also agreed well with the standard structure (JCPDS 87-1526) [310]. Two characteristic peaks were observed in this pattern. The weak peak at 2θ=13.1° was assigned to the (1 0 0) plane and attributed to the tri-s-triazine units, while the strong peak at 2θ=27.2°, indicating the (0 0 2) plane, represented the typical graphitic layered structure [311]. Moreover, in the series of g-C_3N_4/UiO-66 composite samples, the pronounced peaks related to UiO-66 and g-C_3N_4 could be distinctly identified, and no additional impurities were detected, indicating that the original crystallinity of the parent compound was maintained, and no additional impurities generated in the preparation process. Moreover, the peak at 2θ=27.2° of g-C_3N_4 became more distinct with the increment of g-C_3N_4 ratio, indicating that the precursor components were combined closely to form a composite rather than just mixing together [312].

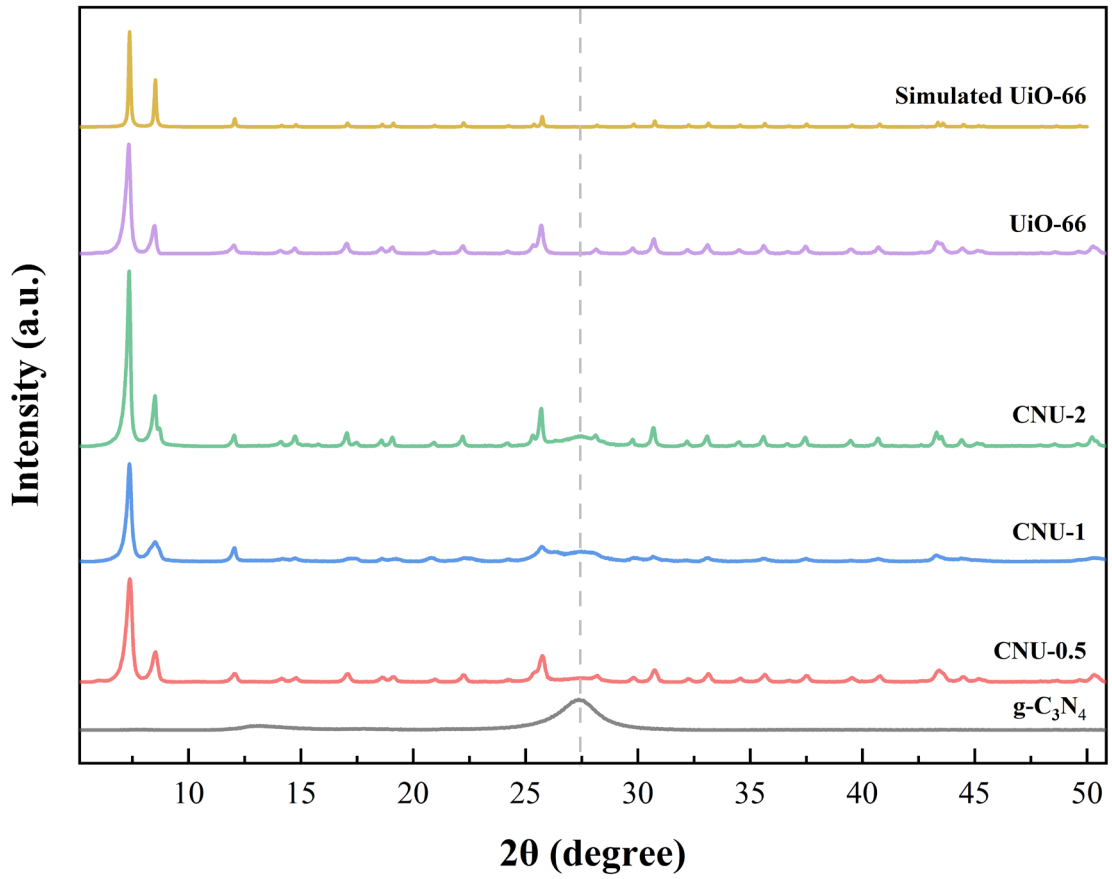

Figure 6.2 XRD results of g-C_3N_4, UiO-66 and a series of CNU-X composites

In addition, an FTIR spectrum was obtained to confirm the functionalities of the materials. It was illustrated in Figure 6.3 that the spectra analysis confirmed the existence of the basic structures of g-C_3N_4 and UiO-66 in the nanohybrids. The peak at 810 cm^{-1} of the CNU-X nanohybrids could be corresponding to the s-triazine units in g-C_3N_4, and the peaks in the region of 1200 to 1700 cm^{-1} could be assigned to the skeletal vibrations of C-N rings in g-C_3N_4 [313]. Moreover, the characteristic peaks between 600-800 cm^{-1} could be identified more clearly with increasing fraction of UiO-66 in the nanohybrids, which was ascribed to Zr-O_2 from UiO-66 [292].

Applied Surface Science [J] Volume 655, 15 May 2024, 159623.

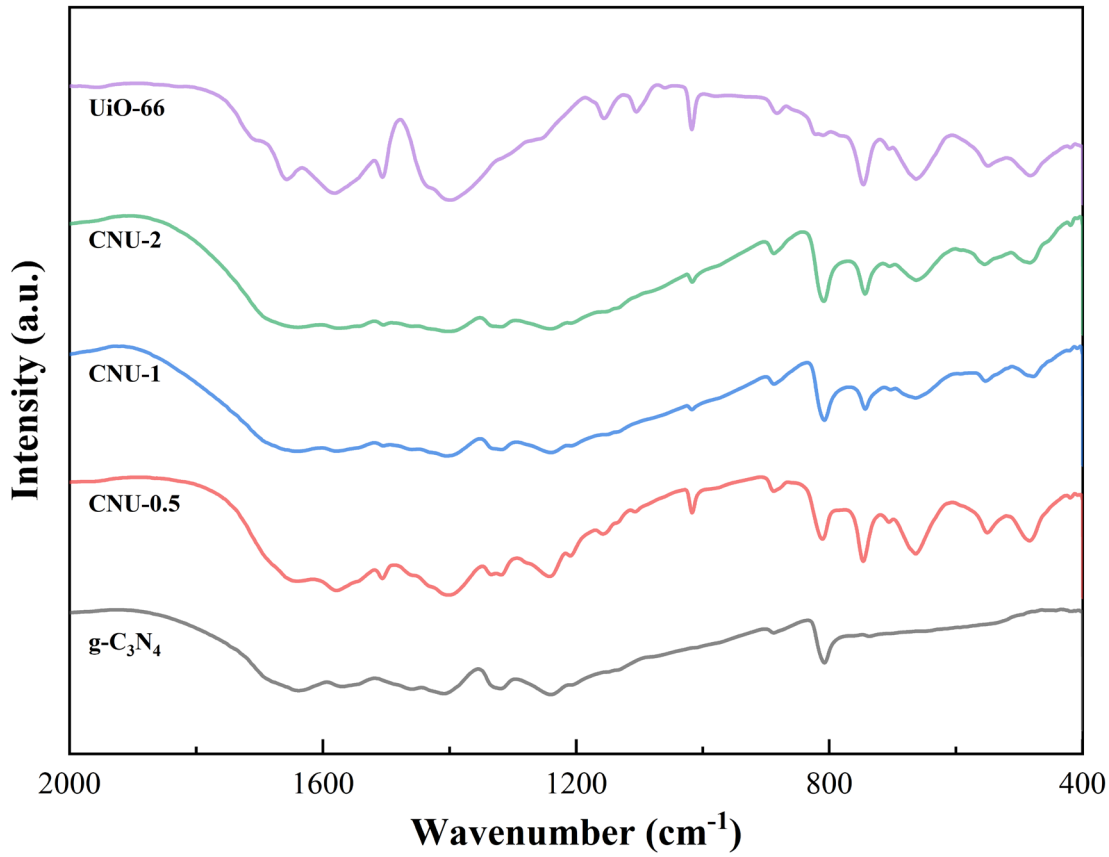

Figure 6.3 FT-IR spectrum of porous g-C_3N_4, UiO-66 and series composites.

The XPS test was applied for investigating the bonding state and chemical composition on the surface of the prepared samples [314]. As can be seen in Figure 6.4a, all the related elements can be seen in the g-C_3N_4/UiO-66 nanohybrids. As depicted in Figure 6.4b, the C 1s spectrum of CNU-0.5 can be divided into four peaks. The peak situated in 288.24 eV was corresponding to the N-C=N bond in the framework of g-C_3N_4. The peak around 284.80 eV was ascribed to the C atom in the BDC linker, just like UiO-66. While the peaks situated around 289.13 and 286.45 eV should be corresponding to the C-N and C-H/C-C bonds, further confirming the presence of g-C_3N_4 again [315]. Moreover, the binding energy of Zr 3d in Figure 6.4c had two peaks at 182.89 and 185.28 eV, which were corresponding to the Zr $3d_{5/2}$ and Zr $3d_{3/2}$ derived from UiO-66. The energy difference (2.39 eV) between these two peaks was very similar to those of ZrO_2, indicating that Zr-N and Zr-C bonds were not formed in the

Applied Surface Science [J] Volume 655, 15 May 2024, 159623.

nanohybrid [316]. Furthermore, as depicted in Figure 6.4d, the O 1s spectrum were divided into three distinct peaks. The peaks situated in 531.80 and 530.21 eV were assigned to C=O and Zr-O bonds, while the peak at 533.64 eV might be due to O-H groups [317]. In addition, three matched peaks at 398.70, 399.99 and 401.25 eV were found in the N 1s spectrum (Figure 6.4e). The peaks located in 398.70 eV and 399.99 eV were assigned to C=N-C bonds in the s-triazine units and amino group linking hydrogen [318]. The other peak in N 1s, located at 401.35 eV, is likely due to the charge effect. The above results clearly revealed that the nanocomposite was successfully prepared and contained both compounds derived from the starting materials.

Applied Surface Science [J] Volume 655, 15 May 2024, 159623.

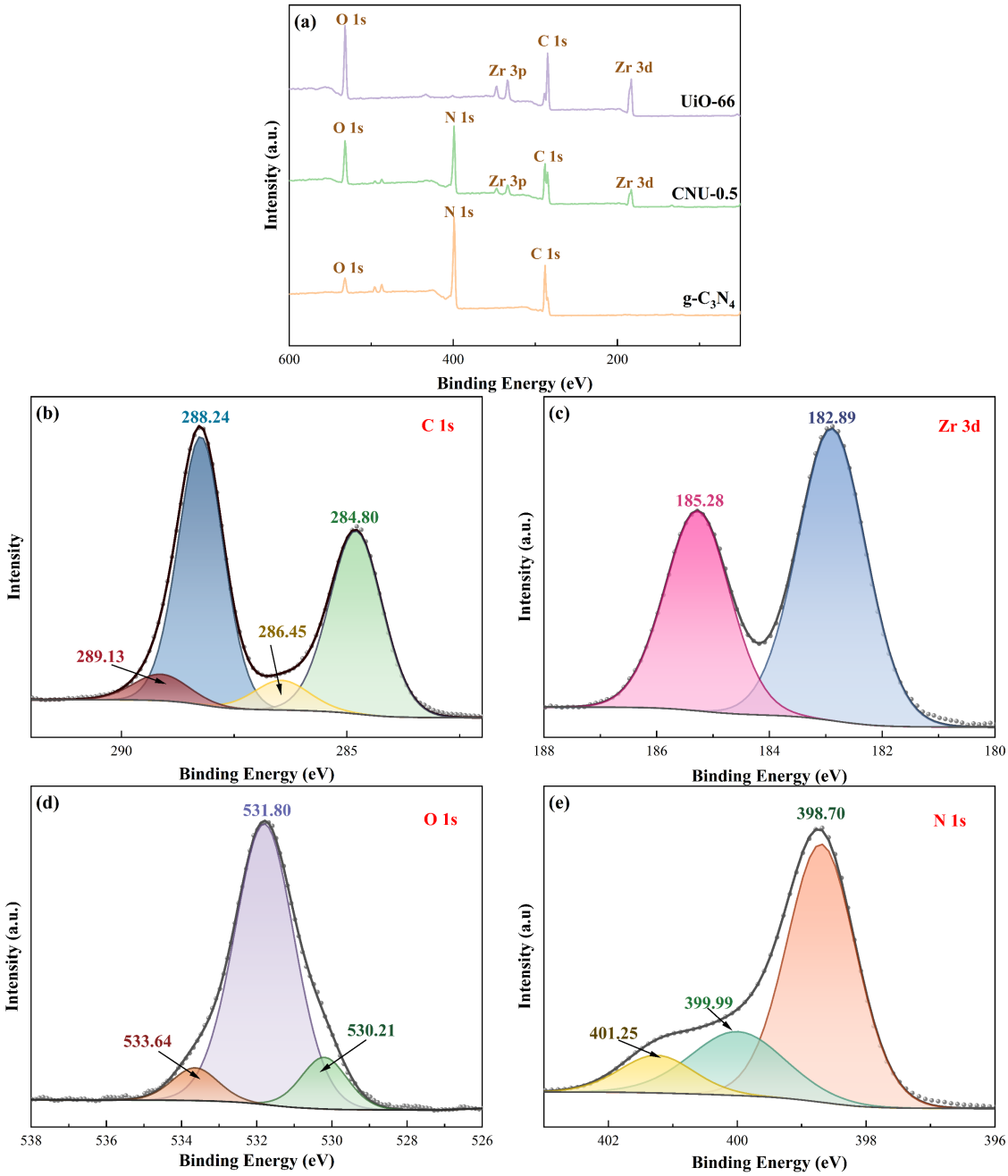

Figure 6.4 XPS spectra of CNU-0.5: survey (a), C 1s (b), Zr 3d (c), O 1s (d), N 1s (e).

6.3.2 Morphological analysis

The microscopic morphology of the photocatalysts prepared in this way can be seen at SEM in Figure 6.5. The porous g-C_3N_4 showed irregular folds and furrows in the nanosheet with in-plane holes forming a sponge-like morphology. The presence of these in-plane holes increased the porosity of these samples, thereby providing a larger

quantity of active sites. It was displayed that the synthesized UiO-66 possessed a smooth and clear surface, exhibiting a well-defined octahedral structure with a 88 nm average particle diameter (Figure 6.5b). [319]. The SEM micrograph of CNU-0.5 revealed that porous g-C_3N_4 was successfully grown on the g-C_3N_4 surface, forming a nanohybrid structure without compromising the integrity of g-C_3N_4 and UiO-66 (Figure 6.5c-e). The close interfacial contact between these two components was positive to form the heterojunctions as well as improve the interfacial transfer efficiency of the photo-generated electrons [185].

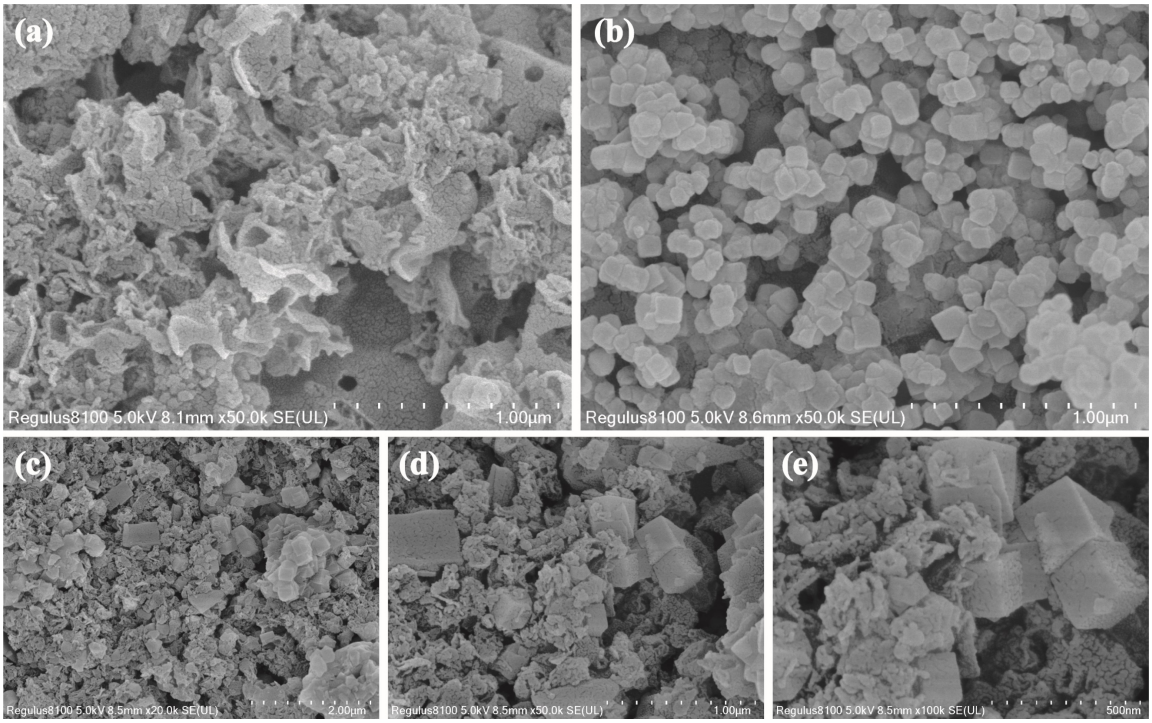

Figure 6.5 SEM of porous g-C_3N_4 (a), pristine UiO-66 (b), CNU-0.5 nanohybrid (c-e).

In addition, TEM and EDS tests were performed for a more detailed investigation to further elucidate the microscopic structure of the CNU-0.5 nanohybrids. It can be clearly confirmed that the g-C_3N_4 nanosheets were obviously embedded in UiO-66 (Figure 6.6). Moreover, the EDS elemental assignments in Figure 6.6f show that all the elements are uniformly distributed in the CNU-0.5 nanocomposites. All the above analysis validated the successful fabrication of g-C_3N_4/UiO-66 heterojunctions via the

Applied Surface Science [J] Volume 655, 15 May 2024, 159623.

in- situ growth approach using oil bath.

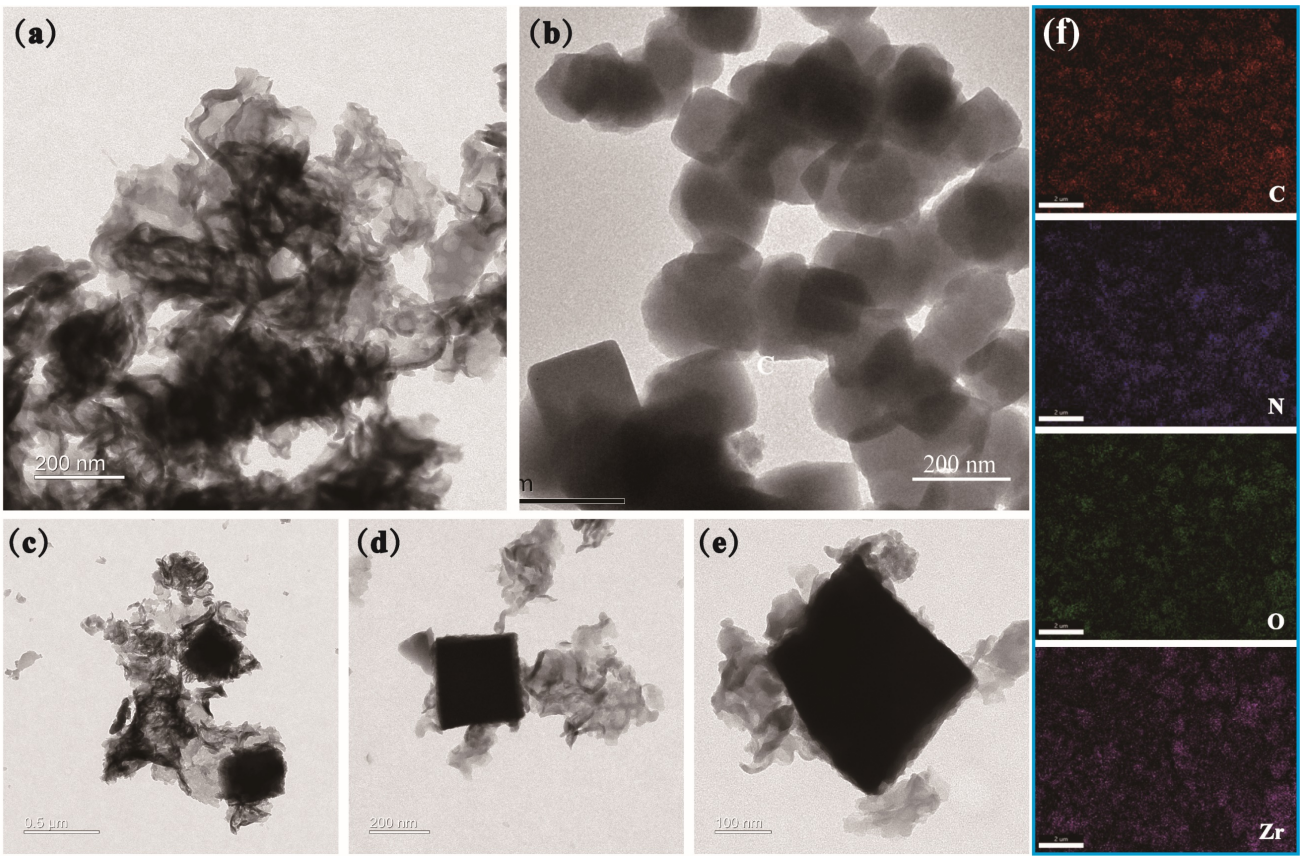

Figure 6.6 SEM of porous g-C_3N_4 (a), pristine UiO-66 (b), CNU-0.5 nanohybrid (c-e). EDS mapping of CNU-0.5 (f).

6.3.3 BET analysis

Nitrogen adsorption–desorption tests were performed to calculate the porosity parameters. Figure 6.7 showed the isotherms of different samples, and the calculations were tabulated in Table. 6.1. It was depicted from Figure 6.7 that the isotherms of all materials fitted well with the IV type model, indicating that the that the photocatalysts prepared in this manner exhibited a featured mesoporous structures [320]. From Table. S1, The obtained g-C_3N_4 showed a S_{BET} value of 84.51 m^2/g, which was almost 10 times larger compared with reported bulk g-C_3N_4 from previous literature, confirming the high porosity of this synthesized sample [321]. In addition, it was shown that the porosity of g-C_3N_4/UiO-66 nanocomposites was much lower than that of pristine UiO-

Applied Surface Science [J] Volume 655, 15 May 2024, 159623.

66, and the BET result of pristine UiO-66 was 855.73 m^2/g. With an increasing loading ratio of porous g-C_3N_4, the materials demonstrated an obvious decrease in S_{BET} values. While the average pore size of CNU-X decreased with increasing ratio of UiO-66, indicating that g-C_3N_4 was embedded onto UiO-66 surface [322]. The surface area of CNU-1 and CNU-2 was 386.19 and 347.19 m^2/g, respectively, which was still 4.57 and 4.11 times larger compared with porous g-C_3N_4. It was known that larger surface area (BET) can offer an increased number of active sites to promote photocatalytic performance [323].

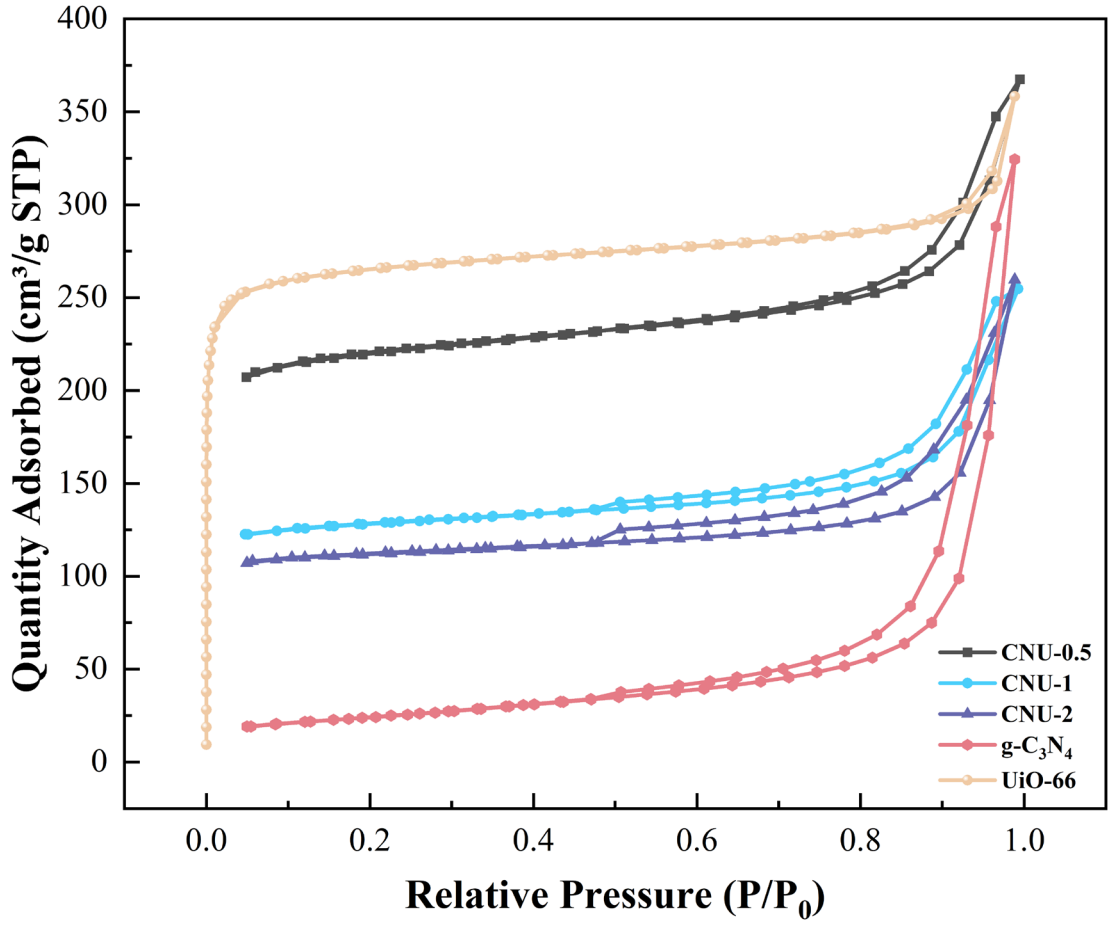

Figure 6.7 N_2 adsorption-desorption isotherms of g-C_3N_4, UiO-66 and CNU-X composites.

Applied Surface Science [J] Volume 655, 15 May 2024, 159623.

Table 6.1 Porosity parameters of the photocatalysts.

Samples	S_{BET} (m^2/g)	Pore volume (m^3/g)	Pore size (nm)
UiO-66	855.73	0.55	93.75
g-C_3N_4	84.51	0.50	220.83
CNU-0.5	679.71	0.57	90.79
CNU-1	386.19	0.39	131.54
CNU-2	347.19	0.40	152.72

6.3.4 Band structure analysis

Th UV-vis DRS was applied for studying the band gap energy along with optical absorption property for all the samples. It was shown in Figure 6.8 that the adsorption band of UiO-66 located at about 340 nm, and it can only absorb UV light. While the as-prepared porous g-C_3N_4 had an adsorption band situated around 480 nm in visible light range. Both the results were consistent with reported literatures [324, 325]. Meanwhile the CNU-0.5 nanohybrids had an adsorption edge at 480 nm in visible light region, exhibited a notable red shift and better light-harvesting capability than pristine UiO-66, which was assigned to the g-C_3N_4 component working as a visible-light sensitizer [326]. The band gap energy (E_g) was computed based on following Eq. 6.1:

$$\alpha h\nu = A(h\nu - E_g)^{n/2} \quad \text{6.1 [307]}$$

Applied Surface Science [J] Volume 655, 15 May 2024, 159623.

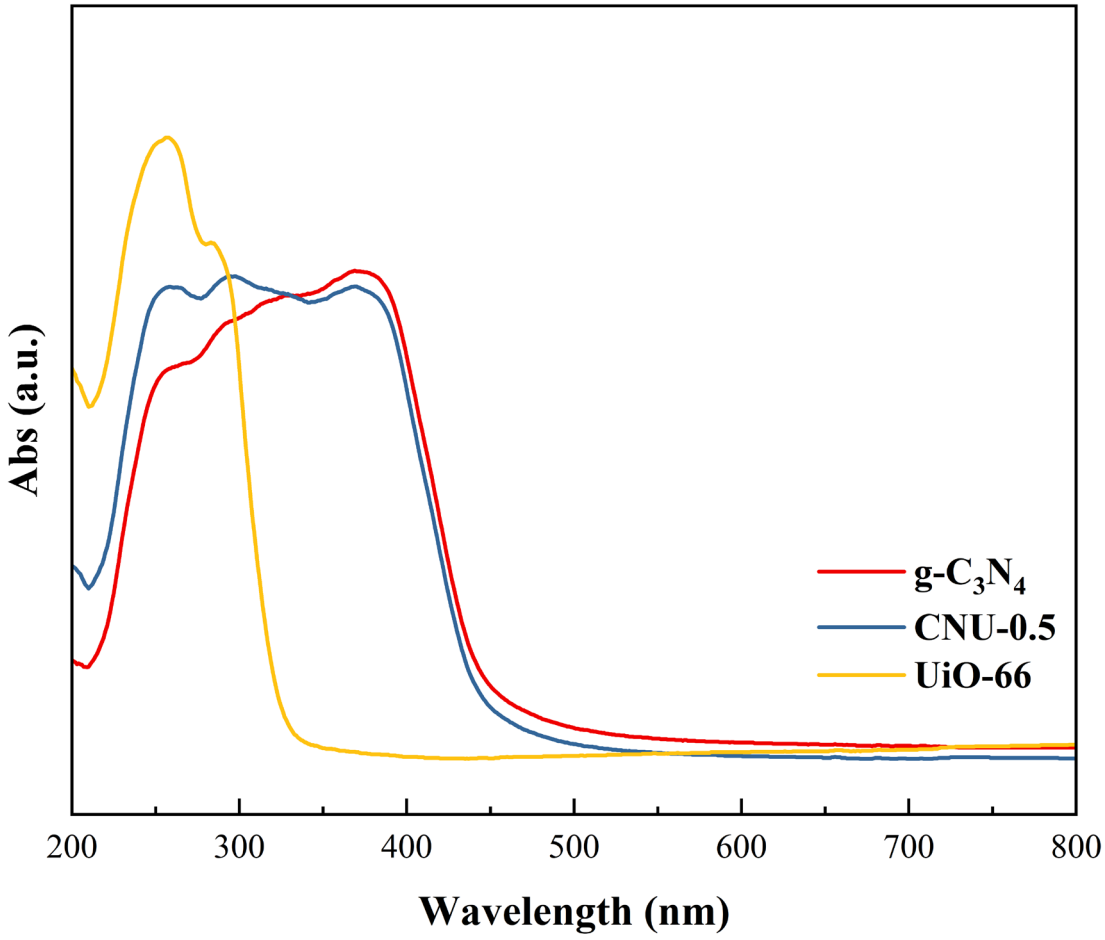

Figure 6.8 UV–Vis DRS spectrum of g-C_3N_4, UiO-66 and CNU-0.5

In this work, the n value is 4. The plots of $(\alpha h\nu)^2$ vs. hν were displayed (Figure 6.9) to estimate E_g of different samples. The E_g value of UiO-66 and g-C_3N_4 were calculated to be 3.96 and 2.88 eV. Moreover, the E_g value of CNU-0.5 was 2.92 eV, which was in just between those of g-C_3N_4 and UiO-66, confirming the successful heterojunction between g-C_3N_4 and MOFs to form nanohybrids. The band gap of CNU-0.5 also implied a much better visible light utilisation of CNU-0.5 than that of pure UiO-66.Furthermore, According to the formula of Eq. 6.2 and Eq. 6.3 [327]. The conduction band (E_{CB}) and valence band (E_{VB}) could be estimated based on following equations:

$$E_{VB}=\chi-E^e+1/2E_g. \quad 6.2\ [312]$$

$$E_{CB}=E_{VB}-E_g \quad 6.3\ [312]$$

Based on previous research reports, the χ of g-C_3N_4 is 4.7 eV, while that of UiO-66 is

Applied Surface Science [J] Volume 655, 15 May 2024, 159623.

5.6 eV [304, 328]. Therefore, according to the UV-vis DRS analysis, the conduction band energy of g-C_3N_4 and UiO-66 could be -1.24 and -0.88, eV. While valence band energy of these materials was 1.64 and 3.08 eV. The band gap energy of UiO-66 and g-C_3N_4 showed an obvious overlap, indicating that these two materials can be combined to form a valid heterojunction.

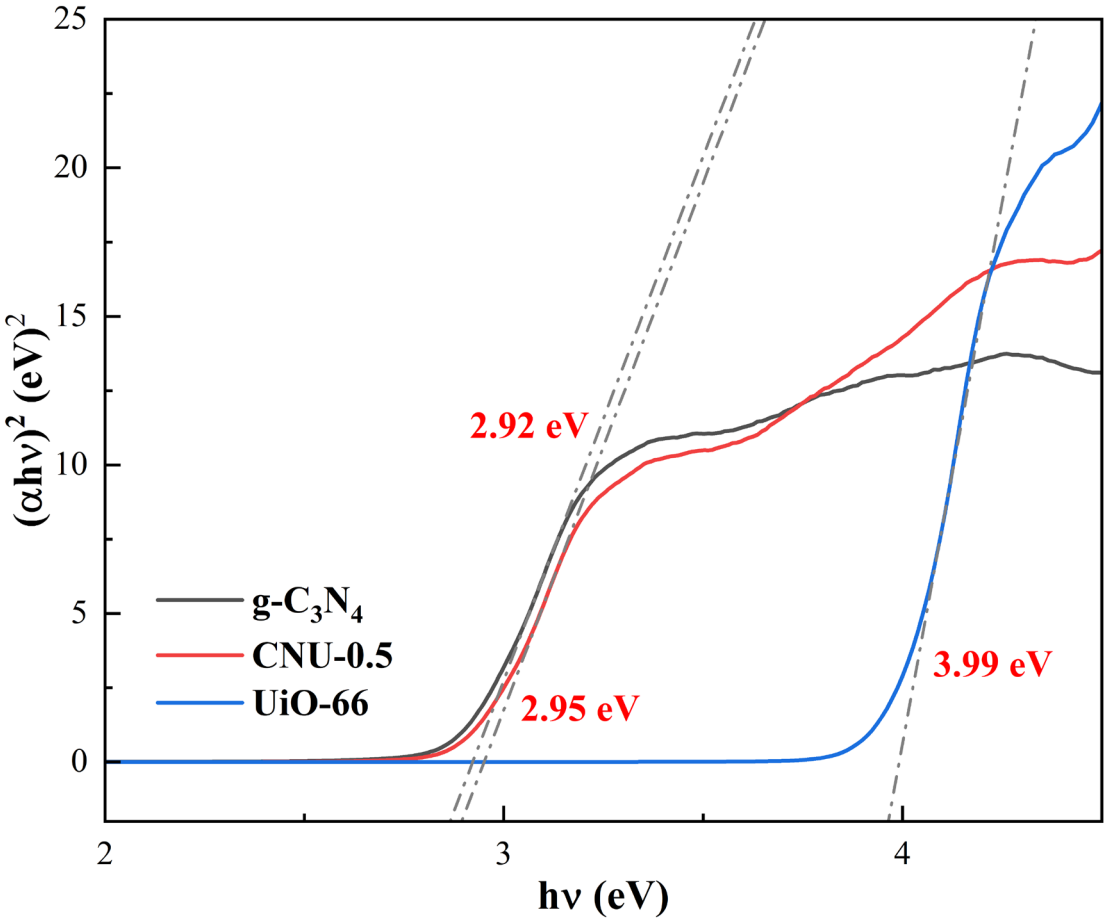

Figure 6.9 Tauc curves of g-C_3N_4, UiO-66 and CNU-0.5.

6.3.5 Photoluminescence and photoelectrochemical analysis

Photoluminescence (PL) spectra was carried out to verify the separation and recombination of photo-induced electrons and holes in the as-obtained photocatalysts [329]. As shown in Figure 6.10, the pristine g-C_3N_4 presented the strongest peak around 460 nm. Notably, all the nanohybrids showed obviously weaker emission intensity than original g-C_3N_4, indicating that the heterojunction structures had a rapid charge transfer

Applied Surface Science [J] Volume 655, 15 May 2024, 159623.

and thereby could significantly suppress the recombination of e^-/h^+ pairs with an improved photocatalytic property subsequently [330].

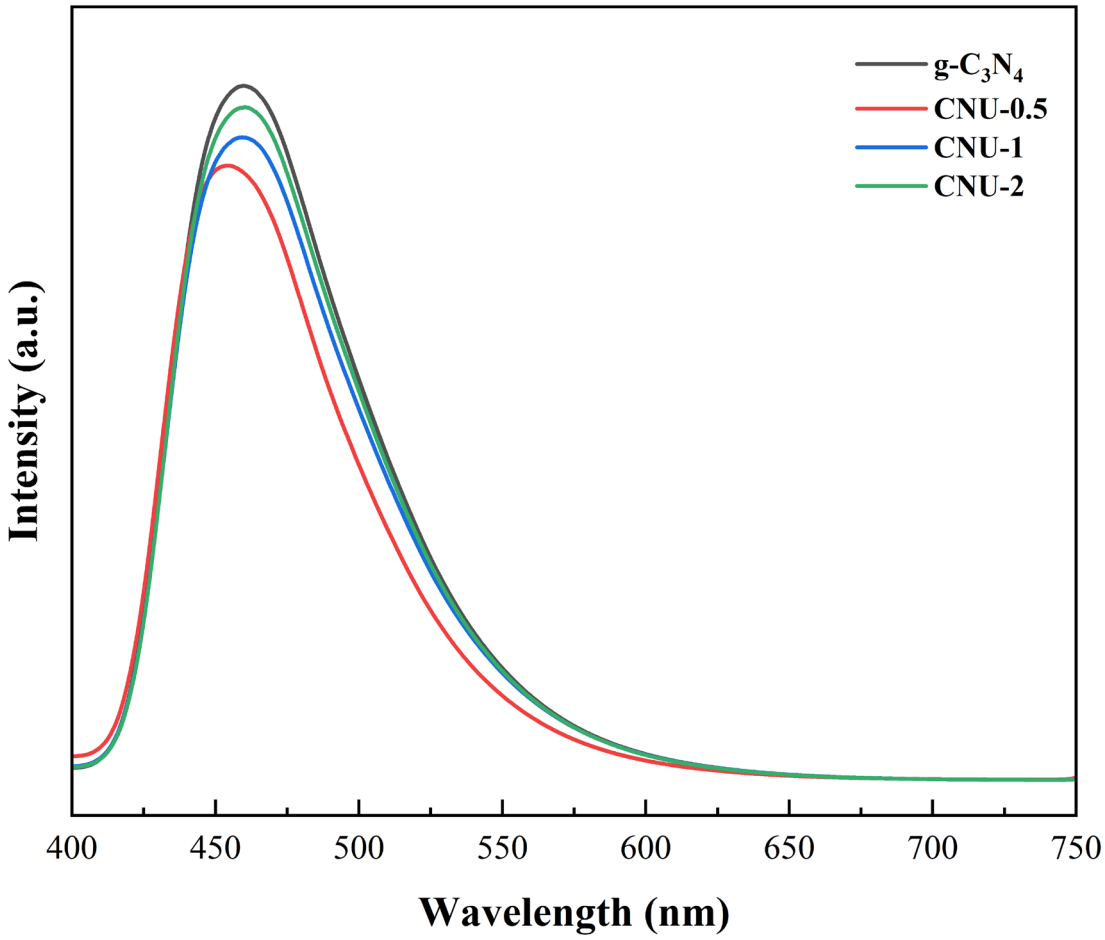

Figure 6.10 Photoluminescence spectra of g-C_3N_4, CNU-0.5, CNU-1 and CNU-2.

Electrochemical analysis such as EIS and photocurrent response analysis were also employed to analyse the photocatalytic properties of these materials. Figure 6.11a showed the EIS curves of different photocatalysts, it was found that the CNU-0.5 nanohybrids exhibited the lowest arc radius, confirming that the heterojunction nanocomposites exhibited a better transfer efficiency of photogenerated electron/hole than the starting materials [331]. In addition, photocurrent spectra of different samples were performed in Figure 6.11b. It was found that the photocurrent intensity of CNU-0.5 was much larger compared with pristine g-C_3N_4 and UiO-66, indicating that the heterojunction had much better transmission rate of e^-/h^+ pairs, leading to excellent

Applied Surface Science [J] Volume 655, 15 May 2024, 159623.

photocatalytic performance [332]. The electrochemical analysis results were both consistent with the improved photocatalytic performance described above.

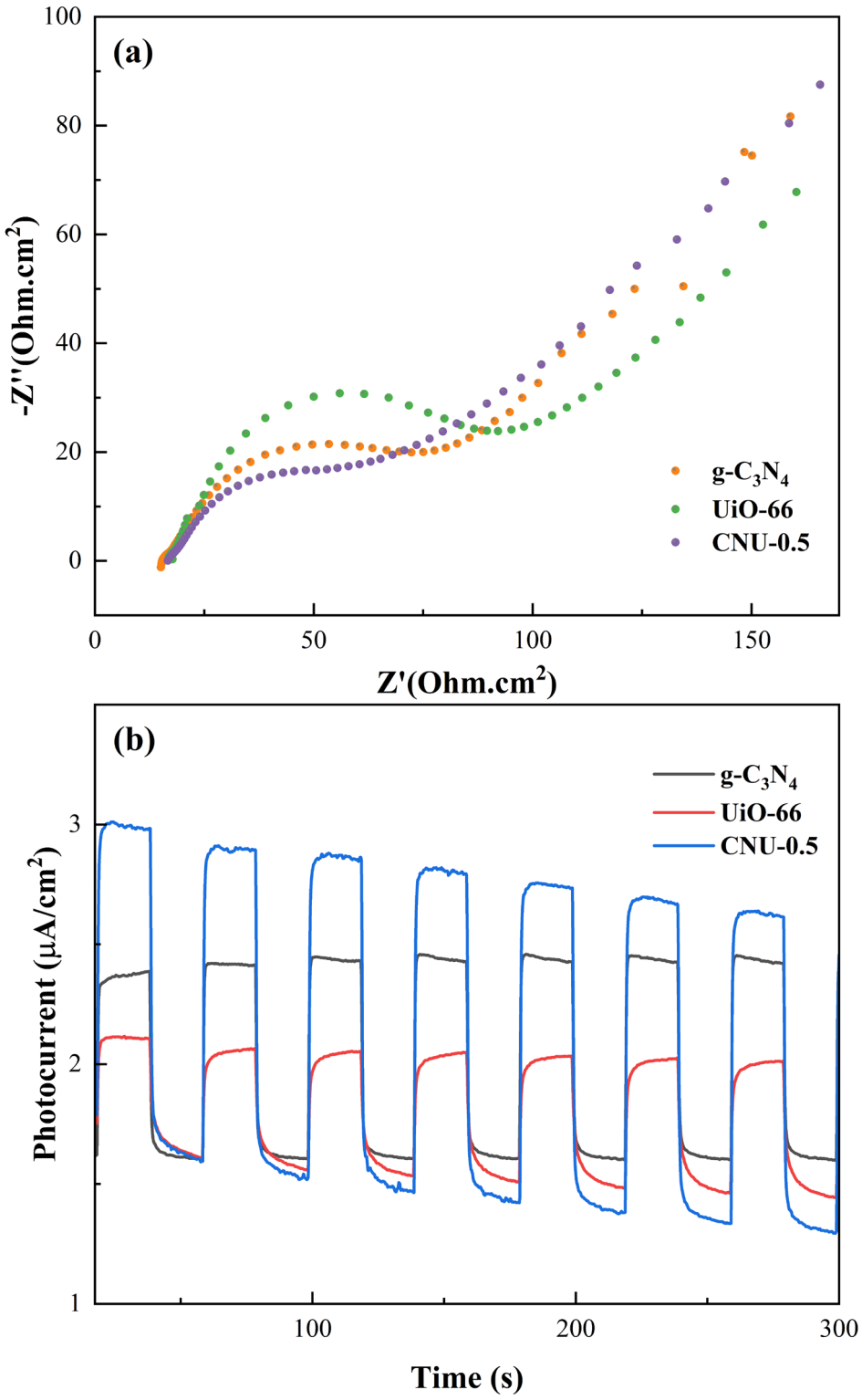

Figure 6.11 (a) EIS curves and (b) photocurrent responses of g-C_3N_4, UiO-66 and CNU-0.5.

Applied Surface Science [J] Volume 655, 15 May 2024, 159623.

6.3.6 Photocatalytic properties tests

A series of photocatalytic experiments were conducted with visible light to assess the photocatalytic performance of as-obtained materials. The removal efficiency was calculated based on $1-C/C_0$, in which C_0 and C represented the initial and residual concentration in certain time of RhB solution. Figure 6.12 showed that the RhB concentration decreased with increasing reaction time. No obvious decay was observed in the blank experiments, suggesting that the RhB molecule exhibited a high degree of stability when exposed to visible light. The solution was stirred thoroughly for 60 minutes before irradiation with visible light. It was found that all samples exhibited adsorption capacities for RhB and could reach adsorption-desorption equilibrium within 60 minutes. CNU-0.5 showed the best adsorption capacity, which was ascribed to the excellent porosity and the interaction of UiO-66 with porous g-C_3N_4. After the onset of light irradiation, all CNU-X nanohybrids showed better photocatalytic properties in the degradation of RhB than both the parent materials. CNU-0.5 completed the photocatalytic effect first. It achieved almost 100% removal efficiency in 70 min, and CNU-1 reached the same efficiency in 100 min., while the removal efficiencies of the other samples were much lower, 54.31% for UiO-66 and 72.51% for g-C_3N_4 in the same 100 min.

Applied Surface Science [J] Volume 655, 15 May 2024, 159623.

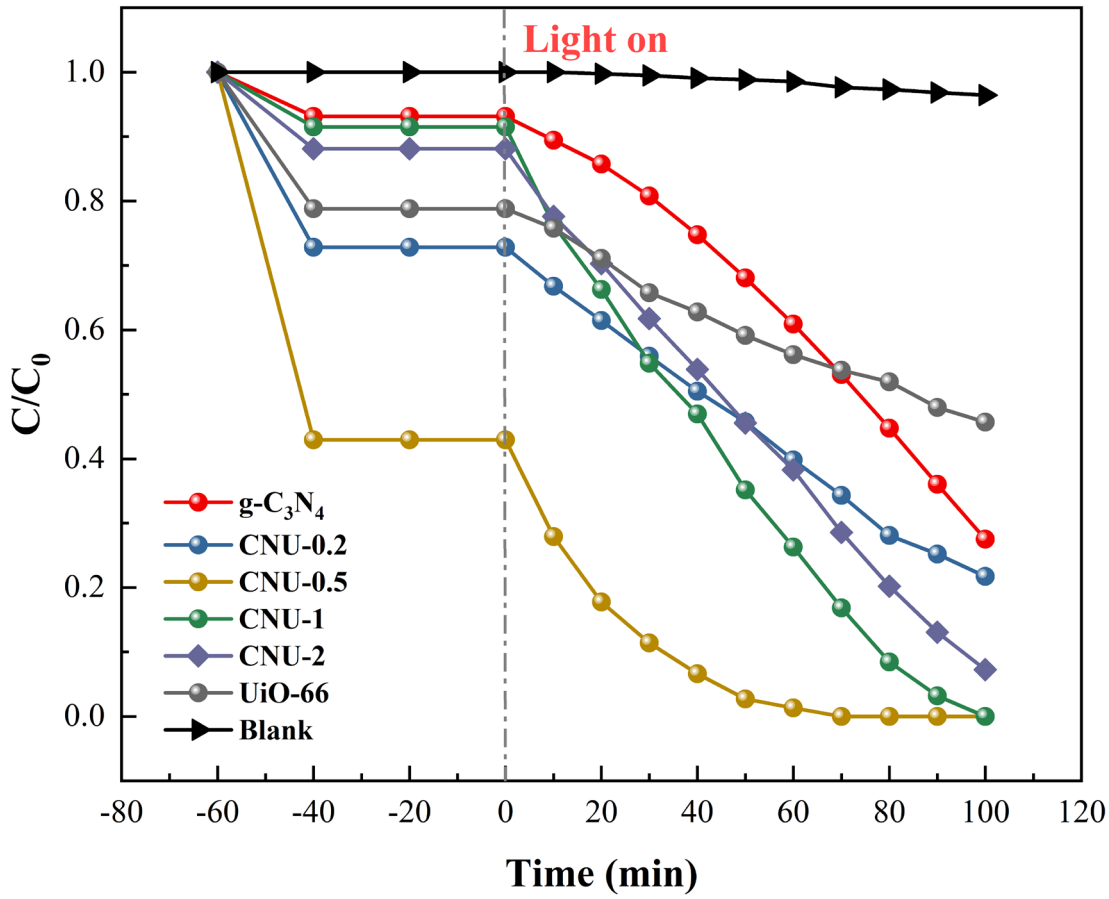

Figure 6.12 The RhB photodegradation process of different samples

In addition, the kinetic diagrams of the RhB photodegradation process were verified, and the k values could be calculated with ln (C_e/C) = kt in Figure 6.13, where C_e, C, and k were the RhB concentration at adsorption equilibrium, the residual concentrations in various time, and the reaction rate value, respectively. The photocatalytic rate of all samples was in the range: CNU-0.5 > CNU-1 > CNU-2 > CNU-0.2 > g-C_3N_4 > UiO-66, confirming the results of the analysis of PL. And the highest rate was for CNU-0.5 (0.05764 min^{-1}), which was 10.56 and 6.46 times faster compared with UiO-66 and g-C_3N_4. The results also showed that the successful heterojunction of Zr-MOFs with g-C_3N_4 can promote photocatalytic properties significantly. The results obtained in this work were compared with other similar literature reports to assess the photocatalytic effectiveness (Table 6.3). It displayed that the photocatalytic performance of this nanohybrid is at an excellent level.

Applied Surface Science [J] Volume 655, 15 May 2024, 159623.

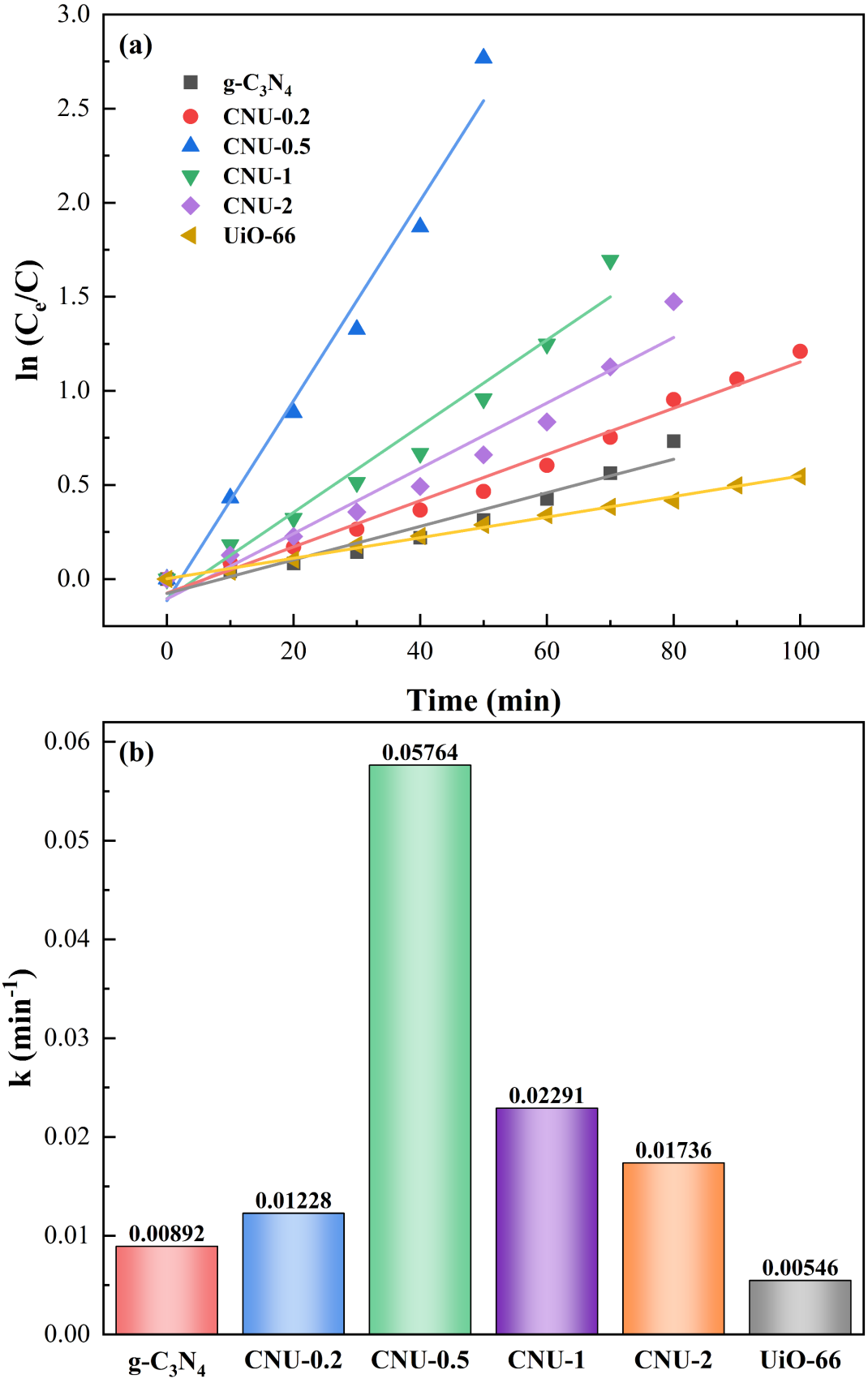

Figure 6.13 Fitting kinetic curves (a) and photocatalytic rates (b) of different samples.

Applied Surface Science [J] Volume 655, 15 May 2024, 159623.

Table 6.2 Comparison of the RhB degradation between the g-C_3N_4/UiO-66 nanocomposite and other reported photocatalysts

Photocatalyst	RhB concentration	Amount (g/L)	Light source	Time (min)	Degradation (%)	Ref.
Ce/Mo-V_4O_9	0.01 mM	0.8	Visible light	1180	88	[333]
$ZnFe_2O_4$/g-C_3N_4	10 mg/L	0.2	Visible light	30	96	[334]
ZnO-graphene-TiO_2	0.01 mM	1	Visible light	180	92	[286]
$NiFe_2O_4$/MIL-53(Fe)	0.03 mM	0.2	Visible light	180	95	[290]
TiO_2/ZrO_2	20 mg/L	0.8	Visible light	180	99	[288]
Bi_2MoO_6/UiO-66	10 mg/L	0.5	Visible light	120	96	[292]
g-C_3N_4/UiO-66	60 mg/L	0.2	Visible light	70	99	This work

6.3.7 Practical application

To evaluate the practical potential of the as-prepared photocatalysts, the photocatalytic tests of CNU-0.5 in different water environments were performed. Deionized water, tap water and river water were used to simulate different water conditions. It was shown in Figure 6.14a that the removal efficiency could reach 97.96% for deionized water in 60 min. While the removal efficiencies were obviously lower for

Applied Surface Science [J] Volume 655, 15 May 2024, 159623.

tap water (89.65%) and (river water 75.21%) in the same period. And the removal efficiencies in tap water and river water could also achieved nearly same performance when the reaction continued for enough time. In addition, the reaction rate in tap water (0.03741 min^{-1}) and river water (0.02311 min^{-1}) were also much lower than that of deionized water, as shown in Figure 6.14b. The decreased photocatalytic performance could be attributed to the increase of organic and inorganic species in the water environment. The organic matter could compete the ROS and active sites with target pollutants on photocatalysts, and inorganic ion like Cl^- could react with h^+ and ·HO[335]. Nevertheless, the photocatalytic degradation could still maintain a good performance in real water, which indicated a promising potential in practical application.

Applied Surface Science [J] Volume 655, 15 May 2024, 159623.

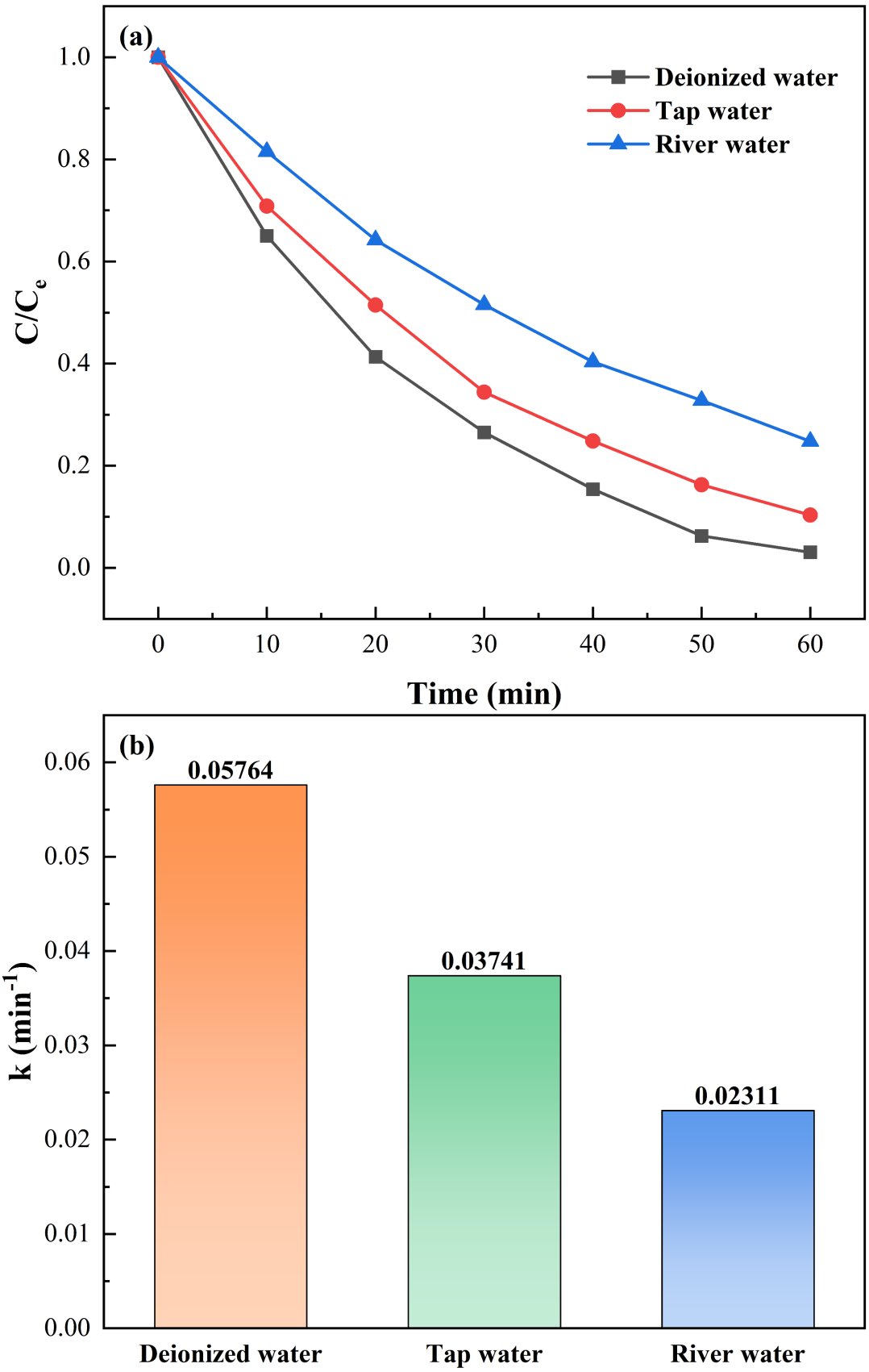

Figure 6.14 Removal efficiencies (a) and reaction rates (b) of CNU-0.5 in different water environments.

Applied Surface Science [J] Volume 655, 15 May 2024, 159623.

In addition, stability is also an important factor for the practical application of the obtained photocatalyst. It was conducted for five cycles for the photocatalytic degradation of RhB on CNU-0.5. As shown in Figure 6.15a, the removal efficiency retained 95.43% after five cycles, which was just a small decline compared to the first cycle. Moreover, XRD test was performed on the pristine sample and the used sample which has been recycled for five rounds. It was demonstrated that the XRD patterns (Figure 6.15b) of these two samples were highly similar, which indicated that the structure of CNU-0.5 maintained well after five cycles, further confirming the superior stability of this material.

Applied Surface Science [J] Volume 655, 15 May 2024, 159623.

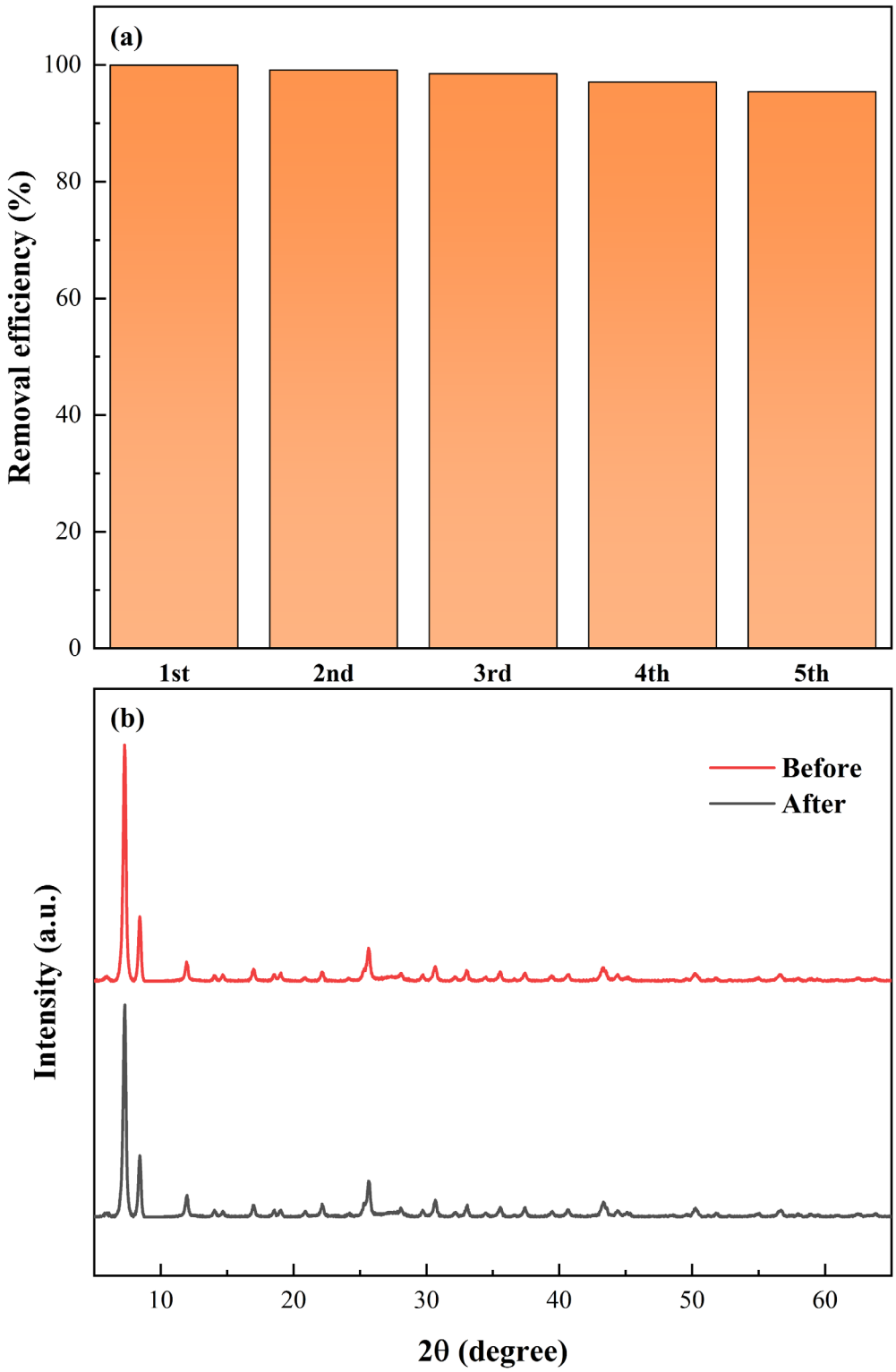

Figure 6.15 Photocatalytic efficiency of CNU-0.5 (a); XRD patterns of pristine CNU-0.5 and used CNU-0.5 (b).

6.3.8 Proposed photocatalytic mechanisms.

The photodecomposition mechanism of the nanocomposites was investigated by

Applied Surface Science [J] Volume 655, 15 May 2024, 159623.

determining the possible roles of $\bullet O_2^-$, h^+ and •OH during the process. It is widely recognized that the photocatalytic effectiveness mainly relies on these active species [336]. Therefore, BQ, EDTA-2Na and IPA were used as species trapper to measure the impacts of different active species by introducing them separately into the decomposition process. Take CNU-1 as example, it was illustrated in Figure 6.16 that the photocatalytic efficiency decreased slightly when EDTA-2Na or IPA were introduced into the system, indicating that both h^+ and •OH play a minor role in RhB photodegradation. In contrast, the adding of BQ substantially impeded the decomposition efficiency of RhB, implying that $\bullet O_2^-$ was the dominant active specie during this photodegradation process of RhB, as $\bullet O_2^-$ could originate from the reaction between electron and oxygen [337].

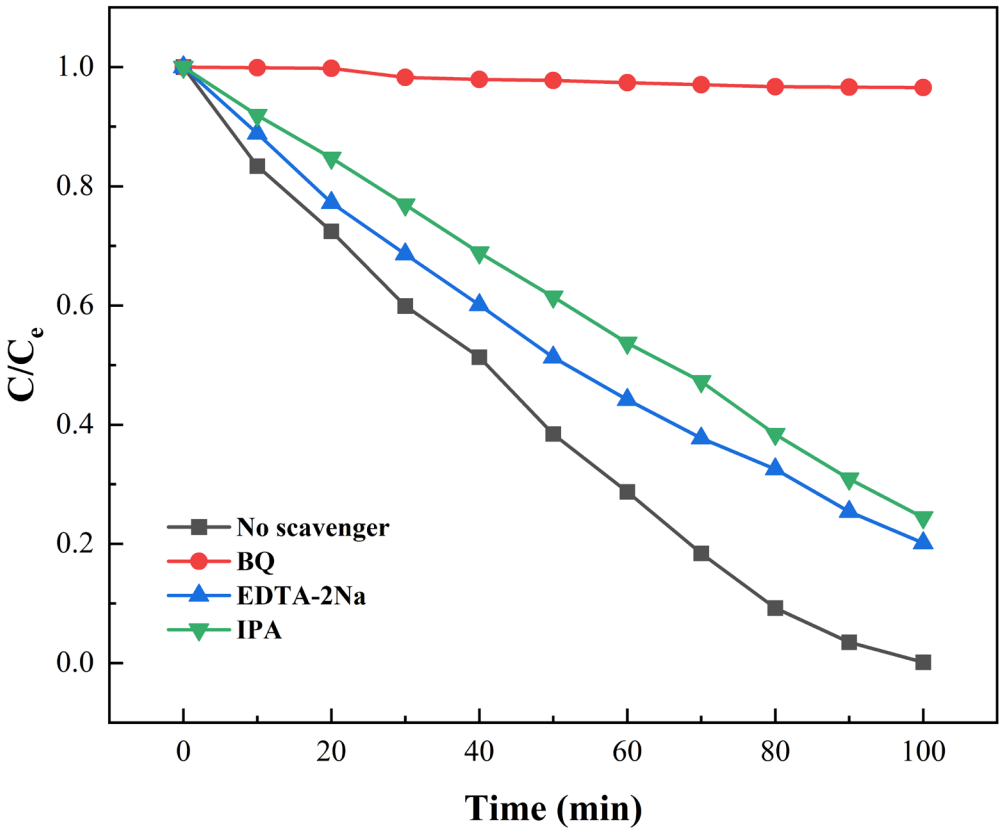

Figure 6.16 Trapping experiments with different scavengers on CNU-1.

To validate the existence of •OH and $\bullet O_2^-$ in this process and gain a deeper insight of the associated mechanism, ESR analysis was applied for observing the radicals in

Applied Surface Science [J] Volume 655, 15 May 2024, 159623.

the reaction using DMPO as a scavenger. It was displayed in Figure 6.17 that no signal could be found in the dark for both $\bullet O_2^-$ and •OH. In contrast, when irradiated with visible light, four characteristic peaks were observed for DMPO$\bullet O_2^-$ and DMPO-•OH, also proving that both $\bullet O_2^-$ and •OH were generated in this reaction process.

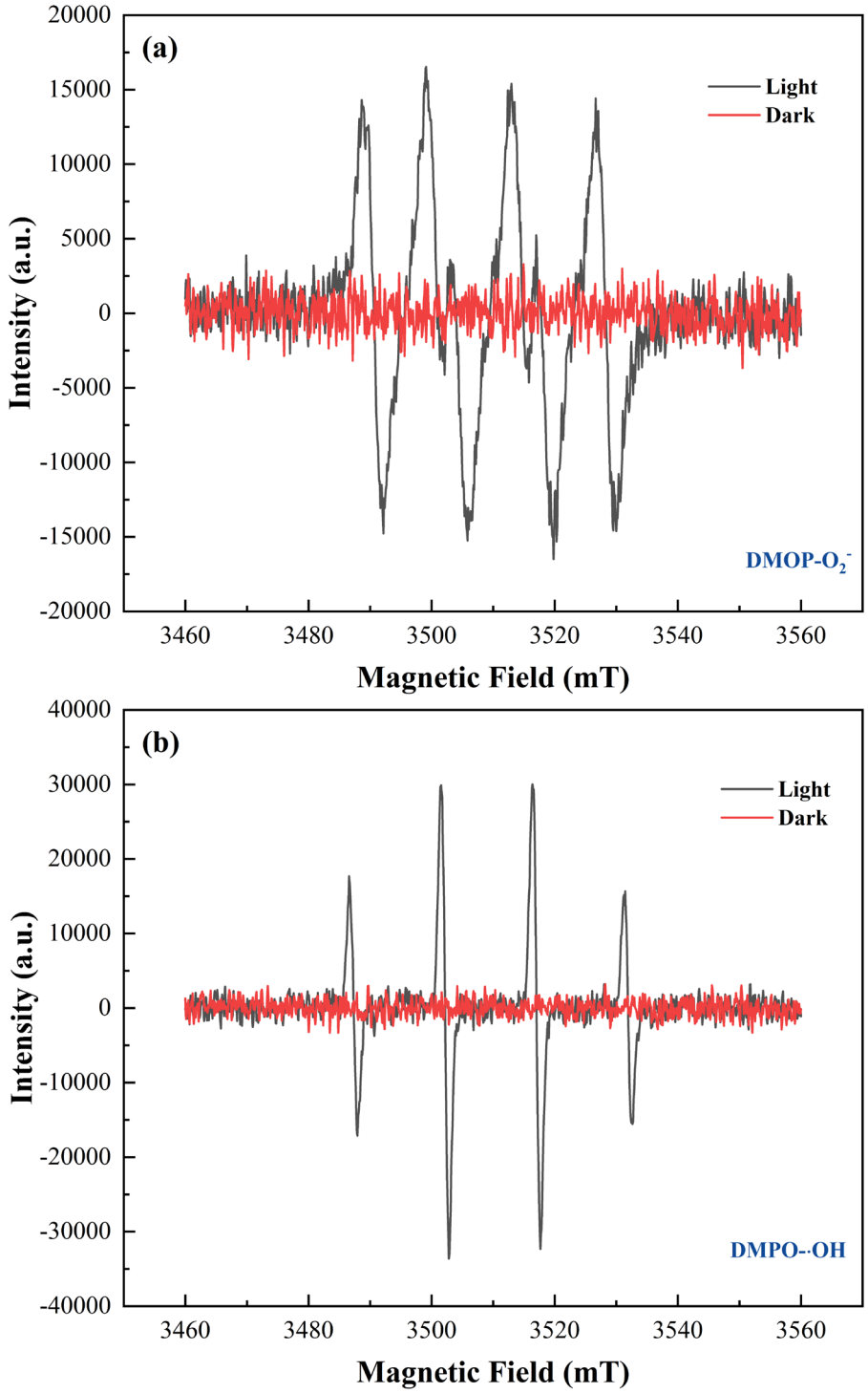

Figure 6.17 ESR signals of the (a) DMPO-$\bullet O_2^-$; (b) DMPO-$\bullet OH^-$ with visible light

Applied Surface Science [J] Volume 655, 15 May 2024, 159623.

irradiation for CNU-.05 nanocomposites.

Both g-C_3N_4 and UiO-66 can be excited under visible light to generate electrons and holes. For the holes induced on UiO-66, they would be retained on its VB. While the electrons of UiO-66 could be immigrated from the CB of UiO-66 to the VB of g-C_3N_4, and finally transferred to the CB of g-C_3N_4 to recombine with the holes. For this process, g-C_3N_4 could act as an electron sink to receive the electrons from UiO-66. Thus, the electron delocalization effect facilitated the migration of charge carrier and promoted the separation of photo-induced electrons and holes, which further lengthen the lifetime of e^-/h^+ and enhance the photoactivity of the heterojunction materials consequently. According to the band gap analysis, the E_{VB} of UiO-66 was more positive compared with standard potential of $•OH/OH^-$ (2.40 eV vs. NHE), which means that the photogenerated holes from UiO-66 can theoretically convert H_2O into •OH [338]. Upon irradiation with visible light, electrons could be generated on valence band of semiconductors and migrate to CB, leaving photoinduced holes in VB. Since the E_{CB} of g-C_3N_4 was negative compared with UiO-66, thus the electrons were probably migrated to UiO-66 via the conduction band of g-C_3N_4 through internal electric field formed from the heterojunction, which limited the recombination of e^-/h^+ pairs and improved the photocatalytic properties [339]. Moreover, both the conduction bands of g-C_3N_4 and UiO-66 were negative than $O_2/•O_2^-$ potential (-0.33 eV vs. NHE). Hence, the molecular oxygen absorbed at the surface of the nanohybrids may be reduced to form $•O_2^-$ radicals [340]. Accordingly, both the g-C_3N_4 and UiO-66 could produce $•O_2^-$, while only UiO-66 can convert H_2O into •OH, which mean much more $•O_2^-$ would be generated, this may be the reason that the O_2^- played an essential role in this reaction. Finally, $•O_2^-$, •OH and holes on VB of CNU-0.5 all had impacts on the decomposition of RhB, which also confirmed the findings in previous active species analysis. As a

result, the RhB molecule could be generated to RhB^* firstly upon irradiation with visible light, followed by electron migration from RhB^* to CNU-0.5. $RhB^{\bullet+}$ was degraded by $\bullet O_2^-$, •OH and holes lastly. This reaction process could be encapsulated in several steps as follows and illustrate in Figure 6.18:

$RhB + h\nu \rightarrow RhB^* \rightarrow RhB^{\bullet+} + e^-$

$g\text{-}C_3N_4 + h\nu \rightarrow RhB^* \rightarrow g\text{-}C_3N_4\ (h^+ + e^-)$

$UiO\text{-}66 + h\nu \rightarrow UiO\text{-}66\ (h^+ + e^-)$

$UiO\text{-}66\ (h^+) + H_2O \rightarrow UiO\text{-}66 + \bullet OH$

$UiO\text{-}66\ (e^-) + O_2 \rightarrow \bullet O_2^- + UiO\text{-}66$

$RhB/\ RhB^{\bullet+} + \bullet O_2^-/\bullet OH \rightarrow$ degradation products

$RhB/\ RhB^{\bullet+} + h^+ \rightarrow$ degradation products

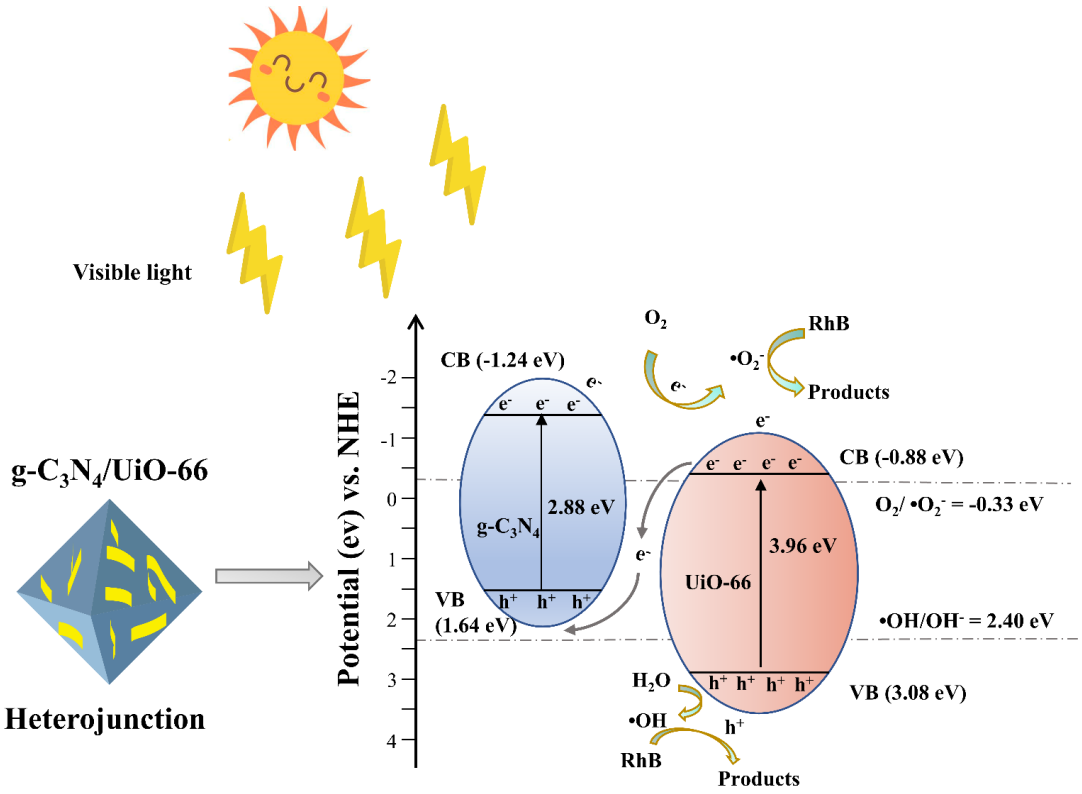

Figure 6.18 Proposed photodegradation mechanism of RhB on $g\text{-}C_3N_4$/UiO-66 nanohybrids.

Applied Surface Science [J] Volume 655, 15 May 2024, 159623.

6.4 Summary

In summary, various g-C_3N_4/ UiO-66 nanohybrids were prepared with an in-situ growth route in oil bath, which demonstrated improved excellent photocatalytic property for the removal of RhB. The successful preparation of these photocatalysts as heterojunctions was confirmed by various structural characterizations. Numerous characterization results documented that the promoted photocatalytic activities are owing to the bigger surface area, increased optical adsorption ability and excellent heterojunction. The high S_{EBT} means more active sites, so that more dye molecules are adsorbed on the surface and photocatalysis is enhanced. The improved optical adsorption enabled more extensive utilization of photo-energy. And the successful heterojunction improved the charge separation and prevent the electron-hole from recombining, resulting in higher photocatalytic efficiency in the removal of RhB. The best photocatalytic property was shown in CNU-0.5. It could complete the photocatalytic process in 70 min and the photodecomposition rate was 0.05764 min^{-1}, which was 10.56 and 6.46 times faster compared with pure UiO-66 and g-C_3N_4, respectively. Moreover, active species experiments, ESR tests and band gap analysis revealed the possible corresponding RhB photodegradation mechanism. This research provides a comprehensive understanding for the fabrication of effective MOF-based materials on the photodecomposition of contaminants in environmental remediation.

Applied Surface Science [J] Volume 655, 15 May 2024, 159623.

Chapter 7 Conclusions and prospectives

This chapter mainly introduces the conclusions of the thesis and proposes potential prospectives for future research.

7.1 Conclusions

This research mainly focuses on the design and synthesis of porous materials for the removal of organic dyes in wastewater treatment. Adsorption and photocatalysis were chosen as the key techniques to remove these organic pollutants. Subsequently, novel adsorbents and photocatalysts were prepared and tested on the removal performances. A series of characterisations are carried to analyse the structure of the prepared materials and reveal the mechanisms of the reaction process. It was demonstrated as follows:

(1) Metal-doped modification method demonstrated a promising possibility on improving the adsorption performance of MOFs materials. A novel Co-doped UiO-66 adsorbent was prepared via a facile in-situ growth approach. The characterisation results indicated that this modification route did not change the basic structure of UiO-66. With smaller particle size, higher surface area and more active sites, the Co-doped UiO-66 showed superior adsorption performances on MG (628.93 mg/g) and RhB (1106.22 mg/g).

(2) A green and simple method to fabricate mesoporous g-C_3N_4 was proven to be feasible. The mesoporous property of the as-obtained sample was verified by TEM and BET characterisations. With an improved surface area, CN-1.5 exhibited the highest photoactivity. Experimental results showed that it could achieve 99.60% removal efficiency in 100 min under visible light, while the bulk g-C_3N_4 only exhibited 25.63%

degradation efficiency in the same period. In addition, the reaction rate of CN-1.5 was 11.19 times faster than that of CN-0. Revealed by a series of characterisation tests, the improved photoactivity of mesoporous g-C_3N_4 could be assigned to the enhanced optical adsorption ability and charge carriers transfer efficiency.

(3) The heterojunction of UiO-66 and porous g-C_3N_4 proved to be a potential route to synthesize effective photocatalysts. The heterojunction structure of the nanohybrid was confirmed by a series of characterisation tests. The best photocatalytic property was shown to be almost 100% removal efficiency in 70 min by CNU-0.5. Moreover, the degradation rate of CNU-0.5 (0.05764 min^{-1}) was 10.56 and 6.46 times faster than that of pristine UiO-66 and g-C_3N_4. The nanocomposites had an improved charge separation and lower electron-hole from recombining, which could result in the promoted photoactivity.

7.2 Future work

Although a series of research work has been performed on the fabrication and application of porous materials for the removal of organic dyes, there still exits various issues that could be further addressed in the future.

(1) Following the work in chapter 3, easy recovery and recyclability could be focused on for further work. For example, the adsorption energy of MOFs materials on pollutants could be studied by DFT calculations, in order to further confirm and reveal the mechanism of the different adsorption performances by prepared materials. Moreover, more experiments on the influence of ionic strength could be further investigated, which is a crucial aspect for the practical application of adsorbents in real water. Furthermore, for industrial potential, low-cost, easy separation, non-toxicity and no harmful by-product has always been great significance for the design of new adsorbents. Hence, for the future work, design some new materials that could be easy

recovery should be an important direction for real industrial application. For instance, adding some magnetic counterpart for facile separation, or design some new adsorbents based on membrane engineering. In addition, the toxicity of designed adsorbents should also be further studied to ensure a good practical potential.

(2) Based on the work in chapter 4, the synthesis process of mesoporous g-C_3N_4 could be more sophisticated to further improve the porosity and photoactivity. Like use some different precursor to introduce elemental doping, control the fabrication conditions to form more vacancies, introduce some typical semiconductor metal elements, etc. All these routes could be possible ways to further improve the photoactivity of mesoporous g-C_3N_4. In addition, more experiments in rea water could be conducted to assess the practical application. More characterisations could be carried out to investigate the product in the photocatalytic reaction process.

(3) On the basis of the research in chapter 5, there are also some further works could be done. First of all, some more characterisation test, such as LC-MS, could be carried out to identify the final product of degradation process. Meanwhile, DFT calculations could be performed to further reveal the mechanism and pathway of the whole photocatalysis reaction. In addition, the role of each counterpart in the heterojunction and how they work in the reaction still could be further studied.

References

[1] A.M. Ghaedi, A. Vafaei, Applications of artificial neural networks for adsorption removal of dyes from aqueous solution: A review, Advances in Colloid and Interface Science, 245 (2017) 20-39.

[2] V.K. Gupta, R. Kumar, A. Nayak, T.A. Saleh, M.A. Barakat, Adsorptive removal of dyes from aqueous solution onto carbon nanotubes: A review, Advances in Colloid and Interface Science, 193-194 (2013) 24-34.

[3] I. Anastopoulos, G.Z. Kyzas, Agricultural peels for dye adsorption: A review of recent literature, Journal of Molecular Liquids, 200 (2014) 381-389.

[4] N. Dizge, C. Aydiner, E. Demirbas, M. Kobya, S. Kara, Adsorption of reactive dyes from aqueous solutions by fly ash: Kinetic and equilibrium studies, Journal of Hazardous Materials, 150 (2008) 737-746.

[5] K.B. Tan, M. Vakili, B.A. Horri, P.E. Poh, A.Z. Abdullah, B. Salamatinia, Adsorption of dyes by nanomaterials: Recent developments and adsorption mechanisms, Separation and Purification Technology, 150 (2015) 229-242.

[6] M.T. Yagub, T.K. Sen, S. Afroze, H.M. Ang, Dye and its removal from aqueous solution by adsorption: A review, Advances in Colloid and Interface Science, 209 (2014) 172-184.

[7] V.K. Gupta, Suhas, Application of low-cost adsorbents for dye removal – A review, Journal of Environmental Management, 90 (2009) 2313-2342.

[8] S. Rangabhashiyam, N. Anu, N. Selvaraju, Sequestration of dye from textile industry wastewater using agricultural waste products as adsorbents, Journal of Environmental Chemical Engineering, 1 (2013) 629-641.

[9] W.S. Wan Ngah, L.C. Teong, M.A.K.M. Hanafiah, Adsorption of dyes and heavy

metal ions by chitosan composites: A review, Carbohydrate Polymers, 83 (2011) 1446-1456.

[10] E.N. Zare, A. Motahari, M. Sillanpää, Nanoadsorbents based on conducting polymer nanocomposites with main focus on polyaniline and its derivatives for removal of heavy metal ions/dyes: A review, Environmental Research, 162 (2018) 173-195.

[11] B. Liu, D. Wang, G. Yu, X. Meng, Adsorption of heavy metal ions, dyes and proteins by chitosan composites and derivatives — A review, Journal of Ocean University of China, 12 (2013) 500-508.

[12] S. Afroze, T.K. Sen, A Review on Heavy Metal Ions and Dye Adsorption from Water by Agricultural Solid Waste Adsorbents, Water, air, and soil pollution, 229 (2018) 1-50.

[13] V. Katheresan, J. Kansedo, S.Y. Lau, Efficiency of various recent wastewater dye removal methods: A review, Journal of Environmental Chemical Engineering, 6 (2018) 4676-4697.

[14] A.K. Verma, R.R. Dash, P. Bhunia, A review on chemical coagulation/flocculation technologies for removal of colour from textile wastewaters, Journal of Environmental Management, 93 (2012) 154-168.

[15] M.A.M. Salleh, D.K. Mahmoud, W.A.W.A. Karim, A. Idris, Cationic and anionic dye adsorption by agricultural solid wastes: A comprehensive review, Desalination, 280 (2011) 1-13.

[16] C.X.-H. Su, L.W. Low, T.T. Teng, Y.S. Wong, Combination and hybridisation of treatments in dye wastewater treatment: A review, Journal of Environmental Chemical Engineering, 4 (2016) 3618-3631.

[17] B.E. Barragán, C. Costa, M. Carmen Márquez, Biodegradation of azo dyes by bacteria inoculated on solid media, Dyes and Pigments, 75 (2007) 73-81.

[18] S.-J. You, J.-Y. Teng, Anaerobic decolorization bacteria for the treatment of azo dye in a sequential anaerobic and aerobic membrane bioreactor, Journal of the Taiwan Institute of Chemical Engineers, 40 (2009) 500-504.

[19] A. Ahmad, S.H. Mohd-Setapar, C.S. Chuong, A. Khatoon, W.A. Wani, R. Kumar, M. Rafatullah, Recent advances in new generation dye removal technologies: novel search for approaches to reprocess wastewater, RSC Advances, 5 (2015) 30801-30818.

[20] S.P. Buthelezi, A.O. Olaniran, B. Pillay, Textile dye removal from wastewater effluents using bioflocculants produced by indigenous bacterial isolates, Molecules, 17 (2012) 14260-14274.

[21] F. Fu, Q. Wang, Removal of heavy metal ions from wastewaters: A review, Journal of Environmental Management, 92 (2011) 407-418.

[22] T.A. Khan, E.A. Khan, Shahjahan, Removal of basic dyes from aqueous solution by adsorption onto binary iron-manganese oxide coated kaolinite: Non-linear isotherm and kinetics modeling, Applied Clay Science, 107 (2015) 70-77.

[23] H.K. Shon, S. Phuntsho, D.S. Chaudhary, S. Vigneswaran, J. Cho, Nanofiltration for water and wastewater treatment – a mini review, Drink. Water Eng. Sci., 6 (2013) 47-53.

[24] R.F. Gomes, A.C.N. de Azevedo, A.G.B. Pereira, E.C. Muniz, A.R. Fajardo, F.H.A. Rodrigues, Fast dye removal from water by starch-based nanocomposites, Journal of Colloid and Interface Science, 454 (2015) 200-209.

[25] B. Mu, A. Wang, Adsorption of dyes onto palygorskite and its composites: A review, Journal of Environmental Chemical Engineering, 4 (2016) 1274-1294.

[26] M. Asif Tahir, H.N. Bhatti, M. Iqbal, Solar Red and Brittle Blue direct dyes adsorption onto Eucalyptus angophoroides bark: Equilibrium, kinetics and thermodynamic studies, Journal of Environmental Chemical Engineering, 4 (2016)

2431-2439.

[27] D.T. Cestarolli, A. das Graças de Oliveira, E.M. Guerra, Removal of Eriochrome Black textile dye from aqueous solution by combined electrocoagulation–electroflotation methodology, Applied Water Science, 9 (2019) 101.

[28] E. Pajootan, M. Arami, N.M. Mahmoodi, Binary system dye removal by electrocoagulation from synthetic and real colored wastewaters, Journal of the Taiwan Institute of Chemical Engineers, 43 (2012) 282-290.

[29] S. Moshtaghi, S. Gholamrezaei, M. Salavati Niasari, P. Mehdizadeh, New controllable procedure for preparation of SrSnO3 nanostructures: photo-degradation of azo dyes and photovoltaic measurement, Journal of Materials Science: Materials in Electronics, 27 (2016) 414-424.

[30] Y. Zhou, X. Fang, T. Wang, Y. Hu, J. Lu, Chelating agents enhanced CaO2 oxidation of bisphenol A catalyzed by Fe3+ and reuse of ferric sludge as a source of catalyst, Chemical Engineering Journal, 313 (2017) 638-645.

[31] A.B. dos Santos, F.J. Cervantes, J.B. van Lier, Review paper on current technologies for decolourisation of textile wastewaters: Perspectives for anaerobic biotechnology, Bioresource Technology, 98 (2007) 2369-2385.

[32] J. Wang, X. Wang, G. Zhao, G. Song, D. Chen, H. Chen, J. Xie, T. Hayat, A. Alsaedi, X. Wang, Polyvinylpyrrolidone and polyacrylamide intercalated molybdenum disulfide as adsorbents for enhanced removal of chromium(VI) from aqueous solutions, Chemical Engineering Journal, 334 (2018) 569-578.

[33] A. Bhatnagar, M. Sillanpää, Utilization of agro-industrial and municipal waste materials as potential adsorbents for water treatment—A review, Chemical Engineering Journal, 157 (2010) 277-296.

[34] N.P. Raval, P.U. Shah, N.K. Shah, Adsorptive amputation of hazardous azo dye

Congo red from wastewater: a critical review, Environmental Science and Pollution Research, 23 (2016) 14810-14853.

[35] R.K. Ghosh, D.D. Reddy, Crop Residue Ashes as Adsorbents for Basic Dye (Methylene Blue) Removal: Adsorption Kinetics and Dynamics, CLEAN – Soil, Air, Water, 42 (2014) 1098-1105.

[36] E.I. Unuabonah, A. Taubert, Clay–polymer nanocomposites (CPNs): Adsorbents of the future for water treatment, Applied Clay Science, 99 (2014) 83-92.

[37] J.J.M. Órfão, A.I.M. Silva, J.C.V. Pereira, S.A. Barata, I.M. Fonseca, P.C.C. Faria, M.F.R. Pereira, Adsorption of a reactive dye on chemically modified activated carbons—Influence of pH, Journal of Colloid and Interface Science, 296 (2006) 480-489.

[38] R.K. Gautam, A. Mudhoo, G. Lofrano, M.C. Chattopadhyaya, Biomass-derived biosorbents for metal ions sequestration: Adsorbent modification and activation methods and adsorbent regeneration, Journal of Environmental Chemical Engineering, 2 (2014) 239-259.

[39] Y. Zhu, J. Gao, Y. Li, F. Sun, J. Gao, S. Wu, Y. Qin, Preparation of activated carbons for SO2 adsorption by CO2 and steam activation, Journal of the Taiwan Institute of Chemical Engineers, 43 (2012) 112-119.

[40] R. Baccar, J. Bouzid, M. Feki, A. Montiel, Preparation of activated carbon from Tunisian olive-waste cakes and its application for adsorption of heavy metal ions, Journal of Hazardous Materials, 162 (2009) 1522-1529.

[41] M.M. Karim, A.K. Das, S.H. Lee, Treatment of colored effluent of the textile industry in Bangladesh using zinc chloride treated indigenous activated carbons, Analytica Chimica Acta, 576 (2006) 37-42.

[42] R. Ubago-Pérez, F. Carrasco-Marín, D. Fairén-Jiménez, C. Moreno-Castilla,

Granular and monolithic activated carbons from KOH-activation of olive stones, Microporous and Mesoporous Materials, 92 (2006) 64-70.

[43] P. Sathishkumar, M. Arulkumar, T. Palvannan, Utilization of agro-industrial waste Jatropha curcas pods as an activated carbon for the adsorption of reactive dye Remazol Brilliant Blue R (RBBR), Journal of Cleaner Production, 22 (2012) 67-75.

[44] L. Wu, B. Li, M. Liu, Influence of aromatic structure and substitution of carboxyl groups of aromatic acids on their sorption to biochars, Chemosphere, 210 (2018) 239-246.

[45] M. Choudhary, R. Kumar, S. Neogi, Activated biochar derived from Opuntia ficus-indica for the efficient adsorption of malachite green dye, Cu+2 and Ni+2 from water, Journal of Hazardous Materials, 392 (2020) 122441.

[46] S. Sahu, S. Pahi, S. Tripathy, S.K. Singh, A. Behera, U.K. Sahu, R.K. Patel, Adsorption of methylene blue on chemically modified lychee seed biochar: Dynamic, equilibrium, and thermodynamic study, Journal of Molecular Liquids, 315 (2020) 113743.

[47] S. Chen, C. Qin, T. Wang, F. Chen, X. Li, H. Hou, M. Zhou, Study on the adsorption of dyestuffs with different properties by sludge-rice husk biochar: Adsorption capacity, isotherm, kinetic, thermodynamics and mechanism, Journal of Molecular Liquids, 285 (2019) 62-74.

[48] S. Iijima, Helical microtubules of graphitic carbon, Nature, 354 (1991) 56-58.

[49] H. Dai, Carbon nanotubes: opportunities and challenges, Surface Science, 500 (2002) 218-241.

[50] A. Aqel, K.M.M.A. El-Nour, R.A.A. Ammar, A. Al-Warthan, Carbon nanotubes, science and technology part (I) structure, synthesis and characterisation, Arabian Journal of Chemistry, 5 (2012) 1-23.

[51] A. Eatemadi, H. Daraee, H. Karimkhanloo, M. Kouhi, N. Zarghami, A. Akbarzadeh, M. Abasi, Y. Hanifehpour, S.W. Joo, Carbon nanotubes: properties, synthesis, purification, and medical applications, Nanoscale Research Letters, 9 (2014) 393.

[52] M. Terrones, Science and Technology of the Twenty-First Century: Synthesis, Properties, and Applications of Carbon Nanotubes, Annual Review of Materials Research, 33 (2003) 419-501.

[53] X. Wang, Q. Li, J. Xie, Z. Jin, J. Wang, Y. Li, K. Jiang, S. Fan, Fabrication of Ultralong and Electrically Uniform Single-Walled Carbon Nanotubes on Clean Substrates, Nano Letters, 9 (2009) 3137-3141.

[54] R.H. Baughman, A.A. Zakhidov, W.A. de Heer, Carbon Nanotubes--the Route Toward Applications, Science, 297 (2002) 787.

[55] M.F.L. De Volder, S.H. Tawfick, R.H. Baughman, A.J. Hart, Carbon Nanotubes: Present and Future Commercial Applications, Science, 339 (2013) 535.

[56] L. Ai, J. Jiang, Removal of methylene blue from aqueous solution with self-assembled cylindrical graphene–carbon nanotube hybrid, Chemical Engineering Journal, 192 (2012) 156-163.

[57] Y. Li, Q. Du, T. Liu, X. Peng, J. Wang, J. Sun, Y. Wang, S. Wu, Z. Wang, Y. Xia, L. Xia, Comparative study of methylene blue dye adsorption onto activated carbon, graphene oxide, and carbon nanotubes, Chemical Engineering Research and Design, 91 (2013) 361-368.

[58] Ihsanullah, A. Abbas, A.M. Al-Amer, T. Laoui, M.J. Al-Marri, M.S. Nasser, M. Khraisheh, M.A. Atieh, Heavy metal removal from aqueous solution by advanced carbon nanotubes: Critical review of adsorption applications, Separation and Purification Technology, 157 (2016) 141-161.

[59] S. Gotovac, H. Honda, Y. Hattori, K. Takahashi, H. Kanoh, K. Kaneko, Effect of

Nanoscale Curvature of Single-Walled Carbon Nanotubes on Adsorption of Polycyclic Aromatic Hydrocarbons, Nano Letters, 7 (2007) 583-587.

[60] S. Zhang, T. Shao, S.S.K. Bekaroglu, T. Karanfil, The Impacts of Aggregation and Surface Chemistry of Carbon Nanotubes on the Adsorption of Synthetic Organic Compounds, Environmental Science & Technology, 43 (2009) 5719-5725.

[61] S. Zhang, T. Shao, H.S. Kose, T. Karanfil, Adsorption kinetics of aromatic compounds on carbon nanotubes and activated carbons, Environmental Toxicology and Chemistry, 31 (2012) 79-85.

[62] S. Agnihotri, J.P.B. Mota, M. Rostam-Abadi, M.J. Rood, Theoretical and Experimental Investigation of Morphology and Temperature Effects on Adsorption of Organic Vapors in Single-Walled Carbon Nanotubes, The Journal of Physical Chemistry B, 110 (2006) 7640-7647.

[63] V.K.K. Upadhyayula, S. Deng, M.C. Mitchell, G.B. Smith, Application of carbon nanotube technology for removal of contaminants in drinking water: A review, Science of The Total Environment, 408 (2009) 1-13.

[64] S.S. Fiyadh, M.A. AlSaadi, W.Z. Jaafar, M.K. AlOmar, S.S. Fayaed, N.S. Mohd, L.S. Hin, A. El-Shafie, Review on heavy metal adsorption processes by carbon nanotubes, Journal of Cleaner Production, 230 (2019) 783-793.

[65] M. Rajabi, K. Mahanpoor, O. Moradi, Removal of dye molecules from aqueous solution by carbon nanotubes and carbon nanotube functional groups: critical review, RSC Advances, 7 (2017) 47083-47090.

[66] F. Mashkoor, A. Nasar, Inamuddin, Carbon nanotube-based adsorbents for the removal of dyes from waters: A review, Environmental Chemistry Letters, 18 (2020) 605-629.

[67] M. Ghaedi, H. Khajehsharifi, A.H. Yadkuri, M. Roosta, A. Asghari, Oxidized

multiwalled carbon nanotubes as efficient adsorbent for bromothymol blue, Toxicological & Environmental Chemistry, 94 (2012) 873-883.

[68] K.S. Novoselov, A.K. Geim, S.V. Morozov, D. Jiang, Y. Zhang, S.V. Dubonos, I.V. Grigorieva, A.A. Firsov, Electric Field Effect in Atomically Thin Carbon Films, Science, 306 (2004) 666.

[69] K.P. Loh, Q. Bao, P.K. Ang, J. Yang, The chemistry of graphene, Journal of Materials Chemistry, 20 (2010) 2277-2289.

[70] L.P. Lingamdinne, J.R. Koduru, R.R. Karri, A comprehensive review of applications of magnetic graphene oxide based nanocomposites for sustainable water purification, Journal of Environmental Management, 231 (2019) 622-634.

[71] K.S. Novoselov, V.I. Fal′ko, L. Colombo, P.R. Gellert, M.G. Schwab, K. Kim, A roadmap for graphene, Nature, 490 (2012) 192-200.

[72] J.A. González, M.E. Villanueva, L.L. Piehl, G.J. Copello, Development of a chitin/graphene oxide hybrid composite for the removal of pollutant dyes: Adsorption and desorption study, Chemical Engineering Journal, 280 (2015) 41-48.

[73] B.Y.Z. Hiew, L.Y. Lee, X.J. Lee, S. Thangalazhy-Gopakumar, S. Gan, S.S. Lim, G.-T. Pan, T.C.-K. Yang, W.S. Chiu, P.S. Khiew, Review on synthesis of 3D graphene-based configurations and their adsorption performance for hazardous water pollutants, Process Safety and Environmental Protection, 116 (2018) 262-286.

[74] K. Thakur, B. Kandasubramanian, Graphene and Graphene Oxide-Based Composites for Removal of Organic Pollutants: A Review, Journal of Chemical & Engineering Data, 64 (2019) 833-867.

[75] B.C. Brodie, XIII. On the atomic weight of graphite, Philosophical Transactions of the Royal Society of London, 149 (1859) 249-259.

[76] L. Staudenmaier, Verfahren zur Darstellung der Graphitsäure, Berichte der

deutschen chemischen Gesellschaft, 31 (1898) 1481-1487.

[77] W.S. Hummers, R.E. Offeman, Preparation of Graphitic Oxide, Journal of the American Chemical Society, 80 (1958) 1339-1339.

[78] M.J. McAllister, J.-L. Li, D.H. Adamson, H.C. Schniepp, A.A. Abdala, J. Liu, M. Herrera-Alonso, D.L. Milius, R. Car, R.K. Prud'homme, I.A. Aksay, Single Sheet Functionalized Graphene by Oxidation and Thermal Expansion of Graphite, Chemistry of Materials, 19 (2007) 4396-4404.

[79] Y. Zhu, S. Murali, W. Cai, X. Li, J.W. Suk, J.R. Potts, R.S. Ruoff, Graphene and Graphene Oxide: Synthesis, Properties, and Applications, Advanced Materials, 22 (2010) 3906-3924.

[80] C.K. Chua, M. Pumera, Chemical reduction of graphene oxide: a synthetic chemistry viewpoint, Chemical Society Reviews, 43 (2014) 291-312.

[81] D. Robati, B. Mirza, M. Rajabi, O. Moradi, I. Tyagi, S. Agarwal, V.K. Gupta, Removal of hazardous dyes-BR 12 and methyl orange using graphene oxide as an adsorbent from aqueous phase, Chemical Engineering Journal, 284 (2016) 687-697.

[82] P. Sharma, M.R. Das, Removal of a Cationic Dye from Aqueous Solution Using Graphene Oxide Nanosheets: Investigation of Adsorption Parameters, Journal of Chemical & Engineering Data, 58 (2013) 151-158.

[83] F. Liu, S. Chung, G. Oh, T.S. Seo, Three-Dimensional Graphene Oxide Nanostructure for Fast and Efficient Water-Soluble Dye Removal, ACS Applied Materials & Interfaces, 4 (2012) 922-927.

[84] H. Furukawa, K.E. Cordova, M. O'Keeffe, O.M. Yaghi, The Chemistry and Applications of Metal-Organic Frameworks, Science, 341 (2013) 1230444.

[85] H. Deng, C.J. Doonan, H. Furukawa, R.B. Ferreira, J. Towne, C.B. Knobler, B. Wang, O.M. Yaghi, Multiple Functional Groups of Varying Ratios in Metal-Organic

Frameworks, Science, 327 (2010) 846.

[86] N.A. Khan, Z. Hasan, S.H. Jhung, Adsorptive removal of hazardous materials using metal-organic frameworks (MOFs): A review, Journal of Hazardous Materials, 244-245 (2013) 444-456.

[87] M. Tong, D. Liu, Q. Yang, S. Devautour-Vinot, G. Maurin, C. Zhong, Influence of framework metal ions on the dye capture behavior of MIL-100 (Fe, Cr) MOF type solids, Journal of Materials Chemistry A, 1 (2013) 8534-8537.

[88] P. Silva, S.M.F. Vilela, J.P.C. Tomé, F.A. Almeida Paz, Multifunctional metal–organic frameworks: from academia to industrial applications, Chemical Society Reviews, 44 (2015) 6774-6803.

[89] B. Li, H.-M. Wen, Y. Cui, W. Zhou, G. Qian, B. Chen, Emerging Multifunctional Metal–Organic Framework Materials, Advanced Materials, 28 (2016) 8819-8860.

[90] E. Haque, J.W. Jun, S.H. Jhung, Adsorptive removal of methyl orange and methylene blue from aqueous solution with a metal-organic framework material, iron terephthalate (MOF-235), Journal of Hazardous Materials, 185 (2011) 507-511.

[91] S.-H. Huo, X.-P. Yan, Metal–organic framework MIL-100(Fe) for the adsorption of malachite green from aqueous solution, Journal of Materials Chemistry, 22 (2012) 7449-7455.

[92] N. Ahmad, H.A. Younus, A.H. Chughtai, K. Van Hecke, Z.A.K. Khattak, Z. Gaoke, M. Danish, F. Verpoort, Synthesis of 2D MOF having potential for efficient dye adsorption and catalytic applications, Catalysis Science & Technology, 8 (2018) 4010-4017.

[93] L. Yang, X. Li, C.-Y. Sun, H. Wu, C.-G. Wang, Z.-M. Su, A stable pillared-layer Cu(ii) metal–organic framework with magnetic properties for dye adsorption and separation, New Journal of Chemistry, 41 (2017) 3661-3666.

[94] J. Qiu, X. Zhang, Y. Feng, X. Zhang, H. Wang, J. Yao, Modified metal-organic frameworks as photocatalysts, Applied Catalysis B: Environmental, 231 (2018) 317-342.

[95] J. Hu, H. Yu, W. Dai, X. Yan, X. Hu, H. Huang, Enhanced adsorptive removal of hazardous anionic dye “congo red” by a Ni/Cu mixed-component metal–organic porous material, RSC Advances, 4 (2014) 35124-35130.

[96] J.-M. Yang, R.-J. Ying, C.-X. Han, Q.-T. Hu, H.-M. Xu, J.-H. Li, Q. Wang, W. Zhang, Adsorptive removal of organic dyes from aqueous solution by a Zr-based metal–organic framework: effects of Ce(iii) doping, Dalton Transactions, 47 (2018) 3913-3920.

[97] R. Bibi, L. Wei, Q. Shen, W. Tian, O. Oderinde, N. Li, J. Zhou, Effect of Amino Functionality on the Uptake of Cationic Dye by Titanium-Based Metal Organic Frameworks, Journal of Chemical & Engineering Data, 62 (2017) 1615-1622.

[98] Q. Chen, Q. He, M. Lv, Y. Xu, H. Yang, X. Liu, F. Wei, Selective adsorption of cationic dyes by UiO-66-NH2, Applied Surface Science, 327 (2015) 77-85.

[99] X. Zhao, K. Wang, Z. Gao, H. Gao, Z. Xie, X. Du, H. Huang, Reversing the Dye Adsorption and Separation Performance of Metal–Organic Frameworks via Introduction of −SO3H Groups, Industrial & Engineering Chemistry Research, 56 (2017) 4496-4501.

[100] W. Liang, C.J. Coghlan, F. Ragon, M. Rubio-Martinez, D.M. D'Alessandro, R. Babarao, Defect engineering of UiO-66 for CO2 and H2O uptake – a combined experimental and simulation study, Dalton Transactions, 45 (2016) 4496-4500.

[101] J. Qiu, Y. Feng, X. Zhang, M. Jia, J. Yao, Acid-promoted synthesis of UiO-66 for highly selective adsorption of anionic dyes: Adsorption performance and mechanisms, Journal of Colloid and Interface Science, 499 (2017) 151-158.

[102] K. Wang, C. Li, Y. Liang, T. Han, H. Huang, Q. Yang, D. Liu, C. Zhong, Rational construction of defects in a metal–organic framework for highly efficient adsorption and separation of dyes, Chemical Engineering Journal, 289 (2016) 486-493.

[103] P. Ghosh, Y.J. Colón, R.Q. Snurr, Water adsorption in UiO-66: the importance of defects, Chemical Communications, 50 (2014) 11329-11331.

[104] Y. Feng, Q. Chen, M. Jiang, J. Yao, Tailoring the Properties of UiO-66 through Defect Engineering: A Review, Industrial & Engineering Chemistry Research, 58 (2019) 17646-17659.

[105] H.R. Abuzeid, A.F.M. El-Mahdy, S.-W. Kuo, Covalent organic frameworks: Design principles, synthetic strategies, and diverse applications, Giant, 6 (2021) 100054.

[106] X. Feng, X. Ding, D. Jiang, Covalent organic frameworks, Chemical Society Reviews, 41 (2012) 6010-6022.

[107] P.J. Waller, F. Gándara, O.M. Yaghi, Chemistry of Covalent Organic Frameworks, Accounts of Chemical Research, 48 (2015) 3053-3063.

[108] I. Ahmed, S.H. Jhung, Covalent organic framework-based materials: Synthesis, modification, and application in environmental remediation, Coordination Chemistry Reviews, 441 (2021) 213989.

[109] N. Huang, P. Wang, D. Jiang, Covalent organic frameworks: a materials platform for structural and functional designs, Nature Reviews Materials, 1 (2016) 16068.

[110] C.S. Diercks, O.M. Yaghi, The atom, the molecule, and the covalent organic framework, Science, 355 (2017) eaal1585.

[111] X. Liu, H. Pang, X. Liu, Q. Li, N. Zhang, L. Mao, M. Qiu, B. Hu, H. Yang, X. Wang, Orderly Porous Covalent Organic Frameworks-based Materials: Superior Adsorbents for Pollutants Removal from Aqueous Solutions, The Innovation, 2 (2021) 100076.

[112] N. Zhang, A. Ishag, Y. Li, H. Wang, H. Guo, P. Mei, Q. Meng, Y. Sun, Recent investigations and progress in environmental remediation by using covalent organic framework-based adsorption method: A review, Journal of Cleaner Production, 277 (2020) 123360.

[113] J. Wang, S. Zhuang, Covalent organic frameworks (COFs) for environmental applications, Coordination Chemistry Reviews, 400 (2019) 213046.

[114] M. Afshari, M. Dinari, Synthesis of new imine-linked covalent organic framework as high efficient absorbent and monitoring the removal of direct fast scarlet 4BS textile dye based on mobile phone colorimetric platform, Journal of Hazardous Materials, 385 (2020) 121514.

[115] Y. Li, W. Chen, W. Hao, Y. Li, L. Chen, Covalent Organic Frameworks Constructed from Flexible Building Blocks with High Adsorption Capacity for Pollutants, ACS Applied Nano Materials, 1 (2018) 4756-4761.

[116] J.-Y. Yue, L. Wang, Y. Ma, P. Yang, Y.-Q. Zhang, Y. Jiang, B. Tang, Metal ion-assisted carboxyl-containing covalent organic frameworks for the efficient removal of Congo red, Dalton Transactions, 48 (2019) 17763-17769.

[117] I. Hamed, F. Özogul, J.M. Regenstein, Industrial applications of crustacean by-products (chitin, chitosan, and chitooligosaccharides): A review, Trends in Food Science & Technology, 48 (2016) 40-50.

[118] J. Mo, Q. Yang, N. Zhang, W. Zhang, Y. Zheng, Z. Zhang, A review on agro-industrial waste (AIW) derived adsorbents for water and wastewater treatment, Journal of Environmental Management, 227 (2018) 395-405.

[119] P.S. Bakshi, D. Selvakumar, K. Kadirvelu, N.S. Kumar, Chitosan as an environment friendly biomaterial – a review on recent modifications and applications, International Journal of Biological Macromolecules, 150 (2020) 1072-1083.

[120] A. Bhatnagar, M. Sillanpää, Applications of chitin- and chitosan-derivatives for the detoxification of water and wastewater — A short review, Advances in Colloid and Interface Science, 152 (2009) 26-38.

[121] S. Olivera, H.B. Muralidhara, K. Venkatesh, V.K. Guna, K. Gopalakrishna, Y. Kumar K, Potential applications of cellulose and chitosan nanoparticles/composites in wastewater treatment: A review, Carbohydrate Polymers, 153 (2016) 600-618.

[122] M. Vakili, M. Rafatullah, B. Salamatinia, A.Z. Abdullah, M.H. Ibrahim, K.B. Tan, Z. Gholami, P. Amouzgar, Application of chitosan and its derivatives as adsorbents for dye removal from water and wastewater: A review, Carbohydrate Polymers, 113 (2014) 115-130.

[123] G.L. Dotto, L.A.A. Pinto, Adsorption of food dyes onto chitosan: Optimization process and kinetic, Carbohydrate Polymers, 84 (2011) 231-238.

[124] N.M. Mahmoodi, R. Salehi, M. Arami, H. Bahrami, Dye removal from colored textile wastewater using chitosan in binary systems, Desalination, 267 (2011) 64-72.

[125] M.J. Ahmed, B.H. Hameed, E.H. Hummadi, Review on recent progress in chitosan/chitin-carbonaceous material composites for the adsorption of water pollutants, Carbohydrate Polymers, 247 (2020) 116690.

[126] A. Mirmohseni, M.S. Seyed Dorraji, A. Figoli, F. Tasselli, Chitosan hollow fibers as effective biosorbent toward dye: Preparation and modeling, Bioresource Technology, 121 (2012) 212-220.

[127] K. Azlan, W.N. Wan Saime, L. Lai Ken, Chitosan and chemically modified chitosan beads for acid dyes sorption, Journal of Environmental Sciences, 21 (2009) 296-302.

[128] P.O. Osifo, A. Webster, H. van der Merwe, H.W.J.P. Neomagus, M.A. van der Gun, D.M. Grant, The influence of the degree of cross-linking on the adsorption

properties of chitosan beads, Bioresource Technology, 99 (2008) 7377-7382.

[129] E. Guibal, Interactions of metal ions with chitosan-based sorbents: a review, Separation and Purification Technology, 38 (2004) 43-74.

[130] P. Miretzky, A.F. Cirelli, Hg(II) removal from water by chitosan and chitosan derivatives: A review, Journal of Hazardous Materials, 167 (2009) 10-23.

[131] T. Ngulube, J.R. Gumbo, V. Masindi, A. Maity, An update on synthetic dyes adsorption onto clay based minerals: A state-of-art review, Journal of Environmental Management, 191 (2017) 35-57.

[132] M.K. Uddin, A review on the adsorption of heavy metals by clay minerals, with special focus on the past decade, Chemical Engineering Journal, 308 (2017) 438-462.

[133] A.M. Awad, S.M.R. Shaikh, R. Jalab, M.H. Gulied, M.S. Nasser, A. Benamor, S. Adham, Adsorption of organic pollutants by natural and modified clays: A comprehensive review, Separation and Purification Technology, 228 (2019) 115719.

[134] A. Kausar, M. Iqbal, A. Javed, K. Aftab, Z.-i.-H. Nazli, H.N. Bhatti, S. Nouren, Dyes adsorption using clay and modified clay: A review, Journal of Molecular Liquids, 256 (2018) 395-407.

[135] S. Gu, X. Kang, L. Wang, E. Lichtfouse, C. Wang, Clay mineral adsorbents for heavy metal removal from wastewater: a review, Environmental Chemistry Letters, 17 (2019) 629-654.

[136] J. Ma, Y. Jia, Y. Jing, Y. Yao, J. Sun, Kinetics and thermodynamics of methylene blue adsorption by cobalt-hectorite composite, Dyes and Pigments, 93 (2012) 1441-1446.

[137] H. Chen, J. Zhao, A. Zhong, Y. Jin, Removal capacity and adsorption mechanism of heat-treated palygorskite clay for methylene blue, Chemical engineering journal 174 (2011) 143-150.

[138] E. Da'na, Adsorption of heavy metals on functionalized-mesoporous silica: A review, Microporous and Mesoporous Materials, 247 (2017) 145-157.

[139] M. Kruk, M. Jaroniec, A. Sayari, New insights into pore-size expansion of mesoporous silicates using long-chain amines, Microporous and Mesoporous Materials, 35-36 (2000) 545-553.

[140] R. Kishor, A.K. Ghoshal, APTES grafted ordered mesoporous silica KIT-6 for CO2 adsorption, Chemical Engineering Journal, 262 (2015) 882-890.

[141] K.Y. Ho, G. McKay, K.L. Yeung, Selective Adsorbents from Ordered Mesoporous Silica, Langmuir, 19 (2003) 3019-3024.

[142] V.B. Cashin, D.S. Eldridge, A. Yu, D. Zhao, Surface functionalization and manipulation of mesoporous silica adsorbents for improved removal of pollutants: a review, Environmental Science: Water Research & Technology, 4 (2018) 110-128.

[143] A. Sayari, S. Hamoudi, Y. Yang, Applications of Pore-Expanded Mesoporous Silica. 1. Removal of Heavy Metal Cations and Organic Pollutants from Wastewater, Chemistry of Materials, 17 (2005) 212-216.

[144] C.-H. Huang, K.-P. Chang, H.-D. Ou, Y.-C. Chiang, C.-F. Wang, Adsorption of cationic dyes onto mesoporous silica, Microporous and Mesoporous Materials, 141 (2011) 102-109.

[145] J. Chen, Y. Sheng, Y. Song, M. Chang, X. Zhang, L. Cui, D. Meng, H. Zhu, Z. Shi, H. Zou, Multimorphology Mesoporous Silica Nanoparticles for Dye Adsorption and Multicolor Luminescence Applications, ACS Sustainable Chemistry & Engineering, 6 (2018) 3533-3545.

[146] R. Cui, Y. Lin, J. Qian, Y. Zhu, N. Xu, F. Chen, C. Liu, Z. Wu, Z. Chen, X. Zhou, Two-Dimensional Porous SiO2 Nanostructures Derived from Renewable Petal Cells with Enhanced Adsorption Efficiency for Removal of Hazardous Dye, ACS Sustainable

Chemistry & Engineering, 5 (2017) 3478-3487.

[147] P.N.E. Diagboya, E.D. Dikio, Silica-based mesoporous materials; emerging designer adsorbents for aqueous pollutants removal and water treatment, Microporous and Mesoporous Materials, 266 (2018) 252-267.

[148] S.A. Jadhav, I. Miletto, V. Brunella, G. Berlier, D. Scalarone, Controlled post-synthesis grafting of thermoresponsive poly(N-isopropylacrylamide) on mesoporous silica nanoparticles, Polymers for Advanced Technologies, 26 (2015) 1070-1075.

[149] S. Hozhabr Araghi, M.H. Entezari, Amino-functionalized silica magnetite nanoparticles for the simultaneous removal of pollutants from aqueous solution, Applied Surface Science, 333 (2015) 68-77.

[150] W. Yantasee, R.D. Rutledge, W. Chouyyok, V. Sukwarotwat, G. Orr, C.L. Warner, M.G. Warner, G.E. Fryxell, R.J. Wiacek, C. Timchalk, R.S. Addleman, Functionalized Nanoporous Silica for the Removal of Heavy Metals from Biological Systems: Adsorption and Application, ACS Applied Materials & Interfaces, 2 (2010) 2749-2758.

[151] P. Wang, X. Wang, S. Yu, Y. Zou, J. Wang, Z. Chen, N.S. Alharbi, A. Alsaedi, T. Hayat, Y. Chen, X. Wang, Silica coated Fe3O4 magnetic nanospheres for high removal of organic pollutants from wastewater, Chemical Engineering Journal, 306 (2016) 280-288.

[152] A. Ajmal, I. Majeed, R.N. Malik, H. Idriss, M.A. Nadeem, Principles and mechanisms of photocatalytic dye degradation on TiO2 based photocatalysts: a comparative overview, RSC Advances, 4 (2014) 37003-37026.

[153] D. Chen, Y. Cheng, N. Zhou, P. Chen, Y. Wang, K. Li, S. Huo, P. Cheng, P. Peng, R. Zhang, L. Wang, H. Liu, Y. Liu, R. Ruan, Photocatalytic degradation of organic pollutants using TiO2-based photocatalysts: A review, Journal of Cleaner Production, 268 (2020) 121725.

[154] Q. Guo, C. Zhou, Z. Ma, X. Yang, Fundamentals of TiO2 Photocatalysis: Concepts, Mechanisms, and Challenges, Advanced Materials, 31 (2019) 1901997.

[155] S.-Y. Lee, S.-J. Park, TiO2 photocatalyst for water treatment applications, Journal of Industrial and Engineering Chemistry, 19 (2013) 1761-1769.

[156] R.S. Dariani, A. Esmaeili, A. Mortezaali, S. Dehghanpour, Photocatalytic reaction and degradation of methylene blue on TiO2 nano-sized particles, Optik, 127 (2016) 7143-7154.

[157] J. Thomas, M. Yoon, Facile synthesis of pure TiO2(B) nanofibers doped with gold nanoparticles and solar photocatalytic activities, Applied Catalysis B: Environmental, 111-112 (2012) 502-508.

[158] R. Velmurugan, B. Krishnakumar, B. Subash, M. Swaminathan, Preparation and characterization of carbon nanoparticles loaded TiO2 and its catalytic activity driven by natural sunlight, Solar Energy Materials and Solar Cells, 108 (2013) 205-212.

[159] T.-D. Nguyen-Phan, E.W. Shin, Morphological effect of TiO2 catalysts on photocatalytic degradation of methylene blue, Journal of Industrial and Engineering Chemistry, 17 (2011) 397-400.

[160] B. Abebe, H.C.A. Murthy, E. Amare, Enhancing the photocatalytic efficiency of ZnO: Defects, heterojunction, and optimization, Environmental Nanotechnology, Monitoring & Management, 14 (2020) 100336.

[161] N. Bhattacharjee, I. Som, R. Saha, S. Mondal, A critical review on novel eco-friendly green approach to synthesize zinc oxide nanoparticles for photocatalytic degradation of water pollutants, International Journal of Environmental Analytical Chemistry, (2022) 1-28.

[162] V. Batra, I. Kaur, D. Pathania, Sonu, V. Chaudhary, Efficient dye degradation strategies using green synthesized ZnO-based nanoplatforms: A review, Applied

Surface Science Advances, 11 (2022) 100314.

[163] S. Goktas, A. Goktas, A comparative study on recent progress in efficient ZnO based nanocomposite and heterojunction photocatalysts: A review, Journal of Alloys and Compounds, 863 (2021) 158734.

[164] R. Singh, S. Dutta, The role of pH and nitrate concentration in the wet chemical growth of nano-rods shaped ZnO photocatalyst, Nano-Structures & Nano-Objects, 18 (2019) 100250.

[165] S. Tian, Q. Liu, J. Sun, M. Zhu, S. Wu, X. Zhao, Mesoporous ZnO nanorods array with a controllable area density for enhanced photocatalytic properties, Journal of Colloid and Interface Science, 534 (2019) 389-398.

[166] L. He, Z. Tong, Z. Wang, M. Chen, N. Huang, W. Zhang, Effects of calcination temperature and heating rate on the photocatalytic properties of ZnO prepared by pyrolysis, Journal of Colloid and Interface Science, 509 (2018) 448-456.

[167] Y. Guo, H. Wang, C. He, L. Qiu, X. Cao, Uniform Carbon-Coated ZnO Nanorods: Microwave-Assisted Preparation, Cytotoxicity, and Photocatalytic Activity, Langmuir, 25 (2009) 4678-4684.

[168] K. Kumar, M. Chitkara, I.S. Sandhu, D. Mehta, S. Kumar, Photocatalytic, optical and magnetic properties of Fe-doped ZnO nanoparticles prepared by chemical route, Journal of Alloys and Compounds, 588 (2014) 681-689.

[169] D. Li, J.-F. Huang, L.-Y. Cao, H.-B. OuYang, J.-Y. Li, C.-Y. Yao, Microwave hydrothermal synthesis of K+ doped ZnO nanoparticles with enhanced photocatalytic properties under visible-light, Materials Letters, 118 (2014) 17-20.

[170] X. Liu, K. Chen, J.-J. Shim, J. Huang, Facile synthesis of porous Fe2O3 nanorods and their photocatalytic properties, Journal of Saudi Chemical Society, 19 (2015) 479-484.

[171] C. Chen, F. Duan, S. Zhao, W. Wang, F. Yang, W. Nuansing, B. Zhang, Y. Qin, M. Knez, Porous Fe2O3 nanotubes with α-γ phase junction for enhanced charge separation and photocatalytic property produced by molecular layer deposition, Applied Catalysis B: Environmental, 248 (2019) 218-225.

[172] S. Adhikari, K. Sarath Chandra, D.-H. Kim, G. Madras, D. Sarkar, Understanding the morphological effects of WO3 photocatalysts for the degradation of organic pollutants, Advanced Powder Technology, 29 (2018) 1591-1600.

[173] D. Chen, J. Ye, Hierarchical WO3 Hollow Shells: Dendrite, Sphere, Dumbbell, and Their Photocatalytic Properties, Advanced Functional Materials, 18 (2008) 1922-1928.

[174] M. Dhanalakshmi, S. Lakshmi Prabavathi, K. Saravanakumar, B. Filip Jones, V. Muthuraj, Iridium nanoparticles anchored WO3 nanocubes as an efficient photocatalyst for removal of refractory contaminants (crystal violet and methylene blue), Chemical Physics Letters, 745 (2020) 137285.

[175] Y. Zheng, G. Chen, Y. Yu, Y. Zhou, F. He, Synthesis of carbon doped WO3·0.33H2O hierarchical photocatalyst with improved photocatalytic activity, Applied Surface Science, 362 (2016) 182-190.

[176] S. Zhang, C. Hu, H. Ji, L. Zhang, F. Li, Facile synthesis of nitrogen-deficient mesoporous graphitic carbon nitride for highly efficient photocatalytic performance, Applied Surface Science, 478 (2019) 304-312.

[177] Y. Chen, F. Ding, A. Khaing, D. Yang, Z. Jiang, Acetic acid-assisted supramolecular assembly synthesis of porous g-C3N4 hexagonal prism with excellent photocatalytic activity, Applied Surface Science, 479 (2019) 757-764.

[178] Y. Wang, Y. Wang, Y. Li, H. Shi, Y. Xu, H. Qin, X. Li, Y. Zuo, S. Kang, L. Cui, Simple synthesis of Zr-doped graphitic carbon nitride towards enhanced photocatalytic

performance under simulated solar light irradiation, Catalysis Communications, 72 (2015) 24-28.

[179] W. Jiang, X. Yin, F. Xin, Y. Bi, Y. Liu, X. Li, Preparation of CdIn2S4 microspheres and application for photocatalytic reduction of carbon dioxide, Applied Surface Science, 288 (2014) 138-142.

[180] J. Abdi, M. Vossoughi, N.M. Mahmoodi, I. Alemzadeh, Synthesis of metal-organic framework hybrid nanocomposites based on GO and CNT with high adsorption capacity for dye removal, Chemical Engineering Journal, 326 (2017) 1145-1158.

[181] T. Ghanbari, F. Abnisa, W.M.A. Wan Daud, A review on production of metal organic frameworks (MOF) for CO2 adsorption, Science of The Total Environment, 707 (2020) 135090.

[182] X. Liu, G. Verma, Z. Chen, B. Hu, Q. Huang, H. Yang, S. Ma, X. Wang, Metal-organic framework nanocrystal-derived hollow porous materials: Synthetic strategies and emerging applications, The Innovation, 3 (2022) 100281.

[183] T.-T. Li, Y.-M. Liu, T. Wang, Y.-L. Wu, Y.-L. He, R. Yang, S.-R. Zheng, Regulation of the surface area and surface charge property of MOFs by multivariate strategy: Synthesis, characterization, selective dye adsorption and separation, Microporous and Mesoporous Materials, 272 (2018) 101-108.

[184] S.-Y. Fang, P. Zhang, J.-L. Gong, L. Tang, G.-M. Zeng, B. Song, W.-C. Cao, J. Li, J. Ye, Construction of highly water-stable metal-organic framework UiO-66 thin-film composite membrane for dyes and antibiotics separation, Chemical Engineering Journal, 385 (2020) 123400.

[185] W. Dong, D. Wang, H. Wang, M. Li, F. Chen, F. Jia, Q. Yang, X. Li, X. Yuan, J. Gong, H. Li, J. Ye, Facile synthesis of In2S3/UiO-66 composite with enhanced adsorption performance and photocatalytic activity for the removal of tetracycline

under visible light irradiation, Journal of Colloid and Interface Science, 535 (2019) 444-457.

[186] Z. Liang, C. Qu, W. Guo, R. Zou, Q. Xu, Pristine Metal–Organic Frameworks and their Composites for Energy Storage and Conversion, Advanced Materials, 30 (2018) 1702891.

[187] H.D. Lawson, S.P. Walton, C. Chan, Metal–Organic Frameworks for Drug Delivery: A Design Perspective, ACS Applied Materials & Interfaces, 13 (2021) 7004-7020.

[188] R. Hu, X. Zhang, K.-N. Chi, T. Yang, Y.-H. Yang, Bifunctional MOFs-Based Ratiometric Electrochemical Sensor for Multiplex Heavy Metal Ions, ACS Applied Materials & Interfaces, 12 (2020) 30770-30778.

[189] G.C. Shearer, J.G. Vitillo, S. Bordiga, S. Svelle, U. Olsbye, K.P. Lillerud, Functionalizing the Defects: Postsynthetic Ligand Exchange in the Metal Organic Framework UiO-66, Chemistry of Materials, 28 (2016) 7190-7193.

[190] F. Ahmadijokani, H. Molavi, M. Rezakazemi, S. Tajahmadi, A. Bahi, F. Ko, T.M. Aminabhavi, J.-R. Li, M. Arjmand, UiO-66 metal–organic frameworks in water treatment: A critical review, Progress in Materials Science, 125 (2022) 100904.

[191] R.M. Rego, M.D. Kurkuri, M. Kigga, A comprehensive review on water remediation using UiO-66 MOFs and their derivatives, Chemosphere, 302 (2022) 134845.

[192] Z. Hasan, N.A. Khan, S.H. Jhung, Adsorptive removal of diclofenac sodium from water with Zr-based metal–organic frameworks, Chemical Engineering Journal, 284 (2016) 1406-1413.

[193] S. Das, P. Heasman, T. Ben, S. Qiu, Porous Organic Materials: Strategic Design and Structure–Function Correlation, Chemical Reviews, 117 (2017) 1515-1563.

[194] P. Hu, Z. Zhao, X. Sun, Y. Muhammad, J. Li, S. Chen, C. Pang, T. Liao, Z. Zhao, Construction of crystal defect sites in N-coordinated UiO-66 via mechanochemical in-situ N-doping strategy for highly selective adsorption of cationic dyes, Chemical Engineering Journal, 356 (2019) 329-340.

[195] Y. Han, M. Liu, K. Li, Q. Sun, W. Zhang, C. Song, G. Zhang, Z. Conrad Zhang, X. Guo, In situ synthesis of titanium doped hybrid metal–organic framework UiO-66 with enhanced adsorption capacity for organic dyes, Inorganic Chemistry Frontiers, 4 (2017) 1870-1880.

[196] Z.-h. Yang, J. Cao, Y.-p. Chen, X. Li, W.-p. Xiong, Y.-y. Zhou, C.-y. Zhou, R. Xu, Y.-r. Zhang, Mn-doped zirconium metal-organic framework as an effective adsorbent for removal of tetracycline and Cr(VI) from aqueous solution, Microporous and Mesoporous Materials, 277 (2019) 277-285.

[197] J. Cao, Z.-h. Yang, W.-p. Xiong, Y.-y. Zhou, Y.-r. Peng, X. Li, C.-y. Zhou, R. Xu, Y.-r. Zhang, One-step synthesis of Co-doped UiO-66 nanoparticle with enhanced removal efficiency of tetracycline: Simultaneous adsorption and photocatalysis, Chemical Engineering Journal, 353 (2018) 126-137.

[198] C. Chen, D. Chen, S. Xie, H. Quan, X. Luo, L. Guo, Adsorption Behaviors of Organic Micropollutants on Zirconium Metal–Organic Framework UiO-66: Analysis of Surface Interactions, ACS Applied Materials & Interfaces, 9 (2017) 41043-41054.

[199] C.A. Trickett, K.J. Gagnon, S. Lee, F. Gándara, H.-B. Bürgi, O.M. Yaghi, Definitive Molecular Level Characterization of Defects in UiO-66 Crystals, Angewandte Chemie International Edition, 54 (2015) 11162-11167.

[200] Y. Bai, Y. Dou, L.-H. Xie, W. Rutledge, J.-R. Li, H.-C. Zhou, Zr-based metal–organic frameworks: design, synthesis, structure, and applications, Chemical Society Reviews, 45 (2016) 2327-2367.

[201] S.M. Prabhu, C. Chuaicham, C.M. Park, B.-H. Jeon, K. Sasaki, Synthesis and characterization of defective UiO-66 for efficient co-immobilization of arsenate and fluoride from single/binary solutions, Environmental Pollution, 278 (2021) 116841.

[202] H. Molavi, A. Hakimian, A. Shojaei, M. Raeiszadeh, Selective dye adsorption by highly water stable metal-organic framework: Long term stability analysis in aqueous media, Applied Surface Science, 445 (2018) 424-436.

[203] A.M. Ebrahim, T.J. Bandosz, Ce(III) Doped Zr-Based MOFs as Excellent NO2 Adsorbents at Ambient Conditions, ACS Applied Materials & Interfaces, 5 (2013) 10565-10573.

[204] Y. Wang, N. Zhang, D. Chen, D. Ma, G. Liu, X. Zou, Y. Chen, R. Shu, Q. Song, W. Lv, Facile synthesis of acid-modified UiO-66 to enhance the removal of Cr(VI) from aqueous solutions, Science of The Total Environment, 682 (2019) 118-127.

[205] A. Zhang, B. Liu, M. Liu, Z. Xie, D. Wang, G. Feng, The adsorption properties of defect controlled metal-organic frameworks of UiO-66, Separation and Purification Technology, 270 (2021) 118842.

[206] C.-Y. Wang, Y.-J. Zhang, W.-K. Wang, D.-N. Pei, G.-X. Huang, J.-J. Chen, X. Zhang, H.-Q. Yu, Enhanced photocatalytic degradation of bisphenol A by Co-doped BiOCl nanosheets under visible light irradiation, Applied Catalysis B: Environmental, 221 (2018) 320-328.

[207] Z. Ding, X. Chen, M. Antonietti, X. Wang, Synthesis of Transition Metal-Modified Carbon Nitride Polymers for Selective Hydrocarbon Oxidation, ChemSusChem, 4 (2011) 274-281.

[208] A.S. Eltaweil, H.M. Elshishini, Z.F. Ghatass, G.M. Elsubruiti, Ultra-high adsorption capacity and selective removal of Congo red over aminated graphene oxide modified Mn-doped UiO-66 MOF, Powder Technology, 379 (2021) 407-416.

[209] J. Lyu, H. Liu, Z. Zeng, J. Zhang, Z. Xiao, P. Bai, X. Guo, Metal–Organic Framework UiO-66 as an Efficient Adsorbent for Boron Removal from Aqueous Solution, Industrial & Engineering Chemistry Research, 56 (2017) 2565-2572.

[210] S. Zhuang, R. Cheng, J. Wang, Adsorption of diclofenac from aqueous solution using UiO-66-type metal-organic frameworks, Chemical Engineering Journal, 359 (2019) 354-362.

[211] L. Fu, S. Wang, G. Lin, L. Zhang, Q. Liu, J. Fang, C. Wei, G. Liu, Post-functionalization of UiO-66-NH2 by 2,5-Dimercapto-1,3,4-thiadiazole for the high efficient removal of Hg(II) in water, Journal of Hazardous Materials, 368 (2019) 42-51.

[212] L. Zeng, L. Xiao, Y. Long, X. Shi, Trichloroacetic acid-modulated synthesis of polyoxometalate@UiO-66 for selective adsorption of cationic dyes, Journal of Colloid and Interface Science, 516 (2018) 274-283.

[213] F. Ahmadijokani, S. Tajahmadi, M.H. Haris, A. Bahi, M. Rezakazemi, H. Molavi, F. Ko, M. Arjmand, Fe3O4@PAA@UiO-66-NH2 magnetic nanocomposite for selective adsorption of Quercetin, Chemosphere, 275 (2021) 130087.

[214] C.A. Clark, K.N. Heck, C.D. Powell, M.S. Wong, Highly Defective UiO-66 Materials for the Adsorptive Removal of Perfluorooctanesulfonate, ACS Sustainable Chemistry & Engineering, 7 (2019) 6619-6628.

[215] M.R. Azhar, H.R. Abid, V. Periasamy, H. Sun, M.O. Tade, S. Wang, Adsorptive removal of antibiotic sulfonamide by UiO-66 and ZIF-67 for wastewater treatment, Journal of Colloid and Interface Science, 500 (2017) 88-95.

[216] Q. Yang, Y. Wang, J. Wang, F. Liu, N. Hu, H. Pei, W. Yang, Z. Li, Y. Suo, J. Wang, High effective adsorption/removal of illegal food dyes from contaminated aqueous solution by Zr-MOFs (UiO-67), Food Chemistry, 254 (2018) 241-248.

[217] Y. Jiao, Y. Liu, G. Zhu, J.T. Hungerford, S. Bhattacharyya, R.P. Lively, D.S. Sholl,

K.S. Walton, Heat-Treatment of Defective UiO-66 from Modulated Synthesis: Adsorption and Stability Studies, The Journal of Physical Chemistry C, 121 (2017) 23471-23479.

[218] A. Jamali, F. Shemirani, A. Morsali, A comparative study of adsorption and removal of organophosphorus insecticides from aqueous solution by Zr-based MOFs, Journal of Industrial and Engineering Chemistry, 80 (2019) 83-92.

[219] Y. Gao, K. Liu, R. Kang, J. Xia, G. Yu, S. Deng, A comparative study of rigid and flexible MOFs for the adsorption of pharmaceuticals: Kinetics, isotherms and mechanisms, Journal of Hazardous Materials, 359 (2018) 248-257.

[220] S. Zaboon, H.R. Abid, Z. Yao, R. Gubner, S. Wang, A. Barifcani, Removal of monoethylene glycol from wastewater by using Zr-metal organic frameworks, Journal of Colloid and Interface Science, 523 (2018) 75-85.

[221] S. Huang, H. Pang, L. Li, S. Jiang, T. Wen, L. Zhuang, B. Hu, X. Wang, Unexpected ultrafast and high adsorption of U(VI) and Eu(III) from solution using porous Al2O3 microspheres derived from MIL-53, Chemical Engineering Journal, 353 (2018) 157-166.

[222] S.-W. Lv, J.-M. Liu, H. Ma, Z.-H. Wang, C.-Y. Li, N. Zhao, S. Wang, Simultaneous adsorption of methyl orange and methylene blue from aqueous solution using amino functionalized Zr-based MOFs, Microporous and Mesoporous Materials, 282 (2019) 179-187.

[223] S.N. Tambat, P.K. Sane, S. Suresh, N. Varadan O, A.B. Pandit, S.M. Sontakke, Hydrothermal synthesis of NH2-UiO-66 and its application for adsorptive removal of dye, Advanced Powder Technology, 29 (2018) 2626-2632.

[224] J. Tang, J. Zhao, S. Wang, L. Zhang, M. Zhao, Z. Huang, Y. Hu, Pre-modification strategy to prepare a novel Zr-based MOF for selective adsorption of Palladium(II) from

solution, Chemical Engineering Journal, 407 (2021) 127223.

[225] J. Wu, J. Zhou, S. Zhang, A. Alsaedi, T. Hayat, J. Li, Y. Song, Efficient removal of metal contaminants by EDTA modified MOF from aqueous solutions, Journal of Colloid and Interface Science, 555 (2019) 403-412.

[226] W. Qu, T. Yuan, G. Yin, S. Xu, Q. Zhang, H. Su, Effect of properties of activated carbon on malachite green adsorption, Fuel, 249 (2019) 45-53.

[227] L. Leng, X. Yuan, G. Zeng, J. Shao, X. Chen, Z. Wu, H. Wang, X. Peng, Surface characterization of rice husk bio-char produced by liquefaction and application for cationic dye (Malachite green) adsorption, Fuel, 155 (2015) 77-85.

[228] Z. Shi, L. Li, Y. Xiao, Y. Wang, K. Sun, H. Wang, L. Liu, Synthesis of mixed-ligand Cu–MOFs and their adsorption of malachite green, RSC Advances, 7 (2017) 30904-30910.

[229] F. Jiang, D.M. Dinh, Y.-L. Hsieh, Adsorption and desorption of cationic malachite green dye on cellulose nanofibril aerogels, Carbohydrate Polymers, 173 (2017) 286-294.

[230] M. Mobarak, E.A. Mohamed, A.Q. Selim, M.F. Eissa, M.K. Seliem, Experimental results and theoretical statistical modeling of malachite green adsorption onto MCM–41 silica/rice husk composite modified by beta radiation, Journal of Molecular Liquids, 273 (2019) 68-82.

[231] Z. Shi, C. Xu, H. Guan, L. Li, L. Fan, Y. Wang, L. Liu, Q. Meng, R. Zhang, Magnetic metal organic frameworks (MOFs) composite for removal of lead and malachite green in wastewater, Colloids and Surfaces A: Physicochemical and Engineering Aspects, 539 (2018) 382-390.

[232] C. Li, Z. Xiong, J. Zhang, C. Wu, The Strengthening Role of the Amino Group in Metal–Organic Framework MIL-53 (Al) for Methylene Blue and Malachite Green Dye

Adsorption, Journal of Chemical & Engineering Data, 60 (2015) 3414-3422.

[233] L. Sun, S. Hu, H. Sun, H. Guo, H. Zhu, M. Liu, H. Sun, Malachite green adsorption onto Fe3O4@SiO2-NH2: isotherms, kinetic and process optimization, RSC Advances, 5 (2015) 11837-11844.

[234] A.A. Alqadami, M. Naushad, Z.A. Alothman, T. Ahamad, Adsorptive performance of MOF nanocomposite for methylene blue and malachite green dyes: Kinetics, isotherm and mechanism, Journal of Environmental Management, 223 (2018) 29-36.

[235] W. Xiao, Z.N. Garba, S. Sun, I. Lawan, L. Wang, M. Lin, Z. Yuan, Preparation and evaluation of an effective activated carbon from white sugar for the adsorption of rhodamine B dye, Journal of Cleaner Production, 253 (2020) 119989.

[236] Z.-L. Cheng, Y.-X. Li, Z. Liu, Novel adsorption materials based on graphene oxide/Beta zeolite composite materials and their adsorption performance for rhodamine B, Journal of Alloys and Compounds, 708 (2017) 255-263.

[237] S.H. Alwan, H.A.H. Alshamsi, L.S. Jasim, Rhodamine B removal on A-rGO/cobalt oxide nanoparticles composite by adsorption from contaminated water, Journal of Molecular Structure, 1161 (2018) 356-365.

[238] S. Wang, B. Yang, Y. Liu, Synthesis of a hierarchical SnS2 nanostructure for efficient adsorption of Rhodamine B dye, Journal of Colloid and Interface Science, 507 (2017) 225-233.

[239] M.A. Nazir, M.S. Bashir, M. Jamshaid, A. Anum, T. Najam, K. Shahzad, M. Imran, S.S.A. Shah, A.u. Rehman, Synthesis of porous secondary metal-doped MOFs for removal of Rhodamine B from water: Role of secondary metal on efficiency and kinetics, Surfaces and Interfaces, 25 (2021) 101261.

[240] H. Deng, Z. Mao, H. Xu, L. Zhang, Y. Zhong, X. Sui, Synthesis of fibrous LaFeO3

perovskite oxide for adsorption of Rhodamine B, Ecotoxicology and Environmental Safety, 168 (2019) 35-44.

[241] C. Yang, J. Cheng, Y. Chen, Y. Hu, Enhanced adsorption performance of MoS2 nanosheet-coated MIL-101 hybrids for the removal of aqueous rhodamine B, Journal of Colloid and Interface Science, 504 (2017) 39-47.

[242] W. Cui, X. Kang, X. Zhang, X. Cui, Gel-like ZnO/Zr-MOF(bpy) nanocomposite for highly efficient adsorption of Rhodamine B dye from aqueous solution, Journal of Physics and Chemistry of Solids, 134 (2019) 165-175.

[243] Y. Zhang, K. Li, J. Liao, Facile synthesis of reduced-graphene-oxide/rare-earth-metal-oxide aerogels as a highly efficient adsorbent for Rhodamine-B, Applied Surface Science, 504 (2020) 144377.

[244] Y. Zhang, J. Zhou, W. Cai, J. Zhou, Z. Li, Enhanced photocatalytic performance and degradation pathway of Rhodamine B over hierarchical double-shelled zinc nickel oxide hollow sphere heterojunction, Applied Surface Science, 430 (2018) 549-560.

[245] Z. Li, S. Wang, J. Wu, W. Zhou, Recent progress in defective TiO2 photocatalysts for energy and environmental applications, Renewable and Sustainable Energy Reviews, 156 (2022) 111980.

[246] Z. Mirzaeifard, Z. Shariatinia, M. Jourshabani, S.M. Rezaei Darvishi, ZnO Photocatalyst Revisited: Effective Photocatalytic Degradation of Emerging Contaminants Using S-Doped ZnO Nanoparticles under Visible Light Radiation, Industrial & Engineering Chemistry Research, 59 (2020) 15894-15911.

[247] S. Velanganni, S. Pravinraj, P. Immanuel, R. Thiruneelakandan, Nanostructure CdS/ZnO heterojunction configuration for photocatalytic degradation of Methylene blue, Physica B: Condensed Matter, 534 (2018) 56-62.

[248] M.F.R. Samsudin, S. Sufian, B.H. Hameed, Epigrammatic progress and

perspective on the photocatalytic properties of BiVO4-based photocatalyst in photocatalytic water treatment technology: A review, Journal of Molecular Liquids, 268 (2018) 438-459.

[249] Z. Wang, B. Mi, Environmental Applications of 2D Molybdenum Disulfide (MoS2) Nanosheets, Environmental Science & Technology, 51 (2017) 8229-8244.

[250] C.H. Nguyen, C.-C. Fu, R.-S. Juang, Degradation of methylene blue and methyl orange by palladium-doped TiO2 photocatalysis for water reuse: Efficiency and degradation pathways, Journal of Cleaner Production, 202 (2018) 413-427.

[251] J. Zhang, Z. Zhang, W. Zhu, X. Meng, Boosted photocatalytic degradation of Rhodamine B pollutants with Z-scheme CdS/AgBr-rGO nanocomposite, Applied Surface Science, 502 (2020) 144275.

[252] M.M. Sajid, N. Amin, N.A. Shad, S.B. khan, Y. Javed, Z. Zhang, Hydrothermal fabrication of monoclinic bismuth vanadate (m-BiVO4) nanoparticles for photocatalytic degradation of toxic organic dyes, Materials Science and Engineering: B, 242 (2019) 83-89.

[253] F. Dong, Z. Zhao, T. Xiong, Z. Ni, W. Zhang, Y. Sun, W.-K. Ho, In Situ Construction of g-C3N4/g-C3N4 Metal-Free Heterojunction for Enhanced Visible-Light Photocatalysis, ACS Applied Materials & Interfaces, 5 (2013) 11392-11401.

[254] H. Chen, T. Liu, Y. Meng, Y. Cheng, J. Lu, H. Wang, Novel graphene oxide/aminated lignin aerogels for enhanced adsorption of malachite green in wastewater, Colloids and Surfaces A: Physicochemical and Engineering Aspects, 603 (2020) 125281.

[255] Q. Zhu, Z. Xu, B. Qiu, M. Xing, J. Zhang, Emerging Cocatalysts on g-C3N4 for Photocatalytic Hydrogen Evolution, Small, 17 (2021) 2101070.

[256] M. Aggarwal, S. Basu, N.P. Shetti, M.N. Nadagouda, E.E. Kwon, Y.-K. Park, T.M.

Aminabhavi, Photocatalytic carbon dioxide reduction: Exploring the role of ultrathin 2D graphitic carbon nitride (g-C3N4), Chemical Engineering Journal, 425 (2021) 131402.

[257] X. Liu, R. Ma, L. Zhuang, B. Hu, J. Chen, X. Liu, X. Wang, Recent developments of doped g-C3N4 photocatalysts for the degradation of organic pollutants, Critical Reviews in Environmental Science and Technology, 51 (2021) 751-790.

[258] R.-t. Guo, J. Wang, Z.-x. Bi, X. Chen, X. Hu, W.-g. Pan, Recent advances and perspectives of g–C3N4–based materials for photocatalytic dyes degradation, Chemosphere, 295 (2022) 133834.

[259] X. Yuan, C. Zhou, Y. Jin, Q. Jing, Y. Yang, X. Shen, Q. Tang, Y. Mu, A.-K. Du, Facile synthesis of 3D porous thermally exfoliated g-C3N4 nanosheet with enhanced photocatalytic degradation of organic dye, Journal of Colloid and Interface Science, 468 (2016) 211-219.

[260] U. Ghosh, A. Pal, Defect engineered mesoporous 2D graphitic carbon nitride nanosheet photocatalyst for rhodamine B degradation under LED light illumination, Journal of Photochemistry and Photobiology A: Chemistry, 397 (2020) 112582.

[261] J. Wen, J. Xie, X. Chen, X. Li, A review on g-C3N4-based photocatalysts, Applied Surface Science, 391 (2017) 72-123.

[262] Y. Li, X. Li, H. Zhang, J. Fan, Q. Xiang, Design and application of active sites in g-C3N4-based photocatalysts, Journal of Materials Science & Technology, 56 (2020) 69-88.

[263] M. Ismael, A review on graphitic carbon nitride (g-C3N4) based nanocomposites: Synthesis, categories, and their application in photocatalysis, Journal of Alloys and Compounds, 846 (2020) 156446.

[264] Z. Chen, S. Zhang, Y. Liu, N.S. Alharbi, S.O. Rabah, S. Wang, X. Wang, Synthesis

and fabrication of g-C3N4-based materials and their application in elimination of pollutants, Science of The Total Environment, 731 (2020) 139054.

[265] J. Wang, S. Wang, A critical review on graphitic carbon nitride (g-C3N4)-based materials: Preparation, modification and environmental application, Coordination Chemistry Reviews, 453 (2022) 214338.

[266] N. Tian, Y. Zhang, X. Li, K. Xiao, X. Du, F. Dong, G.I.N. Waterhouse, T. Zhang, H. Huang, Precursor-reforming protocol to 3D mesoporous g-C3N4 established by ultrathin self-doped nanosheets for superior hydrogen evolution, Nano Energy, 38 (2017) 72-81.

[267] P. Xia, B. Zhu, J. Yu, S. Cao, M. Jaroniec, Ultra-thin nanosheet assemblies of graphitic carbon nitride for enhanced photocatalytic CO2 reduction, Journal of Materials Chemistry A, 5 (2017) 3230-3238.

[268] X. Fan, Z. Xing, Z. Shu, L. Zhang, L. Wang, J. Shi, Improved photocatalytic activity of g-C3N4 derived from cyanamide–urea solution, RSC Advances, 5 (2015) 8323-8328.

[269] H. Yu, R. Shi, Y. Zhao, T. Bian, Y. Zhao, C. Zhou, G.I.N. Waterhouse, L.-Z. Wu, C.-H. Tung, T. Zhang, Alkali-Assisted Synthesis of Nitrogen Deficient Graphitic Carbon Nitride with Tunable Band Structures for Efficient Visible-Light-Driven Hydrogen Evolution, Advanced Materials, 29 (2017) 1605148.

[270] J. Xu, L. Zhang, R. Shi, Y. Zhu, Chemical exfoliation of graphitic carbon nitride for efficient heterogeneous photocatalysis, Journal of Materials Chemistry A, 1 (2013) 14766-14772.

[271] Y. Shi, J. Chen, Z. Mao, B.D. Fahlman, D. Wang, Construction of Z-scheme heterostructure with enhanced photocatalytic H2 evolution for g-C3N4 nanosheets via loading porous silicon, Journal of Catalysis, 356 (2017) 22-31.

[272] Q. Fan, J. Liu, Y. Yu, S. Zuo, B. Li, A simple fabrication for sulfur doped graphitic carbon nitride porous rods with excellent photocatalytic activity degrading RhB dye, Applied Surface Science, 391 (2017) 360-368.

[273] J. Fu, B. Zhu, C. Jiang, B. Cheng, W. You, J. Yu, Hierarchical Porous O-Doped g-C3N4 with Enhanced Photocatalytic CO2 Reduction Activity, Small, 13 (2017) 1603938.

[274] L. Shi, L. Liang, F. Wang, M. Liu, S. Zhong, J. Sun, Tetraethylorthosilicate induced preparation of mesoporous graphitic carbon nitride with improved visible light photocatalytic activity, Catalysis Communications, 59 (2015) 131-135.

[275] Y. Shiraishi, Y. Kofuji, H. Sakamoto, S. Tanaka, S. Ichikawa, T. Hirai, Effects of Surface Defects on Photocatalytic H2O2 Production by Mesoporous Graphitic Carbon Nitride under Visible Light Irradiation, ACS Catalysis, 5 (2015) 3058-3066.

[276] Y. Zhu, M. Zhu, L. Kang, F. Yu, B. Dai, Phosphotungstic Acid Supported on Mesoporous Graphitic Carbon Nitride as Catalyst for Oxidative Desulfurization of Fuel, Industrial & Engineering Chemistry Research, 54 (2015) 2040-2047.

[277] C. Wang, Y. Xue, P. Wang, Y. Ao, Effects of water environmental factors on the photocatalytic degradation of sulfamethoxazole by AgI/UiO-66 composite under visible light irradiation, Journal of Alloys and Compounds, 748 (2018) 314-322.

[278] J. Zhang, M. Zhang, R.-Q. Sun, X. Wang, A Facile Band Alignment of Polymeric Carbon Nitride Semiconductors to Construct Isotype Heterojunctions, Angewandte Chemie International Edition, 51 (2012) 10145-10149.

[279] J.M. Yassin, A.M. Taddesse, M. Sánchez-Sánchez, Sustainable synthesis of semicrystalline Zr-BDC MOF and heterostructural Ag3PO4/Zr-BDC/g-C3N4 composite for photocatalytic dye degradation, Catalysis Today, 390-391 (2022) 162-175.

[280] Y. Guo, Q. Liu, Z. Li, Z. Zhang, X. Fang, Enhanced photocatalytic hydrogen evolution performance of mesoporous graphitic carbon nitride co-doped with potassium and iodine, Applied Catalysis B: Environmental, 221 (2018) 362-370.

[281] M. Razavi-Esfali, T. Mahvelati-Shamsabadi, H. Fattahimoghaddam, B.-K. Lee, Highly efficient photocatalytic degradation of organic pollutants by mesoporous graphitic carbon nitride bonded with cyano groups, Chemical Engineering Journal, 419 (2021) 129503.

[282] J. Liu, H. Xu, Y. Xu, Y. Song, J. Lian, Y. Zhao, L. Wang, L. Huang, H. Ji, H. Li, Graphene quantum dots modified mesoporous graphite carbon nitride with significant enhancement of photocatalytic activity, Applied Catalysis B: Environmental, 207 (2017) 429-437.

[283] S. Fang, K. Lv, Q. Li, H. Ye, D. Du, M. Li, Effect of acid on the photocatalytic degradation of rhodamine B over g-C3N4, Applied Surface Science, 358 (2015) 336-342.

[284] W. Li, Z. Wang, Y. Li, J.B. Ghasemi, J. Li, G. Zhang, Visible-NIR light-responsive 0D/2D CQDs/Sb2WO6 nanosheets with enhanced photocatalytic degradation performance of RhB: Unveiling the dual roles of CQDs and mechanism study, Journal of Hazardous Materials, 424 (2022) 127595.

[285] S. Nayak, G. Swain, K. Parida, Enhanced Photocatalytic Activities of RhB Degradation and H2 Evolution from in Situ Formation of the Electrostatic Heterostructure MoS2/NiFe LDH Nanocomposite through the Z-Scheme Mechanism via p–n Heterojunctions, ACS Applied Materials & Interfaces, 11 (2019) 20923-20942.

[286] P. Nuengmatcha, S. Chanthai, R. Mahachai, W.-C. Oh, Visible light-driven photocatalytic degradation of rhodamine B and industrial dyes (texbrite BAC-L and texbrite NFW-L) by ZnO-graphene-TiO2 composite, Journal of Environmental

Chemical Engineering, 4 (2016) 2170-2177.

[287] Q.W. Cao, Y.F. Zheng, X.C. Song, Enhanced visible-light-driven photocatalytic degradation of RhB by AgIO3/WO3 composites, Journal of the Taiwan Institute of Chemical Engineers, 70 (2017) 359-365.

[288] J. Abdi, M. Yahyanezhad, S. Sakhaie, M. Vossoughi, I. Alemzadeh, Synthesis of porous TiO2/ZrO2 photocatalyst derived from zirconium metal organic framework for degradation of organic pollutants under visible light irradiation, Journal of Environmental Chemical Engineering, 7 (2019) 103096.

[289] Q. Fan, Y. Huang, C. Zhang, J. Liu, L. Piao, Y. Yu, S. Zuo, B. Li, Superior nanoporous graphitic carbon nitride photocatalyst coupled with CdS quantum dots for photodegradation of RhB, Catalysis Today, 264 (2016) 250-256.

[290] V.H. Nguyen, L.G. Bach, Q.T.P. Bui, T.D. Nguyen, D.-V.N. Vo, H.T. Vu, S.T. Do, Composite photocatalysts containing MIL-53(Fe) as a heterogeneous photo-Fenton catalyst for the decolorization of rhodamine B under visible light irradiation, Journal of Environmental Chemical Engineering, 6 (2018) 7434-7441.

[291] K. Wangkawong, S. Phanichphant, D. Tantraviwat, B. Inceesungvorn, Photocatalytic efficiency improvement of Z-scheme CeO2/BiOI heterostructure for RHB degradation and benzylamine oxidation under visible light irradiation, Journal of the Taiwan Institute of Chemical Engineers, 108 (2020) 55-63.

[292] J. Ding, Z. Yang, C. He, X. Tong, Y. Li, X. Niu, H. Zhang, UiO-66(Zr) coupled with Bi2MoO6 as photocatalyst for visible-light promoted dye degradation, Journal of Colloid and Interface Science, 497 (2017) 126-133.

[293] X. Chen, Z. Wu, D. Liu, Z. Gao, Preparation of ZnO Photocatalyst for the Efficient and Rapid Photocatalytic Degradation of Azo Dyes, Nanoscale Research Letters, 12 (2017) 143.

[294] W. Cui, W. An, L. Liu, J. Hu, Y. Liang, Synthesis of CdS/BiOBr composite and its enhanced photocatalytic degradation for Rhodamine B, Applied Surface Science, 319 (2014) 298-305.

[295] M. Yan, Y. Wu, Y. Yan, X. Yan, F. Zhu, Y. Hua, W. Shi, Synthesis and Characterization of Novel BiVO4/Ag3VO4 Heterojunction with Enhanced Visible-Light-Driven Photocatalytic Degradation of Dyes, ACS Sustainable Chemistry & Engineering, 4 (2016) 757-766.

[296] F.V. de Andrade, G.M. de Lima, R. Augusti, M.G. Coelho, J.D. Ardisson, O.B. Romero, A versatile approach to treat aqueous residues of textile industry: The photocatalytic degradation of Indigo Carmine dye employing the autoclaved cellular concrete/Fe2O3 system, Chemical Engineering Journal, 180 (2012) 25-31.

[297] G.E. Decker, Z. Stillman, L. Attia, C.A. Fromen, E.D. Bloch, Controlling Size, Defectiveness, and Fluorescence in Nanoparticle UiO-66 through Water and Ligand Modulation, Chemistry of Materials, 31 (2019) 4831-4839.

[298] H. Zeng, Z. Yu, L. Shao, X. Li, M. Zhu, Y. Liu, X. Feng, X. Zhu, Ag2CO3@UiO-66-NH2 embedding graphene oxide sheets photocatalytic membrane for enhancing the removal performance of Cr(VI) and dyes based on filtration, Desalination, 491 (2020) 114558.

[299] Q. Wang, Q. Gao, A.M. Al-Enizi, A. Nafady, S. Ma, Recent advances in MOF-based photocatalysis: environmental remediation under visible light, Inorganic Chemistry Frontiers, 7 (2020) 300-339.

[300] H.-P. Jing, C.-C. Wang, Y.-W. Zhang, P. Wang, R. Li, Photocatalytic degradation of methylene blue in ZIF-8, RSC Advances, 4 (2014) 54454-54462.

[301] P. George, N.R. Dhabarde, P. Chowdhury, Rapid synthesis of Titanium based Metal Organic framework (MIL-125) via microwave route and its performance

evaluation in photocatalysis, Materials Letters, 186 (2017) 151-154.

[302] R. Liang, F. Jing, L. Shen, N. Qin, L. Wu, MIL-53(Fe) as a highly efficient bifunctional photocatalyst for the simultaneous reduction of Cr(VI) and oxidation of dyes, Journal of Hazardous Materials, 287 (2015) 364-372.

[303] C.-C. Wang, J.-R. Li, X.-L. Lv, Y.-Q. Zhang, G. Guo, Photocatalytic organic pollutants degradation in metal–organic frameworks, Energy & Environmental Science, 7 (2014) 2831-2867.

[304] R. Wang, L. Gu, J. Zhou, X. Liu, F. Teng, C. Li, Y. Shen, Y. Yuan, Quasi-Polymeric Metal–Organic Framework UiO-66/g-C3N4 Heterojunctions for Enhanced Photocatalytic Hydrogen Evolution under Visible Light Irradiation, Advanced Materials Interfaces, 2 (2015) 1500037.

[305] L. Shi, T. Wang, H. Zhang, K. Chang, J. Ye, Electrostatic Self-Assembly of Nanosized Carbon Nitride Nanosheet onto a Zirconium Metal–Organic Framework for Enhanced Photocatalytic CO2 Reduction, Advanced Functional Materials, 25 (2015) 5360-5367.

[306] X.-H. Yi, S.-Q. Ma, X.-D. Du, C. Zhao, H. Fu, P. Wang, C.-C. Wang, The facile fabrication of 2D/3D Z-scheme g-C3N4/UiO-66 heterojunction with enhanced photocatalytic Cr(VI) reduction performance under white light, Chemical Engineering Journal, 375 (2019) 121944.

[307] Y. Zhang, J. Zhou, Q. Feng, X. Chen, Z. Hu, Visible light photocatalytic degradation of MB using UiO-66/g-C3N4 heterojunction nanocatalyst, Chemosphere, 212 (2018) 523-532.

[308] X. Zhang, Y. Yang, W. Huang, Y. Yang, Y. Wang, C. He, N. Liu, M. Wu, L. Tang, g-C3N4/UiO-66 nanohybrids with enhanced photocatalytic activities for the oxidation of dye under visible light irradiation, Materials Research Bulletin, 99 (2018) 349-358.

[309] G.C. Shearer, S. Chavan, S. Bordiga, S. Svelle, U. Olsbye, K.P. Lillerud, Defect Engineering: Tuning the Porosity and Composition of the Metal–Organic Framework UiO-66 via Modulated Synthesis, Chemistry of Materials, 28 (2016) 3749-3761.

[310] Y. Zhou, L. Zhang, W. Huang, Q. Kong, X. Fan, M. Wang, J. Shi, N-doped graphitic carbon-incorporated g-C3N4 for remarkably enhanced photocatalytic H2 evolution under visible light, Carbon, 99 (2016) 111-117.

[311] X. Chen, R. Shi, Q. Chen, Z. Zhang, W. Jiang, Y. Zhu, T. Zhang, Three-dimensional porous g-C3N4 for highly efficient photocatalytic overall water splitting, Nano Energy, 59 (2019) 644-650.

[312] Z. Zhou, D. Chen, N. Li, Q. Xu, H. Li, J. He, J. Lu, Three-Dimensional g-C3N4/NH2-UiO-66 graphitic aerogel hybrids with recyclable property for enhanced photocatalytic elimination of nitric oxide, Chemical Engineering Journal, 418 (2021) 129117.

[313] L. Ye, J. Liu, Z. Jiang, T. Peng, L. Zan, Facets coupling of BiOBr-g-C3N4 composite photocatalyst for enhanced visible-light-driven photocatalytic activity, Applied Catalysis B: Environmental, 142-143 (2013) 1-7.

[314] Y. Ma, Q. Tang, W.-Y. Sun, Z.-Y. Yao, W. Zhu, T. Li, J. Wang, Assembling ultrafine TiO2 nanoparticles on UiO-66 octahedrons to promote selective photocatalytic conversion of CO2 to CH4 at a low concentration, Applied Catalysis B: Environmental, 270 (2020) 118856.

[315] H. Dong, X. Guo, C. Yang, Z. Ouyang, Synthesis of g-C3N4 by different precursors under burning explosion effect and its photocatalytic degradation for tylosin, Applied Catalysis B: Environmental, 230 (2018) 65-76.

[316] K. Dai, J. Lv, J. Zhang, C. Liang, G. Zhu, Band structure engineering design of g-C3N4/ZnS/SnS2 ternary heterojunction visible-light photocatalyst with ZnS as

electron transport buffer material, Journal of Alloys and Compounds, 778 (2019) 215-223.

[317] F. Dong, L. Wu, Y. Sun, M. Fu, Z. Wu, S.C. Lee, Efficient synthesis of polymeric g-C3N4 layered materials as novel efficient visible light driven photocatalysts, Journal of Materials Chemistry, 21 (2011) 15171-15174.

[318] X. Peng, L. Ye, Y. Ding, L. Yi, C. Zhang, Z. Wen, Nanohybrid photocatalysts with ZnIn2S4 nanosheets encapsulated UiO-66 octahedral nanoparticles for visible-light-driven hydrogen generation, Applied Catalysis B: Environmental, 260 (2020) 118152.

[319] K.Y. Cho, J.Y. Seo, H.-J. Kim, S.J. Pai, X.H. Do, H.G. Yoon, S.S. Hwang, S.S. Han, K.-Y. Baek, Facile control of defect site density and particle size of UiO-66 for enhanced hydrolysis rates: insights into feasibility of Zr(IV)-based metal-organic framework (MOF) catalysts, Applied Catalysis B: Environmental, 245 (2019) 635-647.

[320] J. Zhou, Z. Zhang, B. Cheng, J. Yu, Glycine-assisted hydrothermal synthesis and adsorption properties of crosslinked porous α-Fe2O3 nanomaterials for p-nitrophenol, Chemical Engineering Journal, 211-212 (2012) 153-160.

[321] K. Dai, L. Lu, C. Liang, Q. Liu, G. Zhu, Heterojunction of facet coupled g-C3N4/surface-fluorinated TiO2 nanosheets for organic pollutants degradation under visible LED light irradiation, Applied Catalysis B: Environmental, 156-157 (2014) 331-340.

[322] Y. Wang, L. Guo, Y. Zeng, H. Guo, S. Wan, M. Ou, S. Zhang, Q. Zhong, Amino-Assisted NH2-UiO-66 Anchored on Porous g-C3N4 for Enhanced Visible-Light-Driven CO2 Reduction, ACS Applied Materials & Interfaces, 11 (2019) 30673-30681.

[323] W. Chen, T. Huang, Y.-X. Hua, T.-Y. Liu, X.-H. Liu, S.-M. Chen, Hierarchical CdIn2S4 microspheres wrapped by mesoporous g-C3N4 ultrathin nanosheets with enhanced visible light driven photocatalytic reduction activity, Journal of Hazardous

Materials, 320 (2016) 529-538.

[324] Y.-H. Li, X.-H. Yi, Y.-X. Li, C.-C. Wang, P. Wang, C. Zhao, W. Zheng, Robust Cr(VI) reduction over hydroxyl modified UiO-66 photocatalyst constructed from mixed ligands: Performances and mechanism insight with or without tartaric acid, Environmental Research, 201 (2021) 111596.

[325] C. Zhang, D. Qin, Y. Zhou, F. Qin, H. Wang, W. Wang, Y. Yang, G. Zeng, Dual optimization approach to Mo single atom dispersed g-C3N4 photocatalyst: Morphology and defect evolution, Applied Catalysis B: Environmental, 303 (2022) 120904.

[326] H. Wang, X. Yuan, Y. Wu, G. Zeng, X. Chen, L. Leng, H. Li, Synthesis and applications of novel graphitic carbon nitride/metal-organic frameworks mesoporous photocatalyst for dyes removal, Applied Catalysis B: Environmental, 174-175 (2015) 445-454.

[327] J. Xu, Y. Qi, L. Wang, In situ derived Ni2P/Ni encapsulated in carbon/g-C3N4 hybrids from metal–organic frameworks/g-C3N4 for efficient photocatalytic hydrogen evolution, Applied Catalysis B: Environmental, 246 (2019) 72-81.

[328] R. Hao, G. Wang, H. Tang, L. Sun, C. Xu, D. Han, Template-free preparation of macro/mesoporous g-C3N4/TiO2 heterojunction photocatalysts with enhanced visible light photocatalytic activity, Applied Catalysis B: Environmental, 187 (2016) 47-58.

[329] J. Wang, Y. Wang, W. Wang, Z. Ding, R. Geng, P. Li, D. Pan, J. Liang, H. Qin, Q. Fan, Tunable mesoporous g-C3N4 nanosheets as a metal-free catalyst for enhanced visible-light-driven photocatalytic reduction of U(VI), Chemical Engineering Journal, 383 (2020) 123193.

[330] Y. Wang, H. Liu, M. Zhang, W. Duan, B. Liu, A dual-functional UiO-66/TiO2 composite for water treatment and CO2 capture, RSC Advances, 7 (2017) 16232-16237.

[331] Y. Ao, K. Wang, P. Wang, C. Wang, J. Hou, Synthesis of novel 2D-2D p-n

heterojunction BiOBr/La2Ti2O7 composite photocatalyst with enhanced photocatalytic performance under both UV and visible light irradiation, Applied Catalysis B: Environmental, 194 (2016) 157-168.

[332] L. Yu, X. Zhang, G. Li, Y. Cao, Y. Shao, D. Li, Highly efficient Bi2O2CO3/BiOCl photocatalyst based on heterojunction with enhanced dye-sensitization under visible light, Applied Catalysis B: Environmental, 187 (2016) 301-309.

[333] R. Arunadevi, B. Kavitha, M. Rajarajan, A. Suganthi, Synthesis of Ce/Mo-V4O9 nanoparticles with superior visible light photocatalytic activity for Rhodamine-B degradation, Journal of Environmental Chemical Engineering, 6 (2018) 3349-3357.

[334] S. Borthakur, L. Saikia, ZnFe2O4@g-C3N4 nanocomposites: An efficient catalyst for Fenton-like photodegradation of environmentally pollutant Rhodamine B, Journal of Environmental Chemical Engineering, 7 (2019) 103035.

[335] R.A. Fernandes, M.J. Sampaio, G. Dražić, J.L. Faria, C.G. Silva, Efficient removal of parabens from real water matrices by a metal-free carbon nitride photocatalyst, Science of The Total Environment, 716 (2020) 135346.

[336] C. Shifu, J. Lei, T. Wenming, F. Xianliang, Fabrication, characterization and mechanism of a novel Z-scheme photocatalyst NaNbO3/WO3 with enhanced photocatalytic activity, Dalton Transactions, 42 (2013) 10759-10768.

[337] C.H. Nguyen, M.L. Tran, T.T.V. Tran, R.-S. Juang, Enhanced removal of various dyes from aqueous solutions by UV and simulated solar photocatalysis over TiO2/ZnO/rGO composites, Separation and Purification Technology, 232 (2020) 115962.

[338] T. Yan, Q. Yan, X. Wang, H. Liu, M. Li, S. Lu, W. Xu, M. Sun, Facile fabrication of heterostructured g-C3N4/Bi2MoO6 microspheres with highly efficient activity under visible light irradiation, Dalton Transactions, 44 (2015) 1601-1611.

[339] S.-R. Zhu, P.-F. Liu, M.-K. Wu, W.-N. Zhao, G.-C. Li, K. Tao, F.-Y. Yi, L. Han, Enhanced photocatalytic performance of BiOBr/NH2-MIL-125(Ti) composite for dye degradation under visible light, Dalton Transactions, 45 (2016) 17521-17529.

[340] Z. Yang, X. Tong, J. Feng, S. He, M. Fu, X. Niu, T. Zhang, H. Liang, A. Ding, X. Feng, Flower-like BiOBr/UiO-66-NH2 nanosphere with improved photocatalytic property for norfloxacin removal, Chemosphere, 220 (2019) 98-106.